Synthesis And Characterization Of Tetravalent Cation Substituted Mn-Zn Ferrite Suitable For High Frequency Applications

THESIS

Submitted to the
Saurashtra University, Rajkot, India
For
The Degree of
DOCTOR OF PHILOSOPHY
In PHYSICS

By

Mr. Kiran G. Saija
(M.Sc., M.Phil., B.Ed., D.C.S., Sp. L.L.B.)

Under the supervision of

Dr. Kunal B. Modi
Associate Professor
Department of Physics
Saurashtra University
RAJKOT, INDIA

April - 2012

CERTIFICATES

Statements under O.Ph.D.7 of Saurashtra University

The work presented in this thesis is my own work carried out under the supervision of Dr. Kunal. B. Modi, leads to some important contributions in Physics supported by necessary references.

Date: April - 2012
Place: Rajkot (K. G. Saija)

CERTIFICATE

This is to certify that the present work submitted for the Ph.D. degree in Physics of Saurashtra University, Rajkot, by Mr. Kiran G. Saija has been the result of several years of work under my supervision and is a valuable contribution in the field of Condensed Matter Physics.

Date: April - 2012
Place: Rajkot

(K. B. Modi)
Associate Professor
Department of Physics
Saurashtra University
Rajkot (INDIA)

ACKNOWLEDGEMENTS

With the blessing of almighty, finally the time has come when my dream, ambitions come true. First of all, I bow my head before god for his endless blessings and giving me patience, encouragement, strength, confidence, ability to achieve this academic milestone.

Knowledge in itself is a continuous process. I would have never succeeded in completing my task with the cooperation, encouragement and help provided to me by various personalities.

Secondly, I would like to express my deep sense of gratitude and sincere thanks to my guide **Dr. Kunal B. Modi**, who provided a meaningful insight into the study and helped to understand the several concepts of physics. His inspiring guidance and consistent encouragement made this work in the present form.

I am highly indebted to Dr. G. J. Baldha for his continues encouragement and useful discussion during the course of work. I am truly grateful to Professor H. H. Joshi, Head, Department of Physics, Saurashtra University, Rajkot, for his kind support during this work. I am pleased to acknowledge the support received from Professors K. N. Iyer, B. J. Mehta, M. J. Joshi, H. P. Joshi, and Dr. J. A. Bhalodia.

I place on record thanks to my research colleagues and friends Mr. Vinay K. Lakhani, Mr. Nimish H. Vasoya, Mr. Tushar K. Pathak, Mr. Kiritsinh B. Zankat, Mrs. Pooja U. Sharma, Mr. Mitesh P. Pandya for their self-less and untiring co-operation during my thesis work.

I offer my special thanks to my research colleagues Miss. Manisha C. Chhantbar, Mr. Ashish R. Tanna and Mrs. Daxa Mehta for their company and making my time cheerful during the laboratory work.

ACKNOWLEDGEMENTS

I express my thanks to Dr. H. J. Pandya for providing me technical advice regarding the experimental set - up. I am also thankful to the workshop staff for their technical help whenever I need. I specially thank Mr. M. J. Meghapara for fabricating sample holder and other technical help during my work.

I wish to express my warm and sincere thanks to honorable Trustees, Principal and members of staff of Smt. R.P. Bhalodia Mahila College, Upleta where I am working for their kind co-operation and goodwill for completing the work.

The X-ray, EDAX, SEM, and IR facilities provided by SICART, V.V.Nagar are gratefully acknowledged.

I prostrate to my most affectionate parents and I express my deepest sense of gratitude for their blessings, eternal inspiration, care and love without that I would not have been able to venture into this work.

I am thankful to my beloved wife NEHA for her close companionship, constant inspiration and encouragement during the tenure of this work and tolerating my negligence in family responsibilities. I am also thankful to my brother Hitesh, sisters Kalpana and Parul, son Krunal, daughter Shivani and all my family members for their unfailing help, encouragement, love and affection.

Many thanks to Purvi Madam and Shrey for a good hospitality during the course work.

Finally, I would like to thank to all those who helped me knowingly or unknowingly during the completion of this work.

April – 2012 **Kiran G. Saija**

Rajkot

Contents

Chapter – 1

Introduction

Brief History of magnetism

The history of magnetic materials appears to go with the development of human civilization. Chinese are understood to have used the compass even before 2500 B.C. The Greek literature from 600 B.C. mentions the power of magnets to attract iron. The scientific story of magnetism begins with a mineral called magnetite (Fe_3O_4), the first magnetic material known to man. Socrates knew that magnetite can induce iron to acquire attractive power, In other words, to become magnetic. Gilbert (1540 – 1603) realizes that earth in a huge magnetic and the compass works on this principle [1, 2]. The word 'Magnet' is derived from then Greek word 'Magnesia' a place where magnetite was widely distribution. In old English it was used for direction finding and was called 'Lode stone', meaning 'way stone. Magnetism is more of an experimental one than the others in the area of physics: in the sense that other experimental knowledge far exceeds the theoretical understanding of the fundamental properties of matter.

1.1 Introduction to ferrites

Materials containing ferric oxide (Fe_2O_3) as one of the components are generally regarded as ferrites. Ferrites crystallize in four different crystal types, namely (i) Spinel ferrite (fcc structure) (ii) Garnet (bcc structure) (iii) Ortho ferrite (orthorhombic structure) and (iv) Hexa ferrite or Magneto plumbite (hexagonal structure).

There are basically two varieties of ferrites: soft ferrite and hard ferrite. This is not a tactile quality but rather a magnetic characteristic. 'Soft ferrite'

does not retain significant magnetism whereas 'Hard ferrite' magnetization is considered permanent. With the advent of 'spinel' ferrites [3], spin glasses and amorphous magnetic materials [4], a link between these emerging fields and 'rock' magnetism was established by Neel [5]. The terms antiferromagnetism and ferrimagnetism were introduced by Neel to explain the properties of MnO and magnetite, Fe_3O_4, respectively. Explanation for antiferromagnetism behavior was proposed by Neel on the basis of the negative inters atomic exchange coupling whereby the spins of neighboring atoms align antiparallel to each other. Thus, an antiferromangnetic material consists of two identical sublattices each of which is ferromagnetically ordered but one is antiparallel to the other. For compounds exhibiting ferrimagnetism, the magnetic moments of the two sublattices are unequal; they do not cancel out but give rise to a net magnetic moment. Thus, ferrimagnetism can be considered as an uncompensated antiferromagnetism. The present day classification of materials is more elaborate and all different types of 'magnetism' and their interrelationships have been discussed by Hurd [6]. Naturally occurring magnetite is a weak 'hard' ferrite. 'Hard' ferrites possess a magnetism which is essentially permanent. In time, man-made; 'hard' ferrites with superior properties were developed but producing an analogous 'soft' magnetic material in the laboratory proved elusive.

During the 1930's research on 'soft' ferrites continued, primarily in Japan and the Netherlands. However, it was not until 1945 that J. L. Snoek of the Philips Research Laboratories in the Netherlands succeeds in producing a 'soft' ferrite for commercial applications. Originally manufactured in a few selected shapes and sizes, primarily for inductor and antenna applications,

'soft' ferrite has proliferated into countless sizes and shapes for a multitude of uses (Figure 1.1).

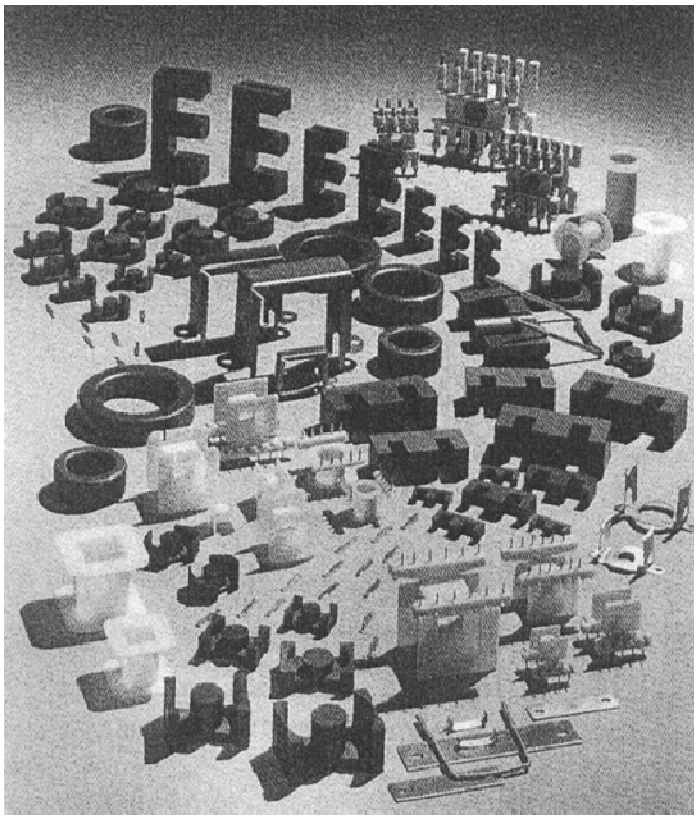

Figure 1.1 Typical ferrite cores for power applications with the mounting and winding accessories.

Ferrites are used predominately in three areas of electronic: low level applications, power applications and Electro-Magnetic Interference (EMI) suppression.

The field of ferrite is well cultivated but due to its potential applications in various fields, and interesting physics involved in it, even after seven-eight decades of its first artificial synthesis, scientists, engineers, technologists and researchers are still interested in various types of ferrite materials synthesized by different preparative techniques, parameters and conditions in bulk, nano crystalline and thin film forms and in the study of structural, magnetic,

electrical, dielectric, elastic, optical etc properties as a function of composition, substitution, frequency, temperature etc.

Ferrite is rigid and brittle. Like other ceramics, ferrite can chip and break if handled roughly. Luckily it is not as fragile as porcelain and often such chips and cracks will be merging cosmetic. Ferrite varies from silver gray to black in colour.

Ferrites have a high magnetic permeability which allows them to store stronger magnetic field than iron. Ferrites are often produced as powder, which can be sintered into solid core. Ferrite shrinks when sintered. Depending on the specific ferrites, this shrinkage can range from 10 – 17% in each dimension. Then, the unfired component's volume may be as much as 60% larger than the sintered value. Maintaining correct dimensional tolerances as well as the prevention of cracking and warp age related to this shrinkage are fundamental concerns of the manufacturing process. Ferrite cores are used in electronic inductors and electro-magnets. Early computer memories stored data in the magnetic field of ferrite cores, which were assembled into arrays of core memory. Ferrite powder is used in the coatings of magnetic recording tapes. The breadth of application of ferrites in electric circuitry continues to grow. The wide range of possible geometrics, the continuing improvements in material characteristics and their relative cost-effectiveness make ferrite components the choice for both conventional and innovative applications.

Applications of ferrites

Professor Kato once said “Something to the effect that the whole world was contained in ferrites” [6]. Ferrites are used in the applications from simple lifting magnets to the most complex micro wave communication. In addition to the new advent of the new development such as radars, satellite communication, memory and computer applications. There has been a corresponding growth in consumer electronics markets in radio, television and more recently video tape recorders.

The most recent reason for the up surge in ferrite interest has been the development of new small, efficient power supplies. These power supplies are being used in computers, microprocessor, communications and entertainment applications [9]. The ferrites core memory was the basis of the IBM 360 computer which would become the standard for the industry [9]. The first use of ferrite materials in a power application was to provide the time dependent magnetic deflection of the electron beam in a television receiver, where Mn-Zn ferrite became the undisputed core material for the line time-base/e.h.t transformer and the field shaping yoke used in the picture tube beam-deflection system. Later, other ferrite compositions such as Li-Zn, Ni-Zn or Mg-Zn ferrites were introduced for deflection yokes requiring high resistivity to facilitate the winding of the coils directly onto the ferrite. However most high performance television deflection yokes are made of Mn-Zn ferrite. In domestic radio receivers ferrite rods or plates enabled compact a.m antennas to be made.

The applications started in the field of telephony transmission where carrier (frequency Division Multiplex) systems, being essentially analogue,

required large numbers of high performance inductors and transformers mainly operating in the frequency range from about 40kHz to 500kHz. The combination of good magnetic properties and high resistivity made these ferrites very suitable as core materials in this application. Since, the resistivity could be at least a million times greater than the values for metallic magnetic materials, laminated or powder cores could be replaced with solid ferrite cores. These could be made in more functional shapes than their metallic counterparts and their better performance enabled frequency division multiplex (FDM) telephony to be extended to higher frequencies than had hither to been possible [7].

Other applications proliferated. Of these the most important were the use of ferrites for recording heads for audio, data, and later, video recorders thus use in inductive elements for radio interference suppression and their application as cores for transformers in switched mode power supplies. In recent years the latter application has increased very strongly and is now comparable to television ferrite applications in terms of production quantities [7].

Today, ferrites are employed as noise filters in power lines on the input to all types of electronic equipment [8]. These are fundamental functional materials of electronic industry. As important parts of magnetic materials ferrite materials play a heavy role in electronic industry, electronic information industry, car industry, motorcycle industry etc. mean while they are also widely used in medical treatment, mining and metallurgy, industrial automation, oil energy industry and civil industry due to their high coercive force, high electric resistance, long time stability and economical price.

In the 1970's about 60% of the soft ferrites were manufactured in Japan. In the 1980's Western Europe and Southeast Asia entered the market and spread out the suppliers geographically. However, for reasons of economy of manufacturing the geographic picture for ferrite vendors has changed. Many mergers and ownership changes have occurred. These include;

1. Change from Siemens to Siemens-Matsushita and finally to EPCOS.
2. Sale of Phillips ferrite (Ferroxcube) to Yageo
3. Sale of Thomson SCF to AVX

More recently, there has been an even more dramatic shift in geography of ferrite manufactures to China. The main reason for this shift has been the lower production costs. Table taken from J.J.Ruther's paper at ICF9 estimates the change from 1980 to 2010. In India ferrites production have also increased but on a much smaller scale.

Year Production in x 1000 m.t.p.y	1980 100	1990 150	1995 180	2000 200	2005 250	2010 350
%Western Europe	15	15	Stable	12	3	2
% Eastern Europe	10		decreasing		1	2
% USA	20		decreasing		2	2
% China	5		increasing		64	75
% Japan	32		decreasing		5	4
% Korea	15		decreasing		6	4
% India	2		increasing		3	4
% Rest of the world	1		increasing		2	7

In some of these cases ferrites yield higher efficiency, small volume, lower costs, greater uniformity, or easier manufacture that cannot be obtained with other materiasl. Several of these applications are [7, 10]:

(i) Filter Inductors

(ii) Antenna Cores

(iii) Fly back Transformers

(iv) Magnetic Amplifiers

(v) Magnetic Memories and Switches

(vi) IF transformers and tuned inductor

(vii) Ceramic magnet for medical treatment

(viii) Ferrite nano particles are used as catalyst, humidity sensor

(ix) Superparamagnetic nano particles of ferrites for different biomedical applications e.g. for achieving local hyperthermia

(x) Mn-Zn nano particles based magnetic fluid is used as a coolant in electric transformer

(xi) Some miscellaneous ferrite applications are: magnetostrictive transducer, copier powder, ferrite tiles for Anechoic chambers [8]

1.2 Aim and outline of the present work

There are basically two types of magnetic materials (i) metallic and (ii) metallic oxide or ceramics. The most common metallic material is laminated steel used in mains transformer This material works well at mains frequency i.e. 50Hz, but as frequency increases due to various types of looses, particularly hysteresis and eddy current looses, this material becomes ineffective. Metallic oxides are called ferrites.

Ferrite materials used for such high frequency applications should have certain characteristics (i) high value of saturation magnetization (ii) low power loss/high value of initial permeability. Furthermore, ferrite material should have high density; it should possess good homogeneity and fine grain structure.

Amongst the soft ferrites, manganese- zinc ferrites are most common, and are used in many more applications than their counterparts, such as nickel-zinc ferrites. Within the Mn-Zn category, large varieties of materials are possible, and the material selection is mainly a function of the application that needs to be accommodated. The application dictates the desirable material characteristics, which in turn determines the chemical composition of the ferrite material. Manganese zinc ferrites are primarily used for frequencies less than 2 MHz. Figure 1.2 shows the composition diagram for MnZn ferrites in mole% for Ferric oxide, Manganese oxide and Zinc oxide. It identifies the composition which gives optimum performance for saturation flux density (Bs), low losses (Q) and high initial permeability (μ_i). It also identifies the Curie temperature (T_C) lines for 100 and 250°C. From this composition chart, it is clear that not one composition of Mn ferrite can fulfill all design objectives.

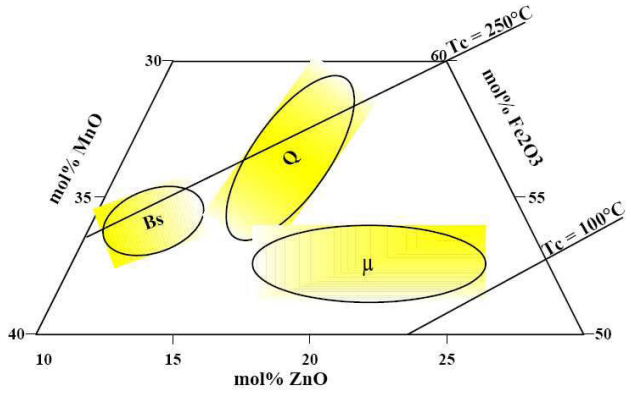

Figure 1.2 - Composition Diagram for Mn-Zn ferrites.

The research work carried out deals with Si^{4+} and Ti^{4+} cations substituted Mn-Zn ferrite with generalchemical formulae:

(i) $Mn^{2+}_{0.7+x}Zn^{2+}_{0.3}Si^{4+}_{x}Fe^{3+}_{2-2x}O^{2-}_{4}$ (x = 0.0, 0.1, 0.2 and 0.3)

(ii) $Mn^{2+}_{0.7+x}Zn^{2+}_{0.3}Ti^{4+}_{x}Fe^{3+}_{1.9-2x}Al^{3+}_{0.1}O^{2-}_{4}$ (x = 0.0, 0.1, 0.2 and 0.3)

The above mentioned ferrites are synthesized by the usual double sintering ceramic technique. The structural, magnetic, electrical, elastic, dielectric, Infrared spectral properties are studied as a function of composition, frequency and temperature.

The substitution of small amount of Al^{3+} -ions (≤ 0.2 ion / formula unit) has some beneficial effects on power handling capacity. On the other hand, incorporation of tetravalent cations like Si^{4+} and Ti^{4+} originate the high grain boundary resistivity due to complex compositions of the grain boundary layer on ferrite grains, as well as it also from strong chemical bond with Fe^{2+} ions thereby reducing the mobility of charge carriers results in decrease in power loss.

Following experimental tools have been employed to characterize the samples.

1. Energy dispersive analysis of X-rays (EDAX) (300K)
2. X-ray powder diffractometry (300K)
3. Scanning electron microscopy (300K)
4. FT-IR spectroscopy (300K) (400-1000 cm^{-1})
5. High field magnetization (300K and 80K) (H = 7kOe)

   Low field Susceptibility (0.5 Oe)(300-700K)
6. Permeability measurements (300-600K) (100Hz-1MHz)

7. DC resistivity measurements (300-700K)
8. Thermo electric power measurements (300-500K)
9. I-V characteristics (0-400V) (300-600K)
10. Dielectric measurements (300-600K) (100Hz-1MHz)

References

1 A. H. Morrish, The Physical Principles of Magnetism, J. Wiley and Sons, New York, (1965).

2 S. Chikazumi, The Physics of ferromagnetic (Oxford university press, Oxford, (1997).

3 J. Smit and H. P. J. Wijn, “Ferrites” John Wiely & Sons, New York (1959).

4 K. Binder and A. P. Young, Rev. Mod. Phys. 58 (1986) 801.

5 L. Neel, Adv. Phys. 4(1955)191.

6 C. M. Hurd, Contemp. Phys. 23(1982)469.

7 E. C. Snelling “ Soft Ferrites, Properties and Applications”. Butterworth and Co. (Publishers) Ltd. London (1988).

8 A. Goldman, “Modern Ferrite Technology” Van Nostrand Reinhold, New York (1990).

9 Martha Pardvi- Horvath, Journal of Magnetism and Magnetic Materials 215-216 (2) (2000) 171.

10 Noboru Ichinose, “Introduction to Fine Ceramics”, Ohmsha (Publishers) Ltd. Japan (1987).

Chapter – 2

Crystal structure and magnetic interactions in spinel ferrites

2.1 Crystal Structure and Chemistry

Spinel structure

The spinel crystal structure is the most well-known, diverse and useful example of uncompensated antiferromagnetism. The spinel structure is named after the mineral spinel, magnesium aluminates ($MgAl_2O_4$) and can be represented as M' M''_2 X_4 , where X represents oxygen or one chalcogenic bivalent anion (S^{2-} , Se^{2-} , Te^{2-}) and M' and M'' are metallic ions. The valences have to fulfill the electroneutrality requirements. Due to large electronegativity of Oxygen, the ionic type of bonds prevails in almost all oxide spinels. The crystallographic structure is formed by a nearly closed packed face centred cubic (fcc) array of anions with two unequivalent sites for cations. These differ in oxygen coordination; four oxygen ions surround tetrahedral cationic sites and octahedral sites by six oxygen ions. These are also called the A- and B-sites, respectively. In a cubic unit cell, 64 tetrahedral sites and 32 octahedral sites are present. of which only 8 and 16 sites are occupied by metal ions respectively. The geometry of the occupied interstitial sites is shown in Figure 2.1, where the primitive cell contains two formula units is shown [1].

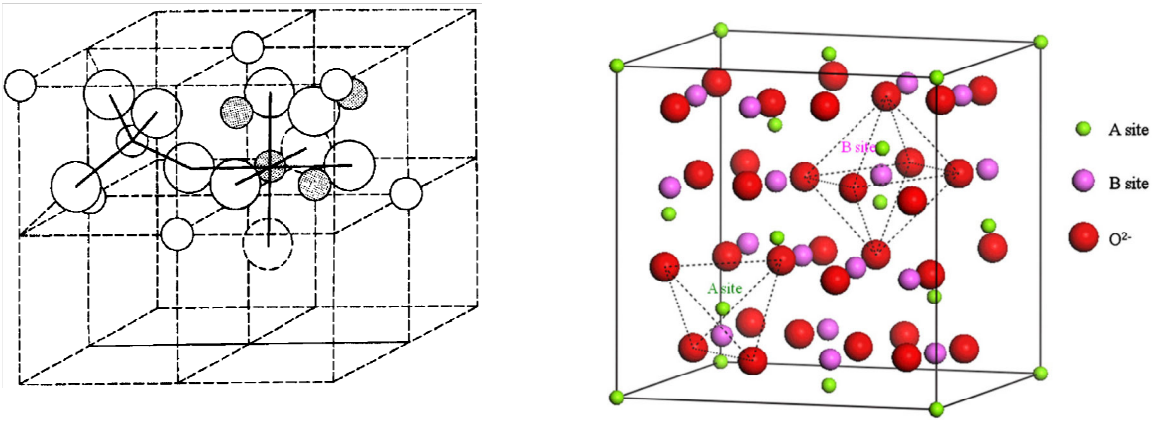

Figure 2.1 The geometry of the occupied interstitial sites in spinel Structure.

The symmetry of the structure is cubic and belongs to the space group O_h^7 (Fd3m). A small displacement defined by a single parameter 'u' of the anions, from their ideal position is allowed along the corresponding body diagonal which enables a better matching of anion positions to the relative radii of the A- and B- sites cations. For the ideal closed packed anion lattice, u = 3/8, but in real situations it is more than 3/8. The local symmetry of the cation sites is cubic in the case of tetrahedral (A) site and trigonal in the case of octahedral (B) site, the trigonal axis being one of the body diagonals. The trigonal symmetry is due to both the configurations of neighbouring cations and the distortion of the anion octahedron if $u \neq 3/8$. Each of the body diagonals belongs to just one of the B cations in the primitive cell. On the other hand the local symmetry of the A positions remain cubic even if $u \neq 3/8$. When considering the aspects for which the local symmetry is irrelevant, all the A positions may be treated as belonging to one sublattice (tetrahedral or A-site), and all the B positions may be unified to form another sublattice (octahedral or B-site).

Both translational and local symmetries corresponding to the O_h^7 space group strictly apply only if each sublattice contains only one kind of cations, i.e. if all M' ions in M' M''_2 X_4 are in tetrahedral and all M" ions are in octahedral positions. The spinel is then called normal spinel. We also have so called inverse spinel structure in which half the cations M" are in A positions and the rest, together with the M' ions, are randomly distributed among the B positions. There are many examples of intermediate cases between a normal and an inverse spinel where a fraction of M' and M" ions are inverted, that is M' occupies B positions and M" occupies A positions. They are termed as

partially inverse spinels. Therefore, in order to characterize the spinel structure fully, a further parameter is needed describing the degree of inversion. The formula may be explicitly written as, $(M'_{1-\delta}\, M''_{\delta})\, [M'_{\delta}\, M''_{2-\delta}]\, X_4$, where, δ is known as inversion parameter, and is equal to zero in case of normal spinel and one in case of inverse spinel. As a part of convention, the cations at the tetrahedral (A) sites are written in parentheses "( )" and those at the octahedral (B) sites in square brackets "[ ]".

The electroneutrality leads to three basic types, according to the cation valency combinations. These are,

$M'^{2+}\, M''^{3+}O_4$: (2-3 spinel), e.g. $Ni^{+2}Fe_2{}^{+3}O_4$, $Cu^{+2}Fe_2{}^{+3}O_4$

$M'^{4+}\, M''^{2+}O_4$: (4-2 spinel), e.g. $Ge^{+4}Fe_2{}^{+2}O_4$, $Ti^{+4}Fe_2{}^{+2}O_4$

$M'^{6+}\, M''^{1+}O_4$: (6-1 spinel), e.g. $Mo^{+6}\, Li_2{}^{+1}O_4$, $W^{+6}Ag_2{}^{+1}O_4$

It is found that practically any cation with radius within the limits 0.4 to 1Å may be incorporated into the spinel structure and most of them can occur in both octahedral and tetrahedral positions. The smallest cations with valency ≥ 4, however, are found in the tetrahedral coordination only, while the monovalent cations occurring mainly in 6-1 spinels are confined to the octahedral sites. Besides the geometrical factors, the distributions of cations among the A and B positions is influenced by many other factors.

Site preferences of the ions

The preference of the individual ions for the two types of lattice sites is determined by:

1. The ionic radii of the specific ions
2. The size of the interstices
3. Temperature
4. The orbital preference for specific coordination

The most important consideration would appear to be the relative size of the ion compared to the size of the lattice site. The divalent ions are generally larger than the trivalent (because the larger charge produces greater electrostatic attraction and so pulls the outer orbits inward). Table 2.1 lists several of the applicable ionic radii. The octahedral sites are also larger than the tetrahedral (Table 2.2). Therefore, it would be reasonable that the trivalent ions such as Fe^{3+} would go into the tetrahedral sites and the divalent ions would go into the octahedral. Two exceptions are found in Zn^{2+} and Cd^{2+} which prefer tetrahedral sites because the electronic configuration is favorable for tetrahedral bonding to the oxygen ions. Thus, Zn takes preference for the tetrahedral sites over the Fe^{3+} ions. Zn^{2+} and Co^{2+} have the same ionic radius but Zn prefers tetrahedral sites and Co^{2+} prefers octahedral sites because of the configurationally exception. Ni^{2+} and Cr^{3+} have strong preferences for octahedral sites, while other ions have weaker preferences.

Table 2.1 Radii of metal ions involved in spinel ferrites.

Metal	Ionic Radius Angstrom units Å
Mg^{2+}	0.78
Mn^{3+}	0.70
Mn^{2+}	0.91
Fe^{2+}	0.83
Fe^{3+}	0.67
Co^{2+}	0.82
Ni^{2+}	0.78
Cu^{2+}	0.70
Zn^{2+}	0.82
Cd^{2+}	1.03
Al^{3+}	0.57
Cr^{3+}	0.64

Table 2.2 Radii of Tetrahedral and Octahedral sites in some ferrites.

Ferrite	Tetrahedral Site Radius Å	Octahedral Site radius Å
$MnFe_2O_4$	0.67	0.72
$ZnFe_2O_4$	0.65	0.70
$FeFe_2O_4$	0.55	0.75
$MgFe_2O_4$	0.58	0.78

Unit Cell Dimensions

The dimensions of the unit cell are given in Angstrom Units which are equivalent to 10^{-8} cm. Table 2.3 lists the lengths, a_o, of some spinel unit cells. If we assume that the ions are perfect spheres and we pack them into a unit cell of measured (X-ray diffraction) dimensions we find certain discrepancies that show that the packing is not ideal. The positions of the ions in the spinel lattice are not perfectly regular (as the packing of hard spheres) and some distortion does occur. The tetrahedral sites are often too small for the metal ions so that the oxygen ions move slightly to accommodate them. The oxygen ions connected with the octahedral sites move in such a way as to shrink the size of the octahedral cell by the same amount as the tetrahedral site expands .The movement of the tetrahedral oxygen is reflected in a quantity called the oxygen parameter which is the distance between the oxygen ion and the face of the cube edge along the cube diagonal of the spinel sub cell. This distance is theoretically equal to $3/8a_o$.

Table 2.3 Unit cell lengths of some simple ferrites.

Ferrite	Unit Cell Length (Å)
Zinc Ferrite	8.44
Manganese Ferrite	8.51
Ferrous Ferrite	8.39
Cobalt Ferrite	8.38
Nickel Ferrite	8.34
Magnesium Ferrite	8.36

Crystal field splitting of energy levels and John-Teller Effect

With respect to the magnetic properties, the interest is primarily in transition metal ions particularly those of $3d^n$ group. The outer d-electrons of these ions may be regarded as practically localized in almost all oxide spinels so that the crystal (or ligand) field theory applies. This theory says that the low lying energy levels are decisive for the magnetic behaviour. The origin of the ligand field splitting of levels is attributed to both the electrostatic crystal field and the covalency between the cation and the surrounding anions (ligands). Both these effects contribute to the stabilization of cations in the given surrounding. Crystal or ligand field stabilization energy = lowering of the ground level with respect to the ground level of the free ion. In an octahedral environment, the five d orbitals on a transition metal atom are no longer degenerate but split into two groups, the t_{2g} group of lower energy and the e_g group of higher energy as shown in Figure 2.2. If possible, electrons occupy orbitals singly, according to Hund's rule of maximum multiplicity. For d^4 to d^7 atoms or ions, two possible configurations occur, giving low spin and high spin states; these are shown for a d^7 ion in Figure 2.3 In these, the increased energy, Δ, required to place an electron in an e_g orbital, and hence maximize the multiplicity, has to be balanced against the repulsive energy or pairing, P, which arises when two electrons occupy the same t_{2g} orbital. The magnitude of Δ depends upon the ligand or anion to which the metal ion is bonded: for weak field anions (ligands), Δ is small and the high spin state configuration occurs, and vice versa for strong field ligands. For magnitude of Δ, generally $\Delta(5d) > \Delta 4(d) > \Delta 3(d)$. Consequently, the high spin behaviour is rarely observed in the 4d and 5d series.

In many transition metal compounds, the metal coordination is distorted octahedral and the distortions are such that the two axial bonds are either shorter than or longer than the other four bonds. The Jahn-Teller effect [2, 3] is responsible for these distortions in d^9, d^7 (low-spin) and d^4 (high spin) ions. Consider the d^9 ion Cu^{2+} whose configuration is $(t_{2g})^6$ $(e_g)^3$. One of the e_g orbitals contains two electrons and the other contains one. The singly occupied orbital can be either d_z^2 or $d_{x^2-y^2}$ and in a free ion situation both would have the same energy. However, since the metal coordination is octahedral the e_g levels, with one doubly and one singly occupied orbitals, are no longer degenerate. The e_g orbitals are high energy orbitals (relative to t_{2g}) since they point directly towards the surrounding ligands and the doubly occupied orbital will experience stronger repulsions and hence have somewhat higher energy than the singly occupied orbital. This has the effect of lengthening of the metal-ligand bonds in the directions of the doubly occupied orbital, e.g. if the d_z^2 orbital is doubly occupied, the two metal-ligand bonds along the z axis will be longer than the other four metal-ligand bonds. The energy level diagram for this latter situation is shown in Figure 2.4. Lengthening of the metal-ligand bond along the z-axis leads to a lowering of the d_z^2 orbital. The distorted structure is stabilized by an amount $(½)\delta_2$ relative to the regular octahedral arrangement and, hence, the distorted structure becomes the observed, ground state.

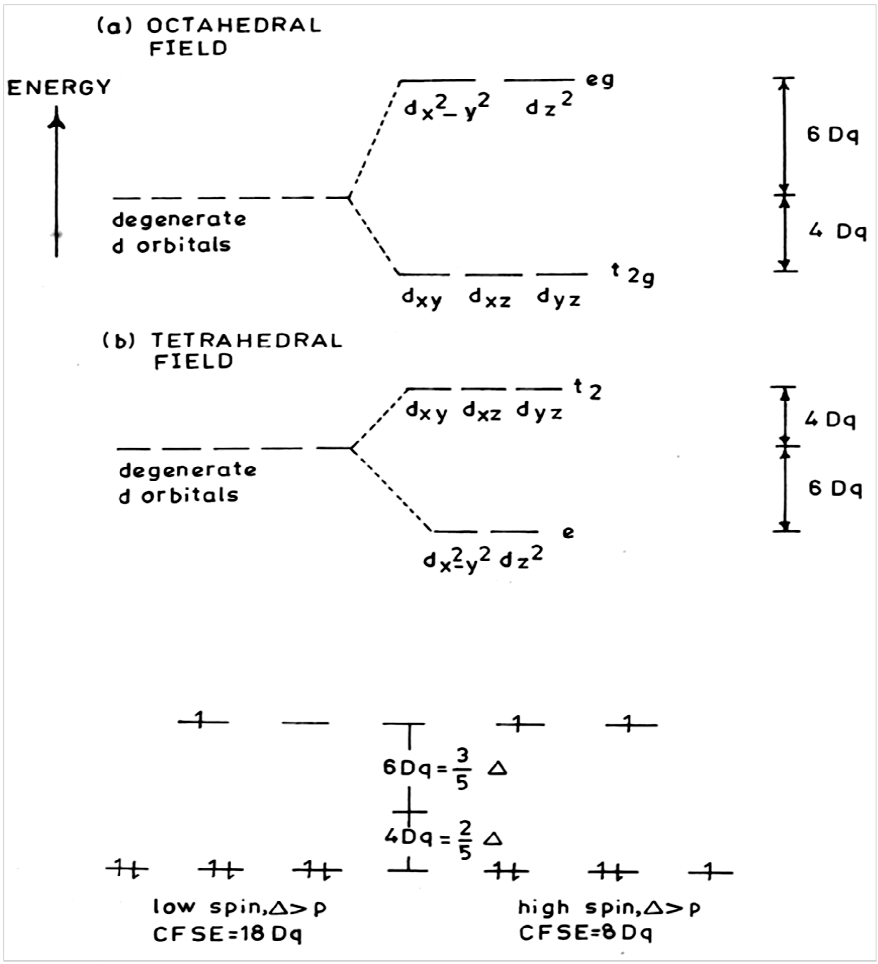

Figure 2.2 Crystal field splitting of Energy level and spin states in octahedral coordination.

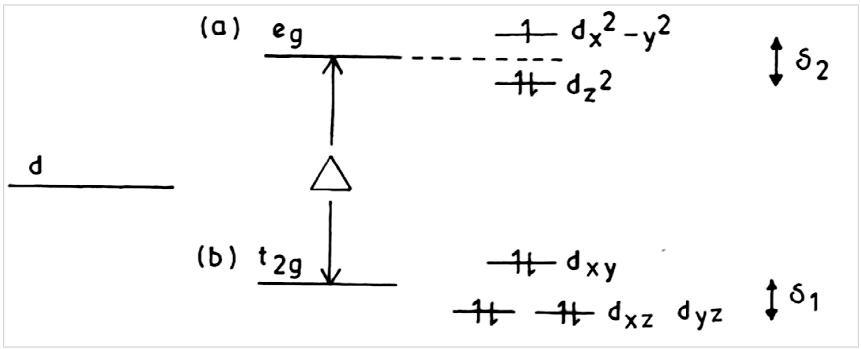

Figure 2.3 Energy level diagram for the d-levels in an ion experiencing a Jahn-Teller distortion.

In the oxide spinels, the cooperative Jahn-Teller effect is frequently encountered. The necessary condition for this to appear is the presence of transition metal ions which have an orbitally degenerate electronic ground

state. The interaction between the degenerate states and the lattice vibrations leads to an effective coupling between electronic states on different cations. When this coupling is sufficiently strong and the concentration of active cations exceeds a certain critical value, the electronic states order and simultaneous a structural phase transition from cubic to lower symmetry appears. Thus, Jahn-Teller effect refers to the condition in which a crystal lattice is distorted from the cubic to tetragonal configuration as a consequence of the possession of some 3d orbitals of fewer electrons than other orbitals. This condition results in an electrostatic imbalance that has the effect of repelling some oxygen anions more than others. In effect, these anions are pushed further away, thus producing the change from cubic to tetragonal symmetry. The phase with lower symmetry is stable only below a critical temperature. In the B-site, there are two ions, namely Mn^{3+} and Cu^{2+} both having doubly degenerate ground state of e_g type, which exhibit the Jahn-Teller effect. The corresponding distortion is always tetragonal with $c/a > 1$. The $CuFe_2O_4$ having the degree of inversion, $0.06 < \delta < 0.24$ exhibits Jahn-Teller effect with c/a ratio ~ 1.06 [4].

Chemistry of Ferrites

The oxide spinels are commonly prepared at elevated temperatures by a direct solid-state reaction between the simple oxides. The relevant temperature range is about 800°C to 1500°C, depending on the type of cations. The thermodynamic stability of spinels compared to the constituent oxides is given by Gibbs free energy of formation (ΔG) for the reaction,

$M' O + M''_2O_3 \rightarrow M' M''_2 O_4$

The largest contribution to the crystal energy in oxide spinels comes from the Coulomb energy of the charged ions (Madelung energy),

$E_c = (-e^2 / a) A_M$

where, e is the charge of electron, a is the lattice parameter and A_M the Madelung constant. The Madelung constant, A_M can be expressed as a function of the mean electric charge q_A of the cations in tetrahedral positions and of the oxygen parameter u. With increasing A_M the stability of the spinel increases. Therefore, owing to its dependence on q_A, the Coulomb energy generally plays an important role in the equilibrium distribution of cations among tetrahedral and octahedral positions, even though in some cases other energy contributions may become important.

According to the formula, $(M'_{1-\delta} M''_{\delta}) [M'_{\delta} M''_{2-\delta}] O_4$, oxide spinels may have various degrees of inversion. If the energy difference between two limiting cases $\delta = 1$ and $\delta = 0$ is not very large, we expect the distribution of cations to be random at high temperatures due to the prevailing influence of entropy term –TS in the free energy. When the temperature is lowered, the spinel tends to be more or less normal or inverse depending on the sign and amount of energy corresponding to the interchange of cations M', M'' in different sublattices. The equilibrium distribution will be given by the requirement that the Gibbs free energy is minimum, i.e.

$dG/d\delta = \{(dH/d\delta) - T(dS/d\delta)\} = 0$

If one restricts to configurationally entropy of cations and assumes total randomization in both sublattices, S may be approximated by,

$S = Nk [- \delta \ln \delta + 2 (\delta - 1) - (\delta + 1) \ln (\delta + 1)]$

Defining further $\Delta P = dH/d\delta$, we find, $\delta (1+ \delta/(1 - \delta)^2 = \exp (- \Delta P/RT)$

which determines the equilibrium value of δ at temperature T. Generally, ΔP depends on δ and frequently a linear expression $\Delta P = H_0 + H_1 \delta$is used to describe the experimental results. Here, H_0 and $H_0 + H_1$ may be interpreted as energies connected with interchange of ions M', M" from different sublattices in the case completely normal and inverse distribution, respectively.

When ΔP < 5 kCal/mol, a partially inverted spinel is usually observed. Otherwise, the energy difference between the normal and inverse structures is sufficient for the spinel to attain either normal or inverse structure. Once again the main contributions to ΔP come from Madelung energy, Born repulsion energy and further from polarization and ligand field effects. On the basis of systematic studies of cation distribution in various spinels it has been recognized that some regularities exist in them pointing to the possibility to connect the distribution to individual site preference of cations. In such a case, the energy ΔP can be expressed as a difference $\Delta P = P(M') - P(M'')$, of individual preference energies P of cations M' and M". Once P(M') and P(M") are known for all relevant cations, the distribution of ions in arbitrary spinel could be predicted. The values of P (M) for different spinels are shown in Figure 2.4.

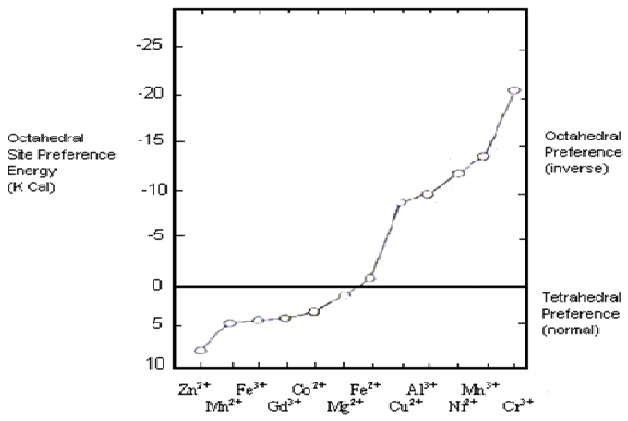

Figure 2.4 Cation site preference energy for various transition metal ions

Chemistry, crystal structure and microstructure determine the engineering material characteristics of ferrites. Many desirable combinations of chemical ingredients and basic structure cannot be obtained because some ions are incompatible with certain crystal structures despite the best efforts of materials scientists. Microstructure includes the size and number of voids, size of grains, and presence of grain boundary phases, grain shape and orientation. In essence, microstructure is the architecture of the materials that is, how the various phases and crystallites are put together, their particular patterns and arrangements, and how these are joined. Ferrite microstructures are extremely sensitive to processing because the pre-reaction and grinding of raw materials, forming technique employed, sintering time, and temperature and cooling conditions influence crystal composition and size, and also the size and volume of pores.

2.2 Magnetic interactions in spinel oxides

After having reviewed the crystallographic and some other associated aspects of spinel ferrites, we shall now review their magnetic behavior.

Atomic magnetic moment is due to the motion of electrons in their orbits and due to their spin motion. Although the orbital motion of electrons may contribute to the atomic magnetic moment when the atom is in free state, when it is a part of solids the contribution of orbital motion is often very small and negligible. For the present case of spinel ferrite, the cations are subjected to the very intense inhomogeneous electric field which influences the orbital angular momentum partly due to the large radius of 3d shell and partly due to the lack of any outer electrostatic shell to screen the 3d shell whose unpaired

electrons are responsible for net magnetic moment. The spin angular momentum is however, not affected by the influence of anion field.

The quenching of the orbital momentum can be pictured as follows: The orbital angular momentum assumes definite orientation relative to the crystal lattice under the influence of the electric field of anions which has the symmetry of crystal. This orbit-lattice coupling is so strong that the angular momentum vector direction and therefore the angular magnetic moment is locked in a particular direction and does not respond to the applied external magnetic field.

The atom with a resultant spin quantum number S gives the spin magnetic moment as follows,

$\mu = g\sqrt{s(s+1)}\mu_B$ g = Lende's splitting factor

Ferromagnetism

Oxide spinels represent a classical example of a crystal structure, which allows a special type of magnetic order called ferromagnetism. In fact, spinels were the first materials where the existence of such magnetic ordering was recognized by Neel [5]. He coined the word 'ferrimagnetism' and elaborated the molecular field theory to account for this type of order. Until the discovery of ferrimagnetism, the magnetic properties of the few magnetic spinels then known, such as magnetites, were classified as ferromagnetics. The difficulty, however, was to understand the low magnetic moments, the deviations from Curie-Weiss law and some other peculiarities [6, 7]. The departure from the ferromagnetic behaviour was excellently explained by Neel in his simple yet elegant theory. Ferrimagnetism can be considered as a special case of

antiferromagnetism, where at least two unequal and antiparallel systems of atomic moments exist giving rise to spontaneous magnetization.

The simplest case of ferrimagnetism is a system with two sub-lattices, where all the octahedrally coordinated sites are considered to compose one sub-lattice (B) and in similar manner all the tetrahedrally coordinated sites to compose (A) sub-lattice. These sites are crystallographically nonequivalent and when both contain paramagnetic ions in sufficiently high concentration the ferrimagnetism may occur. The ferrimagnetism, however, is a broad class and includes materials with more than two sub-lattices and other configurations of moments, rather complicated, like triangular and spiral etc.

The intense short-range electrostatic field causes the interactions, which are responsible for the magnetic ordering. These interactions are quantum mechanical in origin and are related to the overlap of the charge distributions of the atoms concerned.

The exchange interaction coupling the spins of pair of electrons is given as proportional to the scalar product of two spin vectors.

$$\varepsilon_{ij} = -2 \cdot J_{ij} S_i S_j$$

where J_{ij} is the exchange constant given as

$$J_{ij} = \int \Psi_i^*(1) \cdot \Psi_j^*(2) \cdot \left(\frac{2}{r_{12}} + \frac{2}{r_{ij}} - \frac{1}{r_{i1}} - \frac{1}{r_{j2}} - \frac{1}{r_{12}} - \frac{1}{r_{ji}} \right) \cdot \Psi_i(2) \Psi_j(1) dv_1 dv_2$$

where, 1,2 refer to two electrons; i,j refer to two atoms; r's are the distances. The magnitude and sign of the exchange integral decide the type and strength of the magnetic ordering. The ferromagnetism results from strong parallel coupling of spins having large, positive J values. The semi empirical

calculations to decide the type of ordering depending on the type of the ions and distances between them were given by Slater [5].

The interactions causing magnetic ordering in spinels, however, are not the same as described above. In spinels the cations are situated at large distances and have anions as their nearest neighbours. These anions obscure the direct overlap of the cations' orbitals sometimes partially and at times completely. Moreover, the ratio of the distance between two cations to the diameter of the concerned electron orbit comes about 2.5 indicating a moderate to weak positive interaction favouring weak ferromagnetic type of ordering [6]. But experimental evidences favour strong interactions of negative type, as evident from the observed high magnetic transition temperatures of spinel ferrites. So it is unlikely that the interactions are dependent on direct coupling of cations spins. On the other hand since anions possess no magnetic moment the direct coupling with anions are also ruled out.

A "superexchange" mechanism was proposed by Kramer [7] for such cases and was developed by Anderson [8-11] and Van Vleck [12]. The superexchange mechanism between cations operates via the intermediate anions. The superexchange mechanism was explained by Anderson considering a simple example of MnO. In the ground state there cannot be any spin coupling of oxygen (S = 0) possible with cations. But in the excited state, oxygen gives a p electron from a 2p pair, which becomes a temporary part of any one of the Mn ions. The consequence of the process is the emergence of net spin on the oxygen ion due to which it can then after interact with the other Mn ion by direct exchange. If the separation is not very large the interaction will be negative favouring antiparallel arrangement of

spins in the two Mn ions. The spinel ferrites also undergo the same indirect interaction, which is responsible for the strong negative coupling of the cation spins in the above case. The p orbital of the oxygen anion overlaps with cation d orbital which accepts an electron from oxygen's p shell. The p electron will occupy the next available place in d orbital of cation according to the Hund's rule i.e. if 3d is less than half filled the p electron will be placed parallel to the electrons already present in 3d shell. But if 3d is equal to or more than half full the later will be placed antiparallel to the net magnetization. If both the cations are of same type, the Hund's rule applying to both the cations will orient the net spins on both 3d shell antiparallels since 2p electrons are paired according to Pauli Exclusion Principle.

The sign and the strength of the super exchange interactions depend, however, upon the bond angle and the bond distances involving the two cations and an intermediary anion. The bond angles are the angle formed between the bonds connecting the intervening anion with two cations. Several authors including Slater [13], Nagmiya [14], Goodenough [15] and Kanamori [16] have discussed the various types super exchange interactions considering the symmetry properties of electron orbitals. Goodenough [17] and Kanamori came up with some predictions concerning the sign and strength of super exchange interactions in their semi-empirical rules.

The magnetic orbitals involved in the super exchange interactions in spinel are the T_{2g} and E_g orbitals of 3d metal ions and P_x, P_y and P_z orbitals, which are highly directional, of intermediary anions. The T_{2g} orbitals consist of d_{xy}, d_{yz} and d_{zx} while E_g orbitals consist of d_{z^2} and $d_{x^2-y^2}$.

The semi empirical rules given by Goodenough and Kanamori (G.K.) are:

(i) When the two cations have lobes of magnetic orbitals directed towards the anion as to involve a reasonably large overlap (i.e. the 3d orbitals are non-orthogonal with d_{z^2} type orbitals each with one d electron and pointing directly towards the legand ions in 180° configuration) the exchange is antiferromagnetic type because the antiparallel electrons gain energy by spreading into overlapping orbitals.

(ii) When the participating cation orbitals are of the d_{xy} type, for example, each with one d electron and interacting with the P orbital of the legand in 180° configuration, the exchange interaction is antiferromagnetic type but the strength is not as large as in 1.

(iii) In 90° configuration of the above orbitals along with d_{z^2} orbital each with one electron, the P orbital making σ bond with one cation is making π bond with another cation in this configuration. One expects strong overlapping and an antiferromagnetic exchange interaction.

(iv) When magnetically filled cation orbital is in contact with an empty cation orbital via the intervening legand ion, the exchange is ferromagnetic. But it is not as strong as the antiferromagnetic exchange.

Few more qualitative conclusions drawn are:

(a) From the orbital symmetry of cation-anion-cation configuration one yields $J_{d8} > J_{d5} > J_{d3}$ for 180° configuration $J_{d5} >> J_{d8}$ for 90° configuration. J_{d3} can either be ferro or antiferro in nature.

(b) From the valance state of the cation $J_{trivalent} > J_{divalent}$.

The higher charge on any cation increases the covalent nature of bond and results in greater overlap of orbitals giving stronger exchange interaction. The role of the legand ion is more obscure but generally it is observed that exchange interaction decreases with increasing electron negativity.

We refer now ourselves to the possible configurations in the spinel structure. We can identify basically three types of super exchange interactions to operate in the spinels:

- J_{AB} exchange interaction namely the inter sub-lattice interaction between cations on the A- and B- sub-lattices.
- J_{AA}, J_{BB} exchange interaction namely the intra sub-lattice interaction operating among the cations on the A- sites and B- sites.

Figure 2.5 gives the possible M-O-M (where M = A or B) configurations involving these three exchange interactions. Since the exchange forces are of short range in character the interactions including the next nearest are only considered. The hatched circles represent the B-site cations and small circles represent the A-site. Relative magnitude of radii and distances shown are approximately correct. We point out some configurations on the basis of our discussion so for and knowing the nature of the exchange forces. Among AB configurations only p-q-c configuration is favorable since the (M-O) distance as well as angle (M-O-M) (~126°) is favorable for having strong exchange interaction. The other AB configurations such as pre and tqe have much favorable angle (~154° and 180° respectively) but with one very large (M-O) distance .Thus, one cannot expect reasonable exchange interaction between them. Among the B-B configurations, the (M-O) distance is small for ppb

configuration but angle (90°) is unfavorable. Other configurations are p-t-b and p-a-b both, the angle and distance, are unfavorable. For p-t-b the angle (~126°) is favorable but one (M-O) distance is unfavorable. Thus, overall BB interactions are expected to stay lower in strength than AB interactions.

Among the AA configurations, only one configuration is shown in Figure 2.5, r-q-d, having both the (M-O) distances much larger (~3.9 Å) than any BB or AB distance. Besides, for the BB interaction there is a possibility of direct exchange since B-cations direct their T_{2g} orbitals towards each other which is not the case for AA interaction. Thus AA is expected to be the weakest of all.

Now let us apply the conclusions of semi empirical rules of Goodenoguh and Kanamori to the configurations we have pointed out. We see that direct application is possible only for the BB interactions with M-O-M angle to be 90°. The case of A-B interaction with M-O-M angle of 126° is more complicated. The usual way is to interpolate between the 180° and 90° configurations assuming rather arbitrarily that the change is smooth. If the sings of the 180° and 90° configurations happens to be opposite than the interpolation scheme is not reliable.

The AA interaction, as we have seen, are the weakest of all and really do not influence the ordering due to another interactions. This is true, off course, only when there are sufficient numbers of magnetic ions present on both the sites and that is implied throughout in our above discussion.

Based upon the G. K. rules and the interpolation, the following tables predict the interactions between the nearest pairs in the B sub-lattice and inter

sub-lattice interactions between the A and B sub-lattices for different d electron populations.

In general for spinel we find that $|J_{AB}| >> |J_{BB}| >> |J_{AA}|$ with J_{AB}, J_{BB} and J_{AA} all being negative.

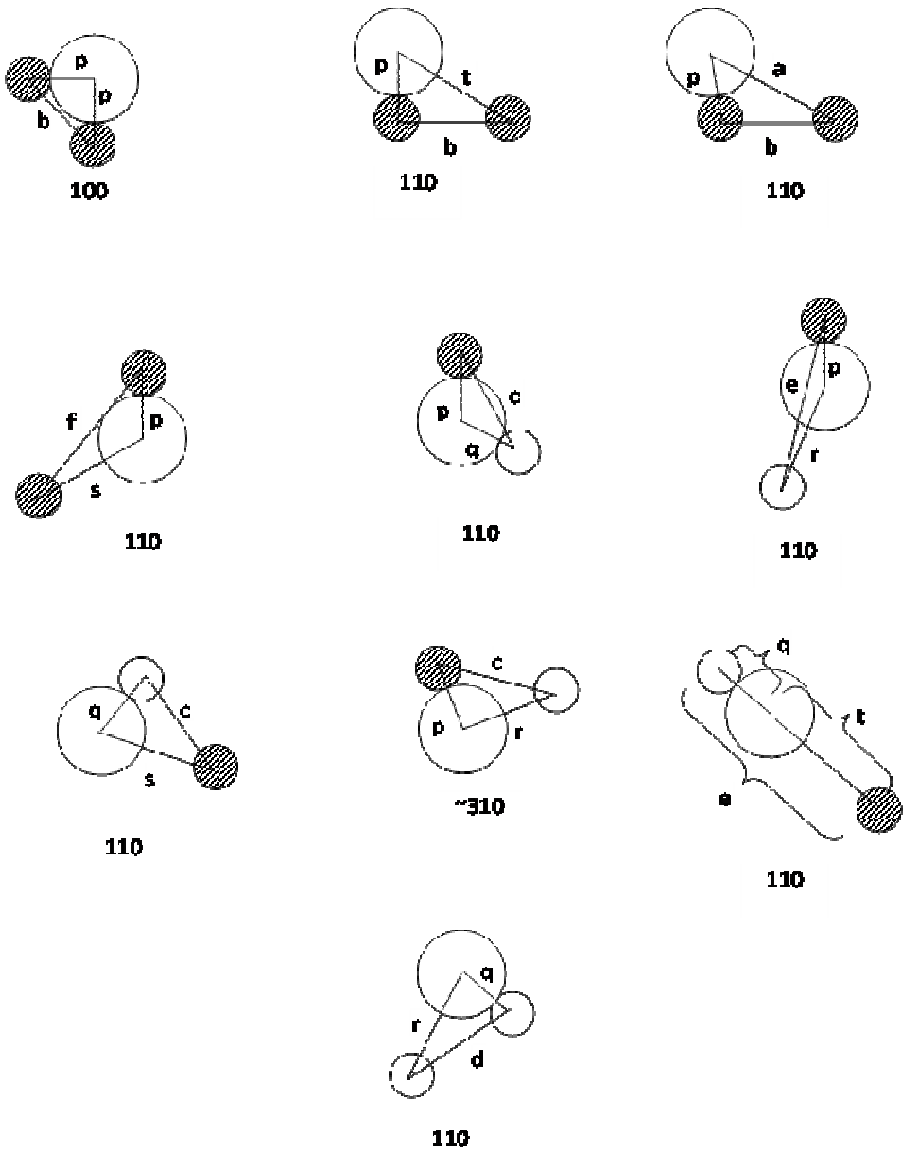

Figure 2.5 Near neighbour configuration in spinel lattice.

2.3 Magnetic ordering in a substituted ferrite

It has been shown that in ferrites, due to sublattice magnetic ordering the ferrimagnetism occurs. From the site preferences like diamagnetic cations such as Li^{+}, Mg^{2+}, Al^{3+}, Ti^{4+} and Nb^{5+} are known to prefer the B-site, while

cations such as Zn^{2+}, Ga^{3+} and Ge^{4+} prefer the A-site [18 - 22]. For example, in $GeCo_2O_4$ a 2-4 spinel, all Ge^{4+} ions are located at the A-site [23, 24]. Similarly in $CoFe_2O_4$ an inverse spinel structure with all Co^{2+} ions at the B-site and Fe^{3+} being equally distributed over the A- and B-sites. The heat treatment given to such ferrites determines the degree of inversion [25].

The addition of extra non-magnetic substance modifies the magnetic properties giving rise to wide spectrum of magnetic structures; ferrimagnetic, antiferromagnetic, spin glass, local canting etc. In particular, models are developed to investigate magnetic properties of diluted systems like spin glass and spin canting. The highly substituted system reveal two transitions in susceptibility versus temperature curve, one at T_N (Neel temperature) for S_Z (Z component of magnetic moment) for conventional collinear order, whereas the other at T_f (freezing temperature) for S_T (the transverse component) for spin glass like ordering.

2.4 Neel theory of ferrimagnetism

Consider the simplest case of two sub-lattices, which have anti parallel and unequal magnetic moments. The inequality may be due to :

a. Different elements in different sites

b. Same elements in different ionic states

c. Different crystalline fields leading to different effective moments for ions having the same spin.

Neel's model is briefly outlined below which is based on a simplified model composed of identical magnetic ions divided unequally between the A and B sub-lattices.

Let there be n identical magnetic ions per unit volume with fraction λ located on the A sites and ν (= 1-λ) on the B sites. Let μ_A and μ_B the average moments of an A ion and B ion in the direction of field at temperature T. Though, the A- and B- sites ions are identical, μ_A and μ_B are not because they feel different fields in different sites.

Let $M_A = n\mu_A$ and $M_B = n\mu_B$

The Molecular fields acting on both sub-lattices are

$H_{mA} = \gamma_{AB} (\lambda\alpha M_A - \nu M_B)$

$H_{mB} = \gamma_{AB}(\beta\nu M_B - \lambda M_A)$

Where $\alpha = \gamma_{AA}/\gamma_{AB}$ and $\beta = \gamma_{BB}/\gamma_{AB}$

γ_{AA},γ_{AB} and γ_{BB} are the Weiss constants

The above equations yield the expression for mass susceptibility as follows which is derived from the solving the equations above T_c

$$\frac{1}{\chi} = \frac{T}{C} + \frac{1}{\chi_o} + \frac{b}{T-\theta'}$$

where, $\frac{1}{\chi_o} = \gamma_{AB}\rho(2\lambda\nu - \alpha\lambda^2 - \beta\nu^2)$

$b = \gamma^2_{AB}\rho^2 C\lambda\nu[\lambda(1+\alpha) - \nu(1+\beta)]^2$

$\theta' = \gamma_{AB}\rho C\lambda\nu(2+\alpha+\beta)$

where, ρ density and C is is Curie constant for the material. From equating χ= 0 in the above equation for negative value of Weiss constants the Neel temperature can be given as $T_N = \gamma_{AB}\rho C/2\ [\alpha\lambda+\beta\nu+\{(\alpha\lambda-\beta\nu)^2 + 4\lambda\nu\}^{1/2}]$

The equation for the mass susceptibility actually represents a hyperbola and physically meaningful part of it is shown in Figure 2.6. The curve cuts the temperature axis at θ_p which is called paramagnetic Curie

point. It is in good agreement with the experimental observed susceptibility v/s temperature which differentiates ferrimagnetics form ferromagnetics.

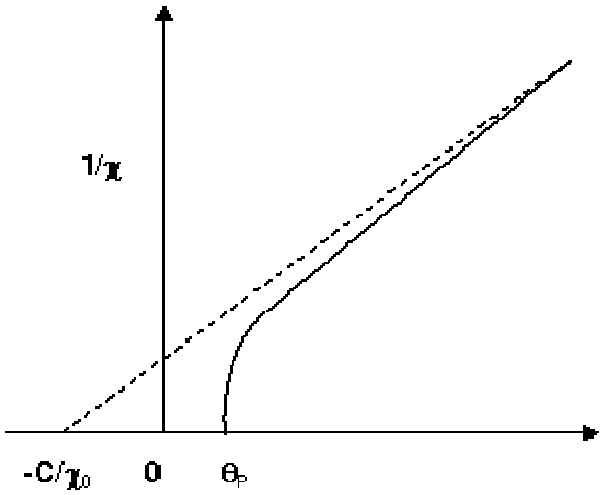

Figure 2.6 Variation of inverse susceptibility with Temperature (K) below T_c .

.

In the ferrimagnetic region each sub-lattice is spontaneously magnetized by the molecular field acing on it. But the two sub-lattice magnetizations are opposite to each other. The observable magnetization is

$|M| = |M_B| - |M_A|$

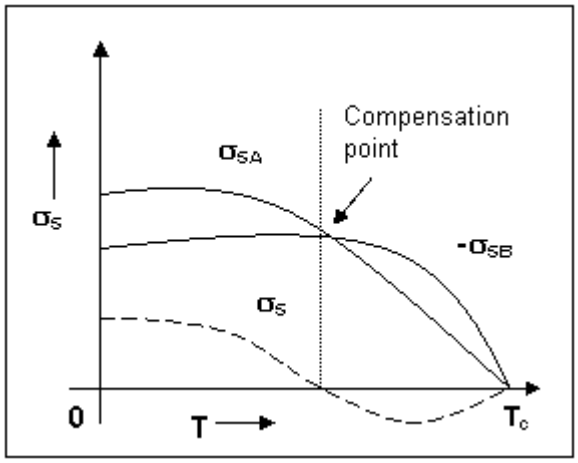

Figure 2.7 Anomalous magnetization v/s temperature curve for ferrimagents.

Each sub-lattice magnetizations are governed by the same relation as ferromagnetics. In terms of specific magnetization, they are given by

$$\frac{\sigma_A}{\sigma_o} = B\left(J, \frac{\mu_H H_{mA}}{kt}\right)$$

$$\frac{\sigma_B}{\sigma_o} = B\left(J, \frac{\mu_H H_{mB}}{kt}\right)$$

Where, k is Boltzmann constant and B is Brillouin function.

These sub-lattice magnetizations will have different temperature response because effective molecular field acting on them are different. This suggests the possibility of having anomalous net magnetization versus temperature curves. For most ferrimagnetics the curves show simple behaviour but in few cases there may be a compensation point or a maximum in the curve at some temperature. The shape of the curve depends on γ, λ, ν and α. There is an interesting possibility of the net magnetization reversing its sign. The situation is depicted in Figure 2.7 where, at some temperature below T_c Both the $|M_B| = |M_A|$ and of opposite sign. So M disappears at that point, which is called compensation point. Gorter [26] observed these types of behaviour in Li-Cr system.

Let's see how beautifully the Neel model explains the observed features of spinel ferrite. Take the case of Nickel ferrite, where the magnetic moments of Ni and Fe are reasonably different. It gives observed magnetic moment 2.3 μ_B. Now let us predict the cation distribution for it.

According to Neel model, if a normal structure is assumed the moment comes out is 8 μ_B as follows :

$M = |M_B| - |M_A| = [2\times 5\mu_B (Fe)]-(1\times 2\mu_B(Ni)) = 8\mu_B$

and an inverse will give 2 μ_B as follows

$M = |M_B| - |M_A| = [1\times 5\mu_B (Fe) + 1\times 2\mu_B(Ni)]-(1\times 5\mu_B(Fe)) = 2\mu_B$

The later is near to observed value which allows us to term the Nickel ferrite as an inverse structure. A nominal observed difference is always present in every cases and may be ascribed to the following factors

(1) g factor may not be exactly 2

(2) the structure may not be completely inverse

(3) particular ion may have different moments when in different sites.

Shortcomings of the Neel model

(1) Saturation magnetization values in many ferrites are found to be much lower than those predicted by Neel model.

(2) Some M v/s T curves have finite slopes at 0 K and cannot be explained by Neel model.

(3) It is based on the assumption that strong negative AB interaction predominates over AA and BB interactions, which is not applicable to each and every case.

2.5 Random Canting of Spin Model

The non-collinear or canted spin arrangement can be explained in terms of the random canting model [27]. Substitution in one sublattice of a ferrimagnet leads to spin canting in the other sublattice. Rosencwaig [28] supposed that the nearest neighbour of the B-site can be considered to be canted with an average angle $\langle\alpha_B\rangle$ due to the A-site substitution which in the average nearest neighbour approximation estimated to the

$$\mathrm{Cos}\langle\alpha_B\rangle = \frac{M_A}{M_B}\left(\frac{J_{AB}}{J_{BB}}\right)$$

The saturation magnetization per formula unit (Magneton number in Bohr magneton, μ_B) is related to canting angle, $\langle\alpha_B^c\rangle$ by, $n_B^c = M_B \cdot \mathrm{Cos}\langle\alpha_B^c\rangle - M_A$

Here, M_A and M_B are sublattice magnetization of the A- and B-sites respectively, to be determined from cation distribution. The J_{AB} and J_{BB} are exchange integrals.

References

1 J. Smit and H.P.J Wijn,
Ferrites-Physical properties of Ferrimagnetic Oxides in Relation to Their Technical Applications, (N.V. Philips Gloeilampenfabrieken, Eindhoven, Holland, (1959) p. 136-176.

2 H. A.John and E. Teller, Proc. R. Soc., London Ser., A161 (1937)220.

3 J. B. Goodenough, Annuan Rev. Materials Science, 28 (1998)1-27.

4 H. Ohnishi and T. Teranishi, J. Phys. Soc. Japan, 16 (1961)35.

5 J. C. Slater, Phys. Rev. 35 (1930)509.

6 J. C. Slater, Phys. Rev. 36 (1930)57.

7 H. A. Kramers, Physica, 1-6 (1934)182.

8 P. W. Anderson, Phys. Rev. 115 (1959)2.

9 P. W. Anderson, Solid State Physics 14 (1963)99.

10 P. W. Anderson, Magnetism, Eds. G. T. Rado and H Shull, 1 (Academic Press, New York, 1963)25.

11 P. W. Anderson and H. Hassgawa, Phys. Rev. 100 (1955)675.

12 J. H. Van Vleck, J. Phys. Radium 12 (1951)262.

13 J.C.Slater, Quart, Porf. Rept. M. I. T. July 15, 1, (1953) and October 15, 1, (1953)

14 T. Nagamiya, K. Yoshida and R. Kubo, Advan. Phys. 4 (1955)1.

15 J. B. Goodenough and A. L. Loeb, Phys. Rev. 98 (1955)391.

16 J. Kanamori, J. Phys. Chem. Solids, 10 (1959)87.

17 J. B. Goodenough, Phys. Rev. 117 (1960)1442.

18 H. Knock and H. Dannheim, Phys. Status Solidi A37 (1976)K135.

19 E. De Grave, C. Druve. A. Govaert and J. De Sitter, Phys. Status Solidi B37 (1976)527.

20 S. K. Kulshreshtha and G. Ritter, J. Mat. Sci. 20 (1985)821.

21 P. Raj and S. K. Kulshreshtha, J. Appl. Phys. 42 (1971)2344.

22 M. Robbins, J. Phys. Chem. Solids 26 (1965)831.

23 F. C. Romenjn, Philips Res. Rep. 8 (1962)304.

24 G. Blasse and J. F. Fast , Philips Res. Rep. 18 (1963)393.

25 R. Plumier, J. Appl. Phys. 39 (1968)635.

26 H. W. Gorter, Philips Res. Repts. 9 (1954)295.

27 J. M. D. Coey, Can. J. Phys. 65 (1987)1210.

28 A. Rosencwaig, Can. J. Phys. 48 (1970) 2857.

Chapter – 3

Synthesis, characterization techniques and experimental details

3.1 Synthesis of spinel ferrites

The properties of spinel ferrite are very much sensitive to the preparation conditions. A number of novel methods have been developed since then for the preparation of homogenous, fine/coarse grained and high density spinel ferrite. The preparation methods have been classified as:

(i) Ceramic method

(ii) Wet-chemical method (co-precipitation method)

(iii) Precursor method (Combustion, Sol-gel technique etc)

(i) Ceramic method

This is the conventional powder processing method which is commercially accepted since it is possible to maintain the stoichiometry of the final product even in large scale industrial production. In this method, the preparation of spinel ferrite takes place at about 1000°C by solid state reaction. The finely grained powder of the required composition is shaped by pressing and finally sintered to obtain ceramically prepared spinel ferrite.

The appropriate metal oxides or their salts, which decompose to give metal oxides are accurately weighed in the desired proportion and mixed thoroughly. The mixing is usually carried out in liquid suspension (water, acetone, alcohol or kerosene) in agate mortar and pestle or ball mill. The slurry is dried or filtered depending upon the suspension medium and then transferred to ceramic crucibles and pre- sintered in air or oxygen atmosphere.

The pre-sintered powder contains nucleation centres that are mixed homogeneously using agate mortar and pestle or ball mill, which helps in the

distribution of nucleation centres formed during pre-sintering. The mixing at this stage determines the size as well as the grain size distribution. An organic binder like polyvinyl alcohol (PVA) or Carbon tetrachloride (CTC) is often added at this stage. The sample is then pressed in a suitable die at about 5 to 10×10^6 kg/m^2. The pressed material is then fired in oxygen or air between 1000˚-1300˚C depending upon the substitutions in the ferrites. The completion of solid state reaction gives rise to homogeneous ferrites.

The ceramic method can be briefly described in four steps:

(i) Initial mixing, grinding and pelletizing

(ii) First sintering or pre-sintering

(iii) Regrinding and re-pelletizing

(iv) Final sintering

Synthesis of the solid solutions by ceramic technique

The most widely used technique for the synthesis of polycrystalline ferrite materials is the double sintering ceramic route which is adopted for the present study. Two different ferrite systems were prepared by the ceramic technique in the present study.

(1) $Zn_{0.3}Mn_{0.7+x}Si_xFe_{2-2x}O_4$ and $Zn_{0.3}Mn_{0.7+x}Ti_xAl_{0.1}Fe_{1.9-2x}O_4$ (x = 0.0 to 0.3, step = 0.1)

The spinel ferrites are usually prepared at elevated temperatures by a direct solid state reaction between oxide powders. Polycrystalline samples of this solid solution series were prepared by double sintering ceramic technique. Four samples of the spinel systems: $Zn_{0.3}Mn_{0.7+x}Si_xFe_{2-2x}O_4$ (x = 0.0 to 0.3)

$Zn_{0.3}Mn_{0.7+x}Ti_xAl_{0.1}Fe_{1.9-2x}O_4$ (x = 0.0 to 0.3,step = 0.1) were synthesized by the double sintering ceramic technique. The starting materials were analytical grade powders of ZnO, TiO_2 both supplied by LOBA chemicals and $MnCO_3$, Al_2O_3, SiO_2 Fe_2O_3; all 99.9 % pure supplied by Thomas & Backer. The oxides were mixed thoroughly in stoichiometric proportions to yield the desired compositions, intensively wet ground and pre-sintered at 1000^oC for 24 hrs. The pre-heated powders were again wet-milled and the resulting powders were then compressed in the form of pellets. The binder used was the acetone, which evaporates at 300^0C. The pellets prepared by compressing the fine powder with application of the pressure of about three tones. The pellets were finally sintered in air at 1100^0C for 24 hrs and furnace-cooled at the rate of 100^0C/hour.

(ii) Co-precipitation (wet-chemical) method

The preparation of ferrites powders by the co-precipitation method consists of oxidation by bubbling oxygen gas through an aqueous suspension of hydroxides of ferrous and other di or trivalent ions after an alkaline solution has been added. Thus powders with high homogeneity and purity are obtained [1]. In this method, the starting solution is prepared by mixing required amount of aqueous solutions of corresponding sulphates/nitrates/chlorates in proper proportions. A solution of Sodium hydroxide (NaOH) of appropriate molarity (generally about 2M) is used as a precipitant. It has been suggested that the solubility product constant (K_{sp}) [2] of all the constituents is always exceeded when the starting solution is added into the precipitant. Therefore in order to achieve simultaneous precipitation of hydroxides, the starting solution (pH < 7) is added to the precipitant and the

suspension (pH > 7) is heated at about 60^0-100^0C and oxygen gas is bubbled uniformly into the suspension to promote oxidation reaction until all the precipitates change into the precipitates of ferrites. The samples are filtered, washed and dried at 200^0C under vacuum.

The wet samples when annealed in air at about 1000^0C, exhibit generally weight loss because of removal of water and hydroxyl ions even after the prolonged drying process.

The wet-chemical method can be briefly described in five steps:

(i) Preparation of starting solution

(ii) Precipitation of hydroxides

(iii) Oxidation at $\approx 60^0$C with stirring

(iv) Filtering and washing the precipitate of ferrites

(v) Drying at 100-200^0C

(iii) Precursor method

This method involves preparing a precursor, which is a solid solution or a compound containing metal ions in the desired ratio and the decomposition of precursor to yield the ferrites. Some of the precursor methods used are:

(a) Hydroxide precursor

(b) Carbonate precursor

(c) Oxalate precursor

(d) Hydrazine carboxylate precursor

This method requires low sintering temperature and hence it is possible to maintain proper stoichiometry and obtain fine particle ferrite. The

disadvantage in this method is that the hydroxides are gelatinous and therefore it is difficult to handle, filter and wash them. Sometimes the losses of ions like Cu, Ni occur on complexing with ammonia. The incomplete precipitation may result in undesired compositions [3].

Structural and micro- structural characterizations

3.2 Energy Dispersive Analysis of X-rays (EDAX)

EDAX stands for Energy Dispersive Analysis of X-rays. It is sometimes referred to as EDS analysis. Energy dispersive X-ray spectroscopy is an analytical technique used predominantly for the elemental analysis or chemical characterization of a specimen. Being a type of spectroscopy, it relies on the investigation of a sample through interactions between electromagnetic radiation and matter, analyzing X-rays emitted by the matter in this particular case. Its characterization capabilities are due in large part to the fundamental principle that each element of the periodic table has a unique atomic structure allowing X-rays that are characteristic of an element's atomic structure to be uniquely distinguished from each other.

To stimulate the emission of characteristic X-rays from a specimen, an high energy beam of charged particles such as electrons or protons, or a beam of X-rays, is focused into the sample to be characterized. At rest, an atom within the sample contains ground state (or unexcited) electrons situated in discrete energy levels or electron shells bound to the nucleus. The incident beam may excite an electron in an inner shell, prompting its ejection and resulting in the formation of an electron hole within the atom’s electronic structure. An electron

from an outer, higher-energy shell then fills the hole, and the difference in energy between the higher-energy shell and the lower energy shell is released in the form of an X-ray. The X-ray released by the electron is then detected and analyzed by the energy dispersive spectrometer. These X-rays are characteristic of the difference in energy between the two shells, and of the atomic structure of the element form which they were emitted (Figure 3.1). [4]

Working Principle of EDAX

During EDAX analysis the specimen is bombarded with an electron beam inside the scanning electron microscope. The bombarding electrons collide with the specimen atoms own electrons, knocking some of them off in the process. A position vacated by an ejected inner shell electron is eventually occupied by a higher energy electron from an outer shell. To be able to do so, however the transferring outer electron must give up some of its energy by emitting an x-ray.

The amount of energy released by the transferring electron depends on which shell it is transferring from, as well as which shell it is transferring to. Furthermore, the atom of very element releases X-rays with unique amounts of energy during the transferring process. Thus, by measuring the amounts of energy present in the x-rays being released by a specimen during electron beam bombardment, the identity of the atom from which the X-rays was emitted can be established [4].

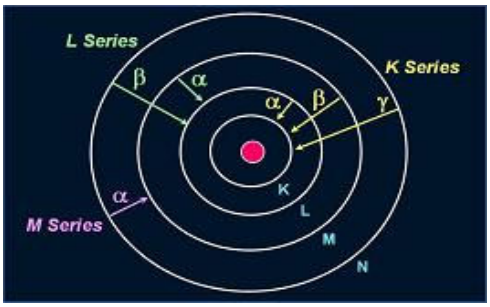

Figure 3.1 Elements in an EDX spectrum are identified based on the energy content of the X-rays emitted by their electrons as these electrons transfer from a higher-energy shell to a lower-energy one

The output of an EDAX analysis is an EDAX spectrum. The EDAX spectrum is just a plot of how frequently an X-ray is received for each energy level. An EDAX spectrum normally displays peak corresponding to the energy levels for which the most x-rays had been received (Figure 3.2) Each of these peaks are unique to an atom, and therefore corresponds to a single element. The higher a peak in a spectrum, the more concentrated the element is in the spectrum

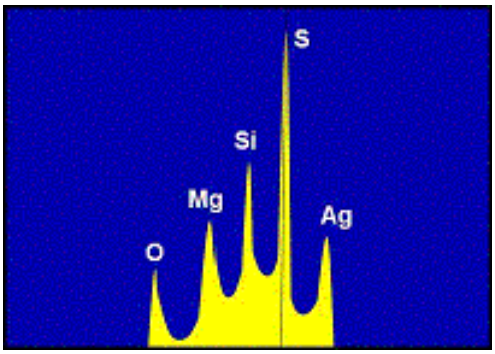

Figure 3.2 Example of an EDX spectrum

Construction and working of spectrometer

The essential parts of the Energy Dispersive spectrometer are shown in the diagram (Figure 3.3).

The sample specimen is bombarded with x-rays of enough high energy generated from the X-ray tube. The fluorescence radiation, emitted by the sample comprising of various wavelengths according to the various elements present in the sample is analyzed and various wavelengths are separated on the basis of their energies by means of a Si (Li) counter and a multichannel analyzer (MCA).

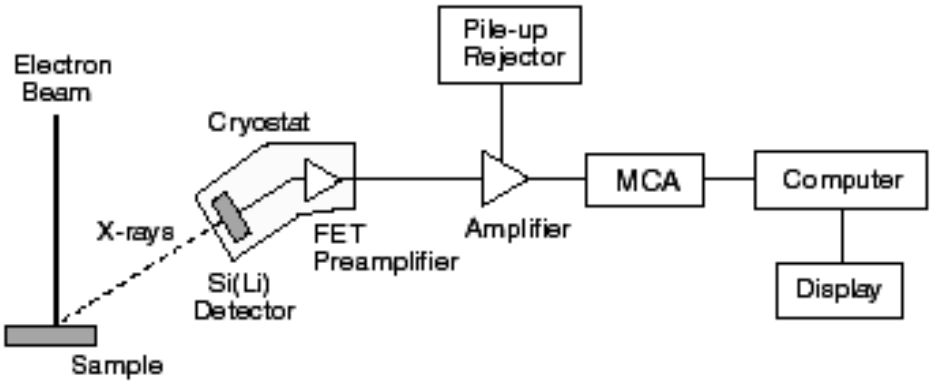

Figure 3.3 Energy Dispersive spectrometer

The counter produces the pulses proportional in height to the energies in the incident beam and MCA sorts out the various pulse heights. The excellent energy resolution of the Si (Li) counter with FET preamplifier and the ability of the MCA to perform rapid pulse height analysis make the spectrometer to measure the intensities of all the spectral lines from the sample in about a minute, unless there are elements in very low concentration are to be determined [4].

3.3 X-ray powder diffractometry

When X-ray radiation passes through matter, the radiation interacts with the electrons in the atoms, resulting in scattering of the radiation. If the atoms are organized in planes (i.e. the matter is crystalline) and the distances between the atoms are of the same magnitude as the wavelength of the X-rays, constructive and destructive interference will occur. This result in diffraction where X-rays are emitted at characteristic angles based on the spaces between the atoms organized in crystalline structures called planes. Most crystals can have many sets of planes passed through their atoms. Each set of planes has a specific inter planer distance and will give rise to a characteristic angle of diffracted X-rays. The relationship between wavelength, atomic spacing (d) and angle was solved as the Bragg Equation. If the illuminating wavelength is known (depends on the type of X-ray tube used and if a monochromator is employed) and the angle can be measured (with a diffractometer) then the inter planer distance can be calculated from the Bragg equation. A set of 'd-spaces' obtained from a single compound will be represent the set of planes that can be passed through the atoms and can be used for comparison with sets of d-spaces obtained from standard compounds.

Diffraction of X-ray beam striking a crystal occurs because the λ of the X-ray beam is equivalent to the spacing of atoms in minerals (1-10 Å). When an X-ray beam encounters the regular, 3-D arrangement of atoms in a crystal most of the x-rays will destructively interfere with each other and cancel each other

out, but in some specific directions they constructively interfere and reinforce one another. It is these reinforced (diffracted) X-rays that produce the characteristic X-ray diffraction patterns that used for mineral identification. W.L. Bragg (early 1900's) showed that diffracted X-rays act as if they were "reflected" from a family of planes within crystals. Bragg's planes are the rows of atoms that make up the crystal structure.

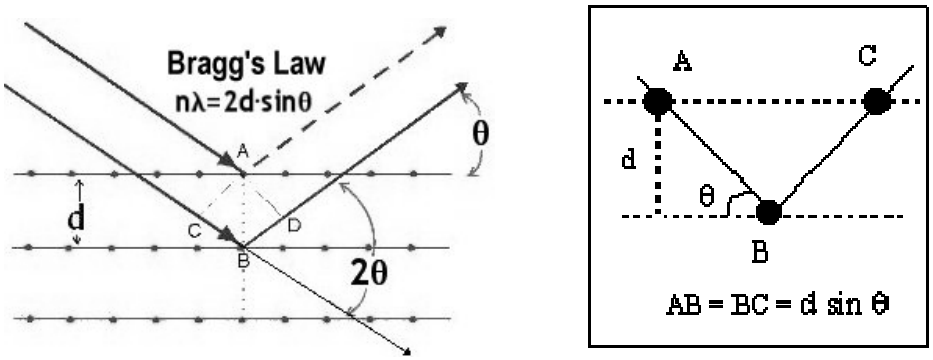

Figure 3.4 Bragg's law is satisfied when the inter planer spacing equals to 2dsinθ .

These "reflections" were shown to occur under certain conditions, which satisfy the equation: $n\lambda = 2d\sin\theta$, where, n is an integer (1, 2, 3, ..., n), λ the wavelength, d the distance between atomic planes, and θ the angle of incidence of the X-ray beam and the atomic planes. $2d\sin\theta$ is the path length difference between two incident X-ray beams where one X-ray beam takes a longer (but parallel) path because it "reflects" off an adjacent atomic plane. This path length difference must be equal to an integer value of the λ of the incident X-ray beams for constructive interference to occur such that a reinforced diffracted beam is

produced. For a given λ of incident X-rays and inter planer spacing (d) in a mineral, only specific angles (θ) will satisfy the Bragg equation. For example, on focusing a monochromatic X-ray beam (X-rays with a single λ.on a cleavage fragment of calcite and slowly rotating the crystal, no "reflections" will occur until the incident beam makes an angle θ that satisfies the Bragg equation with n = 1. Continued rotation leads to other "reflections" at higher values of λ and correspond to when n = 2, 3 ... etc; these are known as 1^{st}, 2^{nd}, 3^{rd} order, etc., "reflections".

Powder Methods

This method is essential for minerals that do not form large crystals (i.e. clays) and eliminates the problem of precise orientation necessary in single-crystal methods with its primary application being for mineral identification. It can also be used to determine mineral compositions (if d-spacing is a function of mineral chemistry) and to determine relative proportions of minerals in a mixture. Monochromatic X-rays are focused on pellet or slide mounted on rotating stage. Since sample is powder, all possible diffractions are recorded simultaneously from hypothetical randomly oriented grains. Mount is then rotated to ensure all diffractions are obtained. Older methods used photographic techniques while most modern applications employ X-ray powder diffractometers.

X-ray powder diffractometry

X-ray powder diffractometry uses monochromatic X-rays on powder mounted on glass slide that is attached to a stage which systematically rotates into the path of the x-ray beam through θ = 0 to 90°. The diffracted x-rays are detected electronically and recorded on an inked strip chart. The detector rotates simultaneously with the stage, but rotates through angles = 2θ. The strip chart also moves simultaneously with the stage and detector at a constant speed. The strip chart records the intensity of X-rays as the detector rotates through 2θ. Thus, the angle 2θ at which diffractions occur and the relative intensities can be read directly from the position and heights of the peaks on the strip chart. Use is then made of the Bragg equation to solve for the inter planer spacing (d) for all the major peaks and look up a match with JCPDS cards. JCPDS = Joint Committee on Powder Diffraction Standards.

Figure 3.5 Photograph of a typical X-ray diffractometer.

The X-ray diffractograms were recorded on Philips PW 1710 automated X-ray powder diffractometer using CuK_α radiation, graphite monochromator, and Xe-filled proportional counter with following specifications.

Scanning rate: 1 degree /minute

Chart speed : 2 cm /minute

The X-ray diffraction patterns were obtained from SICART, Vallabh Vidya nagar, Gujarat.

The procedure of indexing the X-ray diffractograms, determination of lattice parameter and X-ray intensity calculations are briefly explained below: In the case of a cubic lattice,

$$\frac{1}{d^2} = \frac{h^2 + k^2 + l^2}{a^2} \qquad (1)$$

Where, a = lattice parameter, d = Inter planer spacing between adjacent planes

(hkl) = Miller indices.

Using Bragg's law in Equation (1),

$$\mathrm{Sin}^2\theta_{hkl} = \frac{\lambda^2}{4a^2}\left(h^2 + k^2 + l^2\right) \qquad (2)$$

where λ = incident wavelength.

In equation (2) the sum $(h^2 + k^2 + l^2)$ is always an integer while $\lambda^2/4a^2$ is constant for any one pattern. The equation further suggests that for a particular cubic crystal, the diffraction takes place at all possible values of Bragg's angle from the planes (hkl). The indices of different planes of a diffractogram for the cubic system can be derived as:

$$\frac{\mathrm{Sin}^2\theta}{\left(h^2+k^2+l^2\right)}=\frac{\lambda^2}{4a^2} \quad (3)$$

Lattice parameter 'a' can be determined using the formula,

$a = N^{1/2}\, d$ (4)

where, $N = (h^2 + k^2 + l^2)$

In order to determine the cation distribution, X-ray diffraction line intensities were calculated using the formula suggested by Buerger:

$$I_{hkl} = \left|F_{hkl}\right|^2 PL_p$$

where I_{hkl} = Relative integrated intensity

F_{hkl} = Structure factor

P = Multiplicity factor

L = Lorentz-polarization factor

θ = Bragg's angle

The Rietveld refinement method

There are six factors affecting the relative intensities of the diffraction lines on a powder pattern, namely, (i) Polarization factor, (ii) Structure factor, (iii) Multiplicity factor, (iv) Lorentz factor, (v) absorption factor and (vi) Temperature factor. A very important technique for analysis is powder diffraction data is the whole pattern fitting method proposed by Rietveld (1969) [5, 6]. The Rietveld method is an extremely powerful tool for the structural analysis of virtually all types of crystalline materials not available as single crystals. The method makes use of the fact that the peal shapes of Bragg reflection can be described analytically and

the variations of their width (FWHM) with the scattering angle 2θ. The analysis can be divided into number of separate steps. While some of these steps rely on the correct completion of the previous one(s), they generally constitute independent task to be completed by experimental and depending of the issue to be addressed by any particular experiment, one, several of all these tasks will be encountered [7].

The parameters refined in the Rietveld method fall into mainly three classes: peak shape function, profile parameters and atomic and structural parameters. The peak shapes observed are function of the both the sample (e.g. domain size, stress/strain, defects) and the instrument (e.g. radiation source, geometry, slit sizes) and they vary as a function of 2θ. The profile parameters include the lattice parameters and those describing the shape and width of Bragg peaks (changes in FWHM and peak asymmetry as a function of 2θ, 2θ correction, unite cell parameters). In particular, the peak widths are smooth function of the scattering angle 2θ. It uses only five parameters (usually called U, V, W, X and Y) to describe the shape of all peaks in powder pattern. The structural parameters describe the underlying atomic model include the positions, types and occupancies of the atoms in the structural model and isotropic of anisotropic thermal parameters. The changes in the positional parameters cause changes in structure factor magnitudes and therefore in relative peak intensities, whereas atomic displacements (thermal) parameters have the effect of emphasizing the high angle region (smaller thermal parameters) or de-emphasizing it (larger thermal parameters). The scale, the occupancy

parameters and the thermal parameters are highly correlated with one another and are more sensitive to the background correction than are the positional parameters. Thermal parameter refinement with neutron data is more reliable and anisotropic refinement is sometimes possible. Occupancy parameters are correspondingly difficult to refine and chemical constraints should be applied whenever possible [8].

Once the structure is known and a suitable starting model is found, the Rietveld method allows the least-squares refinement [chi-squared (χ^2) minimization] of an atomic model (crystal structure parameters) combined with an appropriate peak shape function, i.e. a simulated powder pattern, directly against the measured powder pattern without extracting structure factor of integrated intensities. With a complete structural model and good starting values of background contribution, the unit cell parameters and the profile parameters, the Rietveld refinement of structural parameters can begin. A refinement of structure of medium complexity can require hundred cycles, while structure of high complexity may easily require several hundreds. The progress of refinement can be seen from the resultant profile fit and the values of the reliability factors or R-values. The structure should be refined to convergence. All parameters (profile and structural) should be refined simultaneously to obtain correct estimated standard deviations can be given numerically in terms of reliability factors of R-values [9]. The weighted profile R value, R_{WP} is defined as,

$$R_{wp} = \{ \sum_i w_i \{ y_i(obs) - y_i(calc) \}^2 / \sum_i w_i y_i(obs)^2 \}^{1/2} \times 100\%$$

Ideally, the final R_{WP}, should approach the statistically expected R Value, R_{exp},

$$R_{exp} = \{ (N - P + C) / \sum_{i} w_i y_i(obs)^2 \}^{1/2} \times 100\%$$

where, N is the number of observations and P the number of parameters and *C* is the number of constraints used in the refinement.. R_{exp} reflects the quality of data. Thus, the ratio between the two (goodness of fit),

$$\chi^2 = (R_{wp} / R_{exp})^2$$

An R value is observed and calculated structure factors, F_{hkl}, can also be calculated by distributing the intensities of the overlapping reflections according to the structural model,

$$R_F = (\sum_{hkl} | F_{hkl}(obs) - F_{hkl}(calc) | / \sum_{hkl} F_{hkl}(obs)) \times 100\%$$

Similarly, the Bragg-intensity R value can be given as,

$$R_I = (\sum_{hkl} | I_{hkl}(obs) - I_{hkl}(calc) | / \sum_{hkl} I_{hkl}(obs)) \times 100\%$$

R values are useful indicators for the evaluation of refinement, especially in the case of small improvements to the model, but they should not be over interpreted. The most important criteria for judging the quality of a Rietveld refinement are (i) the fit of the calculated patterns to the observed data and (ii) the chemical sense of structural model.

3.4 Scanning electron microscopy (SEM)

The SEM was pioneered by Manfred von Ardenne in 1937. The instrument was further developed by Charles Oatley and first commercialized by Cambridge Instruments.

Figure 3.6 SEM opened sample chamber.

The scanning electron microscope (SEM) is a type of electron microscope that creates various images by focusing a high energy beam of electrons onto the surface of a sample and detecting signals from the interaction of the incident electrons with the sample's surface. [10, 11]

The type of signals gathered in a SEM varies and can include secondary electrons, characteristic X-rays, and back scattered electrons. In a SEM, these signals come not only from the primary beam impinging upon the sample, but from other interactions within the sample near the surface. The SEM is capable of producing high-resolution images of a sample surface in its primary use mode, secondary electron imaging. Due to the manner in which this image is created, SEM images have great depth of field yielding a characteristic three-dimensional appearance useful for understanding the surface structure of a sample. This great depth of field and the wide range of magnifications are the most familiar imaging mode for specimens in the SEM. Characteristic x-rays are emitted when the primary beam causes the ejection of inner shell electrons from the sample

and are used to tell the elemental composition of the sample. The back-scattered electrons emitted from the sample may be used alone to form an image or in conjunction with the characteristic x-rays as atomic number contrast clues to the elemental composition of the sample.

In a typical SEM, electrons are thermionically emitted from a tungsten or lanthanum hexaboride (LaB_6) cathode and are accelerated towards an anode; alternatively, electrons can be emitted via field emission (FE). Tungsten is used because it has the highest melting point and lowest vapour pressure of all metals, thereby allowing it to be heated for electron emission. The electron beam, which typically has an energy ranging from a few hundred eV to 100 keV, is focused by one or two condenser lenses into a beam with a very fine focal spot sized 0.4 nm to 5 nm. The beam passes through pairs of scanning coils or pairs of deflector plates in the electron optical column, typically in the objective lens, which deflect the beam horizontally and vertically so that it scans in a raster fashion over a rectangular area of the sample surface. When the primary electron beam interacts with the sample, the electrons lose energy by repeated scattering and absorption within a teardrop-shaped volume of the specimen known as the interaction volume, which extends from less than 100 nm to around 5 μm into the surface. The size of the interaction volume depends on the electrons' landing energy, the atomic number of the specimen and the specimen's density. The energy exchange between electron beam and the sample results in emission of electrons and electromagnetic radiation. That can be detected to produce an image.

Electronic devices are used to detect and amplify the signals and display them as an image on a cathode ray tube in which the faster scanning is synchronized with that of the microscope. The image displayed is therefore a distribution map of the intensity of the signal being emitted from the scanned area of the specimen. The image may be captured by photography from a high resolution cathode ray tube, but in modern machines is digitally captured and displayed on a computer monitor.

Resolution of the SEM

The spatial resolution of the SEM depends on the size of the electron spot, which in turn depends on both the wavelength of the electrons and the magnetic electron-optical system which produces the scanning beam. The resolution is also limited by the size of the interaction volume, or the extent to which the material interacts with the electron beam. The spot size and the interaction volume both might be large compared to the distances between atoms, so the resolution of the SEM is not high enough to image individual atoms, as is possible in the shorter wavelength (i.e. higher energy) transmission electron microscope (TEM). The SEM has compensating advantages, though, including the ability to image a comparatively large area of the specimen; the ability to image bulk materials (not just thin films of foils); and the variety of analytical modes available for measuring the compositions and nature of the specimen. Depending on the instrument, the resolution can fall somewhere between less than 1nm and 20nm. The world's highest SEM resolution is obtained with the Hitachi S-5500. Resolution is 0.4 nm at 30kV and 1.6 nm at 1 kV.

3.5 Infrared Spectroscopy

Introduction

Studies of the relation between structure and the electromagnetic response of ferromagnetic semiconductor are useful in understanding their properties. Since the electric and magnetic properties of these materials are decisively dependent on the precise configuration of the atoms or ions in these structures, methods of nondestructive analysis are especially suited to such investigations. In particular, the vibrational, electric and magnetic dipole, spectra can give information about the position and valence of the ions in the crystal lattice [12].

Infrared spectroscopy is one of the most powerful analytical techniques, which offers the possibility of chemical identification. One of the prime advantage of infrared spectroscopy over the other methods of structural analysis is that it provides useful information about the structure of molecule rapidly and also without cumbersome evaluation methods.

The technique is based upon the simple fact that a chemical substance shows marked selective absorption in the infrared region. After the absorption of IR radiations, the molecules of a chemical substance vibrate at many rates of vibrations, giving rise to closed-packed absorption bands, called “IR Absorption Spectrum”, which May extend over a wide wavelength range. Various bands will be present in IR spectrum that will correspond to the characteristic functional groups and bonds present in chemical substance. Hence, an IR spectrum of a chemical substance is the fingerprint for its identification. Band position in a

infrared may be expressed conveniently by wave number $\bar{\upsilon}$ whose unit is cm^{-1}.

The relation between wave number $\bar{\upsilon}$, wavelength λ and frequency f is as follows

$$f = C/\lambda$$

or

$$\bar{\upsilon} = f/C = 1/\lambda$$

Where, C is the velocity of light.

From the above relations, it follows that wave number is the reciprocal of wavelength. The range of infrared radiation is divided into four sections.

i The photographic region: This ranges from visible to 1.2μm

ii The very near infrared region. This also known as overtone region and ranges from 1.2 to 2.5μm

iii The near infrared region: This is also known as vibration region and ranges from 2.5 to 25μm

iv The far infrared region: This is known as rotation region. This ranges from 25 to 300-400 μm

The spectrographic apparatus is divided into three parts as follows:

(1) Sources of radiation

(2) The spectrometer in which the radiation is deviated, the amount of deviation depending on the frequency (or wavelength) of radiation; and

(3) a unit for detecting, quantatively, the presence of radiation, together with an amplifier and recorder which are required in most instances.

The components selected and the method of operation of the spectrograph varies from one instrument to another. The usual optical materials, glass or quartz absorb strong in the infrared region, consequently the apparatus for measurement of infrared spectra is different from that for the visible and ultra regions.

The magnetic properties of ferrites are decisively dependent on the precise configuration of the atoms or ions in the structure. Therefore, the non-destructive methods of characterization such as infra-red spectra especially suited for such investigations.

The bands in the 300-700 cm^{-1} region are assigned to the fundamental vibration of the ions of the crystal lattice. In the spinel oxide, the metal ions are situated in to the different sites tetrahedral (A) and octahedral (B); according to the geometrical configuration of the oxygen nearest neighbors. Since no isolated molecular grouping occurs in the structure, we can assign the ferrites to the class “Continuous bounded crystal”. In this type of crystals the atoms are bounded to all nearest neighbours by equivalent forces (ionic, Covalent or Vander Walls). The complete frequency distribution consists of 42N vibrational modes and the selection rules [12] require that only modes of proper symmetry absorb infra-red radiation. The symmetry classification of vibration and the normal coordinates of infrared active vibration have been discussed in detail by R.D.Waldron [12].

Infrared spectroscopy is used to determine the local symmetry in crystalline [13] and non-crystalline solid [14] and also ordering phenomenon in spinel [15]. The absorption bands in spinel ferrites mainly arise from lattice

vibrations of oxygen ions with cations, producing various frequencies of unit cell. The frequencies of the vibrations depend on cation oxygen bonding, lattice parameters and cation mass. The possible presence of Fe^{2+} ion and its influence on far-infrared spectra can also be studied.

Ferrites possess the structure of mineral ($MgAl_2O_4$) and crystallizes in face centered in face centered cubic (fcc) from with space group Fd3m-O_h^{-7}. The group theoretical calculation based on the space group and symmetry show four IR – active fundamentals in the vibrational spectra of normal as well as inverse cubic spinel. The two high frequency bands are broad and asymmetric depending on the preparation conditions which two low frequency bands are weaker and are unaffected by preparation conditions.

An absorption band ν_1 (around 550 cm^{-1}) is caused by stretching of tetrahedral metal oxygen bonds or to intrinsic vibrations of tetrahedral complexes. The second absorption band ν_2 (around 400 cm^{-1}) is due to oxygen vibrations in a direction perpendicular to tetrahedral cations oxygen axis. The remaining bands ν_3 and ν_4 are associated with the vibrations of metal oxygen ions in the isotropic force field of the octahedral and tetrahedral environment respectively.

When the symmetry of the spinel structure is lower than cubic or/and supplementary ordering of cation exists more IR bands may appear. A splitting of one IR band is observed in some spinels containing octahedrally coordinated Jahn-Teller ions Mn^{3+}, and Cu^{2+}. It is to be noted that the bands may be splits also due to the presence of two different kinds of ions in the same sublattice.

The IR spectra provide important information about:

(i) Completion of solid state reaction

(ii) Distribution of cations among non-equivalent sites and their valency

(iii) Nature of metal oxygen bonds

(iv) Calculation of force constant, molar heat capacity, Elastic constants etc.

(v) Nature of electronic transitions and calculations of activation energy.

Typical infrared absorption spectra of $ZnFe_2O_4$, $NiFe_2O_4$, $CoFe_2O_4$, $MnFe_2O_4$, $MgFe_2O_4$ and Fe_3O_4 are shown in Figure 3.7. The band position and force constant for the tetrahedral (A-site) and octahedral (B-site) for some selected spinel ferrites are given in the Table 3.1.

Table 3.1 IR Band position (ν) and force constant (k) for spinel ferrites [12].

Formula	ν_1	ν_2	k_1	k_0
	cm^{-1}		$(dynes/cm)\times10^5$	
$CoFe_2O_4$	575	374	1.66	0.85
$FeFe_2O_4$	570	370-380	1.65	0.84
$MgFe_2O_4$	565	406	1.52	0.86
$MnFe_2O_4$	550	392	1.40	0.92
$NiFe_2O_4$	587	396	1.67	0.95
$ZnFe_2O_4$	555	393	1.477	0.925

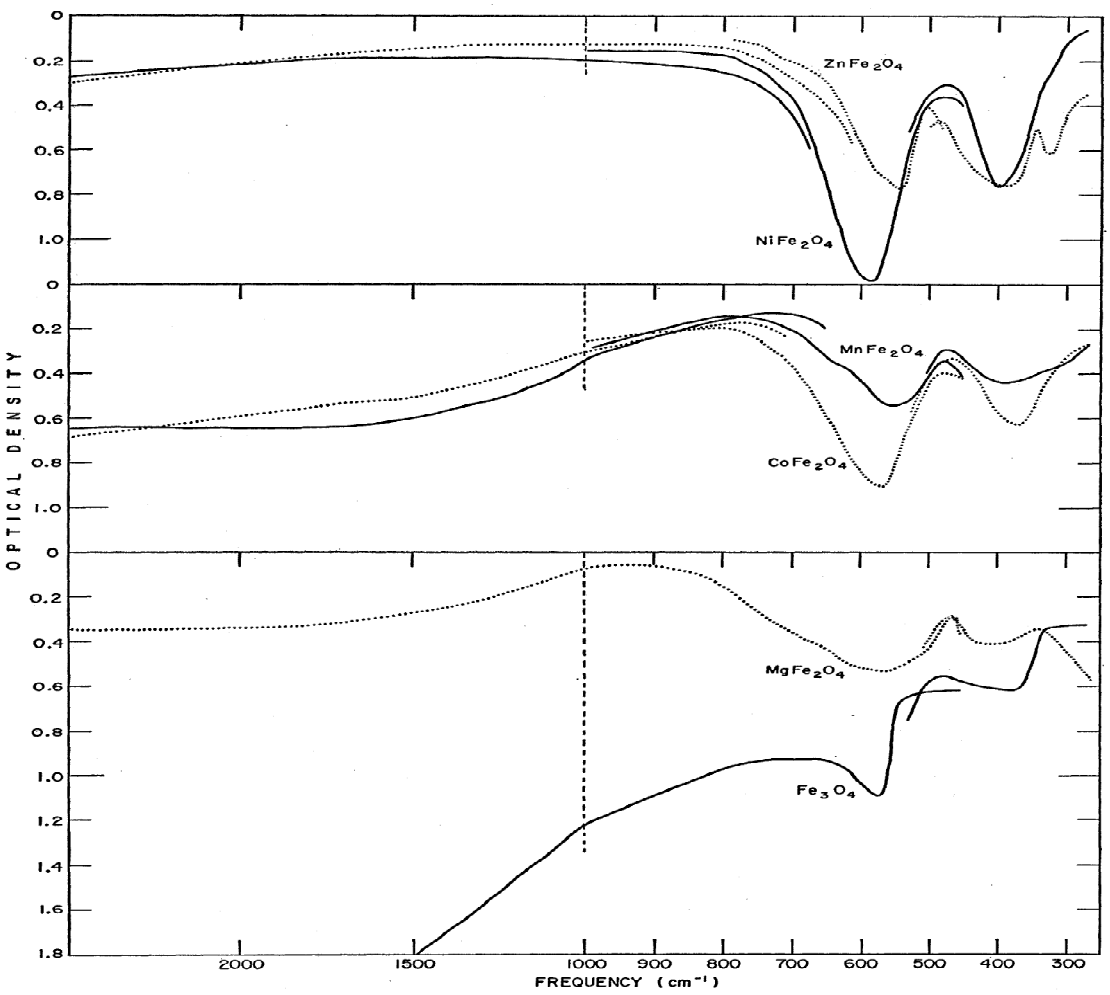

Figure 3.7: Infrared absorption spectra of simple ferrites at 300 K.

The infrared spectra for all the compositions were recorded in the wave number range of 400 – 1000 cm^{-1}, using BRUKER IFS 66V FT-IR spectrometer at SICART, VV Nagar. The experimental resolution was 4 cm^{-1}. The details of the FTIR spectrometer are given by Willard et al. [16]. A photograph of IR spectrometer is shown in Figure 3.9.

.Infrared Spectrometer

The essential part of the infrared spectrometer and how sample is analyzed by spectrometer is discussed below and shown in Figure 3.8 [17]:

The normal instrumental process is as follows:

1. The Source: Infrared energy is emitted from a glowing black-body source. This beam passes through an aperture which controls the amount of energy presented to the sample (and, ultimately, to the detector).

2. The Interferometer: The beam enters the interferometer where the "spectral encoding" takes place. The resulting interferogram signal then exits the interferometer.

3. The Sample: The beam enters the sample compartment where it is transmitted through or reflected off of the surface of the sample, depending on the type of analysis being accomplished. This is where specific frequencies of energy, which are uniquely characteristic of the sample, are absorbed.

4. The Detector: The beam finally passes to the detector for final measurement. The detectors used are specially designed to measure the special interferogram signal.

5. The Computer: The measured signal is digitized and sent to the computer where the Fourier transformation takes place. The final infrared spectrum is then presented to the user for interpretation and any further manipulate

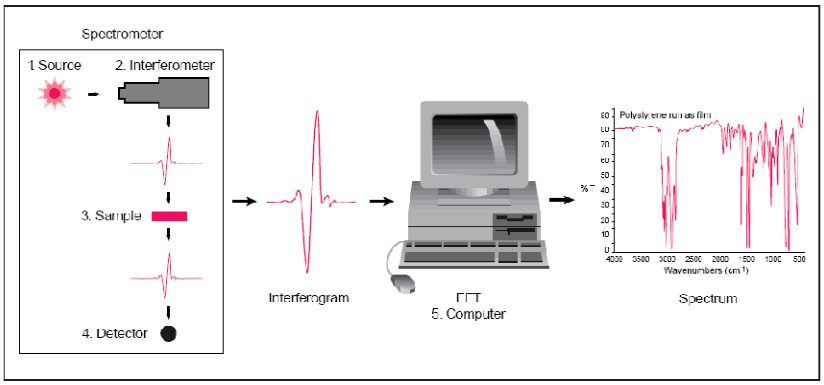

Figure 3.8 Essential parts of infrared spectrometer.

Because there needs to be a relative scale for the absorption intensity, a background spectrum must also be measured. This is normally a measurement with no sample in the beam. This can be compared to the measurement with the sample in the beam to determine the "percent transmittance." This technique results in a spectrum which has all of the instrumental characteristics removed thus, all spectral features which are present are strictly due to the sample. A single background measurement can be used for many sample measurements because this spectrum is characteristic of the instrument itself.

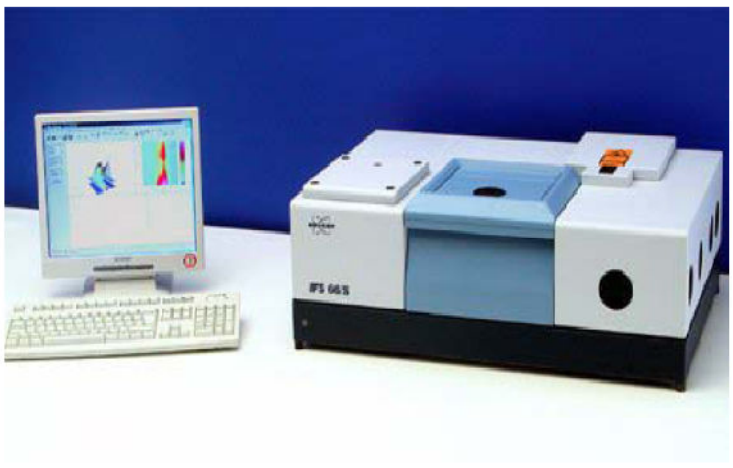

Figure 3.9 IR spectrometer used to record IR spectra.

Elastic Constants determination by spectral analysis

The elastic constants are of much importance because they elucidate the nature of binding forces in solids and to understand the thermal properties of the solids. In engineering practice, the elastic moduli often used are Young modulus, rigidity modulus and Poisson's ratio. The most conventional technique for the determination of elastic constants and Debye temperature is the ultrasonic pulse transmission technique [18]. The sample size requires for such measurements is around 1 cm in length. In the study of elastic properties of recent technologically important nanoparticles, superconductors, single crystal, irradiated by swift heavy ions or specially treated materials, where sample quantity is very small or it may be not possible to convert them into hard pellet such technique may not be useful. We have developed a new method to study the elastic properties of spinel ferrites, garnets and perovskites through infrared spectroscopy [19, 20, 21] where only a few milligram of material is sufficient for the characterization. When any polycrystalline oxide materials are subjected to high magnetic field, electric field, pressure or temperature, large stresses developed in the material. The elastic moduli values represent mechanical strength, fracture toughness and thermal shock resistance. The mechanical properties are of critical importance in the incorporation of the material in to a functional device.

(i) Young's modulus (E)

This characterizes the restoring forces appropriate to longitudinal extensions of a substance. In the Figure 3.10 (a) shown below opposite shows two rigid planes

of area A separated in equilibrium by a distance a and held together by 'springs' (analogous to planes within a solid held together by atomic bonds).

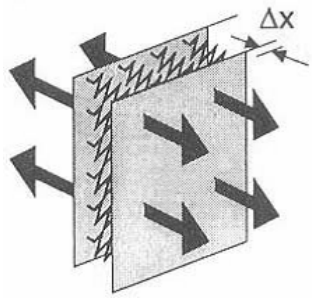

Figure 3.10 (a) Changing length of sample due to mutually opposite forces acting on the Solid.

Young's modulus is defined by:

$$\frac{F}{A} = E\frac{\Delta x}{a}$$

where, F is the force exerted on each plane. Notice that, if a rod of material is stretched in this way, it will tend to 'neck' i.e. its cross-sectional area will be reduced (shown in the Figure). This tendency is characterized by the Poisson ratio, σ, of a substance. If we apply a stress Sx (force per unit area) in the x-direction, we induce stress Sy in the y-direction. The Poisson ratio is defined as:

$$\sigma = \frac{S_y}{S_x}$$

(ii) Shear or rigidity modulus (G)

This characterizes the restoring forces appropriate to shear or transverse deformations of the substance. Figure 3.10 (b) opposite shows two rigid planes

of area A held together by 'springs' (analogous to planes within a solid held together by atomic bonds). The rigidity modulus is defined by:

$$\frac{F}{A} = G\theta$$

where F is the force on each plane.

(iii) Bulk modulus (B)

Here it should be noted that the bulk modulus (and its inverse, the compressibility K) describes the restoring forces appropriate to volume compressions of the substance. It is defined by:

$$B = -V\frac{\partial P}{\partial V}$$

where, P is the pressure and V is the volume of the substance.

If the material is easily compressed or easily sheared, than for a given strain, the restoring force will be small. In other words, a high modulus (E, G, or B) indicates that the corresponding deformation of the solid is difficult and the solid has a strong tendency to 'spring' back to its equilibrium position.

(iv) Poisson's ratio (σ)

Poisson's ratio σ is the ratio of transverse contraction strain to longitudinal extension strain in the direction of stretching force. Tensile deformation is considered positive and compressive deformation is considered negative. The definition of Poisson's ratio contains a minus sign so that normal materials have a positive ratio.

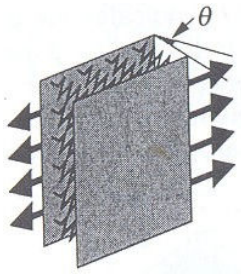

Figure 3.10 (b) Torsion (θ) produced in the solid due to tangential forces.

Virtually, all common materials become narrower in cross section when they are stretched. The reason why, in the continuum view, is that most materials resist a change in volume as determined by the bulk modulus K more than they resist a change in shape, as determined by the shear modulus G. In the structural view, the reason for the usual positive Poisson's ratio is that inter-atomic bonds realign with deformation.

The theory of isotropic elasticity allows Poisson's ratios in the range from –1 to 1/2. Physically the reason is that for the material to be stable, the stiffness must be positive; the bulk and shear stiffness are interrelated by formulae which incorporate Poisson's ratio.

Magnetic Properties

3.6 High field Magnetization

Faraday's experiment helps to make the classification of material mainly in to paramagnetic, diamagnetic and ferromagnetic.

Ferrites being mainly ionic and insulating in nature no free electrons exist. The molecular field theory can be applied to explain the magnetic properties of

ferrites. In molecular field theory neel assumes that magnetic ions are distributed between A and B sites due to the strong negative A-B interaction, moment of A sites are anti-parallel to the moment of B site. He further assumed that A-B and B-A interaction are identical and dominant over A-A and B-B, which are week interaction. The net observed magnetic moment is the difference between the two sub lattice magnetic moments. Increase in temperature results in to the disturbance of the sublattice magnetic moments leading to the zero net moment at a particular temperature known as Neel temperature. Neel's theory can also be applied to some extent for mixed ferrites having general formula as $M'_X\ M"_{1-X}\ Fe_2O_4$, where M' and M" are metallic ions. The magnetization is a powerful tool to study the domain wall motion, anisotropy, magneto-elastic coupling, magnetic hardness (or softness) of material, magnetic ordering, etc. The present work undertakes the study of magnetic ordering in ferrites and spin glass system. The induced magnetic field in a ferrite material can be plotted against applied field as shown in Fig. a. There are three subdivision of the curve (Figure 3.11). The first portion of the curve starting from the origin to in step. This portion having finite slopes of μ_0= dB/dH and is reversible. The nature follows the Raleigh's relationship,

$$\left.\begin{aligned} \mu &= \mu_0 + \nu H \\ \mu H &= \mu_0 + \nu H^2 \end{aligned}\right\}$$

or $B = \mu_0 + \nu H^2$

where $\nu = d\mu / dH$

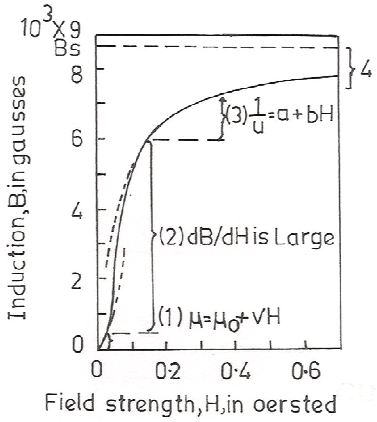

Figure 3.11 Three sections of magnetization curve separated by the "knee" and the "instep".

The second portion of the curve i.e. the region between in step and the knee has the greatest slope i.e. dB/dH is very large. This portion is irreversible.

The third portion of the curve is the part above the knee which is reversible obeying Frolich and Kennely relationship: $1/\mu = a + bH$.

The portion of the curve is based on

(i) reversible boundary displacement

(ii) irreversible bounbary displacement

(iii) reversible rotation

The maximum magnetization attained by magnetic system under the influence of external magnetic field (saturation magnetization) is to be considered as a forth part of the curve. Where the rigorous calculations yield the magnetic ordering of the material under test; since the system can be magnetically ordered according to Neel's model [22] or develops canting following YK model [23]. The difference between the calculated and measured magnetization value, gives the type of magnetic ordering. Further, the strength of inter sublattice exchange

and intra sublattice exchange interaction (J_{AA} , J_{BB}) can be obtained. This in turn identifies the magnetic order or disorder by the canting angle θ_{YK} and exchange interactions.

The spin glass phase in a magnetic disordered system is identified by the decay of remnant magnetization with time.

The saturation magnetization of each sample of $Zn_{0.3}Mn_{0.7+x}Si_xFe_{2-2x}O_4$ (x = 0.0 to 0.3, step = 0.1) and $Zn_{0.3}Mn_{0.7+x}Ti_xAl_{0.1}Fe_{1.9-2x}O_4$ (x = 0.0 to 0.3, step = 0.1) was carried out using the high field hysteresis loop technique at Department of physics, Saurashtra university, Rajkot The instrument was supplied by Arun electronics Pvt. Ltd., Bombay, India. [24]. The instrument consist of (i) Electomagnet and (ii) Pick up coil (Figure 3.12).

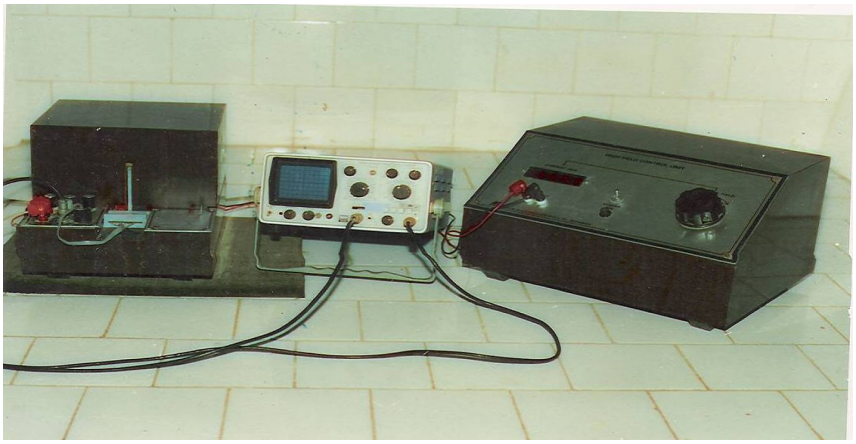

Figure 3.12 Photograph of high field hysteresis loop tracer.

(i) The electromagnet consist copper wire wounded U-shaped iron Yoke which produces magnetic field between the pole pieces. The field intensity can be changed by variation in alternating current supplied to the

winding to a maximum value of 5 kOe. The magnetic intensity is calibrated as: 100 mA = 1 kOe.

(ii) The pick up coil contains double coils with equal area and turns.

The sample was kept in one of the coils. The terminals of the pick up coil are connected to a CRO.

The alternating current is supplied to the electromagnet so that the field between the pole pieces also changes continuously. This will make the magnetic flux of the magnetic sample to change. This in turn develops voltage in the pick up coil. To obtain the magnetization value, the instrument is calibrated using standard spec-pure Nickle powders. The magnetization is plotted on y-axis of CRO whereas the magnetic field is directly read from the unit.

The saturation magnetization of the sample can be obtained from the plot of magnetization against the magnetic field. The measurements of $ZnMnTiAlFe_2O_4$ and $ZnMnSiFe_2O_4$ were carried out for all the samples at 300K.

3.7 Low field ac susceptibility

The measurement of magnetic susceptibility is very useful technique to obtain much important information regarding physical, chemical and magnetic states of the substance.

The ratio of induced magnetization to the applied magnetic field is known as magnetic susceptibility. Therefore, K = M/H emu/$cm^{3.}$ Since M is the magnetic moment of the material per cm^3, H is the applied magnetic field; K also refers to unit volume and is sometimes called the volume susceptibility.

The thermal variation of low field ac susceptibility gives information regarding transition temperature, type of magnetic ordering of the substance.

The mass susceptibility related to the volume susceptibility is defined as, $\chi = K/\rho' = M/H\rho$ emu/g.Oe where, 'ρ' being the density of the material.

The thermal magnetic studies like temperature variation of low field ac susceptibility play a key role in the study of spin glass behavior. The cusp at freezing temperature T_f in the low field ac susceptibility versus temperature characterizes the spin glass behavior [25]. It is also useful to invoke grain size effects. For example, a very fine stable single domain (SD) particle becomes superparamagnetic (SP) on heating to temperature several degrees below the Curie temperature [26]. At an applied magnetic field H, the temperature at which the susceptibility becomes infinite (i.e. the sample has spontaneous magnetization), is known as Curie or Neel temperature. At the transition (ferrimagnetic to paramagnetic) tailing effect is observed, which is due to the short range spin ordering (spin clusters).

It is obvious that the susceptibility (χ) is directly proportional to the magnetic moment M and inversely proportional to coercivity H_C when the thermal energy equals to the volume energy of a single domain (SD) particle it becomes super paramagnetic (SP) and spontaneously fluctuate between their easy directions yields zero coercivity and as a result the peak is observed in the low field χ versus T curve [27].

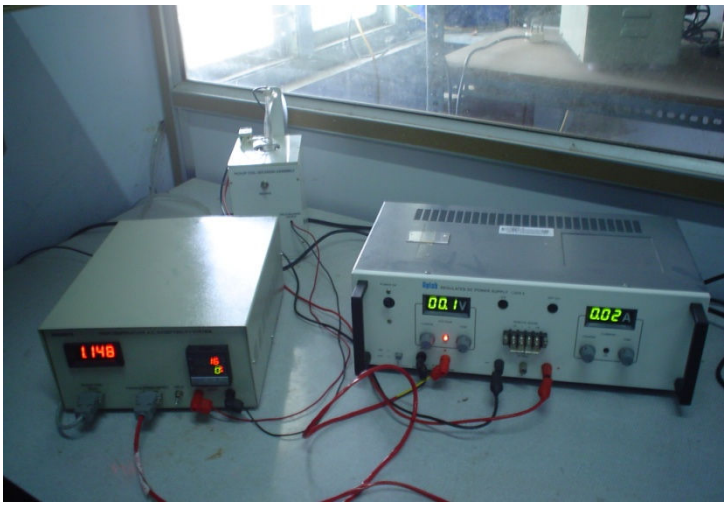

Figure 3.13 Photograph of AC Susceptibility measurement setup.

The ac susceptibility measurements of powdered samples were obtained using the instrument which consists of (i) magnetic field unit , (ii) magnetization unit and (iii) temperature unit (Figure 3.13) supplied by Magneta, Mumbai, India [24]. The block diagram of the susceptibility instrument is shown in Figure 3.14. The double coil set-up (Halmholtz coil,) operating at a frequency of 263 Hz produced magnetic field between 0 to 10 kOe. The two coils are oppositely wound relative to each other producing uniform magnetic field along the axis perpendicular to the coils. A pick-up coil is provided at the center of Halmholtz coil for the magnetization measurements.

A furnace, platinum wire wound on a silica tube, was used to heat the sample. A glass jacket with a provision of water circulation is used to avoid overheating of the coils. The furnace is inserted in a glass jacket and the glass jacket is placed in the center of the pick-up coil. The temperature was sensed by Platinum-Rhodium thermocouple calibrated against the current in the heating

element. Variable current was provided to the heating element by a variable power supply.

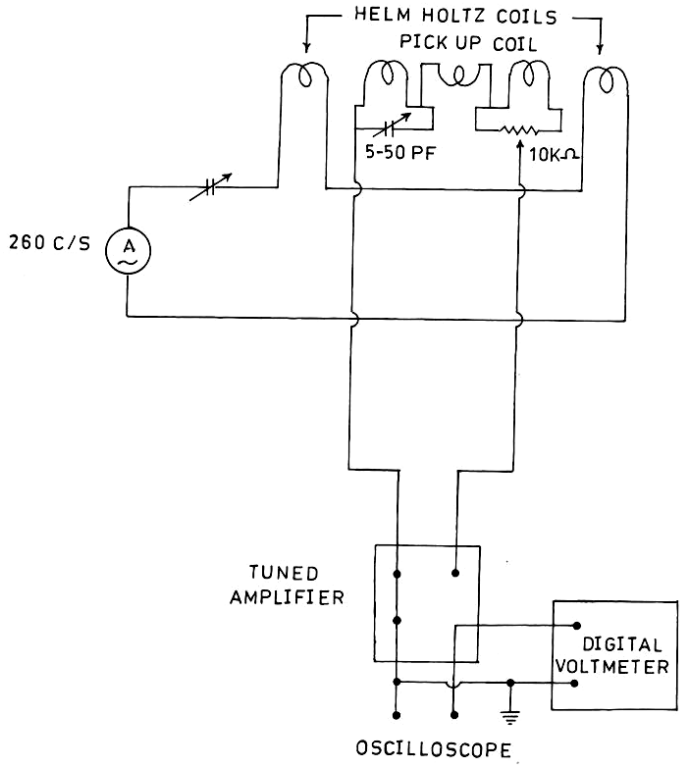

Figure 3.14 Block cum circuit diagram of susceptibility set-up.

The sample tube is held in the middle of the pick-up coil to sense minor change in magnetization of the sample. By applying the current to the Halmholtz coil, the change in magnetization of the sample producing emf in the pick-up coil. The signal is then digitized by an analog to digital converter and then fed to a digital power meter.

Merits

(1) This instrument can measure at room temperature magnetization of 10 Oe. This means that this even weakest paramagnetic sample in 100 mg quantity can be measured with an accuracy of 2%.

(2) This instrument can be used to determine Curie temperature.

(3) The electronic unit of this instrument can be used to measure permeability or hysteresis loops of soft ferrites.

3.8 Permeability Measurements

Historical Background

The magnetic permeability may be considered to be a measure of the efficiency of a magnetic material. That is, it tells us how much polarization of magnetization our input of magnetizing force will give us. In metallic magnetic materials that have much higher saturation magnetizations than ferrites, the highest permeabilities are not usually present in the materials with the highest saturations. The reason why is the dominance of other intrinsic factors such as low magnetostrictions and anisotropies, coupled with good extrinsic factors such as very clean grain boundaries and low residual stresses after annealing. In ferrites, on the other hand, the saturations are lower, the microstructure is not as clean (thicker grain boundaries), and many firing stresses remain. For reversible rotational processes, Chikazumi [28] gave the permeability (1964) as $(\mu - 1) = (\text{constant})\, M^2_s \sin^2\text{Ø} / K_1$, where Ø = angle between M and H.

For reversible wall processes, the permeability is $(\mu - 1) = (\text{constant})\, M^2_s S$ where, S = wall surface area = Second derivative of the wall energy with respect

to wall displacement, we can see that both the permeability caused by domain rotation and that caused by domain wall movement are related to M_s^2. It is not surprising to find the higher permeability in ferrites in the higher saturation Mn-Zn ferrites compared to the others. Of course, the low anisotropy and magnetostriction also help. In fact, high saturation is certainly not the only requirement for high permeability inasmuch as magnetite has a high saturation but very low permeability even at low AC frequencies because of the high eddy current losses. Manganese zinc ferrites have higher permeability at low or medium frequencies. When the frequencies involved are in the upper megahertz range, the permeability drops off owing to the great increase in losses.

Nickel Zinc ferrites are characterized by their high material resistivity, several orders of magnitude higher than MnZn ferrites. Because of its high resistivity NiZn ferrite is the material of choice for operating from l-2 MHz to several hundred MHz. To cover such a wide frequency range and different applications, a large number of nickel-zinc materials have been developed over the years. Use of Nickel Zinc ferrites is limited due to their increasing cost. It should be noted that certain nickel chemistries are stress sensitive and can be adversely changed by some types of stress; this may be a mechanical shock or any grinding operations. Strong magnetic fields from holding devices and fixtures or magnetic chucks used in machining operations may also provide this stress. These resulting changes can include variation in permeability and core loss (lowering of Q). These changes cannot be reversed by degaussing or other electric/magnetic processes.

Manganese Zinc ferrite has the highest permeability and saturation induction of the ferrite class of materials and has the advantage of various stoichiometries with nearly zero magneto-crystalline anisotropy and magneto-restriction, important for stress insensitivity and low noise.

Effect of Iron Content on Permeability

The metal ion present in the largest concentration mole wise in ferrites is $Fe^{3+,}$ and since it has a high ionic moment (5 μ_B) it has the highest potential for controlling the magnetic characteristics. In the completely inverse ferrites such as $NiFe_2O_4$, the large moments of the two Fe^{3+} sublattices cancel each other, and no advantage is taken of the potential Fe^{3+} moment. The large moment of Fe^{3+} is used in the zinc-substituted mixed ferrites in which the Fe^{3+} ions on the two sublattices are disproportionate. These effects are not chemical. With the great variety of possible chemistries of spinal ferrites, the Fe_2O_3 content of the finished ferrite is the least varied of all the metal ions since it is pegged at 50 mole percent by the spinal formula (MO. Fe_2O_3). In most commercially important Mn-Zn ferrite materials, the starting mix may contain slightly more than 50 mole percent of Fe_2O_3. The purpose of the extra ion is to improve the magnetic properties by the formation of Fe^{2+} ions. One such basic property is the magnetostriction which is defined as change in the length of a material when it is subjected to a magnetic field.

The magnetostrictions of several ferrites are shown in the table 3.2. Note that ferrous ferrite is the only ferrite that has positive magnetostriction. Therefore, it would be useful to minimize the net magnetostriction by compensating the

negative values of the other ferrites through the incorporation of ferrous ferrite as a part of the solid solution. Ferrous ferrites, $FeO.Fe_2O_3$ are actually magnetite, a naturally occurring but technically unimportant ferrite. The additional iron for the divalent Fe++ is usually added in the original mix as Fe_2O_3 but then is reduced to FeO or Fe_2O_3 in the sintering or firing process to maintain the 50 % Fe_2O_3 requirement.

Table 3.2 Saturation magnetostriction of some ferrites.

Ferrites	Saturation Magnetostriction
$MnFe_2O_4$	-5×10^{-6}
$FeFe_2O_4$	41×10^{-6}
$CoFe_2O_4$	-110×10^{-6}
$Ni_{0.8}Fe_{2.2}O_4$	-17×10^{-6}
$Li_{0.5}Fe_{2.5}O_4$	-8×10^{-6}
$CuFe_2O_4$	-6×10^{-6}

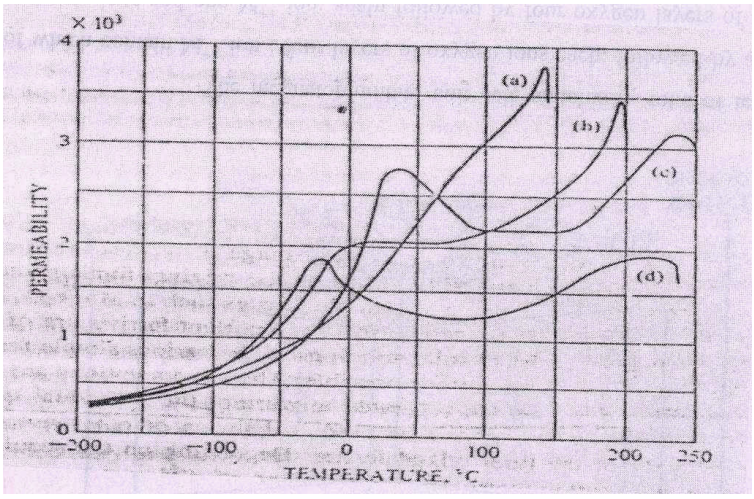

Figure 3.15 Temperature versus Permeability curve for Mn-Zn ferrites with different Fe content.

Guilaud (1957)[29] (Figure 3.15) found that for a fixed Mn concentration , an increase in the Fe content in the initial mix caused the μ versus T slope to be less steep at room temperature. Many Manganese ferrites that contain ferrous ions have a secondary permeability maximum (SPM) , the primary maxima occurring just below Curie temperature.

As the iron content is increased, the secondary maximum moves to lower temperature. If the highest permeability is desired at room temperature, the iron content is usually chosen so that the secondary permeability maximum occurs at room temperature. This change in temperature dependence of the permeability is due to the movement to lower temperature of point where the magnetostriction goes through zero. In instances where the permeability maximum does not occur at zero anisotropy, the deviation may be due to the presence of increased porosity which lowers the permeability prematurely as reported by Stuijts, 1964. [30]

Ferric Ion Substitution

Gellio [31] reported in 1958 that ,in some cases , the substitution of other trivalent ions such as Al^{+++} , Ga^{+++}, or Cr^{+++} for Fe^{+++} is made for special magnetic or electric functions. These may include reducing the saturation magnetization, increasing the temperature stability, or increasing the resistivity. In the spinal ferrites, the substitution of nonmagnetic ions such as Al3+ on octahedral sites in an inverse spinal such as nickel ferrite will reduce the saturation magnetization since it has net compensated moment. Gilleo (1958) [31] investigated the substitution of many ions in garnets; his main interest was to reduce the

saturation for microwave resonance properties and to increase temperature stability. In the garnets, Al^{3+} is often used to reduce the magnetization. however for the garnets, the substitution occurs on the tetrahedral sites which are those that have the uncompensated moments he investigated that when non magnetic ions are substituted for magnetic ions , the curie temperature is reduced, regardless the site where substitution occurs. Divalent ions of metals such as Mn, Fe , and Co can be substituted for Fe^{3+} if equal amounts of quadrivalent Si, or Ge are also added to maintain the equivalent three positive charge of two ferric ions by one divalent and one tetravalent.

Permeability dependence on Zinc

Most commercially important low frequency ferrites contain Zn. Zinc ion substitution for other divalent ion can increase effective magnetic moment. It also contributes in an increase in magnetic permeability. Very often, it is the ratio of ZnO to the other divalent oxides as well as the degree of divalent Fe substitution that gives ferrite material developers greatest latitude in optimizing the properties of a specific ferrite. In the sintered ferrite the zinc content will depend on the amount that went in originally minus that which was lost in the sintering process. Since Zn is a rather volatile ion, incorrect firing will cause its loss which will lead to a gradient in Zn content across the thickness of the ferrite. In addition to loosing the chemistry influence of Zn, strains will be introduced , further deteriorating the ferrite. Zn not only increases the moment , but also lowers magnostriction and anisotropy. The anisotropy of $MnFe_2O_4$ is -28×10^3 ergs / cm^3. (Bozorth, 1955) [32] and that of $Mn_{0.45}$, $Zn_{0.55}$, Fe_2O_4 is -3.8×10^3

ergs / cm^3 . (Galt, 1951) [33]. In Ni – ferrite, λs is reduced from -26×10^{-6} (Smith and Wijn, 1954) [34] to -5×10^{-6} for $Ni_{0.36}\ Zn_{0.64}Fe_2O_4$ (Enz,1955) [35]. MnZn ferrites also have so much Fe^{2+} ion that λs is usually lower than $1x10^{-6}$

Effect of cobalt on permeability

The effect of cobalt is evidenced primarily on the anisotropy. Co – ferrite or mixed ferrites with Co are the only ones that have positive anisotropies. Therefore, the anisotropy of the Co-ferrite can be used to compensate the negative anisotropies of other ferrites. Thus, the anisotropy of the mixed ferrite will be zero. Co-ferrite is quite frequently used in Ni or NiZn ferrites for anisotropy compensation. Both Akashi(1971-71) [36] and Roess(1977) [37] have used cobalt to lower losses and for temperature compensation . Another advantage of cobalt is its ability to make the ferrite susceptible to magnetic annealing. High frequency losses are also lowered by the addition of Co2+, permitting there use in the high megahertz range. Stijntjes (1971) [38] used co stabilization in combination withTiO_2 in low-loss, low-level applications, whereas Buthker (1982) [39] used Co stabilization in high-power applications.

Oxygen Stoichiometry

Small changes in oxygen content may drastically alter the properties of the ferrite. In some situations non equilibrium atmospheres for the stoichiometric spinel may create conditions for slight oxygen surpluses or deficiencies without the apparent presence of a second phase. These situations occur by the formation of either cation or anion vacancies in the spinel lattice. These vacancies can influence the microstructural aspects by affecting the diffusion

rates of the cations. Tanaka (1975) [40] studied the effects of oxygen nonstoichiometry as well as composition on several magnetic and mechanical properties of MnZn ferrites. Tanaka looked at how the initial permeability, the frequency and temperature responses of the initial permeability, and the domain structures were influenced by the same oxygen nonstoichimetry. In polycrystalline ferrites fired to grain boundaries, whereas in those fried to give high oxygen parameters, the patterns are random and nuclear. At lower frequencies, the highest permeabilities are found in the ferrites with low oxygen parameters. The permeability at highest frequency was not dependent on the permeabilities at low frequencies. The permeability is effected by grain size and porosity, but in this case, these effects were minimized by keeping these factors constant.

Effect of Foreign Ions on Permeability

Guillaud (1957) [29] studied the effect of alkali (Na, K) and alkaline earth (Mg, Ca, Ba) impurities on the permeability of MnZn and NiZn ferrites. The impurities were added either by co-precipitating with the original composition or by impregnating the mixture with a salt of the impurity and then decomposing the salt to the oxide. Grain sizes were kept constant. At low impurity concentrations, there is an initial increase in permeability. The steep part of the curve is attributed to the impurity that dissolves in the lattice, whereas the flat portion is the result of saturation and deposition at the grain boundary. The increase in permeability was greater the larger the ionic radius of the impurity, the effect of the ionic radius of the impurity, the effect being great for alkaline earths (+2 valence) than

for alkalines (+1 valence). At higher impurity concentrations the effect will reverse and eventually the permeability will decrease due to microstructural effects such as grain size and porosity. Akashi (1961, 1963,1966) [36] showed that the presence of CaO substantially improved the properties of MnZn ferrites at low concentrations , reached a maximum effectiveness , and then dropped off at higher levels. At still higher concentrations, Impurities such as SiO2 create a duplex structure of giant grains with a fine grain matrix which is very detrimental to permeability. Many metallic elements such as Mo , V . Cu , Cd and Al show similar behavior, with increases in permeability up to 50 percent at very low concentrations. (Lescroel and Pierrot , 1960) [41]. these materials may initially increase the permeability by acting as sintering aid to increase the density and grain size.

Electrical Properties

3.9 DC Resistivity

Introduction

There is a sense in which every property of a solid can be considered an electrical property. This is because the particles that make up solids are fundamentally electrical in nature. The response of solids to externally applied electric fields is referring to as electrical properties.

When any substance is subject to an applied electric field E, a current of electronic charge flows through the substance. The magnitude of the resultant current density, j, is characterized by the electrical resistivity ρ or the electrical

conductivity ($\sigma = 1/\rho$) of the substance. The electrical resistivity and conductivity are determined by: $j = \sigma E$ and $E = \rho j$

If the current density is measured in Am^{-2} and electric field (E) in Vm^{-1}, then the units of σ are $\Omega^{-1} m^{-1}$ or $S\ m^{-1}$. The SI symbol of S stands for Siemens not to be confused with 's' for second. The units of resistivity are Ω m. for an example of cross sectional area A and length L, the resistivity is related to the electrical resistance R by: $\rho = RA / L\ \Omega m$

Electrical Resistivity

The range of resistivity values of ferrite and garnet materials is wide ranging from 10^{-4} to 10^{9} Ω·m at room temperature [26]. In ferrites, the high value of resistivity is associated with the simultaneous presence of ferrous (Fe^{2+}) and ferric (Fe^{3+})ions on equivalent lattice sites (usually the octahedral (B-) sites). The value of resistivity in magnetite, $Fe^{2+}\ Fe_2^{3+}O_4$ (Fe_3O_4), is of the order of 10^{-4} or 10^{-5} Ω·m. In nickel-zinc ferrite it was found that the resistivity was about 10 Ω·m when the material contained 0.42 percent by weight of ferrous oxide but this resistivity increased approximately one thousand fold when the specimen was more completely oxidized.

A mechanism of conduction is known which covers the situation cited above. The extra electron on a ferrous ion requires little energy to move to a similarly situated adjacent ferric ion. The valence states of the two ions are interchanged. Under the influence of an electric field, these extra electrons can be considered to constitute the conduction current, jumping or hopping from one iron ion to the next.

Since the materials are semiconductors, their resistivity ρ should decrease with increase in temperature according to a relation of the form: $\rho = \rho_o \exp(E\rho/kT)$.

This relation is indeed often observed and the activation energy $E\rho$, can then be interpreted as the energy required to cause the electron jump referred to above relation.

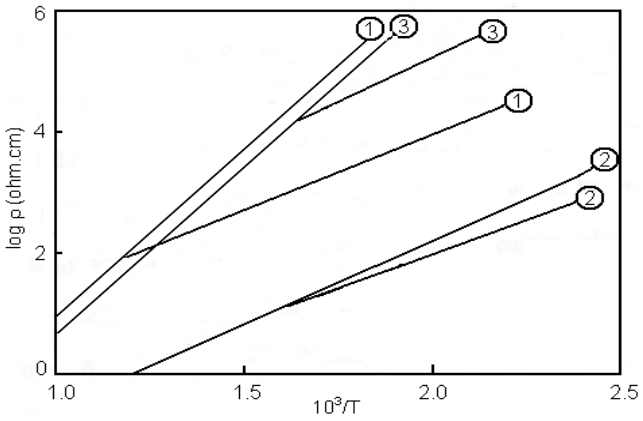

Figure 3.16 Thermal variation of resistivity (1) Nickel ferrite, (2) Copper ferrite and (3) Magnesium ferrite.

. Some examples are given in Figure 3.16 which show the linear relation between $\log\rho$ versus $10^3/T$. Breaks occur in the curves of Figure 3.16 at temperatures which correspond closely with the observed ferrimagnetic Curie temperatures. As would be expected with such a conduction mechanism, the high activation energy is associated with a high resistivity at room temperature.

In the electrical resistivity measurement a typical sample holder shown in Figure 3.8 specially designed and fabricated for the resistivity measurement was used. It consists of two ceramic beads with supporting metal rods. The electrodes E_1 and E_2 are also shown in this figure. The spring loaded brass

electrode (E_2) is introduced into the ceramic beads and it pressed hard against the surface of the pellets. The brass electrode E_1 is fixed at the other end.

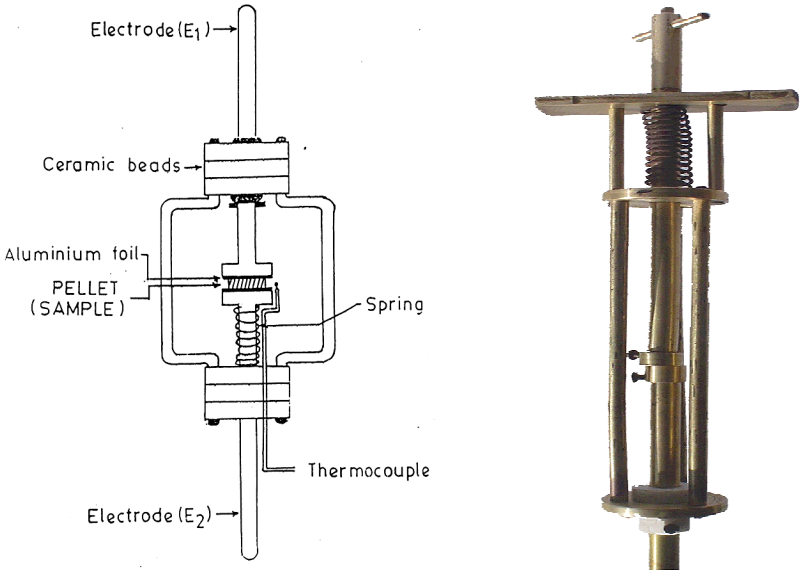

Figure 3.17 Sample holders for two-probe resistivity measurement.

The resistance of a pellet was measured by two terminal method using meg-ohm meter. The sample surfaces were rubbed by graphite and thin aluminum foils were placed between the terminals of sample holder (Figure 3.17) and the pellet surfaces for the proper contacts. The sample holder with the pellet was placed in a horizontal electric furnace to study the change in resistivity with temperature. The temperature of the furnace was controlled by maintaining the current passing through the heater by means of current controller. The temperature of the sample was measured with Cr-Al thermocouple. Experimental set-up is shown in the Figure 3.18. The resistance of the each pellet was measured for raising and falling of temperature at the gap of 20˚C. The thickness

(l) and diameter of the pellets were measured by digital vernier calipers. From these observations the resistivity (ρ) was found us. Logarithm of resistivity was plotted against reciprocal of temperature ($10^3/T$). The activation energies for the ferrimagnetic region (E_f) and paramagnetic region (E_p) in electron volt (eV) were determined from the slopes of these plots.

Figure 3.18 Experimental set-ups for dc resistivity measurement Hopping model of electrons.

Jonker has observed in cobalt ferrites that the transport properties differ considerably from those of normal semiconductors, as the charge carriers are not free to move through the crystal lattice but jump from ion to ion. It was also noted that in this type of materials the possibility exists of changing the valency of a considerable fraction of metal ions and especially that of iron ions [43].

Assuming the number of electrons contributing to be equal to the number of Fe^{2+} ions and the number electron holes to be equal to the number of Co^{3+} ions Jonker has calculated from the resistivity data extremely low values of mobilities $\mu_1 = 10^{-4}$ $cm^2/Vsec$ for electrons and $\mu_2 = 10^{-8}$ cm^2/V sec for holes. Further, even for samples with a large concentration of Fe^{2+} or Co^{3+}ions, a fairly

strong exponential dependence of resistivity on temperature was found. From the ordinary band theory of conduction one would expect metallic behaviour for such high concentration, i.e. a high mobility with only slight temperature dependence. In cobalt ferrite compounds the behaviour is similar to NiO and Fe_2O_3 and the ordinary theory based on simple band picture does not apply. The activation energy does not belong to the energy picture of electrons but to the crystal lattice around the site of electrons. The general expression for the total conductivity where we have two types of charge carriers can be given as [44]

$\sigma = n_1 e\mu_1 + n_2 e\mu_2$

The temperature dependence of conductivity arises only due to mobility and not due to the number of charge carriers in the sample.

Thus, we can conclude that, for the hopping conduction mechanism

1. Low value of mobility.
2. Independence of Seebeck coefficient on temperature. This property is due to the fact that in hopping model the number of charge carriers is fixed.
3. Thermally activated process with activation energy E_a called the hopping activation energy.
4. Occurrence of n-p transition with changes in the Fe^{2+} or oxygen concentration in the system.

Small polaron model

A small polaron is a defect created when an electronic carrier becomes trapped at a given site as a consequence of the displacement of adjacent atoms or ions.

The entire defect (carrier plus distortion) then migrates by an activated hopping mechanism. Small polaron formation can take place in materials whose conduction electrons belong to incomplete inner (d or f) shells which due to small electron overlap; tend to form extremely narrow bands. The possibility for the occurrence of hopping conductivity in certain low mobility semiconductors, especially oxides, has been widely recognized for some time.

The polaron comprises the electron plus its surrounding lattice deformation. (Polaron can also be formed from holes in the valence band). If the deformation extends over many lattice sites, the polaron is “large”, and the lattice can be treated as a continuum. Charge carriers inducing strongly localized lattice distortions form “small” polarons. The concept of large polaron is most useful when the carrier mobility is high and the carrier density and temperature both are low [45].

For a small polaron the spatial extent of its self-trapped charge is comparable to or smaller than interatomic distances. In particular atoms surrounding an excess charge are displaced to new equilibrium positions and produce a potential well which traps the excess particles. Small polaron formation is typically associated with the interaction of the excess charge with the atoms in its immediate vicinity. Thus, unlike the case of the large polaron, the self-trapping is not primarily associated with the long range interaction of an excess charge with the dipolar fields of polar materials. Hence, the name polaron, coined to reflect this latter situation, is a misnomer for the small polaron. Electron and hole small polarons are found in both polar and non-polar

semiconductors and insulators. This includes numerous oxides and molecular solids.

Small polaron motion proceeds relatively slowly via a succession of phonon-assisted hopping events. As a result, the small polaron drift mobility increases as a thermal agitation of the solid increases. Above a temperature comparable to the solid's phonon temperature, the diffusivity increases in an Arrhenius manner with reciprocal temperature.

The migration of small polaron requires the hopping of both the electron and the polarized atomic configuration from one site to an adjacent one [43]. For fcc lattice the drift mobility takes the form $\mu = (1 - c)\, e\, a^{2\Gamma/kT}$, where, e is the electronic charge, a the lattice parameter, c is the fraction of sites which contain an electron (c=n/N), n is the number of electrons and N the number of available sites per unit volume. The quantity Γ is the jump rate of the polaron form one site to a specific neighboring site.

The small polaron model also explains the low value of mobility, temperature independent Seebeck coefficient and thermally activated hopping. In addition to these properties if the hopping electron becomes localized by virtue of its interaction with phonons, then a small polaron is formed and the electrical conduction is due to hopping motion of small polarons.

3.10 Thermo electric power measurements

Introduction

The temperature difference between the two ends of a semiconductor gives rise to an electro motive force (emf) known as thermo emf (∇V). It is found that the

generated thermo emf is proportional to the temperature difference (∇T) and is given by the relation: $\nabla V = \alpha \Delta T$, Where, α is the Seebeck coefficient also often known as the thermo-electric power.

Hall Effect and thermo-electric power study are widely used in the interpretation of the conduction mechanism in semiconductors. The interpretation of the Hall Effect is more straight forward, and it also gives precise results. However, in the case of low mobility materials such as ferrites, garnets and perovskites, it is sometimes difficult to measure the Hall Effect; in such cases the thermo-electric power measurement is the only alternative. The measurement of thermo-emf is simple and its sigh gives vital information about the type of conduction (p-type or n-type) or charge carriers (electrons or holes) responsible for the electrical conduction in semiconductors. Another important significance of thermo-emf is that, it enables one to calculate the values of Fermi energy and carrier concentration. Knowledge of Fermi energy helps in the determination of the various regions viz. impurity conduction, impurity exhaustion and intrinsic conduction regions of a semiconductor.

In the case of a n-type semiconducting material, the hot surface becomes positively charged, as it loses some of its electrons. The cold surface of the semiconductor becomes negatively charged due to the diffusion of free electrons from the hot portion. Conversely, in a p-type semiconducting material, the hot surface becomes negative, and the cold one positive. Thus the type of conduction in a given semiconducting material can readily be determined from the sign of the thermo-emf.

Theory

The Fermi energy in the case of a semiconductor can be obtained from the relation: $\alpha T = (E_G - E_F) + 2kT$ for n-type semiconductors and for p-type semiconductors $\alpha T = E_F + 2kT$, where, E_G = Energy gap of the ferrite semiconductor, E_F = Height of the Fermi energy level from the top of the filled Valence band ,2kT = the term which accounts for the transfer of kinetic energy of the carriers in moving from the hot region of the ferrite to a cold one.

While discussing the electrical properties of $\alpha - Fe_2O_3$, for which the mobility of the charge carrier is, low, Morin [46] assumed that the conduction is occurring in exceedingly narrow bands or in localized levels. This assumption leads to the result that the kinetic energy term in the Seebeck effect can be neglected, so that for electrons alone, $\alpha T = E_G - E_F$, while, for holes alone, $\alpha T = E_F$

Experimental procedure

The experimental set-up to determine thermo-emf of ferrite samples is shown in Figure 3.19**.** It consists of a point contact probe, which acts as a hot junction and a base which acts as a cold junction. Between the two junctions a sample is kept. The temperature of the hot probe is raised to a maximum of around 473K with the help of an electric heater, which is wound round the hot probe.

Figure 3.19 Photograph of thermo electric power measurement set up.

A thermoelectric power study was carried out over a temperature range 300–473 K by the differential method. The temperature gradient was measured by two chromel-alumel thermo-couples that were kept very close to the sample while the thermo-emf was measured with the help of a digital micro voltmeter with an accuracy of ±3%. In order to achieve good thermal stability, the values of the thermo-emf have been recorded while cooling. The sample is maintained at a given temperature for about 5-10 minutes.

A pointed hot probe is used here since ferrite samples are very good thermal conductors; if a pointed probe is not used to upper and the lower surfaces of the samples will attain almost the same temperature and no temperature gradient will be maintained between them.

3.11 Current (I) versus voltage (V) characteristics

The current (I) versus voltage (V) behaviour of any material at low electric field is linear (ohmic) due to the presence of thermally generated carriers. With increasing field I – V characteristic becomes non linear (non-ohmic) in most non-

metallic materials. The current rises rapidly with voltage taking the form of a power relation or exponential dependence in voltage prior to electronic or thermal breakdown of the material. In some materials the current increases linearly upto certain applied field and then rapidly large current flows and voltage decreases. This phenomenon is known as the switching. Switching and memory effects exhibited by thin oxide films and other semi-insulating materials in sandwich configurations are of considerable interest to microelectronics industry.

A large number of oxides and semi insulating materials exhibit similar conduction phenomenon at high fields and in all cases the space charge limited flow trapping and recombination process play a major role. Switching and memory phenomenon has been reported in ferrites. Ferrites like Mg-Mn, Li doped YIG and Li ferrites showed similar behavior [47] Yamashiro [48] was first to report this phenomenon in stoichiomaetric copper ferrite. He attributed this type of behaviour in copper ferrites as due to co-operative Jahn-Teller distortion transformation. Histake et al [47] have observed similar behaviour in Cu ferrite and Li ferrite. This he attributed to Joule self heating which occurs generally in ferrites and garnets, because Li is non Jahn-Teller ion.

Theories of Switching Phenomena

The current (I) versus voltage (V) behaviour of any material at low electric field is linear (ohmic) due to the presence of thermally generated carriers. With increasing field I-V characteristic becomes non-linear (non-ohmic) in most non metallic materials. The current rises rapidly with voltage taking the form of a

power relation or exponential dependence on voltage prior to electronic or thermal breakdown of the material. If the high resistivity materials in the form of thin films are sandwitched between suitable metal electrodes and are appropriately formed electrically then the I-V characteristic show largely reproducible and reversible unstable conduction regions before the ultimate irreversible breakdown of the sandwitch material occurs. Generally, the unstable conduction regions are of three types as shown in Fig. 3.20, where conductivity switches from one value to another via unstable region. The switching behaviour models of disordered material of these unstabilities are given as follows:

a) VCNR: Voltage controlled negative resistance or N type.
b) CCNR: Current controlled negative resistance or S type
c) The bistable or memory switching.

V.C.N.R.

In the case of VCNR it is proposed that the field ionization of impurities from an impurity band located somewhere between the valence and conduction band of the insulator, increase the conductivity. With further increase in the field a compitative recombination process may set in and then the conductivity will be lowered. It is possible that ionic movement and the accompanying space charge play a significant role in VCNR (Figure 3.20 (a)).

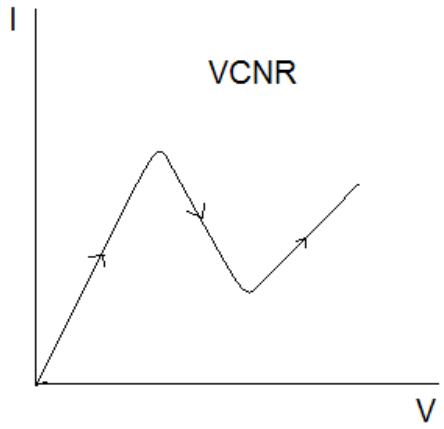

Figure 3.20(a) VCNR type switching,

C.C.N.R.

From the observations the general conclusion can be drawn in the following lines: (Figure 3.20 (b)).

i. This phenomenon is a bulk limited effect characteristic of the semi insulating materials with no or little dependence on the electrode material.

ii. Commonly observed that at high fields for current transport through disordered semi-insulating material with a high density of traps.

iii. The threshold voltage depends on the preparation, treatment, geometry, history and ambient temperature.

iv. Thermal or filamentary processes are present in some cases but there is no evidence that these are dominant processes in all cases [49].

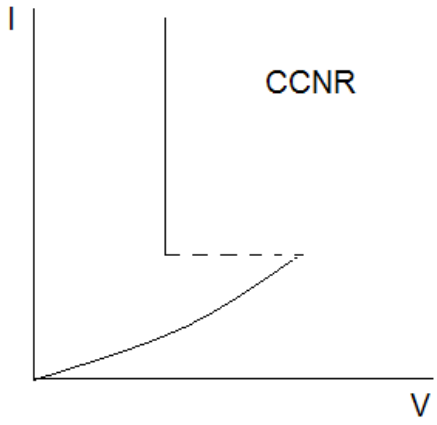

Figure 3.20(b) CCNR type switching.

Memory or Bistable Switching

Bistable switching is characterized by occurance of filamentary conduction and structural changes. In the case of multicomponent semiconducting material cooling from the temperature may result in a state where all electrons are taken up in low conductivity state, while cooling from a different temperature may allow a rearrangement of position of atoms in which segregation of some of the conducting constituents occur forming a high conductivity states (Figure 3.20 (c)).

The circuit diagram of the experimental set-up used for I – V measurements for the present system is shown in the Figure 3.21 A typical sample holder used for resistivity measurement was used as a sample holder whose both ends act as electrodes. High voltage in the range of 0-500 V was applied through Aplab made high voltage d.c regulated power supply (model: 7332). The current and voltage applied across the sample was measured by milliameter and digital voltmeter respectively. The measurements were carried out for two different temperatures 300 K and 450 K. For the measurements at

450 K temperature the sample holder was set in a horizontal furnace and temperature was maintained by the temperature controller. The temperature of sample was measured with Cr-Al thermocouple.

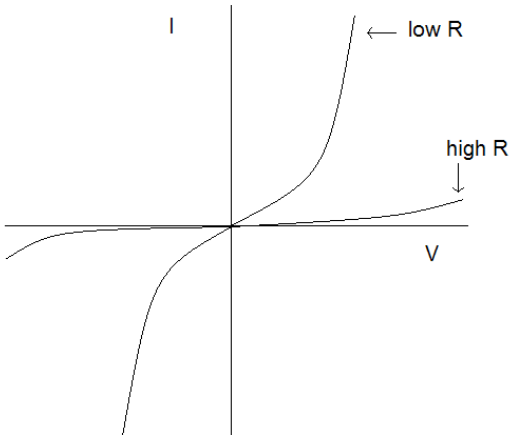

Figure 3.20 (c) MEMORY type switching.

The circuit diagram of the experimental set-up used for I-V measurements for the present system is shown in the Figure 3.21.

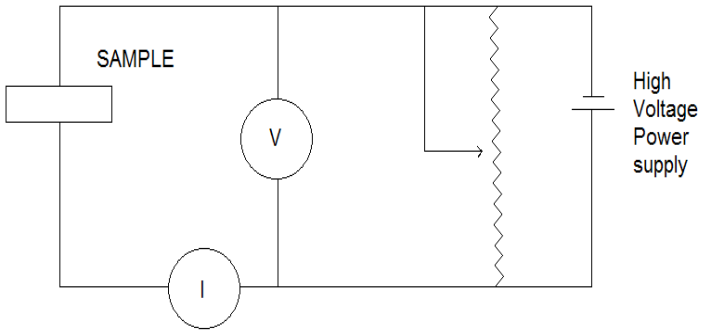

Figure 3.21 Circuit diagram of the experimental set up for I-V measurement.

A typical sample holder used for resistivity measurement was used as a sample holder whose both ends act as electrodes. High voltage in the range of 0-

500 V was applied through Aplab made high voltage d.c. regulated power supply (model: 7332). The current and voltage applied across the sample was measured by milliameter and digital voltmeter respectively. The measurements were carried out for different temperatures. For the high temperature measurements the sample holder was set in a horizontal furnace and temperature was maintained by the temperature controller. The temperature of sample was measured with Cr-Al thermocouple.

Dielectric Properties

3.12 AC resistivity and Dielectric measurements

Field Vector and Polarization

Perhaps the best approach to an explanation of the phenomenon of capacitance is with the aid of field vectors. To begin, for every electric dipole, there is a separation between a positive and a negative electric charge as demonstrated in Figure 3.16. An electric dipole moment p is associated with each dipole as: P=q d, Where q is the magnitude of each dipole charge and d is the distance of separation between them. In reality, a dipole moment is a vector that is directed from the negative to the positive charge, as indicated in Figure 3.16. In the presence of an electric field ε , which is also a vector quantity, a force (or torque) will come to bear on an electric dipole to orient it with the applied field; this phenomenon is illustrated in Figure 3.16 The process of dipole alignment is termed Polarization.

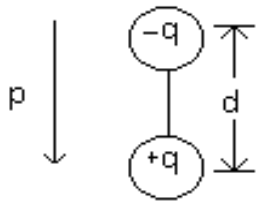

Figure 3.16 Schematic representation of an electric dipole generated by two electric charges (Of magnitude q) separated by the distance d; the associated polarization vector p is also shown.

Again, returning to the capacitor, the surface charge density D, or quantity of charge per unit area of capacitor plate (C/m^2), is proportional to the electric field. When a vacuum is present, then $D_o = \varepsilon_o E$

The constant of proportionality beint ε_o. Furthermore, an analogous expression exists for the dielectric case, that is, $D = \varepsilon E$, Sometimes, D is also called the dielectric displacement (Figure 3.17).

The increase in capacitance, or dielectric constant, can be explained using a simplified model of polarization within a dielectric material. Consider the capacitor in Figure 3.18(a), the vacuum situation, wherein a charge of $+Q_o$ is stored on the top plate, and $-Q_o$ on the bottom one. When a dielectric is introduced and an electric field is applied, the entire solid within the plates becomes polarized (Figure 3.18(c)). As a result of this polarization, there is a net accumulation of negative charge of magnitude –Q' at the dielectric surface near the positively charged plate and, in a similar manner, a surplus of +Q' charge at

the surface adjacent to the negative plate. For the region of dielectric removed from these surfaces, polarization effects are not important.

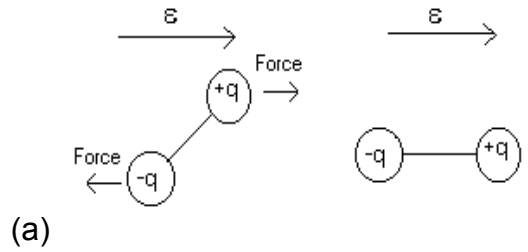

Figure 3.17 (a) Imposed forces (torque) acting on a dipole by an electric field (b) Final dipole alignment with the field.

Thus, if each plate and its adjacent dielectric surface are considered to be a single entity, the induced charge from the dielectric (+Q' or –Q') may be thought of as nullifying some of the charge that originally existed on the plate for a vacuum ($-Q_o$ or $+Q_o$). The voltage imposed across the plates is maintained at the vacuum value by increasing the charge at the negative (or bottom) plate by an amount –Q'. Electrons are caused to flow from the positive to the negative plate by the external voltage source such that the proper voltage is reestablished. And so the charge on each plate is now Q_o +Q', having been increased by an amount Q'.

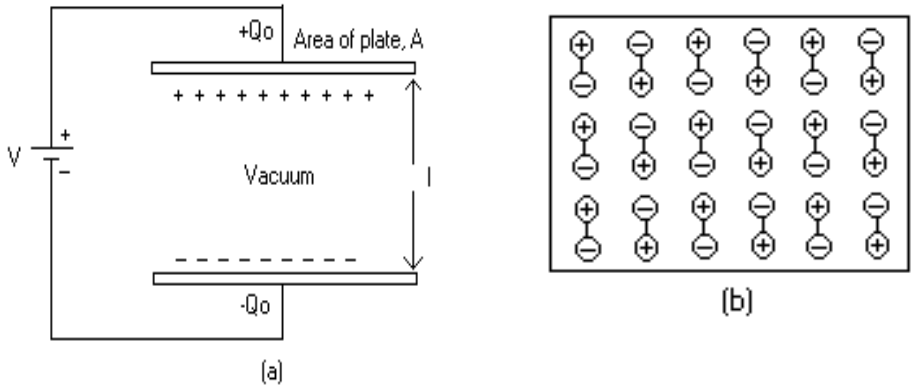

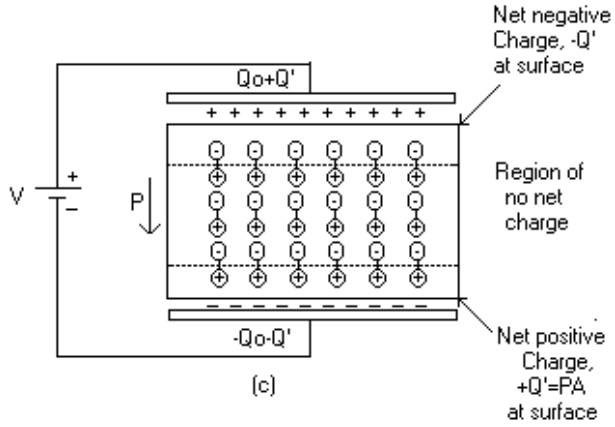

Figure 3.18 Schematic representations of (a) the charge stored on an unpolarized dielectric, and (c) the increased charge stori capacity resulting from the polarization of a dielectric material.

In the presence of a dielectric, the surface charge density on the plates of a capacitor may also be represented by: $D= \varepsilon_o\varepsilon + P$, Where P is the polarization, or the increase in charge density above that for a vacuum because of the presence of the dielectric; or, from Figure 3.18(c), P=Q'/A, Where A is the area of each plate. The units of P are the same as for D (C/m^2).

The polarization P may also be thought of as the total dipole moment per unit volume of the dielectric material, or as a polarization electric field within the dielectric that results from the mutual alignment of the many atomic or molecular dipoles with the externally applied fieldε. For many dielectric materials, P is proportional to ε through the relationship: $P = \varepsilon_o (\varepsilon_r - 1) \varepsilon$, In which case ε_r is independent of the magnitude of the electric field.

TYPES OF POLARIZATION

Polarization is the alignment of permanent or induced molecular dipole moments with an externally applied electric field. There are three types or sources of polarization: electronic, ionic, and orientation. Dielectric materials ordinarily exhibit at least one of these polarization types depending on the material and also the manner of the external field application.

ELECTRONIC POLARIZATION

Electronic polarization may be induced to one degree or another in all atoms. It results from a displacement of the center of the negatively charged electron cloud relative to the positive nucleus of an atom by the electric field (Figure 3.19(a)). This polarization type is found in all dielectric materials, and of course, exists only while an electric field is present.

IONIC POLARIZATION

Ionic polarization occurs only in materials that are ionic. An applied field acts to displace cations in one direction and anions in the opposite direction, which gives rise to a net dipole moment. This phenomenon is illustrated in Figure 3.19(b). The magnitude of the dipole moment for each ion pair p_i is equal to the product of the relative displacement d_i and the charge on each ion, or $p_i = q\, d_i$

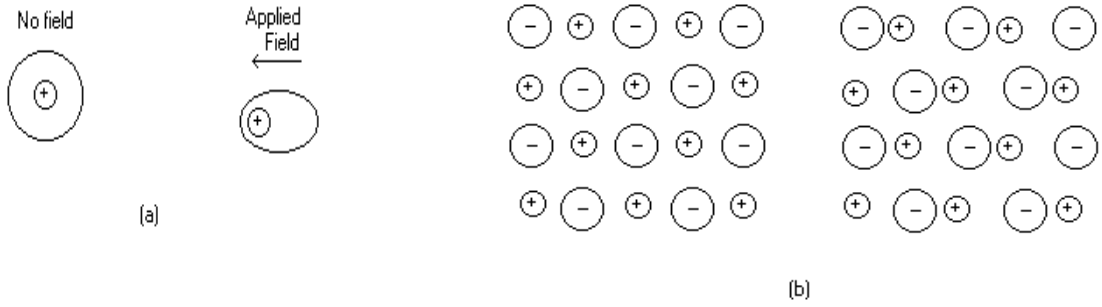

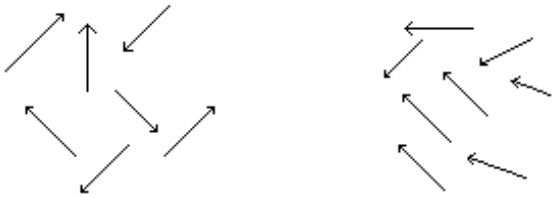

(c)

Figure 3.19 (a) Electronic polarization that results from the distortion of an atomic electric field. (b) Ionic polarization that results from the relative displacement of electrically charged ions in response to an electric field (c) Response of permanent electric dipoles (arrows) to applied electric field, producing orientation polarization.

ORIENTATION POLARIZATION

The third type, orientation polarization, is found only in substances that possess permanent dipole moments. Polarization results from a rotation of the permanent moments into the direction of the applied field, as represented in Figure 3.19(c). The thermal vibrations of the atoms counteract this alignment tendency is counteracted by the thermal vibrations of the atoms, such that polarization decreases with increasing temperature. The total polarization P of a substance is equal to the sum of the electronic, ionic, and orientation polarizations (P_e, P_i, and P_o, respectively),or $P = P_e + P_i + P_o$.

It is possible for one or more of these contributions to the total polarization to be either absent or negligible in magnitude relative to the others. For example, ionic polarization will not exist in covalently bonded materials in which no ions are present.

DIELECTRIC STRENGTH

When very high electric fields are applied across dielectric materials, large numbers of electrons may suddenly be excited to energies within the conduction band. As a result, the current through the dielectric by the motion of these electrons increases dramatically; sometimes localized melting, burning, or vaporization produces irreversible degradation and perhaps even failure of the material. This phenomenon is known as dielectric breakdown. The dielectric strength, sometimes called the breakdown strength, represents the magnitude of an electric field necessary to produce breakdown.

DIELECTRIC MATERIALS

A number of ceramics and polymers are utilized as insulators and/or in capacitors. Many of the ceramics, including glass, porcelain, steatite, and mica, have dielectric constants within the range of 6 to 10. these materials also exhibit a high degree of dimensional stability and mechanical strength. Typical applications include powerline and electrical insulation, switch bases, and light receptacles. The titania (TiO_2) and titanate ceramics, such as barium titanate ($BaTiO_3$), can be made to have extremely high dielectric constants, which render them especially useful for some capacitor applications.

The magnitude of dielectric constant for most polymers is less than for ceramics, since the latter may exhibit greater dipole moments; ε_r values for polymers generally lie between 2 and 5. These materials are commonly utilized for insulation of wires, cables, motors, generators, and so on, and, in addition, for some capacitors [42].

Figure 3.20 Photograph of dielectric constant measurements set-up.

The ac electrical measurements were carried out using Agilent(model 4284 A) made precision LCR meter (Figure 3.20) in the frequency range of 100Hz- 1MHz at different temperatures ranging from 300K-800K. The value of regression coefficient (χ^2) which indicates goodness of data fitting is found near to unity, for all the fittings carried out in this work.

References

1 S. T. Alone and K. M. Jadhav
Parmana J. Phys. 70(1) (2008) 173.

2 R C Weast (Ed.) and M J Astle (Assoc. Ed.)
Handbook of Chaemistry and Physics CRC Press Inc. (Florida) 1981.

3 A. Verma, T. C. Goel, R. G. Mendiratta and R. G. Gupta, J. Magn. and Magn. Mater.192(2)(1999) 271.

4. www.siliconfareast.com

5 H. M. Rietveld, J. Appl. Cryst. 2 (1969) 65.

6 H. M. Rietveld, Acta, Cryst 22 (1967) 151.

7 J. Rodriquez-Cravajal, Physica B, 192 (1993) 55.

8 L. B. McCusker, R. B. Von Dreele, D. E. Cox, D. Louer and P. Scardi, J. Appl Cryst. 32 (1999) 36.

9 R. A. Young, "The Rietveld Method", Oxford University Press Inc (1993).

10 Ian. M. Watt, "The Principles & Practice of Electron Microscopy", 2nd Ed., Cambridge University Press (1997)89.

11 Elton. N. Kaffmann, "Characterization of Materials", John Wiley & Sons, Inc., Hoboken, New Jersey, Vol. 2 (2003).

12 R.D. Waldron, Phys. Rev. 99(1955)1727.

13 A. Chim, Seminars, Ann. Chem. 7(1974) 9

14 W.L. Konijnenijk, Philos. Res. Rep. Suppl. 1(1975) 30

15 J.Preudomme, Ann. Chim. 9(1974) 31 AND W.B. Whike and B.A. De Angelis, Spectrochim, Acta 23A(1967) 985].

16 Willard, Merritt, Deam and Settle, Sixth edition, CBS publishers and disrtibutors.

17 www.thermonicolet.com

18 S.L.Kakani and C.Hemrajani, Solid State Phys., Sultan Chand & Sons (1997)

19 K.B.Modi, J.Mater Sci. 39 (2004) 2887

20 K.B.Modi, P.U.Sharma, M.C.Chhantbar and H.H.Joshi, J Mater Sci Lett 40(5) (2005) 1247

21 J. U. Buch, M.Phil. Dissertation, Saurashtra University, Rajkot (2007)

22 Neel L., Ann. Phys., 3, (1948) 137.

23 S. Geller, Phys. Rev., 181, (1969) 980.

24 C. Radhakrishnamurthy S. D. Likhite and S. P. Sastry, "Philosophical Magazine", 23 (1971) 503.

25 A. P. Murani, J Magn. Magn. Mater, 5 (1977) 95.

26 K. J. Standley, "Oxide Magnetic Materials", Clerendon Press, Oxford, (1962).

27 C. Radhakrishnamurthy, S. D. Likhite, E. R. Deutsch and G. S. Murthy, Phys. Earth and planetary Interiors, 26 (1981) 37.

28 S. Chikazumi, 1964. *Physics of Magnetism,* New York: john Wiley & sons.

29 C. Guillaud, 1957*. Proc. IEEE*, Supp. No: 5, 165.

30 A. L. Stuijts ,, et al. *IEEE Trans. Comm. Elect.83.*

31 M. A. Gilleo, and S. Geller, *Physics.Rev.110,* (1958) *73.*

32 A. J. Bozorth,et al., *Phys.Rev.* (1955) *99.*

33 F. F. Galt, et al., *Phys.Rev, 81,* (1951) *470*

34 H. P. J. Smith et al., 1954. *Advances in Electronics and Electron Physics6, 69*

35 U. Enz, *Thesis* , Zurich (1955).

36 T. Akashi, *Trans. Jap. Inst. Met. 2,* (1961) *1963.*

37 E Roess, 1977. *J. Magn. And Mag. Mat. 4, (1977) 86*.

38 T. G. W., P.Stijntjes,. *Ferrites, Proc. ICFI, Tokyo: University Press,* (1971) *191.*

39 T .G. W.Buthker, et al. *Ceramic Bull. 61,* (1982) *809*.

40 T.Tanaka, *Jap. J. Appl. Phys*. (1975) 1169.

41 Y. Lescroel,, and Pierrot, A., *Cables and Transmissions 14* , (1960) 220.

42 W. D. Callister, JR, Fifth edition, Material Science and Engineering on Introduction John Wiley& Sons, Inc].

43 G. H. Jonker, J.Phys,Chem. Solids,9 (1959)165.

44 B. Vishwanathan and V.R.K. Murthy, Ferrite materials: Science and Technology, (1990) 29.

45 S. L. Kakani and C. Hemrajani, Text book of Solid State Physics, Sultan Chand (1997).

46. F. J. Morin, Phys. Rev., 93(1953)1195.

47 K. Histake, K. Nakayama and K. Ohta, jap, J. Appl. Phys., 12(1973) 1116.

48 T. Yamashiro, Jpn. J. Appl. Phys., 12(1973) 148]

49 K. L. Chopra.,Short course in solid state physics, Vol. 1, Edited by P. C. Auluck, (1971) P.496, Thomason press (India).

Chapter – 4

Results and discussion

Structural and Micro structural Properties

Bulk Magnetic Properties

4.1 Energy Dispersive Analysis of X-ray (EDAX)

The high temperature prolong sintering during the synthesis process may results in loss of ingredient like Zn^{2+}, Cd^{2+}, Li^{1+}, Ca^{2+}, due to volatile nature of these cations [1], that leads to non-stoichiometric composition. Such compositions show un-expected and unusual physical properties that can not be explained on the basis of normal stoichiometry. Thus, it is essential to check the chemical stoichiometry of each synthesized composition before any further characterizations. Energy Dispersive Analysis of X-rays (EDAX) is an important tool for this purpose. In other words, EDAX is used to make a rapid chemical analysis qualitatively.

In Figure 4.1.1, representative EDAX patterns for the typical compositions of the $Zn_{0.3}Mn_{0.7+x}Si_xFe_{2-2x}O_4$ spinel ferrite system with x = 0.0 and 0.2 are shown.

The K. L and M series X-rays increase in energy with increasing atomic number. Within a 'normal' accelerating voltage range (15-20 keV) used for EDAX analysis, as in the present case, light elements will emit X-rays of the K series only, intermediate elements will emit X-rays of the L series or K and L series, while heavy elements will emit X-rays of the M series or L and M series [2]. Thus, one can simultaneously record a wide range of elements during a given scan. In the system under investigation light elements like silicon (Si)(Z = 14) and oxygen (O)(Z= 8) as well as intermediate elements such as iron (Fe)(Z = 26), zinc (Zn)(Z= 39) and manganese (Mn) (Z = 25) are present while heavy elements are absent.

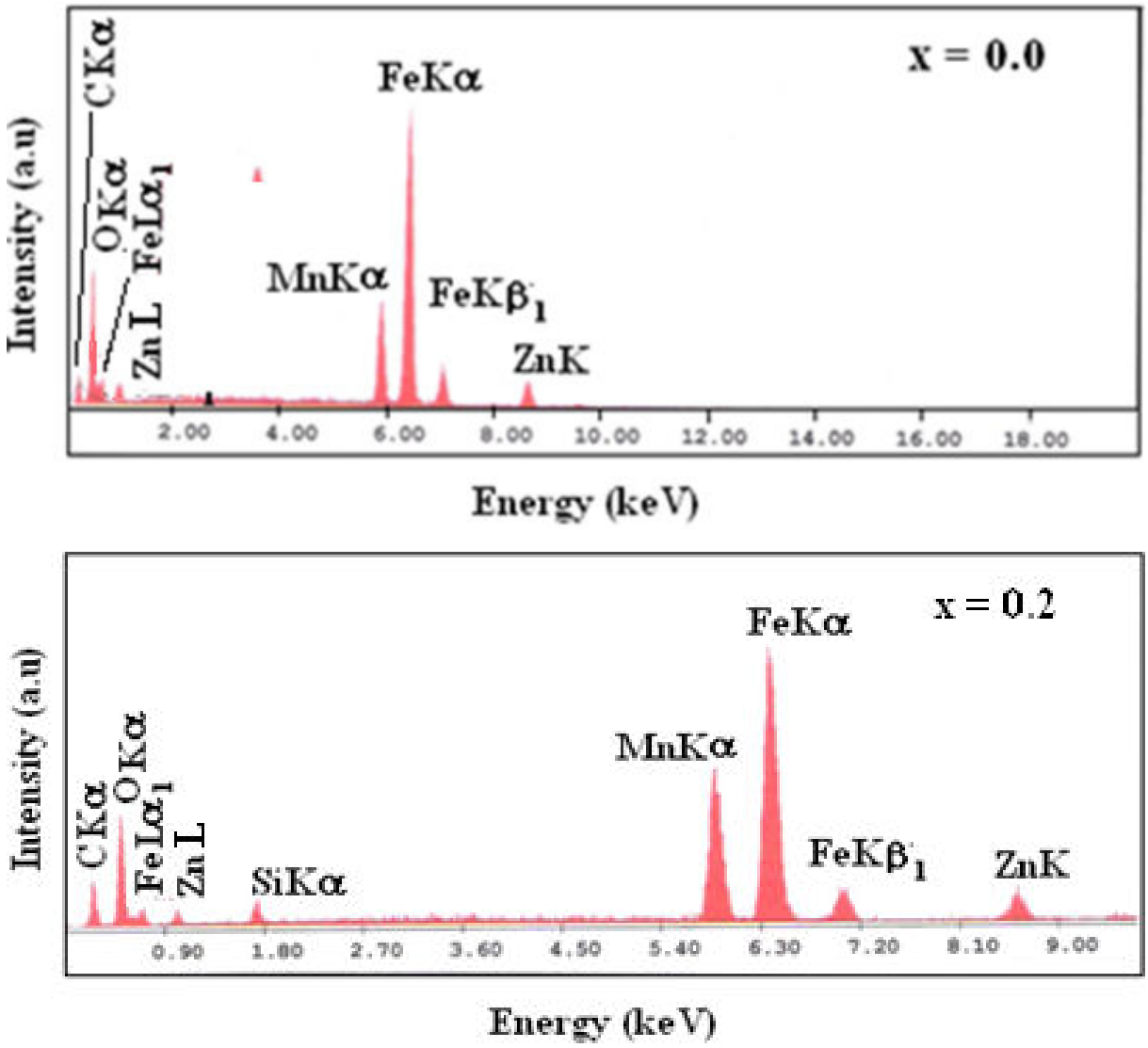

Figure 4.1.1. EDAX patterns for x = 0.0 and x = 0.2 compositions.

From the presented spectra one can clearly see three peaks located between 5.5 and 7 keV. The observed maximum (~6.4 keV) is directly related to the iron (Fe) characteristic of line Kα. The peaks located at ~ 7.0 keV and ~ 6.0 keV are corresponding to $FeK\beta_1$ and MnKα respectively. Here, it is important to note that MnKβ line interferes with FeKα line in the spectra [2]. The peak located at 8.6 keV and hardly visible peak at 1.0 keV confirm the presence of Zn

characteristic lines K and L respectively. The maximum observed on the left part of the spectra at ~ 0.5 keV clearly comes from OKα, while very small peak that located at ~0.75 keV comes from $FeL\alpha_1$ characteristic line. The peak at extreme left of the spectra centered at ~ 0.25 keV connected with carbon (CKα) characteristic line of impurity. The silicon Kα line occurs between 1.5-2.0 keV for x = 0.2 composition. Furthermore, if a Kα line is identified in a spectrum then a Kβ line should exist as well as have approximately one tenth of counts of the Kα line (Kα : Kβ = 10:1) [2]. We have also observed same relationship for FeKα and $FeK\beta_1$ line in the spectra.

The weight percentage (wt%) of different elements (Zn, Mn, Fe, Si, O) calculated theoretically from the chemical compositions : $Zn_{0.3}Mn_{0.7}Fe_2O_4$ (x = 0.0) and $Zn_{0.3}Mn_{0.9}Si_{0.2}Fe_{1.6}O_4$ (x = 0.2) and that obtained from EDAX analysis agrees well with each other. The outcome of the calculations is summarized in Table 4.1.1.

Table 4.1.1. EDAX results for x = 0.0 and 0.2 compositions.

Element	EDAX (wt %) ± 2 %		Expected (wt %)		(P/B) ratio	
	x = 0.0	x = 0.2	x = 0.0	x = 0.2	x = 0.0	x = 0.2
Fe	48.56	40.26	47.78	39.19	105.63	81.18
Mn	16.85	21.63	16.45	21.68	027.95	46.08
Zn	08.83	08.70	08.39	08.59	034.89	15.61
Si	-	02.45	-	02.46	-	05.66
O	25.76	26.96	27.38	28.07	012.12	54.37

The results of EDAX (Table 4.1.1) confirm the expected stoichiometry. No trace of any impurity (except for small amount of carbon) was found indicating the purity of the samples. It is also clear that there is no loss of any ingredient after high temperature sintering during synthesis process. The results suggest that the precursors have fully undergone the chemical reaction to form the expected ferrite compositions. The reason for making EDAX characterization was to ratify the purity and surety of the chemical composition.

Finally, we have also included peak to background (P/B) ratio for different elements of both the compositions in Table 4.1.1. The peak to background ratio was large for the various peaks, so background fitting did not introduce much error.

Illustrative calculation for weight percentage

$x = 0.2$, $Zn_{0.3}Mn_{0.9}Si_{0.2}Fe_{1.6}O_4$

(65.37)(0.3) + (54.94)(0.9) + (28.09)(0.2) + (55.85) (1.6) + (16)(4)

= 19.60 + 49.45 + 5.618 + 89.36 + 64

= 228.03 grams.

For Si

In 228.03 grams of total weight, contribution of Si is 5.618 grams

$\therefore$ for 100 grams of total weight, contribution of Si is ?

= 2.46 % (Expected wt %)

2.45 % (EDAX wt %)

Various studies have shown and it is widely accepted that the non-magnetic tetravalent cations, such as TiO_2 [3], SiO_2 [4-5], are segregated at the grain boundaries and affect the different physical properties in an interesting manner.

In general, the Auger electron spectroscopy (AES) and field emission high resolution transmission electron microscopy (TEM) or scanning electron microscopy (SEM) equipped with EDAX are employed to verify occupancy of Si^{4+} at the grain boundary [3,5]. The EDAX technique that we have employed in the present study can give information about the elements present in the grain region only. Of course, without EDAX spectrum of grain and grain boundary regions , it is rather difficult to say about the presence or absence of $Si^{4+,}$ ions in the grain boundary region or grain region of Mn-Zn ferrites.

Conclusions

(i) The analysis of EDAX spectra have confirm expected stoichiometry without the loss of any ingredient.

(ii) All the peaks are well assign in accordance with the standard positions.

References

1 N. J. Vander Laag, J. European Ceram. Soc., 24(8) (2004) 2417.

2 www.charfac.umm.edu/instruments/eds_on_sem_primer.pdf

3 Y. Zhao, D. X. Huang, Y. Feng, C.H. Cheng, T. Machi, N. Koshizuka and M. Murakami, Appl. Phys. Lett. 80(9) (2002) 1640.

4 M. Han, D. Liang and L. Deng, Appl. Phys. Lett., 90 (2007) 192507-1-3 and references therein.

5 Y. Wu, Z.W. Li, L. Chen, S. J. Wang and C. K. Ong, J. Appl. Phys., 95(8) (2004) 4235.

4.2 X-ray diffraction pattern analysis and structural parameters determination.

X-ray powder diffraction patterns analysis

The room temperature (300K) x-ray diffraction (XRD) patterns of the system $Zn_{0.3}Mn_{0.7+x}Si_xFe_{2-2x}O_4$ with x = 0.0, 0.1, 0.2 and 0.3 were obtained by x-ray powder diffractometry (Figure 4.2.1(a)). Indexing and Rietveld refinement using general scattering analysis software (GSAS) [1] of XRD patterns revealed that these are single phase compounds, crystallizing in fcc structure (space group O_h^7 Fd3m).The un-substituted composition (x = 0.0) possesses major spinel phase and minor α-Fe_2O_3, hematite, phase.

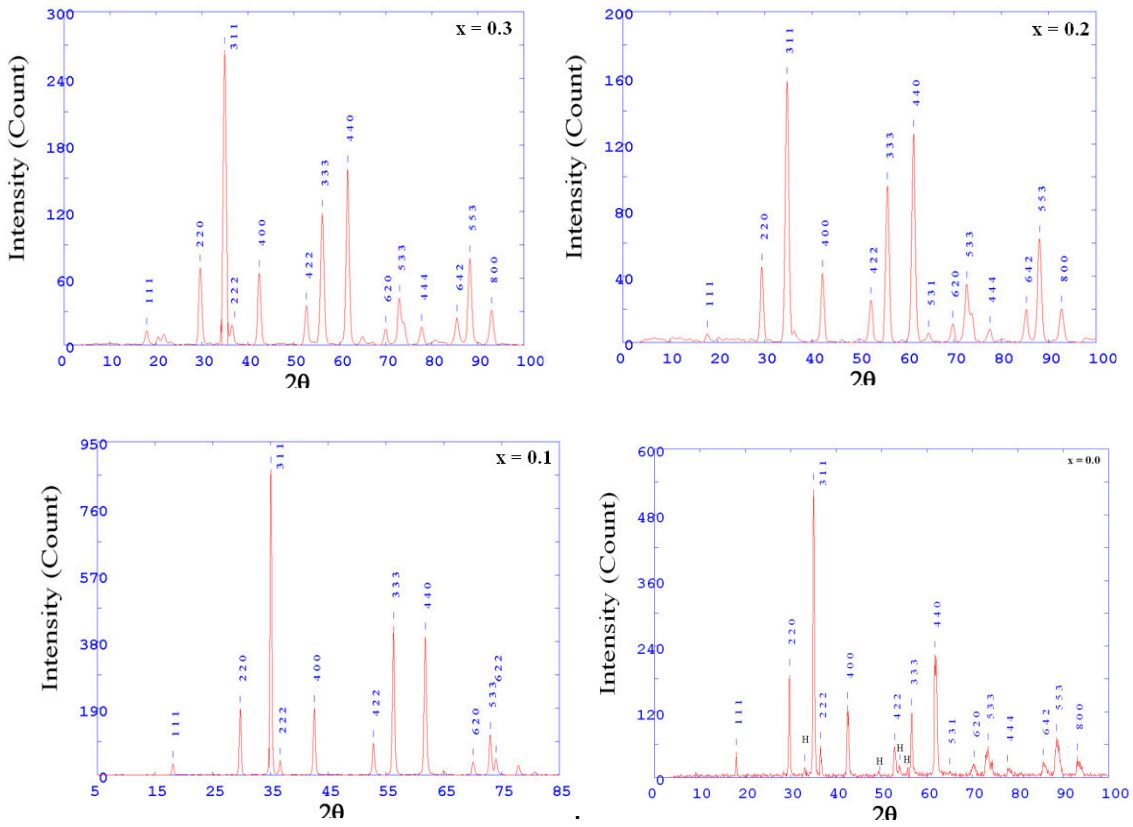

Figure 4.2.1(a). X-ray powder patterns for $Zn_{0.3}Mn_{0.7+x}Si_xFe_{2-2x}O_4$ system at 300K."H" indicates reflection from Hematite phase.

In Rietveld analysis, we fit a model to the data. If the model is correct then it will predict what is the "true" intensity values should be. The refinement of the data was started using a model in which the space group is Fd3m; its origin is at $\bar{3}$m at 1/8, 1/8, 1/8 from the centre $\bar{4}$3m, in which, the oxygen atom occupies the 32e position with fractional coordinates, 1/4, 1/4, 1/4; A-site at 8f and B-site at 16c positions. The experimental profile was fitted using a multiterm Simpson's rule integration of the pseudo-Voigt function [2]. In the first and second refinement cycles of process, the global parameters (2θ-zero, instrumental profile, profile asymmetry, background, specimen displacement) and structural parameter (atomic coordinates, specimen profile breadth parameters, lattice parameter, preferred orientation, and site occupancy) were refined in sequence mode. The site occupancy of the cations in the A- and B-sites were constrained in order to keep the sum of the particular cation in the two sites always have its stoichiometric value. In the last cycle, when the discrepancy factor R_{wp} has reached its minimum values, the parameters were refined simultaneously giving the goodness-of-fit (χ^2).

Although a difference profile plot is probably the best way of following and guiding a Rietveld refinement, the fit of the calculated pattern to the observed data can also be given numerically. The fitting quality of the experimental data were checked by using the various Rietveld discrepancy values, i.e., the weighted profile R-factor (R_{wp}), the expected R factor (R_{exp}) and the goodness-of-fit ($\chi^2 = (R_{wp}/ R_{exp})^2$) [3]. It should be noted that χ^2 should never drop below one. If

a refinement results in χ^2 < 1, which means that one of the two things is true: (i) the standard uncertainties for the data must be overestimated or (ii) so many parameters have been introduced that the model is adjusting to fit noise, which should be unlikely in powder diffraction. On the other hand, if at the end of a refinement χ^2 >> 1, then either: (i) the model is reasonable but the standard uncertainly values are underestimated (ii) the model is incomplete because there are systematic effects (errors) in the data that are not expressed in the model, or (iii) the model is wrong [3].

Table 4.2.1. Rietveld agreement factors $Zn_{0.3}Mn_{0.7+x}Si_xFe_{2-2x}O_4$ system.

Mn-Si content (x)	R_{wp}	R_{exp}	χ^2
0.0	5.11	4.50	1.29
0.1	6.32	5.23	1.46
0.2	4.48	3.81	1.38
0.3	4.04	3.50	1.33

It is found that “Chi squared” or χ^2 for different compositions lie in the range 1.2 -1.4. The χ^2 values obtained in the present analysis suggest good refinement of the data. The Rietveld agreement factors for x =0.0, 0.1, 0.2 and 0.3 are summarized in Table 4.2.1. Figure 4.2.1(b) displays Rietveld fitted XRD patterns for x = 0.0, 0.1, 0.2 and 0.3 compositions.

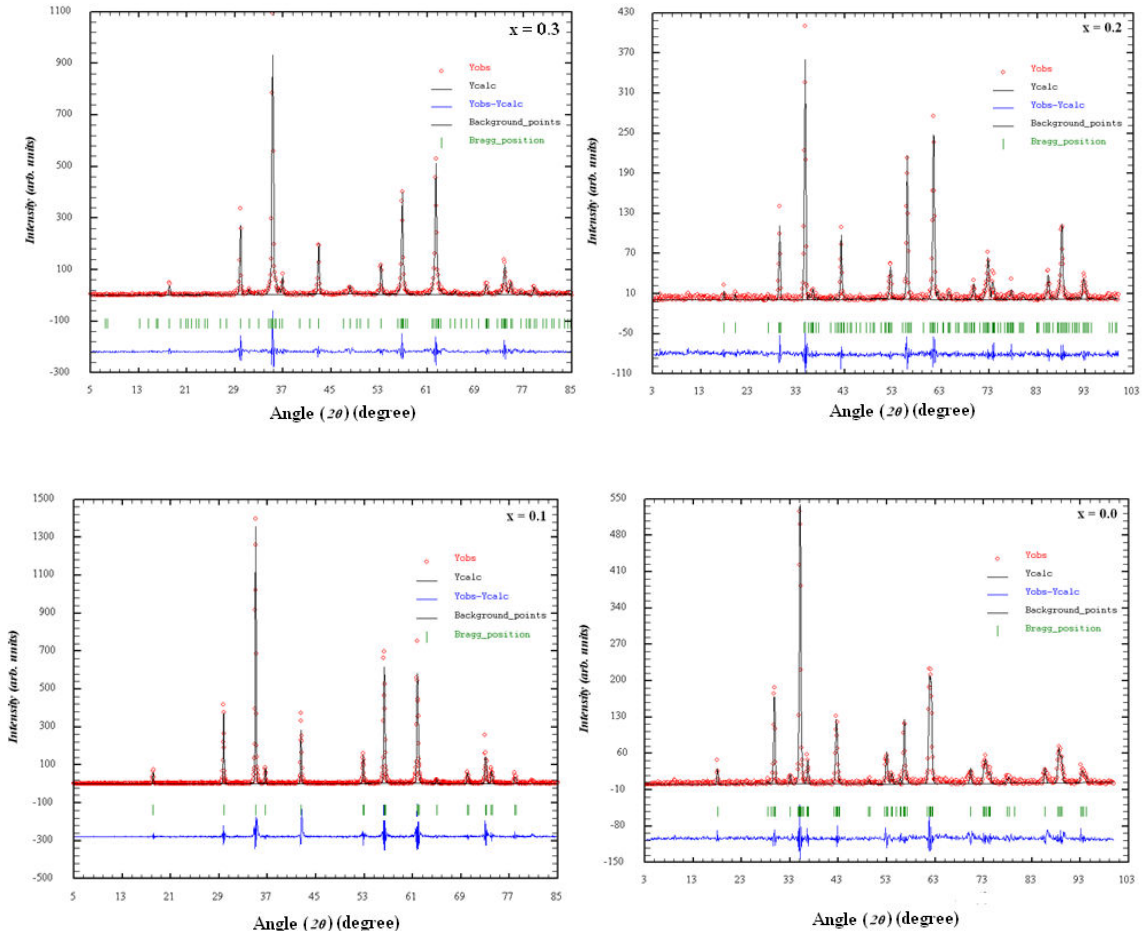

Figure 4.2.1(b). **Observed (Solid Circles) and calculated (Solid line) x-ray powder diffraction patterns for the $Zn_{0.3}Mn_{0.7+x}Si_xFe_{2-2x}O_4$ (x = 0.0,0.1,0.2 and 0.3) system at 300K. The difference between the observed and calculated spectra is plotted at the bottom. The ticks indicate allowed Bragg peaks positions.**

Structural parameters and cation distribution determination

The lattice constant values obtained from the above mentioned refinement are given in Table 4.2.2, from which it is seen that the lattice constant increases with increasing Mn-Si content (x) in the system. Usually in a solid solution of ferrites within the miscibility range, a linear change in lattice constant with concentration of the components is observed [4]. In the present system Fe^{3+} with ionic radius of 0.64 is replaced by simultaneous substitution of Mn^{2+} (0.80Å) and Si^{4+} (0.42) ions according to :

$$2Fe^{3+} \leftrightarrow Si^{4+} + Mn^{2+}$$

$$(0.128\ Å) \leftrightarrow (0.122\ Å)$$

The difference is relatively small and thus, one can expect almost no change or gradual decrease in lattice constant value with increase in Mn-Si content (x). In the present case we have observed slow linear increase in lattice constant with x (Table 4.2.2). It has been reported that majority of Si - ions reside at the grain boundary while some of the Si^{4+} ions did indeed enter the crystal lattice [5]. The concentration of Si ions at the grain boundary is about 5-10 times as compared to that at inter grain for the Sr- ferrite [5]. If we assume all the substituted Si^{4+}- ions deposited at grain boundary, and do not contribute to the lattice constant value, than lattice constant should increase rapidly due to the substitution of larger Mn^{2+} ions for smaller Fe^{3+} ions in the system, but this is not the case. This suggests that most of the Si ions are located at the grain boundary of the grains and only a few Si ions are inside the grains. When the

sintering temperature is sufficiently high (> 1250^0 C) some of the Si ions can diffuse in to the grains [5].

The x-ray density (ρ_x) of the samples was determined using relation given by Smith and Wijn [6]:

$$\rho_x = \frac{8M}{N_A a^3} \qquad (1)$$

where, M is the molecular weight of the composition, N_A the Avogadro's number and 'a' is the lattice constant. As there are 8 formula unit in the unit cell so 8 is included in the formula. The ρ_x is inversely proportional to the lattice constant, which increases with increasing Mn-Si concentration; ρ_x is expected to decrease with increasing (x). Bulk density (ρ) of the samples was determined by employing the Archimedes principle using xylene (ρ = 0.87 gcm^{-3}) as the buoyant to obtain fairly good results. It is observed that ρ_x of each sample is greater than the corresponding sintered density (ρ). This may be due to the existence of pores in the samples. Pore fraction (f) was calculated using the relation $f = (1 - \rho/\rho_x)$ and percentage porosity was calculated using the relation P = f * 100%. The variation of porosity (P) with Mn-Si content (x) is a result of the interplay between ρ and ρ_x. The change percentage shrinkage (S) of the diameter of the disc shape sample before and after final sintering process, with composition is also presented in Table 4.2.2. As expected, porosity and shrinkage behave inversely to each other as a function of Mn-Si concentration (x).

Table 4.2.2. Lattice constant (a), molecular weight (M), x-ray density (ρ_x), bulk density (ρ), pore fraction (f), porosity (P) and shrinkage (S) for $Zn_{0.3}Mn_{0.7+x}Si_xFe_{2-2x}O_4$ system.

Mn –Si content (x)	a(Å) ±0.002Å	M(kg) x 10^{-3}	ρ_x	ρ	f	P (%)	S %
			kg/m^3 x 10^3				
0.0	8.465	233.76	5.12	4.41	0.1387	13.87	4.4
0.1	8.488	230.89	5.02	4.69	0.0657	06.57	7.0
0.2	8.497	228.02	4.94	4.40	0.1093	10.93	6.4
0.3	8.505	225.16	4.86	4.19	0.1379	13.79	6.3

The various physical properties of ferrites are sensitive to the nature, the valence state and distribution of cation over the tetrahedral (A-) and octahedral (B-) sites of spinel lattices. Therefore, the knowledge of cation distribution is essential to understand the structural, magnetic, electrical and infrared spectral properties of spinel ferrites.

Cation arrangements are not unique in spinel ferrites. Each spinel compound possesses at least three degree of freedom, which it uses in its search for an equilibrium structure: oxygen positional parameter (u), lattice constant (a) and cation inversion parameter. The parameter 'u' varies, primarily, in accordance with the radius ratio between the A - and B – sites cations, r_A/r_B (or r_B/r_A). This is to say, the A – and B – sites bond lengths adjust themselves by variation in 'u' until the A- and B- sites volumes "best – fit" the cations. The parameter 'a' varies in accordance with the average of the A – and B- sites cationic radii (i.e. with 0.33 r_A + 0.67 r_B). The entire frame work of the unit cell swells or contracts to accommodate the size of the cations. The cation inversion parameter varies based on a much more complex set of factors. Some of the

principal factors that influence cation inversion include [7]: (i) temperature (ii) the electrostatic contribution to the lattice energy (iii) cationic radii (iv) cationic charge and (v) crystal – field effects.

Precise knowledge of the cation distribution over crystallographic sites in magnetic oxides is crucial for understanding their physical properties. In order to determine the cation distribution, x-ray diffraction line intensity calculations were made using the formula suggested by Buerger [8]:

$$I_{hkl} = \left|F_{hkl}\right|^2 \cdot P \cdot L_p \qquad (2)$$

where, I_{hkl} is the relative integrated intensity, F_{hkl} is the structure factor, P is the multiplicity factor and L_p is the Lorentz polarization factor = $[(1 + \cos^2 2\theta)/\sin^2\theta \cdot \cos\theta]$. According to Ohnishi and Teranishi [9], the intensity ratios of planes I(220) / I(440), I(400) / I(422) and I(220) / I(400) are considered to be sensitive to the any change in cation distribution. The intensities of (220) and (422) planes are mostly sensitive to cations on the tetrahedral sites [10], while the intensity of (400) plane depends on cations on both the sites. There is good contrast in the atomic scattering factor of Si^{4+} and Zn^{2+} to that of Fe^{3+} and Mn^{2+}, but the scattering factor of Mn^{2+} is close to that of Fe^{3+} [10]. We had estimated the amount of Fe^{3+} ions on the tetrahedral (A-) and octahedral (B-) sites, through Mossbauer spectral intensity calculations by considering the integrated areas under the Lorentizians corresponding to the A- and B- sites, which were taken as proportional to the amount of Fe^{3+} ion on these sites. The details are given elsewhere [11]. Any alternation in the distribution of cations causes a significant change in the theoretical values of x-ray diffraction line

intensity ratio. Therefore, in the process of arriving at the final cation distribution the site occupancy of all the cations was varied for many combinations and those that agree well with the experimental intensity ratios, the fitting of the magnetization data at 80K and Mossbauer data analysis [11], were taken into consideration. The comparison of x-ray diffraction line intensity ratios for various possible cation distributions for the studied compositions is shown in Table 4.2.3.

Table 4.2.3. Comparison of X-ray diffraction line intensity ratios, for $Zn_{0.3}Mn_{0.7+x}Si_xFe_{2-2x}O_4$ system.

Mn-Si content (x)	Cation distribution		$\frac{I(400)}{I(422)}$		$\frac{I(220)}{I(400)}$	
	A-site	B-site	Obs.	Cal.	Obs.	Cal.
0.0	$(Zn^{+2}_{0.25}Mn^{+2}_{0.40}Fe^{+3}_{0.35})$	$[Zn^{+2}_{0.05}Mn^{+2}_{0.30}Fe^{+3}_{1.65}]$	1.924	2.303	1.122	1.264
0.1	$(Zn^{+2}_{0.25}Si^{+4}_{0.10}Mn^{+2}_{0.43}Fe^{+3}_{0.22})$	$[Zn^{+2}_{0.05}Mn^{+2}_{0.37}Fe^{+3}_{1.58}]$	2.107	2.457	0.992	1.152
0.2	$(Zn^{+2}_{0.25}Si^{+4}_{0.15}Mn^{+2}_{0.45}Fe^{+3}_{0.15})$	$[Zn^{+2}_{0.05}Si^{+4}_{0.05}Mn^{+2}_{0.45}Fe^{+3}_{1.45}]$	2.071	2.591	1.294	1.006
0.3	$(Zn^{+2}_{0.25}Si^{+4}_{0.21}Mn^{+2}_{0.48}Fe^{+3}_{0.06})$	$[Zn^{+2}_{0.05}Si^{+4}_{0.09}Mn^{+2}_{0.52}Fe^{+3}_{1.34}]$	1.800	2.151	1.066	1.289

Besides using experimentally found value of lattice constant and oxygen positional parameter (u), it is possible to calculate the value of the mean ionic radius per molecule of the tetrahedral and octahedral sites, r_A and r_B, respectively, based on the cation distribution for each composition using the relation [4]:

$$r_A = \left[f_c(Zn^{2+}) \cdot r(Zn^{2+}) + f_c(Mn^{2+}) \cdot r(Mn^{2+}) + f_c(Si^{4+}) \cdot r(Si^{4+}) + f_c(Fe^{3+}) \cdot r(Fe^{3+})\right]$$

$$r_B = \frac{1}{2}\left[f_c(Zn^{2+})\cdot r(Zn^{2+}) + f_c(Mn^{2+})\cdot r(Mn^{2+}) + f_c(Si^{4+})\cdot r(Si^{4+}) + f_c(Fe^{3+})\cdot r(Fe^{3+})\right] \quad (3)$$

where, f_c and r, are the fractional concentration and ionic radius of respective cation on respective site. The ionic radius of Zn^{2+} (0.74 Å), Mn^{2+} (0.80 Å), Si^{4+} (0.42 Å) and Fe^{3+}(.64 Å) ions are taken with reference to coordination 6. Using these formulae, the mean ionic radius of the tetrahedral (A-) sites (r_A) and of the octahedral (B-) sites (r_B) have been calculated and are listed Table 4.2.4.

It can be seen that r_B increases slowly while r_A shows slow increase with increasing Mn-Si content (x) in the system, which in turn causes the lattice constant 'a', to increase with x. It can be concluded that the octahedral sites substitution plays a dominant role in influencing the variation of 'a' with concentration (x).

It is known that there is a correlation between the ionic radius and the lattice constant. The radii of the tetrahedral and octahedral sites in a spinel ferrite can be calculated using the formulae given by [12]:

$$r_A = \sqrt{3}\left(u - \frac{1}{4}\right)a - R_0 \quad (4)$$

$$r_B = \left(\frac{5}{8} - u\right)a - R_0 \quad (5)$$

where, R_0 represents the radius of the oxygen ion (taken as 1.32Å) and u is the oxygen positional parameter. These relationships are further used to calculated the lattice parameter theoretically 'a_{th}' [13].

From equation (5), one can write:

$$u = \frac{5}{8} - \frac{r_B + R_0}{a} \qquad (6)$$

By substituting the value of 'u' from equation (6) in to equation (4) and rearranging the terms,

$$a = \frac{r_A + R_0}{\sqrt{3}\left[\left(\frac{5}{8} - \frac{(r_B + R_0)}{a}\right) - \frac{1}{4}\right]}$$

$$= \frac{8a\,(r_A + R_0)}{\sqrt{3}(5a - 8r_B - 8R_0 - 2a)}$$

$$\frac{\sqrt{3}a}{8a} = \frac{r_A + R_0}{3a - 8(r_B + R_0)}$$

$$3\sqrt{3}a - 8\sqrt{3}(r_B + R_0) = 8(r_A + R_0)$$

$$a_{th} = \frac{8}{3\sqrt{3}}\left[(r_A + R_0) + \sqrt{3}(r_B + R_0)\right] \qquad (7)$$

It has been observed that the theoretically calculated values of lattice constant follow the opposite trend as that obtained experimentally and the values are much smaller than the experimental ones [13 - 15]. Theoretical calculations presume an ideal close packed structure and valence state of the cations and thus corresponding values of ionic radii have to be taken into consideration.

The oxygen positional parameter or anion parameter (u) for each composition was calculated using the formulae available in the literature [7].

$$u^{\bar{3}m} = \frac{\frac{1}{4}R^2 - \frac{2}{3} + \left(\frac{11}{48}R^2 - \frac{1}{18}\right)^{1/2}}{2R^2 - 2} \qquad (8)$$

$$u^{\bar{4}3m} = \frac{\frac{1}{2}R^2 - \frac{11}{12} + \left(\frac{11}{48}R^2 - \frac{1}{18}\right)^{1/2}}{2R^2 - 2} \quad (9)$$

$$u^{\bar{4}3m} = \frac{r_A + R_0}{a\sqrt{3}} + \frac{1}{4} \quad (10)$$

$$u^{\bar{4}3m} = 0.3876\left(\frac{\langle r_B \rangle}{\langle r_A \rangle}\right)^{-0.07054} \quad (11)$$

where, R=(B-O) / (A-O). The bond lengths, B – 0 and A – O are average bond lengths calculated based on the cation distribution listed in Table 4.2.3; where, $B\text{-}O = \langle r_B + R_0 \rangle$ and $A\text{-}O = \langle r_A + R_0 \rangle$. Equation (8) gives 'u' assuming centre of symmetry at (1/4, 1/4, 1/4) for which u_{idea} = 0.250 (origin at B-site), while equations (9) – (11) give 'u' assuming centre of symmetry at (3/8, 3/8, 3/8) for which u_{idea} = 0.375 (origin at A-site). The values of $u^{\bar{4}3m}$ determined from different formulae are in agreement with each other (Table 4.2.4). To convert origin from A-site to B-site, $u^{\bar{4}3m} = u^{\bar{3}m} + 1/8$ [7], relationship has been used. In an ideal fcc structure $u^{\bar{4}3m} = 0.375; u^{\bar{3}m} = 0.250.$

Table 4.2.4 Ionic radius (r), lattice constant (a) and oxygen positional parameter (u) for $Zn_{0.3}Mn_{0.7+x}Si_xFe_{2-2x}O_4$ system.

Mn-Si content (x)	r_A (Å)	r_B (Å)	a_{th} (Å)	$u^{\bar{3}m}$ (1/4,1/4,1/4)	$u^{\bar{4}3m}$ (3/8, 3/8, 3/8) Eq.(9)	Eq.(10)	Eq.(11)
0.0	0.729	0.666	8.452	0.2599	0.3893	0.3897	0.3851
0.1	0.712	0.672	8.440	0.2558	0.3877	0.3881	0.3860
0.2	0.704	0.673	8.431	0.2531	0.3868	0.3875	0.3863
0.3	0.696	0.674	8.421	0.2480	0.3855	0.3868	0.3867

Although, most ferrites generally have 'u' greater than this ideal value [14-20], it is slightly larger in the present series (Table 4.2.4), implying that the oxygen ions are displaced in such a way that in the A-B interaction, the distance between A and O ions and between B - O ions decreased. This leads to an increase in the A – A and B – B interactions. As 'u' increases from its ideal value, anions move away from the tetrahedrally coordinated A - site cations along the ‹111› directions, which increase the volume of each A - site interstice while the octahedral B –sites become correspondingly smaller. The Fe^{2+} - ion is one of the largest divalent ions found in spinels, whereas the Si^{4+} ion is the smallest of the tetravalent spinel cation: thus the $r(Fe^{2+})$ / $r(Si^{4+})$ ratio is large, which favours large u values [7]. The small deviation of 'u' parameter from its ideal value (Table 4.2.4) combined with positive values of quadrupole shift, determined from Mossbauer spectral analysis for cubic phase x = 0.0 – 0.3 compositions of $Zn_{0.3}Mn_{0.7+x}Si_xFe_{2-2x}O_4$ system [4] suggest absence of oblate type deformation of $3d^5$ shell that prevents canting of Fe^{3+} on the B-sites.

Using the experimental values of 'a' and anion parameter (u) of each composition in equations [7, 14, 21-22], interatomic distances have been calculated.

$$d_{AE} = a(2)^{1/2}\left(2u^{\bar{4}3m} - \frac{1}{2}\right)$$ Shared tetrahedral edge

$$d_{BE} = a(2)^{1/2}\left(1 - 2u^{\bar{4}3m}\right)$$ Shared octahedral edge

$$d_{BEu} = a\left[4\left(u^{\bar{4}3m}\right)^2 - 3u^{\bar{4}3m} + \frac{11}{16}\right]^{1/2}$$ Unshared octahedral edge

$$d_{AL} = a\sqrt{3}\left(u^{\bar{4}3m} - \frac{1}{4}\right)$$ Tetrahedral bond length

$$d_{BL} = a\left[3\left(u^{\bar{4}3m}\right)^2 - \frac{11}{4}u^{4\bar{3}m} + \frac{43}{64}\right]^{1/2}$$ Octahedral bond length (12)

Table 4.2.5 Edge length and bond length for $Zn_{0.3}Mn_{0.7+x}Si_xFe_{2-2x}O_4$ system.

Mn-Si content (x)	d_{AE} (Å)	d_{BE} (Å)	d_{BEu} (Å)	d_{AL} (Å)	d_{BL} (Å)
0.0	3.3345	2.6510	3.0025	2.0420	2.0027
0.1	3.3050	2.6971	3.0087	2.0239	2.0203
0.2	3.2881	2.7198	3.0107	2.0136	2.0287
0.3	3.2591	2.7548	3.0122	1.9958	2.0410

The calculated values of edge lengths and bond lengths are given in Table 4.2.5. It is found that with an increase in Mn-Si concentration, shared tetrahedral edge and tetragedral bond length decrease due to the replacement of larger Mn^{2+} and Fe^{3+} ions by smaller Si^{4+} ion on the A-site. The shared octahedral edge and octahedral bond length are found to increase due to the replacement of smaller Fe^{3+} ion by larger Mn^{2+} on the B-site. The constancy of the unshared octahedral edge may be due to overall compensation taking place by decrease in shared tetrahedral edge and increase in shared octahedral edge.

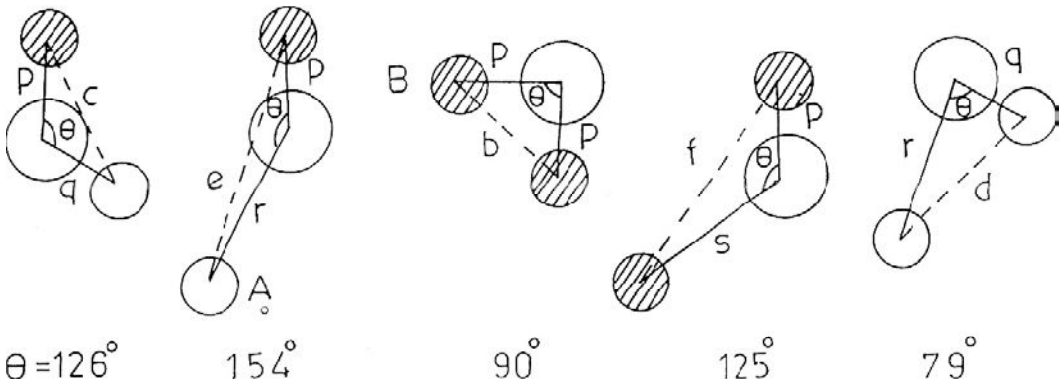

Figure 4.2.2 Configuration of ion pairs in spinel ferrites with favorable distances and angles for effective magnetic interactions.

The configuration of ion pairs in spinel ferrites with favorable distances and angles for magnetic interactions are shown in Figure 4.2.2. The interionic distances between the cations (Me-Me) (b, c, d, e, and f) and between the cation and anion (Me-O) (p, q, r and s) were calculated using the experimental values of lattice constant (a) and oxygen positional parameters (u^{3m}) (Tables 4.2.2 and 4.2.4) by the relations [23, 24]:

M_e – O	**M_e - M_e**
$p = a\left(\frac{1}{2} - u^{3m}\right)$	$b = \left(\frac{a}{4}\right)2^{1/2}$
$q = a\left(u^{3m} - \frac{1}{8}\right)3^{1/2}$	$c = \left(\frac{a}{8}\right)11^{1/2}$
$r = a\left(u^{3m} - \frac{1}{8}\right)11^{1/2}$	$d = \left(\frac{a}{4}\right)3^{1/2}$
$s = \frac{a}{3}\left(u^{3m} + \frac{1}{2}\right)3^{1/2}$	$e = \left(\frac{3a}{8}\right)3^{1/2}$
	$f = \left(\frac{a}{4}\right)6^{1/2}$

(13)

The overall strength of the magnetic interactions (A-B, B-B and A-A) depend upon the bond length and bond angles between the cations and cation - anion. The strength is directly proportional to bond angle but inversely proportional to bond length. It is seen from Table 4.2.6, that both interatomic distances between the cation - anion (p, q, r and s) and between the cations (b, c, d, e and f) increase with increasing Mn-Si concentration (x). These results are accordance with decrease in unit cell volume. The bond angles (θ_1, θ_2, θ_3, θ_4 and θ_5) (Figure 4.2.2) were calculated by simple trigonometric principle using the interionic distances with the help of following formulae:

$$\theta_1 = \cos^{-1}\left[\frac{p^2+q^2-c^2}{2pq}\right] \qquad \theta_2 = \cos^{-1}\left[\frac{p^2+r^2-e^2}{2pr}\right]$$

$$\theta_3 = \cos^{-1}\left[\frac{2p^2-b^2}{2p^2}\right] \qquad \theta_4 = \cos^{-1}\left[\frac{p^2+s^2-f^2}{2ps}\right]$$

$$\theta_5 = \cos^{-1}\left[\frac{r^2+q^2-d^2}{2rq}\right] \qquad (14)$$

It is found that angles θ_1, θ_2 and θ_5 increase while θ_3 and θ_4 decrease with increase in Mn-Si content (x). The observed increase in θ_1, θ_2 and θ_5 suggest strengthening of the A – B and A – A interactions while decrease in θ_3 and θ_4 indicative of weakening of the B-B interaction on Mn-Si substitution in the system. These results are consistent with relative strength of exchange integrals, J_{AB} / J_{BB}, determined from high field magnetization data [15]. It has been found that for x = 0.0 - 0.3 compositions of $Zn_{0.3}Mn_{0.7+x}Si_xFe_{2-2x}O_4$ system, ratio J_{AB} / J_{BB} is found to be~2.2 (Section 4.2.6).

Table 4.2.6 Interionic distances (b, c, d, e, f and p, q, r, s) and bond angles (θ) for $Zn_{0.3}Mn_{0.7+x}Si_xFe_{2-2x}O_4$ system

Mn-Si Content (x)	0.0	0.1	0.2	0.3
b	2.9928	3.0011	3.0040	3.0069
c	3.5094	3.5191	3.5225	3.5259
d	3.6654	3.6755	3.6791	3.6827
e	5.4981	5.5133	5.5187	5.5241
f	5.1837	5.1980	5.2031	5.2082
p	1.9954	2.0146	2.0237	2.0371
q	2.0419	2.0239	2.0135	1.9957
r	3.9100	3.8754	3.8556	3.8216
s	3.7352	3.7376	3.7371	3.7342
θ_1	120.79	121.29	121.56	121.98
θ_2	134.68	136.52	137.51	139.13
θ_3	97.215	96.33	95.88	95.179
θ_4	126.90	126.72	126.62	126.487
θ_5	67.875	69.098	69.74	70.80

(Distances in Å and angles in degrees)

Conclusions

(i) The compositions of the system $Zn_{0.3}Mn_{0.7+x}Si_xFe_{2-2x}O_4$ (x = 0.0,0.1,0.2,0.3) posses single phase spinel structure with minor hematite phase for x = 0.0 composition.

(ii) Various structural parameters and cation distribution can be determined from X-ray powder diffraction patterns analysis and are found useful to explain other physical properties.

(iii) The strength of A-B interaction increases while a B-B interaction decreases with Mn-Si substitution for Fe^{3+} in the system.

References

1 H. M. Rietveld, J. Appl. Cryst. 2(1969) 65.

2 J. A. Games, M. H. Sousa, F. A. Tourinho, J. Mestnik-Filho, R. Itri and J. Depeyrot, J. Magn. Magn. Mater. 289 (2005) 184.

3 B. H. Toby, Powder Diff. 21(2006) 67.

4 C. G. Whinfrey, D. W. Eckart, A. Tauber, J. Am. Chem. Soc. 82(1960)2695.

5 Y. Wu, Z. W. Li, L. Chen, S. J. Wang and C. K. Ong, J. Appl. Phys., 95(8) (2004) 4235.

6 J. Smith, H. P. J. Wijn, Ferrites, John Wiley, New York, 1959.

7 K. E. Siokafus, J. M. Wills, N. W. Grimes, J. Am. Ceram. Soc. 82 (12) (1999)3279.

8 M. J. Buerger, Crystal Structure Analysis, Wiley, NY, 1960.

9 H. Ohinishi, T. Teranishi, J. Phys. Soc. Jpn. 16(1961)35.

10 B. D. Cullity, Elements of x-ray diffraction, 2nd Edn. Addison Wesley Pub. Co. Reading MA 1978.

11 K.G.Saija and K. B. Modi, (unpublished work).

12 K. J. Standly, Oxide magnetic materials, Clarendom Press, Oxford, 1972.

13 S. A. Mazen, M. H. Abdallah, B. A. Sabrah, H. A. M. Hasham Phys. Status. Solidi A 134 (1992)263.

14 R. K. Sharma, Varkey Sebastain, N. Lakshmi, K. Venugopalan, V. R. Reddy, Ajay Gupta, Phys. Rev. B. 75(2007)144419-1.

15 H. Bhargava, N. Lakshmi, V. Sebastina, V. R. Reddy, K. Venugopalan, Ajay Gupta, J. Phys D: Appl. Phys. 42(2009)245003.

16 B. J. Evans, S. S. Hafner, J. Phys. Chem. Solidi. 29(1968) 1573.

17 R. G. Kulkarani, V. G. Panicker, J. Mater. Sci. 19(1984)890.

18 M. Ajmal, A. Maqsood, J. Alloys Compd. 460(2008)54.

19 D. Ravinder, K. V. Kumar, B. S. Boyanov, Mater. Lett. 38(1999) 22 and references their in.

20 K. H. Jani, M. C. Chhanbar, H. H. Joshi, J. Magn. Magn. Mater. 18(2008)2208.

21 C. Arena, J. Blanco, J. Gonzalez, M. Fernandez, J. Math. Psychol. 9(1990)229.

22 T. Abbas, Y. Khan, M. Ahmad, S. Anwar, Solid State Commun. 82(9)(1992)701.

23 J. B. Goodenough, J. Phys. Chem. Solids. 6(1958)287.

24 J. Kanamori, J. Phys. Chem. Solids. 10(2-3)(1959)87.

4.3 Particle size distribution study

Size of particles influences many properties of particulate material. Furthermore, it is a valuable indicator of quality and performance of material. In many applications, particle size plays critical role, for example, it determines (a) appearance and gloss of paint (b) flavor of coco powder (c) reflectivity of highway paint (d) absorption rate of pharmaceuticals (e) appearance of cosmetics and (f) hydration rate and strength of cement. Of course, this is more applicable to nano regime.

Particle size growth may be monitored during operations such as granulation or crystallization. Determining the particle size of powders requiring mixing is common since materials with similar and narrower distributions are less prone to segregation [1].

Particle size distribution data can be presented in tabular format i.e. numerically or graphically. In graphical form data are presented in differential and cumulative distribution curves. Both the forms are interrelated, if one differentiated the cumulative distribution curve, the differential distribution is obtained. On the other hand, if one integrated he differential distribution curve, the cumulative distribution is obtained [2]. The differential distribution shows the relative amount at each particle size. From the different size distribution, measures of central tendency such as the modal and mean diameters are determined. The diameter at the peak of the differential distribution is the modal diameter while the mean diameter is the average diameter.

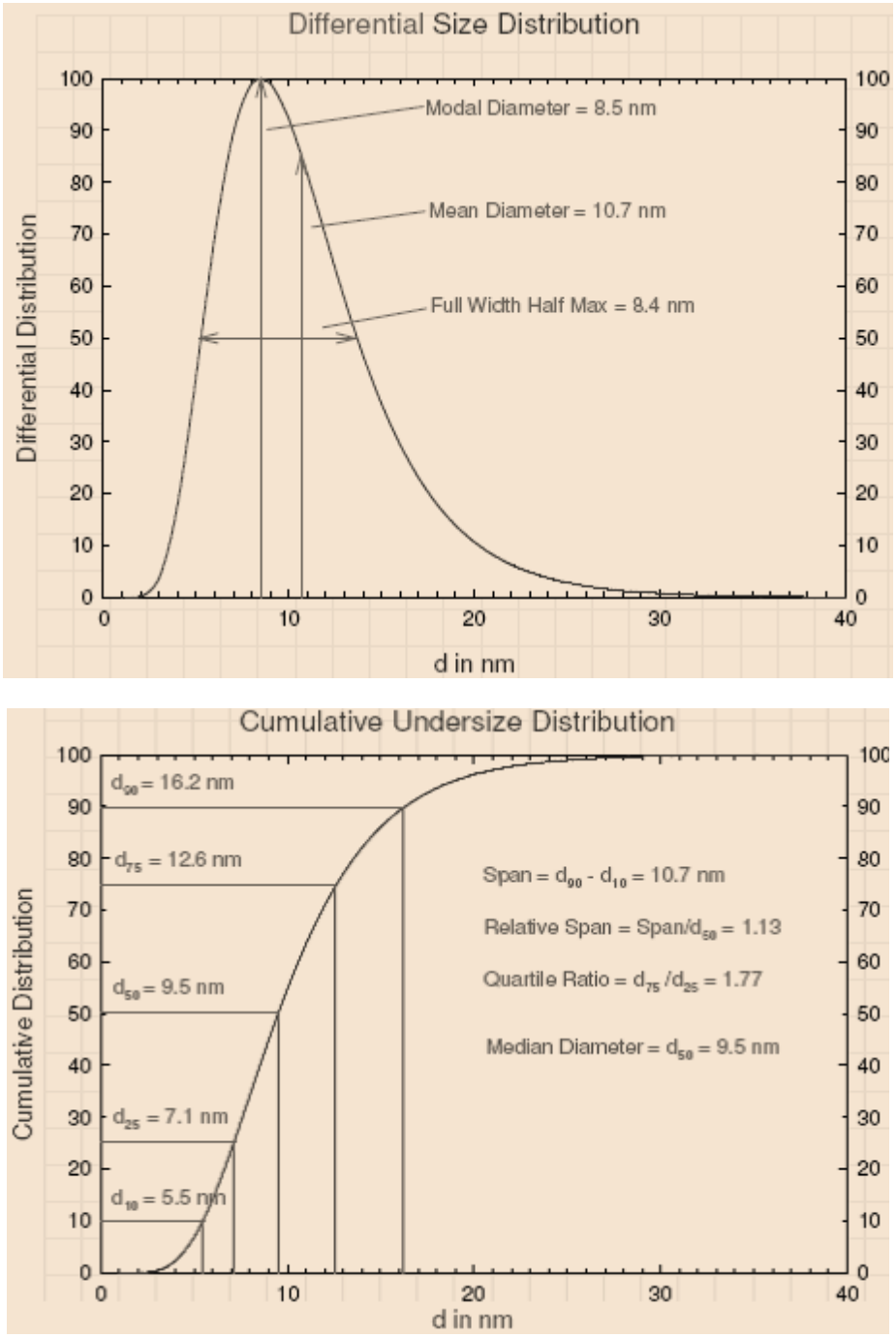

Figure 4.3.1. Illustrative differential size distribution and cumulative undersize distribution curves.

The corresponding cumulative distribution curve demonstrates the relative amount at or below a particular size. The median diameter is another measures of central tendency. It is the diameter at the 50^{th} percentile, designed d_{50}. Quartile diameters include d_{75}, d_{50} and d_{25}. There are several measures of absolute width one can derive given the cumulative distribution. One common measure is the span, d_{90}-d_{10}. A dimensionless measure of width is the relative span defined as span/d_{50}. Other relative measures of width include percentile ratios such as d_{90}/d_{10} and d_{75}/d_{25}.

Typical particle size distribution patterns, differential size distribution and cumulative undersize distribution, for x = 0.0 and 0.2 compositions are shown in Figure 4.3.2. The distribution is uni modal (single peaked) but not mono disperse (all one size). It has a width. There are several measures of width. One measures of width is FWHM, the full width at half maximum. It is obtained by drawing a horizontal line at 50% of the maximum and taking the difference between the two places it intersects the distribution. HWHM, the half width at half maximum, is another measure of width. It is defined as FWHM/2. A relative fractional measure of width is obtained by dividing HWHM by the measure of central tendency from which it was derived, the modal diameter (HWHM/modal diameter). Furthermore, it is seen that the curve tails to the left more than to the right, that means the skew is negative. The skew is positive if curve tails to the right more than to the left. The reference point for tailing is with respect to the modal diameter. A symmetric differential distribution has zero skew.

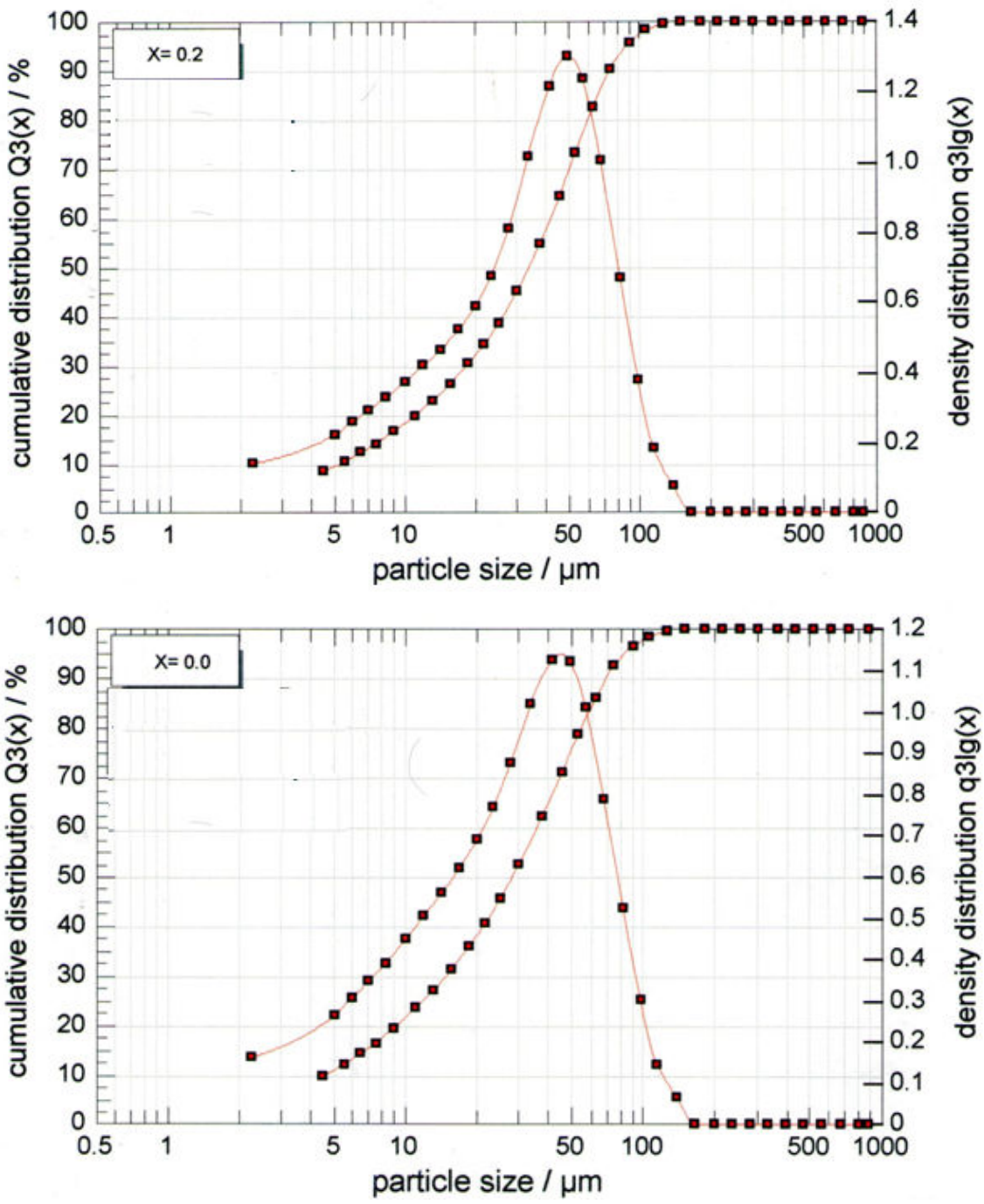

Figure 4.3.2. Particle size distribution curves for x = 0.0 and 0.2 compositions of Si-substituted Mn-Zn ferrite.

The size of the particles shown in Figure 4.3.2 is in micrometer (μm) order. These particles were agglomerates which were found to break further and further to submicron level with more and more powerful ultrasonic de-agglomeration techniques.

The important parameters such as : modal diameter, mean/average diameter, full width half maximum (FWHM), span (d_{90}-d_{10}), relative span (span/d_{50}), quartile ratio (d_{75}/d_{25}) and median diameter (d_{50}), for both the compositions are determined and tabulated in Table 4.3.1.

Table 4.3.1. Measures of central tendency and width for x = 0.0 and 0.2 compositions.

Parameter	Composition	
	x = 0.0	x =0.2
Modal diameter	45.0 μm	50 μm
Average diameter	65.7 μm	69.2 μm
FWHM	55.0 μm	60 μm
Span	65.7 μm	69.2 μm
Relative span	2.31	2.04
Quartile ratio	3.33 μm	3.33 μm
Median diameter	28.39 μm	33.92 μm
Relative percent measures of width	61.1 %	60 %

Conclusions

(i) Particle size distribution curves analysis suggests that the distribution is uni modal but not mono disperse and having negative skew.

(ii) The size of the particles is in micrometer order and ultrasonic de-agglomeration is required before further analysis.

(iii) Various important parameters can be determined from the differential size distribution and cumulative undersize distribution curves.

References

1 www.Horiba.com/fileadmin/scientific/documents/PSA/PSA_guidebook.pdf

2 www.Brookhaveninstruments.com (2011) 1.

4.4 Scanning Electron Microscopy

The scanning electron micrographs (SEM) for x= 0.0, 0.1, 0.2 and 0.3 compositions of $Zn_{0.3}Mn_{0.7+x}Si_xFe_{2-2x}O_4$ system are shown in Figure 4.4.1.

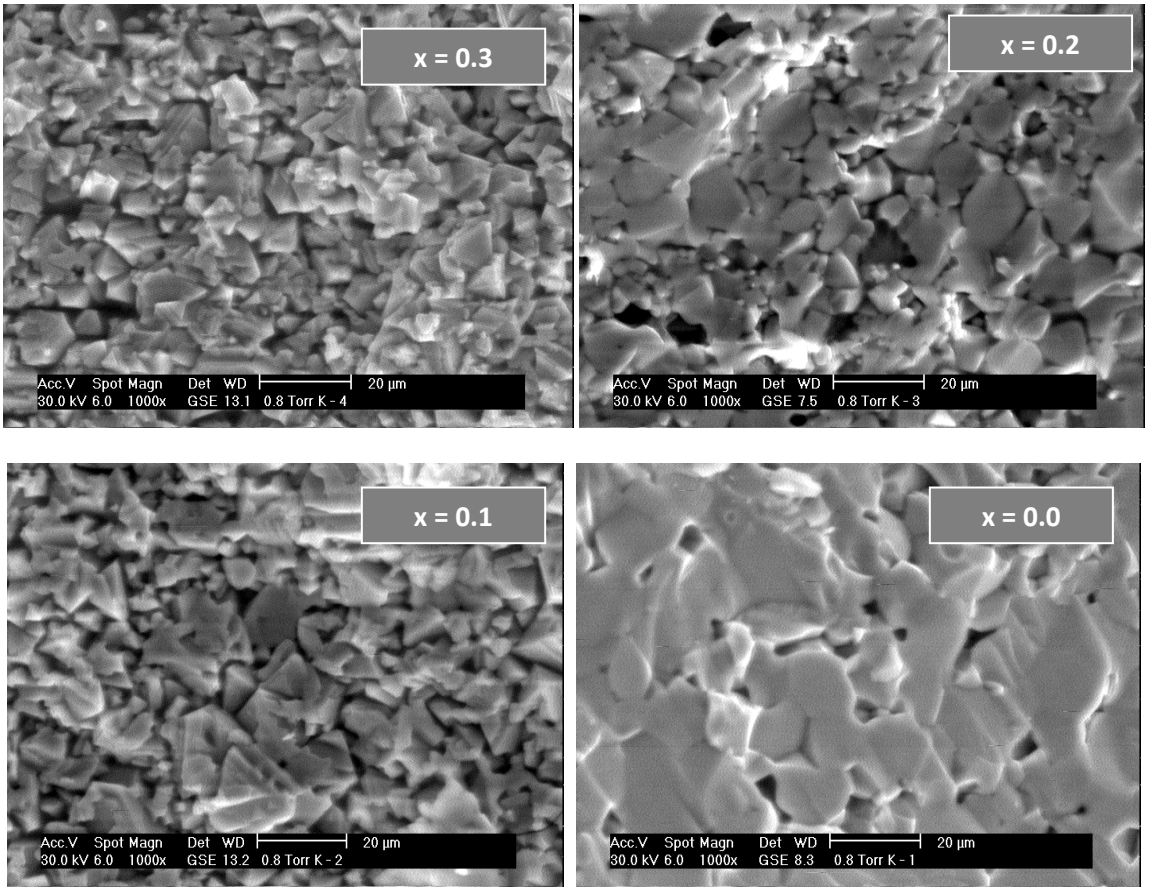

Figure 4.4.1. Scanning electron micrographs for $Zn_{0.3}Mn_{0.7+x}Si_xFe_{2-2x}O_4$ spinel ferrite system with the same magnification (1000x).

It is seen that grain morphology, grain size, shape, uniformity, homogeneity and their distribution, are highly influenced by Si^{4+} - substitution. The un-substituted ferrite composition (x = 0.0) shows large grains stuck to each other (diffused grain structure) in a irregular and non-uniform manner but form a network like structure. The micrograph for x = 0.0 composition ($Zn_{0.3}Mn_{0.7}Fe_2O_4$) shows pores that are trapped in the grains. When the grain growth rate is very

high pores may be left behind by rapidly moving grain boundaries, resulting in pores that are trapped inside the grains. These pores act as pinning centers for the domains wall movement. Consequently, domain wall movement is restricted and this limits the rate of growth of initial permeability.

Furthermore, the intragranular porosity is practically impossible to eliminate, leading to poor magnetic and mechanical properties [1]. Samples with large grains and included porosity still have good magnetic and mechanical properties than those with normally grown grains, provided the distances between pores were the same.

On analyzing Scanning electron photomicrographs for the samples with Si^{4+} - content (x = 0.1, 0.2 and 0.3) following observations can be made: (i) for all the substituted ferrites a large grain size distribution (mixture of small and large grains) with intragranular pores is observed (ii) uniformity and homogeneity increase with Si-substitution (iii) grain size decreases with increasing in Si-content(x) in the system. In advanced ferrite technology, an impurity that is to be controlled very carefully is SiO_2. At higher concentration, impurities such as SiO_2 create a duplex structure of giant grains within a fine grain matrix, that is very detrimental to the permeability and increases the losses [1].It is most often due to segregation of a particular impurities such as SiO_2 which produces rapid grain growth locally while other un-doped areas are unaffected. During the cooling, some of the SiO_2 may remain in the lattice which will affect the magnetic properties.

In general, with Mn-Si substitution, average particle (grain) size reduces from 12μm for x = 0.0 composition to 6 μm for x = 0.3 composition. The decrease in particle size with Mn-Si substitution is attributed to the smaller solid solubility of Si^{4+} - ion in the spinel structure that hampers the grain growth [2]. According to Shekrollahi et al [3], in the present case the decrease in grain size with Si^{4+}-substitution is attributed to the fact that as a result of deviation from the stoichiometric state, a small amount of SiO_2 segregated at the grain boundaries, that inhibit the grain boundary movement, consequently grain size decreases.

The observed reduction in grain size with Si^{4+} substitution may also be explain on the basis of surface tension in the samples. Islam et al [4] have suggested that grains having fewer than six sides will have boundaries which are concave when observed out word from the centre of the grain. In order to reduce their total surface area, boundaries will move towards their centers of curvature. Thus, such grains with less than six sides will grow smaller. We have seen that for the un-substituted (x =0.0) and substituted (x = 0.1, 0.2, 0.3) ferrites grains with less than six sides are clearly observed. The Si^{4+}- substitution may be the driving force that leads to the above discussed grain reduction mechanism. Thus, reduction in grain growth and lower density of Si in comparison with Zn and Fe are main reasons for the reduction in the ferrite density.

Earlier, Lotke et al [5] have reported that for Si- substituted Co-Cd ferrite, grain size remains almost constant for x = 0.0 to x = 0.4 compositions of $Cd_{0.5}Co_{0.5+x}Si_xFe_{2-2x}O_4$ system. On the other hand, Patil et al. [6] have observed enhancement in grain growth with Si^{4+} substitution in $CuFe_2O_4$.

Conclusions

(i) Particle morphology is highly influenced on Si^{4+}-substitution in general and particle morphology is completely different for substituted ferrites as compared to un substituted ferrite, $Zn_{0.3}Mn_{0.7}Fe_2O_4$, in particular.

(ii) Particle size decreases with increase in Si – content (x) in the system and is attributed to smaller solid solubility of Si^{4+} ion in the spinel structure, which hampers the grain growth.

References

1 Alex Goldman, Modern Ferrite Technology, 2nd edition, Springer (2006).

2 C. M. Kanamadi, R. G. Kharabe, R. B. Pujar and B. K. Chougule,, Ind. J. Phys. 79(3) (2005) 257.

3 L. Maghsoudi, M.I. Hadianfard and H. Shokrollahi, J. Alloys. Compd., 481 (2009) 539.

4 S. M. Hosue, Md. A. Choudhary and Md. F. Islam, J. Magn. Magn. Mater. 251 (2002) 292.

5 S. A. Patil, V. C. Mahajan, M. G. Patil, A.K. Ghatage and S. D. Lotke J. Mater. Sci. 34 (1999) 6081.

6 B. L. Patil, S. R. Sawant, S. A. Patil and R. N. Patil, J. Mater. Sci. Lett. 12 (1993) 399.

4.5 Infrared spectroscopy

Introduction

Infrared spectroscopy is one of the most powerful analytical techniques, which offers the possibility of chemical identification, types of vibration modes present, presence/absence of Jahn-Teller, Fe^{2+}, Mn^{3+} ions, determination of force constants, elastic constants, thermo dynamic and optical parameters [1]. It is also useful to study the phase transformation and impurity phase present in the system [2-4].The technique is based upon the simple fact that a chemical substance shows marked selective absorption in the infrared region. After the absorption of infrared radiations, the molecules of a chemical substance vibrate at many rates of vibrations, giving rise to closed packed absorption bands, 'IR absorption spectrum', which may be extended over a wide wavelength range.

Ferrites possess the structure of mineral spinel ($MgAl_2O_4$) that crystallizes in the cubic form with space group Fd3m – Oh^7 [1]. It is generally know that the spinel ferrites exhibit four IR active bands, designated as υ_1, υ_2, υ_3, υ_4. The occurrence of these four bands have been rationalized on the basis of group theoretical calculations employing space group and point symmetry both in normal and inverse spinels.

4.5(a) Infrared spectral analysis

The magnetic properties of ferrites are decisively dependent on the precise configuration of the atoms or ions in the structure. Therefore, the non-destructive method of characterization such as Infrared spectroscopy is especially suited for such investigations.

The infrared (IR) absorption spectra were recorded at 300K in the wave number range 400-1000 cm^{-1}. No IR active absorption bands were observed above 650cm^{-1}.The bands in the 300 – 700 cm^{-1} region are assigned to the fundamental vibrations of the ions of the crystal lattice. The high frequency band, υ_1,is in the range 550 – 560 cm^{-1} and the low frequency band, υ_2, is in the range 400 – 415 cm^{-1}. These bands are common features of all the ferrites [1].

According to Waldron's classification [1], the vibrations of the unit cell of cubic spinel can be constructed in the tetrahedral (A-) site and octahedral (B-) site. So, the absorption band υ_1 is caused by the stretching vibration of the tetrahedral metal-oxygen(t-o) bond, and the absorption band, υ_2, is caused by the metal-oxygen vibrations in the octahedral sites. The band positions (υ_1 and υ_2) for all the compositions are given in Table 4.5.1. The change in the band position is expected because of the difference in the metal ion-oxygen distances for the octahedral and tetrahedral complexes. It has been reported [5] that Fe^{3+}- O^{2-} distance for the A-sites (1.86Å) is smaller than that of the B-sites (2.02Å). This can be interpreted by the stronger covalent bonding of Fe^{3+} ions at the A-sites than the B-sites.

The first principal band, υ_1, shifts from 551.9 cm^{-1} for x=0.1 composition to 557.54 cm^{-1} for x = 0.3 composition. It is known that decrease in site radius enhances the fundamental frequency and therefore, the centre frequency should shift towards higher frequency side. The decrease in site radius may be expected due to the replacement of larger Fe^{3+} ions by smaller Si^{4+} on the tetrahedral site. Similarly, the second principal band, υ_2, shifts from 413.21 cm^{-1} for x = 0.1

composition to 409.7 cm^{-1} for x = 0.3 composition. The increase in site radius by replacement of smaller Fe^{3+} ions by larger Mn^{2+} ions on the B-site hinders the fundamental frequency and as a result centre frequency shifts towards lower frequency side.

A careful examination of IR spectrum reveals the fact that for x = 0.0 composition, high frequency shoulder (ν_{th}) occurs about 630 cm^{-1}, but completely disappeared for x = 0.1, 0.2 and 0.3 compositions (Figure 4.5.1) The high frequency shoulder is due to the disparity in masses of cations reside at the A-site of the spinel lattice [1]. In the present system, on Si^{4+} substitution, that occupy the A-site, disparity in masses increases and as a result intensity of high frequency shoulder should enhanced with increasing Mn-Si content (x), but this is not the case. Thus, the high frequency shoulder (υ_{sh}) centered at 630 cm^{-1} for un-substituted composition, $Zn_{0.3}Mn_{0.3}Fe_2O_4$ (x = 0.0), cannot be assign to disparity in masses of cations present at the A-site. The nature and bands position of the spectrum are consistent with IR spectrum of $MnFe_2O_4$ (υ_1 = 550 cm^{-1}, υ_2 = 392 cm^{-1}, shoulder 645cm^{-1}) and $ZnFe_2O_4$ (υ_1 = 555 cm^{-1}, υ_2 = 393 cm^{-1}, shoulder 645cm^{-1}) spinel ferrites [1].

The presence of a high frequency shoulder near υ_1 may be due to (i) in plane Fe – O bending vibrations [6]. (ii) the appearance of a vibrational band near 630 cm^{-1} is explained by the individual vibrational band for the $FeSiO_3$ compound that is formed on the grain boundaries of the spinel structure [7].

(iii) this shoulder may be due to tetravalent ion-oxygen stretching vibration (i.e.) Si^{4+} - O^{2-}) [3] (iv) This shoulder like vibration frequency band may be attributed to divalent tetrahedral metal ion (Zn^{2+}/Mn^{2+}) oxygen complexes[1]. (v) It has been reported the appearance of absorption bands at 650 cm^{-1} and 470 cm^{-1} are due to hematite (α-Fe_2O_3) phase [4].

The first possibility is ruled out base on the fact that in general band stretching frequency is higher than the band bending frequency [8]. Thus, this band should appear below υ_1 band.

The second and third possibilities are also ruled out because of the fact that for un-substituted composition, SiO_2 is absent and thus the formation $FeSiO_3$ compound or Si^{4+}-O^{-2} stretching vibrations do not occur.

The forth possibility is likely to exist, but if it so such shoulder should occurs for all the compositions as the compositions (x = 0.0 – 0.3) contain almost same amount of Zn^{2+} ion and Mn^{2+} on the A-site of the spinel structure.

In the present system, the formation of an antiferromagnetic rhombohedral α-Fe_2O_3 phase cannot be neglected. The concentration of α-Fe_2O_3 will be so small, the peaks from the α-Fe_2O_3 phase are hardly observable in X-ray powder diffraction pattern.

The α-Fe_2O_3 phase is completely absent for all the substituted ferrites and accordingly no such bands are observed in IR spectra (Figure 4.5.1). The IR spectrum of hematite [9] is shown in inset of Figure 4.5.1 (x = 0.0) as a ready reference.

When the symmetry of the spinel structure is lower than cubic or/and supplementary ordering of cation exists, more IR bands may appear. A splitting of IR band is observed in some spinels containing octahedrally coordinated Jahn-Teller ions. The presence of Fe^{2+} and/or Mn^{3+} ions in the ferrite can cause a splitting of the absorption band. Local deformation can occurs due to Jahn-Teller effect [1] in Fe^{2+}/Mn^{3+} ions which can lead to a non-cubic component of the crystal field potential and hence to splitting of the band. The bands may also spilt due to the presence of different kinds of ions in the same sub-lattice or occupancy of cations in other oxidation state. We have not observed any additional band as well as splitting of principal bands in IR spectra. This suggests overall cubic symmetry is maintain and Mn^{2+} /Fe^{3+} ions are stable in their respective oxidation state.

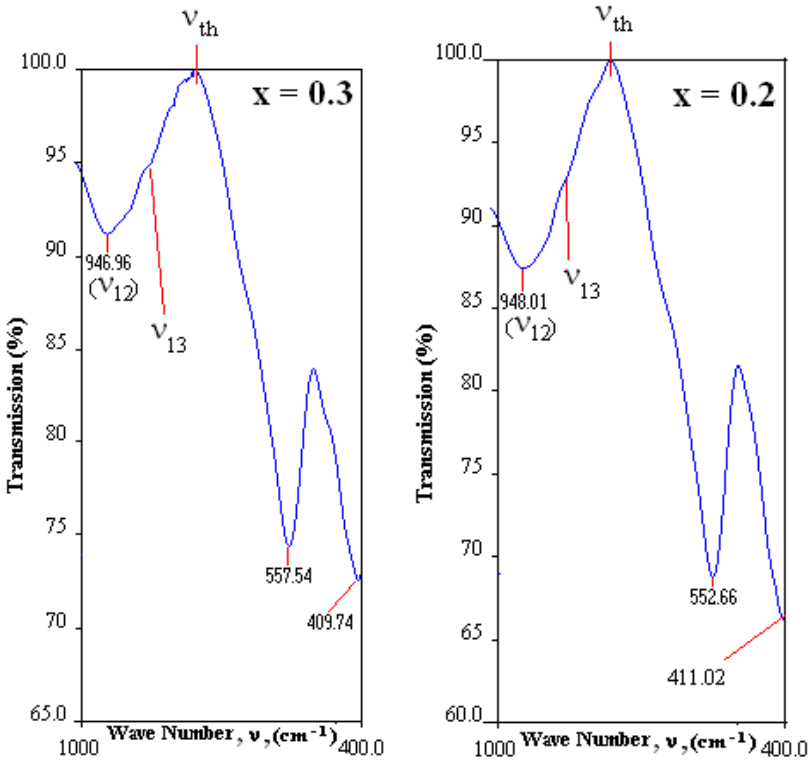

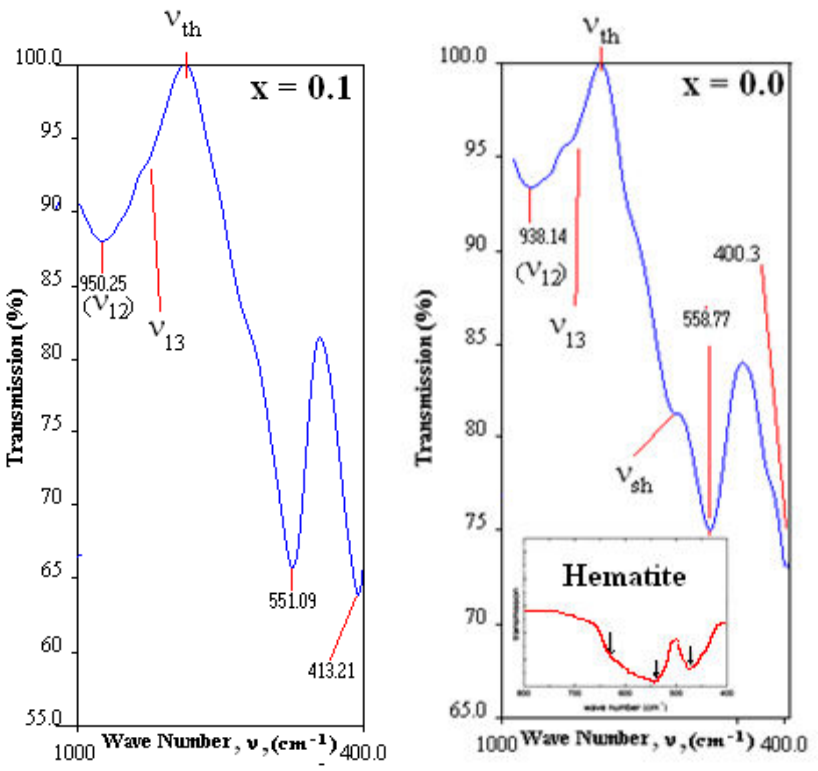

Figure 4.5.1. Infrared absorption spectra for $Zn_{0.3}Mn_{0.7+x}Si_xFe_{2-2x}O_4$ (x=0.0-0.3) system at 300K.

According to Waldron et al [1], the threshold frequency (υ_{th}) for the electronic transition can be determined from the maximum point of the absorption spectra, where it reaches a limiting values as shown in Figure 4.5.1. In other words, the inflection point in the graph of transmittance versus wave number may be chosen as the threshold frequency (ν_{th}) for the electronic transition. Table 4.5.1 shows these threshold frequency values for the ferrite system $Zn_{0.3}Mn_{0.7+x}Si_xFe_{2-2x}O_4$. It is found that the threshold frequency for the electronic transition decreases with increasing Mn-Si content (x) in the system. The corresponding threshold energy was calculated according to the following relation are given in Table 4.5.1.

E_{th} = h.f

= h.c/ λ

= h.c.ν_{th}

= 4.13 * 10^{-15} (eV/sec.) * 3 * 10^{10} (cm.sec^{-1}) * ν_{th} (cm^{-1})

E_{th} (eV) = 12.39 * 10^{-5} (eV.cm) * ν_{th} (cm^{-1})

The values of ν_{th} and E_{th} are consistence with those reported for Ti^{4+} and Ge^{4+} - substituted $CuFe_2O_4$ systems [3].

Illustrative calculations

E_{th}(eV) = 12.39 * 10^{-5} (eV.cm) * ν_{th} (cm^{-1})

x = 0.2, ν_{th} = 765.3 cm^{-1}

E_{th}(eV) = 12.39 * 10^{-5} (eV.cm) * 765.3 (cm^{-1})

= 0.095 eV

Table 4.5.1. IR absorption frequency (υ) and threshold energy (E) for $Zn_{0.3}Mn_{0.7+x}Si_xFe_{2-2x}O_4$ system at 300K.

Mn-Si content (x)	υ_1	υ_2	υ_{th}	υ_{12}	E_{th} (eV)
	cm^{-1}				
0.0	558.77	400.30	778.7	953.14	0.096
0.1	551.09	413.21	771.5	950.25	0.096
0.2	552.66	411.02	765.3	948.01	0.095
0.3	557.54	409.74	757.3	946.96	0.094

These data of ν_{th} and E_{th} are subject to considerable uncertainty because that portion of the scattering caused by the ferrite particles cannot be distinguished from absorption losses. If this absorption represent transitions to a conduction band of the crystal, the tabulated values can be express as activation energies [1].

It is found that the threshold frequency decreases on increasing Mn^{2+}- Si^{+4} concentration in the system. The observed trend is opposite to that observed for Ge^{4+} and Ti^{4+} -substituted $CuFe_2O_4$ [3].

The two distinct bands have been observed for un-substituted (x = 0.0) and substituted (x = 0.1, 0.2 and 0.3) ferrites. The weak high frequency shoulder (υ_{13}) just above υ_{th} can be due to the linear combination of υ_1 and υ_3 bands [7], while absorption band, ν_{12}, could be assigned to the linear combination of the bands, ν_1 and ν_2 [7]. The υ_3 band in spinel ferrite systems generally occurs below 400 cm^{-1}, about 300-350 cm^{-1} and is associated with the divalent octahedral metal ion - oxygen complexes [7]. A low frequency band υ_3 is at frequency below the available experimental range, thus, not observed in the spectra.

Table 4.5.2 shows the relation between the half band width for the tetrahedral (A-) site against Mn- Si content (x). It can be noted that the half band width (Γ_A) for the A- site decreases with increasing concentration(x). Earlier, it has been reputed that broadening of band is commonly observed when the system transfer from inverse to normal spinel structure and have attributed to the statistical distribution of Fe^{3+} ions on the A- and B- sites. In the present system, it is evident from cation distribution formula that, more – more divalent metal ions

(Mn^{2+}) occupy the B-site, that means system becomes more and more inverse spinel on increasing Mn-Si content (x) and thus Γ_A decreases with increases in content (x). No attempt has been made to determine the octahedral site band width (Γ_B) as this band terminated below the present experimental limit. The observed band width can be explained by the degree of degeneracy of the band and the resulting departure from cubic symmetry.

Table 4.5.2 . IR absorption band Intensity (I) and half band width (Γ) for $Zn_{0.3}Mn_{0.7+x}Si_2Fe_{2-2x}O_4$ system.

Mn-Si content (x)	I_A	I_B	Γ_Δ (cm^{-1})
	%		
0.0	10.0	12.2	100.03
0.1	13.6	15.4	74.45
0.2	12.6	14.2	65.31
0.3	10.6	12.6	57.16

It is also noticed from IR spectra that the intensity of υ_1 and υ_2 bands increases from un-substituted ferrite ($Zn_{0.3}Mn_{0.7}Fe_2O_4$) (x = 0.0) to substituted ferrite (x = 0.1) and then decreases with further increase in Mn-Si content (x) (Table 4.5.2).

The measurement of intensities of infrared absorption bands can give useful information concerning to change of electric dipole moment (dp_i) with inter-atomic or nuclear distances (dx_i) and charge on each ion. This value represents the contribution of the ionic bond Fe-O in the lattice. It has been shown from infrared reflectively data of $ZnFe_2O_4$ and $NiFe_2O_4$, that effective ionic charge on

Zn, Fe Ni and O ions is different from the actual ionic valance, with different magnitude at the A- and B-sites [10]. In the case of nickel ferrite ($NiFe_2O_4$), it is found that the effective ionic charge on the A-site occupied Fe is +2.86, while it is + 2.88 for Fe situated at the B-site instead of normal +3 charge of Fe. Similarly, for $ZnFe_2O_4$ effective ionic charge on Fe located at the octahedral (B-) site is found to be +3.1 [10]. Of course, this ionic charge is always close to the ionic valance of respective ion because of the radial spread of the electronic orbital [11]. On the other hand, perturbation occurs in metal ion – oxygen bond by introducing Mn^{2+}-Si^{4+} in the system leads to change in interatomic distances. On the basis of above facts we feel that for the substituted compositions (x = 0.1, 0.2 and 0.3) relative displacement of atoms (d_i) and the effective charge on different ions (q_i) change in such a way that the magnitude of electric dipole moment ($p_i = q_i d_i$) decreases and as a result intensity of the absorption bands. The variation of intensity of low frequency absorption band, υ_2, is similar to that for υ_1, but slightly different order of magnitude. For a thorough understanding infrared reflectivity measurements along with Rietveld refinement of x-ray data may be useful. Thus, it is concluded that the infrared spectra can give an idea about the change in the molecular structure of the ferrite due to the perturbation exerted on Fe-O bonds by introducing Mn^{2+}-Si^{4+} ions. On the other hand, the electronic distribution of Fe-O bonds is affected when Mn^{2+}-Si^{4+} ions are introduced into its neighborhood and this consequently affects the dp_i/dx_i of the Fe-O bond.

Earlier, Barber et al [12] and latter Mazen et al [13] have suggested that the fine structure of the infrared spectra can be considered indicative of the presence of crystallographic ordering. They have observed that in IR spectra of Li-Ti system, the fine structure is much less pronounced with increasing Ti^{4+} - concentration (x) and it first starts to disappear at $x \geq 0.4$ compositions. The weak structure in the IR spectra can be correlated with magnetic short range order or crystallographically deviation from the cubic symmetry. In the present case, the fine structure in the IR spectrum is observed for all the four compositions, which suggest that (i) long range order is maintained in conformity with magnetic properties such as magnetization and Neel's temperature determined from the thermal variation of ac susceptibility measurements. (ii) over all cubic symmetry is maintained.

Conclusions

(i) The IR spectra confirmed the formation of single phase spinel structure for all the Mn-Si substituted Mn-Zn ferrites while un-substituted composition possesses minor hematite phase.

(ii) The distinct bands well above threshold frequency are due to the linear combination of IR active fundamentals.

(iii) The change in intensity of principal bands is due to the perturbation created by Mn-Si substitution in Fe –O bond, while the variation of half bandwidth suggests that system transfer to partially inverse spinel structure.

(iv) The threshold frequency and energy of electronic transition have been determined.

References

1 R. D. Waldron, Phys. Rev., 99(6) (1955) 1727.

2 J. T. Last, Phys. Rev. 105(6) (1957) 1740.

3 S. A. Mazen, Mater. Chem. Phys., 62 (2009) 131.

4 M. I. Ivanovskaya, A. I. Telstik, D. A. Kotsikau and V. V. Pankov, Russ. J. Phys. Chem. A, 83(12) (2009) 2081.

5 C. M. B. Henderson, J. M. Charnock and D. A. Plant, J. Phys. Condens. Matter, 19 (2007) 076214.

6 J. Giri, T. Srihorsha and D. Bahadur, J. Mater. Chem., 14 (2004) 875.

7 M. A. Ahmed, E. Ateia and S. I. El-Dek, Vibrational Spect., 30 (2002) 69.

8 T. T. Srinivasan, C. M. Srivastava, N. Venkat ramani and M. J. Patni, Bull. Mater. Sci. 6(6) (1984) 1063.

9 Andre Angermann and Jorg Topfer, Ceramics International 37 (2011) 995.

10 T. Simada, T. Tachibana, T. Nakagawa and T. A. Yamamoto, J. Alloys. Compd. 379 (2004) 122.

11 L. Nakagawa, Spectrochim Acta, 29A (1973) 1451.

12 V. A. M. Barbers and R. E. Vandengerh, Phys. Lett., 44 (1973) 493.

13 S.A.Mazen, F.Metawe and S.F.Mansour, J.Phys.D:Appl.Phys. 30 (1997) 1799.

4.5(b) Optical parameters determination

When materials are exposed to electromagnetic radiation, it is sometimes important to be able to predict and alter their responses. This is possible when we are familiar with their optical properties and understand the mechanism responsible for their optical behavior.

The index of refraction, η, and the velocity, v, of the infrared radiation in the given ferrite material can be estimated using the relation [1,2]:

$$E_t/E_{ab} = c/v = \eta$$

where, E_t is the transmitted energy , E_{ab} the absorbed energy and c is the velocity of light. The magnitude of η (or the degree of bending) will depend on the wavelength of the incident radiation and decreases with increasing wavelength [3]. The values of refractive indices, η_1 and η_2 have been calculated considering wavelengths, λ_1 and λ_2 , corresponding to the principal infrared absorption bands position, ν_1 and ν_2, respectively. The average refractive index ($\bar{\eta}$) is further used to calculate velocity (v), reflectivity (R), and jump rate (J) for the different compositions. The values of η_1, η_2, $\bar{\eta}$ and v thus obtained are shown in Table 4.5.3. It is found that the refractive index ($\bar{\eta}$) decreases where as the velocity, v , of infrared radiation increases against Mn – Si content (x).

Table 4.5.3 Refractive index (η) , velocity (v), reflectivity (R) and jump rate ` (J) for $Zn_{0.3}Mn_{0.7+x}Si_xFe_{2-2x}O_4$ system.

Mn-Si content (x)	η_1	η_2	$\bar{\eta}$	Velocity (v)	R(%)	J_1	J_2	J
	±0.01			(cm/sec.) * 10^{10}		(Hz)*10^9		
0.0	1.39	1.94	1.67	1.80	6.3	2010.37	2273.70	2142.04
0.1	1.40	1.87	1.63	1.84	5.7	2000.30	2251.22	2125.76
0.2	1.38	1.86	1.62	1.85	5.6	1989.92	2251.16	2120.54
0.3	1.36	1.85	1.60	1.88	5.3	1957.65	2244.12	2100.89

Illustrative Calculations

x = 0.1, ν_1 = 551.09 cm^{-1}, ν_2 = 413.21 cm^{-1}, ν_{th} = 771.5 cm^{-1}

$\eta_1 = E_t / E_{ab} = h\ c\ \nu_{th} / h\ c\ \nu_1$

$= 4.13 * 10^{-15} * 3*10^{10} * 771.5/4.13*10^{-15}*3*10^{10}*551.09$

$\eta_1 = 1.40$

Similarly, $\eta_2 = 1.87$

$\bar{\eta} = (\eta_1 + \eta_2)/2 = 1.63$

$\eta = c/v$

$v = c/\bar{\eta}$

$v = 3*10^{10}$ (cm/sec)/1.63 = 1.84 x 10^{10} cm/sec

Since, the retardation of electromagnetic radiation (infrared radiation) in medium results from electronic polarization, the size of the constituent atoms or ions has a considerable influence on the magnitude of this effect. Generally, the

larger an ion or atom, the greater will be the electronic polarization, the slower the velocity and the greater the index of refraction. The η for a typical soda-lime glass is ~ 1.5; addition of large Ba^{2+} or Pb^{2+} ions to a glass will increase refractive index significantly. For example, highly leaded glasses containing 90 wt% PbO has an index of refraction ~ 2.1 [4]. In the system under investigation $Zn_{0.3}Mn_{0.7+x}Si_xFe_{2-2x}O_4$, Fe^{3+} (0.64 Å) ions are replaced by larger Mn^{2+} (0.83 Å) and smaller Si^{4+} (0.42 Å) ions thus, η is expected to increase or remains unaffected, but we have observed opposite trend (Table 4.5.3). This may be due to crucial role plays by SiO_2 with much smaller refractive index, η = 1.55 [4]. The η values for the different compositions are consistent with those reported for mineral spinel ($MgAl_2O_4$, η = 1.72) [4] and other magnetic oxides; single crystalline yttrium, gadolinium-yttrium and europium iron garnets (η ~ 2.2 ± 0.2) [3]. For crystalline ceramics that have cubic crystal structure, as in the present case, the refractive index (η) is independent of crystallographic direction (i.e. it is isotopic). Non cubic crystals on the other hand have an anisotropic η; that is index is greatest along the direction that has the highest density of ions [4].

An attempt has been made to calculate the reflectivity of given ferrite materials using the relation:

$$R = (\bar{\eta} - 1/ \bar{\eta} + 1)^2$$

where, $\bar{\eta}$ is the refractive index of the material. The higher the index of the refraction of the solid the greater is the reflectivity. As expected R is found to

change from 0.063 for x = 0.0 composition to 0.053 for x = 0.3 composition (Table 4.5.3).

When an ion with incorrect valance enters the structure, charged vacancies may form to maintain local charge neutrality. From the thermoelectric power measurements it is found that all the compositions are n-type semiconducting material or conduction is due to electrons. Thus, the vacancies formed are anion vacancies rather than cation vacancies since the valency of Fe^{2+} ion is less than the valency of Fe^{3+} ion.

Finally, the jump rate (J) of charge carrier (here electron) may be estimated from the relation [1,5]:

$$J = f.e^{-E/k_B t}$$

where, f is the frequency of vibration, k_B is the Boltzmann constant, E is the height of potential barrier (activation energy for hopping of electrons). The jump rate is found to decrease with increasing Mn-Si content (x) and it is attributed to the decrease in anion vacancies produced by the formation of ferrous (Fe^{2+}) ions in the lattice.

Conclusions

(i) Infrared spectral analysis leads to many important optical parameters determination.

(ii) Velocity of the infrared radiation in the given ferrite material is found to increase, index of refraction, reflectivity and jump rate are found to decrease with increase on Mn-Si substitution in the system.

Illustrative Calculations

x = 0.2 $\bar{\eta}$ = 1.62, ν_1 = 552.66 cm^{-1}, v = 1.85 * 10^{10} cm/sec.

$R = (\bar{\eta} - 1/\bar{\eta} + 1)^2$

$= (1.62 - 1/1.62 + 1)^2$

$= (0.62/2.62)^2$

$= (0.2366)^2$

R = 0.056

$J_1 = f_1 . e^{-E_1/k_B t}$

$k_B = 8.6 \times 10^{-5}$ eV/K

T = 300K

$k_B T = 0.0258$ eV

$E_1 = h f_1 = h v \nu_1$

$= 4.13 * 10^{-15}$ eV.sec

$* 1.85 \times 10^{10}$ cm/sec

$* 552.66$ cm^{-1}

$E_1 = 4.2226 * 10^{-2}$ eV

$f_1 = 1.85*10^{10}$ cm/sec * 552.66 cm^{-1}

$f_1 = 1022.421* 10^{10}$ Hz

$e^{-E_1/k_B t} = 194.62 * 10^{-3}$

$J_1 = 1022.421 * 10^{10}$ Hz * 194.628 * 10^{-3}

$J_1 = 1989.92 * 10^9$ Hz

References

1 O. H. Hemada, J. Magn. Magn. Mater. 281 (2004) 36.

2 C. Kittel, Introduction to Solid State Physics, 5th Edn. (1976) p. 323.

3 B. Johnson and A. K. Walton, Brit. J. Appl. Phys. 16 (1965) 475.

4 W. D. Callister, Materials Science and Engineering An-Introduction, 4th Edn. John Wiley & Sons (2000) p.714.

5 Arun Kumar, Introduction to Solid State Physics, PHI Learning Private Ltd. (2010) p. 76.

4.6 High field magnetization study

Figure 4.6.1 shows magnetic field (H) dependence magnetization (σ) curves recorded at 300K for all the four compositions of $Zn_{0.3}Mn_{0.7+x}Si_xFe_{2-2x}O_4$ (x = 0.0-0.3, step 0.1) system. There is a high field slope to magnetization curves which exhibit strong evidence for a canted spin structure, and canting angle varies with applied magnetic field. The high field slope has been established as due to the high magnetic anisotropy [1]. This fact does not apply here since all the compositions may have very low concentration of magnetic anisotropy ions (Fe^{2+}, Mn^{3+}) if any, and therefore, the observed features may be thought of arising from canting of spins. Magnetization (σ) versus reciprocal of applied magnetic field (1/H) curves are shown in the inset of Figure 4.6.1, that has been used to determine saturation magnetization (σ_s) values for the different compositions.

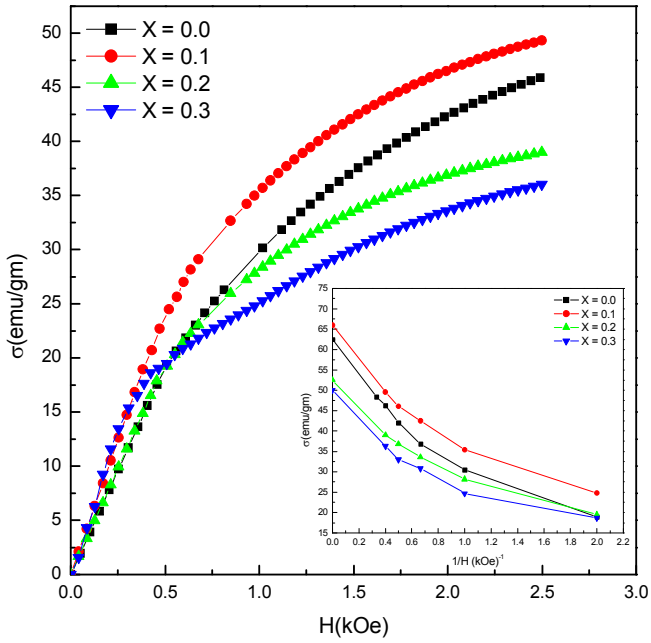

Figure 4.6.1 Field dependence of magnetization at 300K.

The values of saturation magnetization (σ_s) and the magneton number (saturation magnetization per formula unit in Bohr magneton (μ_B)) recorded at 300K and 80K for each composition are listed in Table 4.6.1. The values of magneton number (n_B) and saturation magnetization ($4\pi M_s$) have been calculated from σ_s values using the following formulae:

$n_B(\mu_B)$ = Molecular weight of the composition (Grams)/(5585) * σ_s (emu/gm)

$4\pi M_s$(Gauss) = 4*3.14* X-ray density(g/cm^3) * σ_s (emu/gm)

Table 4.6.1 Molecular weight (M_W) and Magnetic parameters for $Zn_{0.3}Mn_{0.7+x}Si_xFe_{2-2x}O_4$ system.

Mn–Si content (x)	M_w (Grams)	σ_S (emu/gm)		n_B (μ_B)		n_B^{LCS} (μ_B)	4 πM_S (Gauss) (80K)
		300K	80K	300K	80K		
0.0	233.76	62.1	101.4	2.60	4.24	4.57	6520.0
0.1	230.89	66.7	108.5	2.76	4.49	3.96	6841.1
0.2	228.02	52.5	92.4	2.14	3.77	3.63	5733.1
0.3	225.16	56.2	77.4	2.02	3.12	3.29	4724.6

From the field dependence of magnetization and observed magnetic moment, it is clear that the samples with x = 0.0 – 0.3 show ferrimagnetic behavior, which decreases with increasing x values. It is also found that for all the samples coactivity and remanence are negligible (Table 4.6.2), which are often found in magnetic cluster system [2]. The negligible coercively for different compositions also suggests that these are low anisotropic compounds [3].

Based on the Neel's two sub lattice model of ferrimagnetism [4] Neel's magnetic moment per formula unit in μ_B, n_B^N , is given by:

$$n_B^N = M_B(x) - M_A(x) \quad (1)$$

Here, M_A and M_B are the tetrahedral (A-) and octahedral (B-) sub-lattice magnetization to be determined from the cation distributions and the free – ion magnetic moments of the cations involved: $m(Fe^{3+}) = 5\ \mu_B$, $m(Mn^{2+}) = 5\ \mu_B$, $m(Zn^{2+}) = 0\ \mu_B$, $m(Si^{4+}) = 0\ \mu_B$. It is found that the observed values of magnetron number at 80K do not agree with the Neel's magnetic moment (n_B^N) (Table 4.6.2) calculated from the Neel's formula assuming collinear spin arrangement. This suggests that B – site moments are canted significantly. The substitution of non-magnetic (Si^{4+}) ions for magnetic Fe^{3+} in the system, may lead to collapse of long range magnetic ordering in the $Zn_{0.3}Mn_{0.7+x}Si_xFe_{2-2x}O_4$ system.

Table 4.6.2 Coercivity (H_c), remanence magnetization (M_r), Neel's magnetic moment (n_B^N).

Mn – Si content (x)	H_c (Oe)	M_r (emu/gm)	M_B	M_A	n_B^N	$\theta_{(RCS)}$
	300K		(Bohr Magneton)			(Degree)
0.0	24.2	0.28	9.75	3.75	6.00	34.97
0.1	15.9	0.62	9.75	3.25	6.50	37.45
0.2	15.9	1.13	9.53	2.98	6.55	44.92
0.3	19.1	2.38	9.30	2.70	6.60	51.26

It was, therefore, thought appropriate to apply Random Canting of Spins (RCS) model proposed by Rosenwaig [5]. According to this model, the magnetic

ions on the octahedral sites, can be considered to be canted with an average canting angle, (θ_{RCS}), due to non – magnetic (Si^{4+}) ion substitution on, which in the average nearest neighbour approximation is estimated to be :

$$Cos(\theta_{RCS}) = (M_A/M_B)\ (J_{AB}/J_{BB}) \qquad (2)$$

where, J_{AB} and J_{BB} are exchange integrals. The experimental magneton number (n_B), is related to canting angle, θ_{RCS}, by the relation:

$$n_B = M_B(x).Cos(\theta_{RCS}) - M_A(x) \qquad (3)$$

The experimental values of canting angle, $\theta_{RCS,}$ have been calculated from equation (3), and the same are shown in Table 4.6.2.It can be seen that (J_{AB}/J_{BB} ~ 2.2) the calculated n_B^{LCS} are in reasonable agreement with the experimentally observed values of n_B at 80K (Table 4.6.1). This is conceivable because the initial composition $Zn_{0.3}Mn_{0.7}Fe_2O_4$ (x = 0.0) is canted ferrimagnet due to comparable strength of B-B super exchange interaction with A-B super exchange interaction.

Conclusions

(i) The disagreement between the Neel's magnetic moment and the derived magneton number at 80K indicates the presence of canted spin structure.

(ii) The compositional variation of magneton number at 80K can be successfully explained by using the Random Canting of Spin model.

References

1 R. M. Persoons, E. de Grave, P.M.A. de Bakker and R. E. Vandenberghe, Phys. Rev. B. 47(1993)5894.

2 B. C. Zhao, H. W. Hu, B. Xia, L. H. Tan, A. C. Huan and L. Wang, Appl. Phys. Lett. 93(2008)222506.

3 P. S. Anil Kumar, P. A. Joy, S. K. Date, Bull. Mater. Sci. 23(2) (2000)97.

4 L. Néel, Ann. Phys. 3(1948)137.

5 A. Rosencwaig, J. Phys. 48(1970) 2857.

4.7(a) Thermal variation of low field ac susceptibility study

Thermal variation of relative or normalized low field (0.5 Oe) ac susceptibility χ_T/χ_{RT} ($\chi_{ac}(T)$, RT = room temperature) plots for x = 0.0, 0.1, 0.2 and 0.3 compositions of $Zn_{0.3}Mn_{0.7+x}Si_xFe_{2-2x}O_4$ spinel ferrite system are depicted in Figure 4.7.1. It is observed that $\chi_{ac}(T)$ remains constant until the temperature reaches nearer to Neel point. χ_{ac} drops to zero at Neel temperature (T_N). This suggests that, all the samples exhibit normal ferrimagnetic behavior with no indications of any magnetic phase transitions except at the transition temperature (T_N).

The nature of $\chi_{ac}(T)$ curves suggest domain states in the ferrites [1]. There are three types of domain states, viz. multi domain (MD), single domain (SD) and super paramagnetic domain (SP). The samples under investigation contain MD states this is because of the fact that in MD states the χ_{ac} is temperature independent.

The Neel temperature, T_N, determined from ac susceptibility measurements are listed in Table 4.7.1. In general, T_N, decreases with substitution of non-magnetic cation for magnetic cation in the system [2-4], due to weakening of the active magnetic linkages per magnetic ion per formula unit. In the present system also highly magnetic Fe^{3+} ions (5 μ_B) is replaced by non-magnetic Si^{4+} ions (0 μ_B), thus, one can expect decrease in T_N, with increasing Si^{4+} concentration (x). It is evident from the Table 4.7.1 that there is sharp decrease in T_N value for small

additions of silicon, which is due to the breaking and weakening of Fe^{3+} - O^{-2} – Fe^{3+} super exchange linkages resulting from replacement of magnetic Fe^{3+} ions by non-magnetic Si^{4+} ions in the spinel lattice.

Earlier, it has been reported by Patil et al [2] that with Co-Si substitution in $CdFe_2O_4$ Neel temperature increases due to covalent bond formation and domain wall pinning which ultimately change the magnitude of the molecular field. On the other hand, for Si^{4+} substituted $CuFe_2O_4$, $Cu_{1+x}Si_xFe_{2-2x}O_4$ system, T_N is found to decrease with increasing Si –content (x) [5].

Furthermore, from the Figure 4.7.1 it is seen that the plots exhibit the tailing effect for $T > T_N$. It is also important to note that transition temperature and tailing effect decease with increasing Mn-Si content (x). The tailing effect in $\chi_{ac}(T)$ plots is due to “spin clusters”. The clusters are small groups of atoms with a kind of magnetic short range order. These clusters of local spin disorder which constitutes a paramagnetic phase. The observed decrease in tailing effect with Si^{4+} substitution may be due to increase in micro structural uniformity in the material as evident from SEM analysis.

It is also clear from Table 4.7.1 that the values of T/T_N ratios are less than 0.22 for all the compositions at T = 80K which means that the magnetization data recorded at 80K are valid for the explanation by using the magnetic ordering model [8].

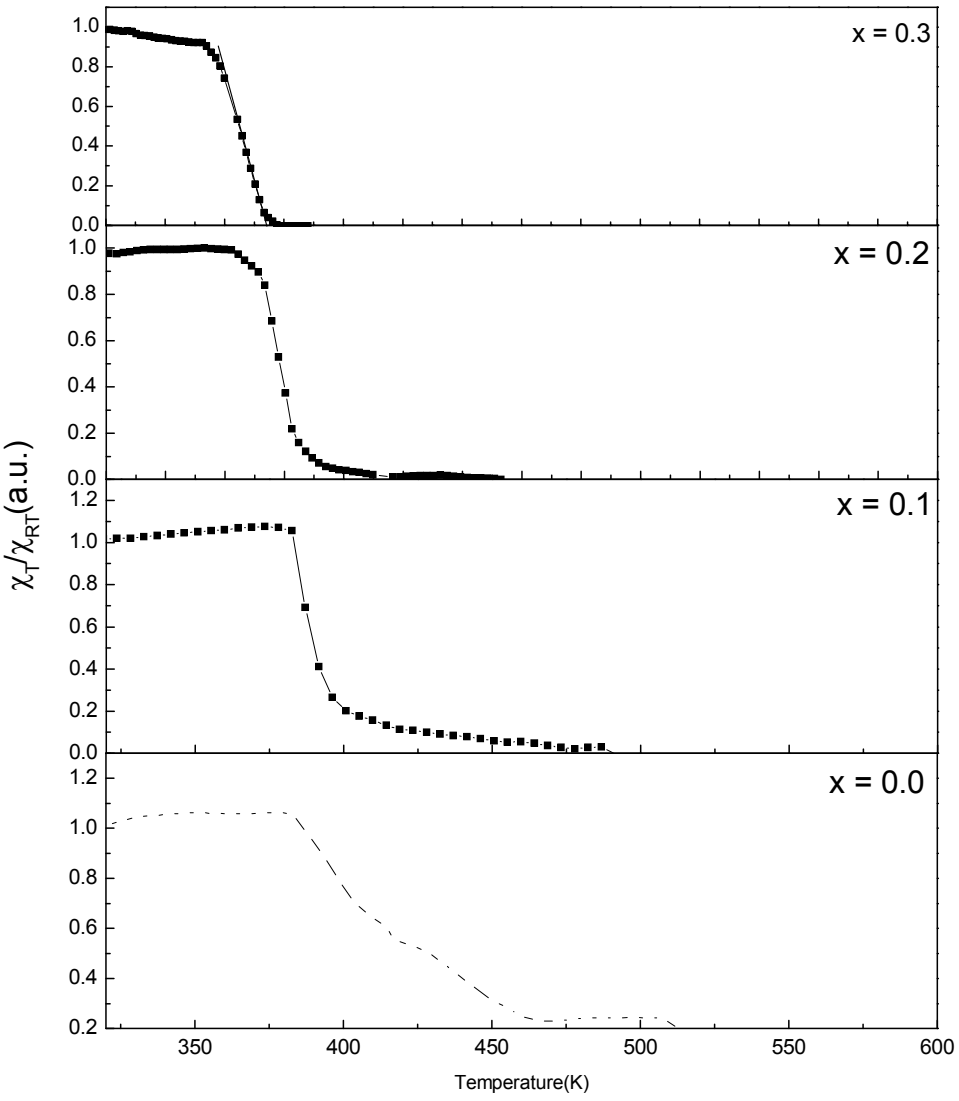

Figure 4.7.1.Temperature dependent ac susceptibility for Mn-Si substituted Mn-Zn ferrites.

4.7(b) Theoretical estimation of Neel temperature

The Neel temperatures (T_N) have also been calculated theoretically for x = 0.1, 0.2 and 0.3 compositions applying molecular field theory and using the cation distribution determined from X-ray diffraction line intensity calculations.

According to Gilleo et al [6], the Neel temperature depends upon the active magnetic linkages per magnetic ion per formula unit. The average number of magnetic interactions, n(x), for a ferrite with non-magnetic substitution(x), is given by :

$$n(x) = \frac{1}{N}\left[f_t . f_0 \left(Z_{BA} k_0 + Z_{AB} . k_t\right)\right] \qquad (1)$$

where, f_t and f_0 are the fraction of magnetic ion concentrations with respect to un-substituted ferrite and k_t and k_0 are number of metal ions at the tetrahedral (A-) and octahedral (B-) sites of the spinel structure respectively. Z_{BA} and Z_{AB} denote the A-site nearest neighbors to the B-site, and the B-site nearest neighbors to the A-site respectively, N is the total number of magnetic ions in a substituted ferrite Thus, equation (1) reduces to :

$$n(x) = \frac{24}{N}\left[f_t . f_0\right] \qquad (2)$$

In the present system, $Zn_{0.3}Mn_{0.7+x}Si_xFe_{2-2x}O_4$, two magnetic cations, Mn^{2+} and Fe^{3+} , are present but their magnetic moment is same i.e. 5 μ_B, thus for the Neel temperature determination they can be considered as a single entity. The Zn^{2+} and Si^{4+} are non-magnetic cations with magnetic moment of $0\mu_B$.

The influence of non-magnetic Si^{4+} ion substitution upon the Neel temperature of un-substituted ferrite $Zn_{0.3}Mn_{0.7}Fe_2O_4$ (x = 0.0) may be approximated through its effect upon the average number of n(x) of Fe^{3+}-O^{2-}-Fe^{3+} super exchange interactions per magnetic ion per formula unit. In un-substituted composition, $Zn_{0.3}Mn_{0.7}Fe_2O_4$ (x = 0.0) , there are 24/2.7 interactions per magnetic ion denoted by n (x = 0.0) which is expressed by using equation as :

$$n\left(x = 0.0\right) = \frac{24}{2.7}\left[\frac{0.75}{0.75} * \frac{1.95}{1.95}\right]$$

$$n\left(x = 0.1\right) = \frac{24}{2.7 - 0.1}\left[\frac{0.65}{0.75} * \frac{1.95}{1.95}\right]$$

$$n\left(x = 0.2\right) = \frac{24}{2.7 - 0.2}\left[\frac{0.6}{0.75} * \frac{1.9}{1.95}\right]$$

$$n\left(x = 0.3\right) = \frac{24}{2.7 - 0.3}\left[\frac{0.54}{0.75} * \frac{1.86}{1.95}\right]$$

Therefore, the Neel temperature of Si^{4+} substituted $Zn_{0.3}Mn_{0.7}Fe_2O_4$, $T_N(x)$, will vary approximately as n(x), so that it can be related with the Neel temperature of $Zn_{0.3}Mn_{0.7}Fe_2O_4$, $T_N(x = 0.0)$, by :

$$T_N(x) = \frac{n(x)}{n(x = 0.0)} T_N(x = 0.0) \qquad (3)$$

The Neel temperatures calculated theoretically for the substituted Mn-Zn ferrites are in good agreement with the Neel temperatures obtained from thermal variation of ac susceptibility measurements and are listed in Table 4.7.1. The observed difference between measured and calculated Neel temperature values is due to the random variation of the number of Fe^{3+}-O^{2-}-Fe^{3+} interactions per Fe^{3+} ion as consequence of the random distribution of Si^{4+} ions in the A- and B-sites [7].

Table 4.7.1 Neel temperature (T_N) for Si^{4+} substituted Mn-Zn ferrites.

Mn-Si Content (x)	n(x)	Neel temperature	
		T_N(K) ± 2 susceptibility	T_N(K) Theory
0.0	8.89	465	--
0.1	8.00	410	418
0.2	7.44	385	389
0.3	6.87	370	359

Illustrative calculations

x = 0.3 $Zn_{0.3}Mn_{1.0}Si_{0.3}Fe_{1.4}O_4$

$(Mn_{0.48}Zn_{0.25}Si_{0.21}Fe_{0.06})^A\ [Mn_{0.52}Zn_{0.05}Si_{0.09}Fe_{1.34}]^B$

$$n(x) = \frac{24}{2.4}\left[\frac{0.54}{0.75} * \frac{1.86}{1.95}\right]$$
$$= 10.0\left[0.75 * 0.954\right]$$
$$= 6.8688$$

$$T_N(x = 0.3) = \frac{6.87}{8.89} * T_N(x = 0.0) \qquad \left[T_N(x = 0.0) = 465\ K\right]$$
$$\therefore T_N(x = 0.3) = 0.7727 * 465\ K$$
$$\approx 359\ K$$

Conclusions

(i) The samples under study contain multi domain states and exhibit normal ferrimagnetic behavior.

(ii) The Neel temperature is directly proportional to the number of active super exchange linkages per magnetic ion per formula unit. The observed decrease in Neel temperature with Si^{4+} - substitution is due to weakening of magnetic coupling.

(iii) The Neel temperatures calculated theoretically using molecular field theory is in reasonable agreement with those deduced experimentally from ac susceptibility measurements.

References

1 C.R.K.Murthy and N.G.Nandikar, PRAMANA-J.Phys. 13 (11979) 413.

2 S.A.Patil, V.C.Mahajan, M.G.Patil, A.K.Ghatage and S.D.Lotke, J.Mater. Sci. 34 (1999) 6081.

3 V.K.Lakhani and K.B.Modi, J.Phys.D:Appl.Phys. 44 (2011)245403.

4 V.K.Lakhnai, B.Zhao. L. Wang, U.N.Trivedi and K.B.Modi, J.Alloys. Compd. 509 (2011) 4861.

5 B.L.Patil, S.R.Sawant, S.A.Patil and R.N.Patil, J.Mater. Sci. Lett. 12 (1993) 399.

6 M.A.Gilleo, J.Phys. Chem. Solids. 13 (1960)33.

7 K.B.Modi, H.H.Joshi and R.G.Kulkarni, J.Mater. Sci. 31 (1996) 1311.

8 K.P.Thummar, M.C.Chhantbar, K.B.Modi, G.J.Baldha and H.H.Joshi, J.Magn.Magn. Mater. 280 (2004) 23.

4.8 Compositional, frequency and temperature dependent initial permeability spectral analysis

Introduction

Permeability is one of the most important parameters used in evaluating magnetic materials. Not only is it a function of the chemical composition and crystal structure but it is strongly dependent on microstructure, temperature, stress, time after magnetization and several other factors [1].These are attributed to the fact that the permeability of polycrystalline ferrite can be described by the superposition of two different magnetization processes: spin rotation and domain wall motion [2-4]. Additionally, there exists a natural resonance due to the effective anisotropy field, resulting in magnetic losses [4].

In this section, a comprehensive study on compositional, frequency and temperature dependence of initial permeability has been carried out on $Zn_{0.3}Mn_{0.7+x}Si_xFe_{2-2x}O_4$ (x = 0.0,0.1,0.2 and 0.3) spinel ferrite system. It has been shown that along with grain size, uniformity and homogeneity of the grain size also play an important role in deciding the nature of permeability spectrum. Various microstructural parameters have been calculated. In these regard this piece of work is important as well as interesting from fundamental and applied research point of view.

The toroidal samples were used to carryout the initial permeability measurement. The toroids were wound by a 32 SWG enameled copper wire with 50 turns avoiding overlapping of each turn. Initial permeability as a function

of frequency (100 Hz to 1 MHz) and temperature (300K-573K), was determined by measuring the inductance of toroids using a 4192 A impedance analyzer. The initial permeability is expressed as μ' = L/L_0 where L is the measured inductance and the air core inductance L_0 (in Henry) is given as $L_0 = 4.6 N_T^{\,2} d \log(r_0 / r_i).10^{-9}$ where, N_T is the number of turns, d the thickness of the toroid in meters, r_0 and r_i are the outer and inner radii of the toroid.

Materials to be used for such high frequency applications should have: (i) High value of saturation magnetization (ii) Low power loss/ high value of resistivity (iii) High amplitude of initial permeability.

Furthermore, ferrite must be dense, exhibiting a homogeneous and fine grained microstructure. Spinel ferrites are only the materials that have these properties in more or lesser extent. In addition spinel ferrites have other advantages like (i) Easy preparation (ii) economical (Iii) mass production possible (iv) reproducibility.

Among the various ferrite systems, most promising consideration for high frequency applications are : (i) Ni-Zn ferrites system (ii) Mn-Zn ferrites system. When we compare various factors essential for high frequency application of Ni-Zn with Mn-Zn, it is clear that Mn-Zn ferrites having superior properties e.g. (i) Ni-Zn ferrites have initial permeability of 640 which it is 1660 in the case of Mn-Zn ferrite which almost 3 times more. (ii) Power loss in Ni-Zn ferrite is 20 times more as compared to Mn-Zn ferrite. (iii) Only drawback with Mn-Zn ferrites is its low resistivity value 10 Ohm..m. as compared 10^8 Ohm.m for Ni-Zn ferrites.

Correlation study on variation of initial permeability with Mn-Si content frequency and temperature.

The variation of real part of complex permeability ($\mu^* = \mu' - j\mu''$) henceforth referred to as initial permeability (μ') with Mn-Si concentration (x) at 325K with applied frequency of 10 kHz is shown in Figure 4.8.1.

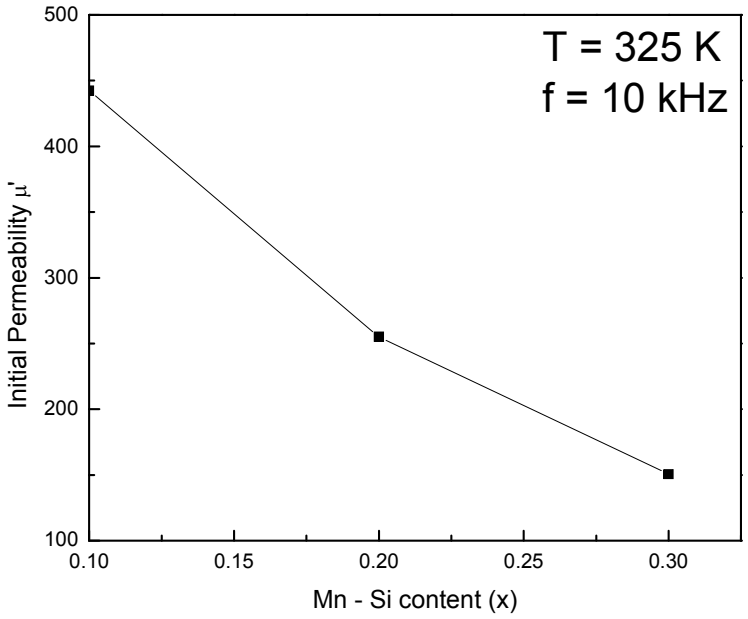

Figure 4.8.1. Variation of μ' with Mn-Si concentration (x) at 325K with applied frequency of 10kHz.

It is seen that μ' decreases on increasing Mn-Si concentration (x) in the system: $Zn_{0.3}Mn_{0.7+x}Si_xFe_{2-2x}O_4$ for x = 0.1 to 0.3 compositions. The observed reduction in μ' with Mn-Si substitution can be explained from several perspectives: (i) According to Went and Wijn [5], the initial permeability is proportional to the square of saturation magnetization. Hence the variation of initial permeability with Mn-Si substitution follows a similar trend to that of saturation magnetization (Table 4.6.1). (ii) According to Brion and Nemback [6],

the aggregation of nonmagnetic substance like SiO_2 at the grain boundaries will reduce the permeability by hindering the magnetization process, for instance, the domain wall movements, which can lower the initial permeability, therefore μ' decreases with Mn-Si substitution. (iii) The grain size reduction on Mn-Si substitution, results in increase in number of grain boundaries present, that impede the domain wall motion, and hence lowering of permeability is expected. In small grains, the formation of domain walls not being energetically favoured, the initial permeability will be lower. (iv) In addition to grain boundaries, ceramic imperfection impedes domain wall motion and thus reduces the permeability. Among these are pores, cracks, inclusions, second phases, as well as residual strains. Imperfections also act as energy wells that pin the domain walls and require higher activation energy to detach.

At high frequencies, the permeability separates into two components μ' and μ''. The first, μ' represents the permeability with the magnetization in phase with the alternating magnetic field and the second, imaginary part of permeability, μ'', the permeability with the magnetization that is out of phase with alternating magnetic field. The two permeabilities are often plotted on the same graph as a function of frequency. This is known as the permeability dispersion or permeability spectrum.

The permeability spectra for x=0.0, 0.1, 0.2 and 0.3 compositions of $Zn_{0.3}Mn_{0.7+x}Si_xFe_{2-2x}O_4$ system at 300K are shown in Figure 4.8.2.

It is seen that μ' continuously decreases with increasing frequency. Such frequency dispersion in μ' is usually attributed to domain wall displacement [7]. According to Globuset al [8-9] the shape of the permeability spectrum is relaxed for uniform and homogeneous grain size samples irrespective of the size of the grain and is the resonance type when the grain size is inhomogeneous. But according to Srivastava et al [10], the grain size is the predominant factor which controls the nature of permeability spectrum.

The spectra shown in Figure 4.8.2 are of relaxed type. The relaxed spectra occur when for larger grains closure domains are present. It is found that for the same composition with constant magnetization on decreasing grain size permeability spectrum transfer from relaxed to mixed, to resonance, type behavior. For different compositions of garnet, range of grain size is very wide, for relaxed spectra it varies from 7.5-20 μm, for mixed spectra it changes from 4.6-15 μm while for resonance spectra grain size is varying from 1.4-6.5 μm [10]. In the present case, average grain size is found to vary between 12 μm for x = 0.0 composition to 6 μm for x = 0.3 composition thus, one can expect relaxed or mixed type nature of frequency dependent permeability spectrum. We have observed relaxed type nature of permeability spectrum for these compositions in the frequency range studied (Figure 4.8.2). We feel that along with size of the grain, uniformity and homogeneity of the grains play important role in deciding the nature of permeability spectrum [8-9]. This argument is more clear based on SEM image of x =0 .3 composition, having average grain size of the order of 6.0 μm but with better homogeneity and uniformity.

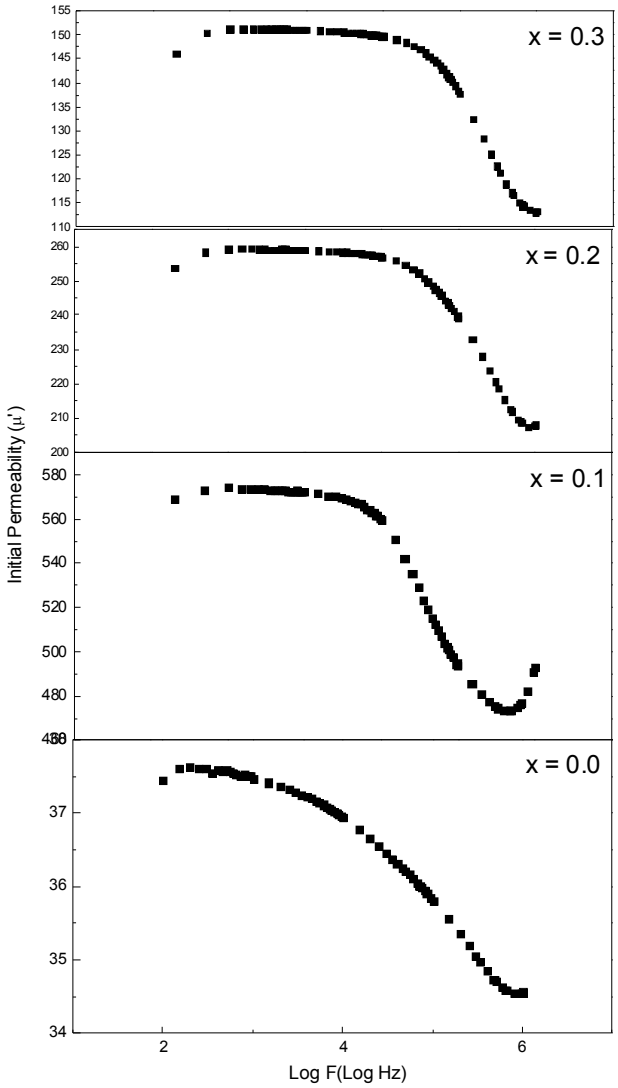

Figure 4.8.2. Frequency dependent initial permeability of $Zn_{0.3}Mn_{0.7+x}Si_xFe_{2-2x}O_4$ system at 300K.

The domain walls dynamics under external time varying fields has been studied by many workers [2, 8, 11,12]. The equation of motion for domain walls is:

$$m_\varpi \ddot{z} + \beta_\varpi \dot{z} + \alpha_\varpi z = 2M_s H$$

Where, m_ϖ is the effective mass per unit area of the domain wall, β_ϖ is the damping constant and σ_ϖ is the stiffness constant. As discussed by Srivastava et al [2, 10,12], the analysis of the relaxed spectrum can be carried out using above equation, if the term in m_ϖ or the term in α_ϖ is negligible. It has been shown that relaxed spectrum is obtained for increasing value of N (number of domain walls within a grain of polycrystalline garnet sample) with increase in M_s (saturation magnetization). In order to understand the result it is necessary to calculate the equilibrium number of domain walls which can exist within a grain of diameter D. This can be obtained by minimizing the total energy consisting of the wall energy and the magneto-static energy. If there are (2n+1) walls within a sphere of diameter D, the ttal energy is given by:

$$\varpi = \frac{\pi D^2}{4}\left[(2n+1) - \frac{n(2n+1)}{3(n+1)}\right]\sigma_\varpi + \frac{1}{2(n+1)}\frac{1}{2}\left(\frac{4}{3}\pi M_s\right)\left(\frac{1}{6}\pi D^3 M_s\right)$$

Minimizing ϖ with respect to n, the total number of domain walls, N within a grain become:

$$N = (2n+1) = 2\left[\frac{\pi}{6}\frac{M_s^2 D}{\sigma_\varpi} - \frac{1}{4}\right]^{\frac{1}{2}} - 1 \qquad (1)$$

The condition for the formation of one domain wall is given by N=1which leads to a critical grain diameter $D=D_c$ given by:

$$D_c = \frac{30}{4\pi}\frac{\sigma_\varpi}{M_s^2} = 2.39\frac{\sigma_\varpi}{M_s^2}$$

Equation (1) suggests that the equilibrium number N of domain walls reduces almost linearly with M_s for a constant grain diameter provided σ_{ϖ} is constant. Thus, it is clear that as the value of M_s is increased the number of domain walls within the grain increases, while for small values of M_s, N would tend to one which would mean that there will be one domain wall. In this case closure domains cannot be formed. The possibility of formation of closure domains increases as the number of walls increases.

For the relaxed spectrum one can expect the inertial term to be insignificant as discussed earlier. This can occur when closure domains are present so that the domain wall can move without any inertia and with a constant velocity as soon as it is subjected to as external force. In such cases the low frequency permeability will be large, as in the present observation. On the other hand, if the domain wall is anchored at the grain boundary, as will be the case without closure domains, the inertial term will be significant, leading to a resonance type spectrum and small low frequency permeability. From this we conclude that the relaxed spectrum is obtained when the closure domains are present and resonance spectrum when there are no closure domains. Drofenik [13,14] has reported results that indicate that distances between pores account for variations in permeability. Samples with giant grains and included porosity owing to exaggerated grain growth still had higher permeabilities than those with normally grown grains provided the distance between pores were the same. Drofenik concludes that the large grained samples are less sensitive to grain

boundary effects and thus the μ(T) curve is more peaked (Figure 4.8.3). The observed flattering of μ(T) curve for x > 0.2 suggests reduction in grain size as evident from SEM analysis.

Finally, an attempt has been made to calculate the total number of domain walls, N within a grain and critical grain diameter D_c for which N reduces to 1, using following formulae [10]:

$$N = 2\left[\frac{\pi}{6}\frac{M_s^2.D}{\sigma_\varpi} - \frac{1}{4}\right]^{\frac{1}{2}} - 1$$

Here, the value of M_s= 334.83 emu/cm^3 and D = 10 μm for x = 0.1 composition and $\sigma_\varpi = 0.60$ erg/cm^2 are taken, therefore,

$$N = 2\left[\frac{3.14}{6}\frac{(334.83)^2(10 * 10^{-4} cm)}{0.60} - \frac{1}{4}\right]^{\frac{1}{2}} - 1$$

$$N = 2[97.79 - 0.25]^{\frac{1}{2}} - 1$$

$$N \sim 18.8$$

and $$Dc = 2.39\frac{\sigma_\varpi}{M_s^2}$$

$$Dc = 2.39\frac{0.60}{(334.83)^2} = 0.13\mu m$$

The value, N~18.8, is in agreement to those reported for relaxed type of permeability spectrum [10].

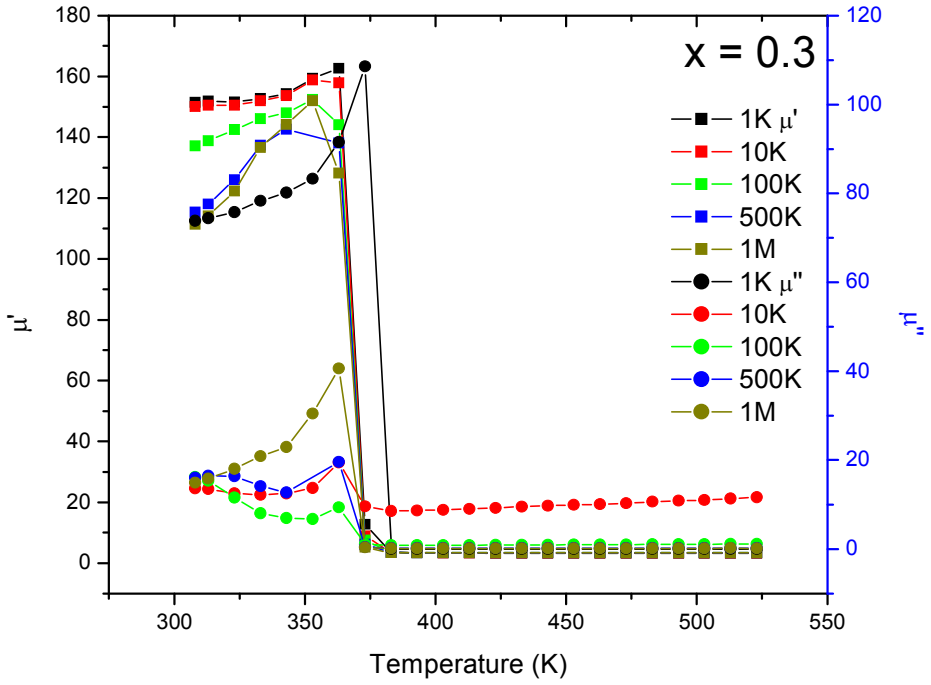
x = 0.3
1K μ'
10K
100K
500K
1M
1K μ"
10K
100K
500K
1M
μ'
μ"
Temperature (K)

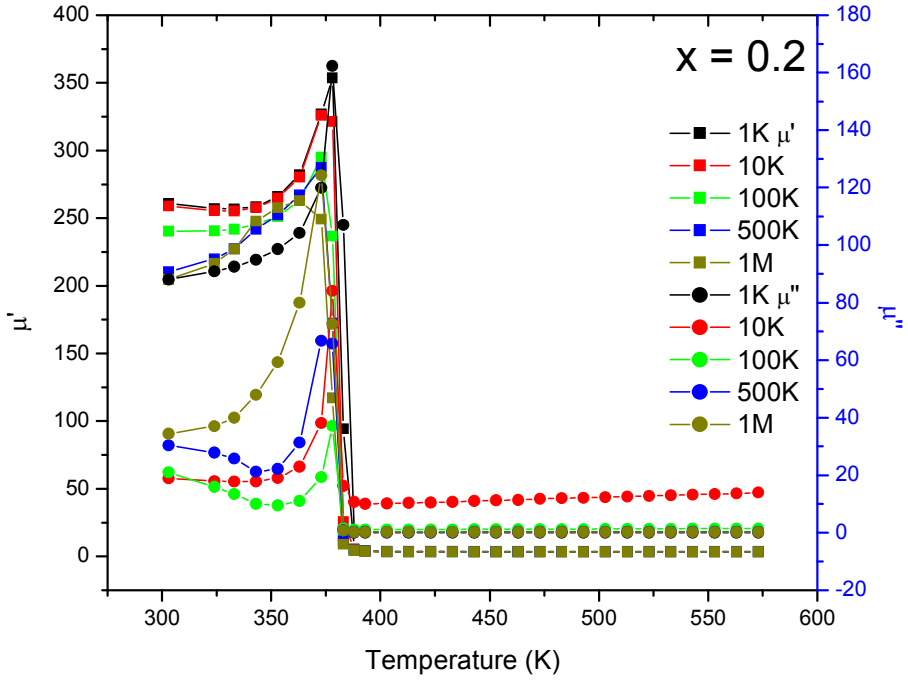
x = 0.2
1K μ'
10K
100K
500K
1M
1K μ"
10K
100K
500K
1M
μ'
μ"
Temperature (K)

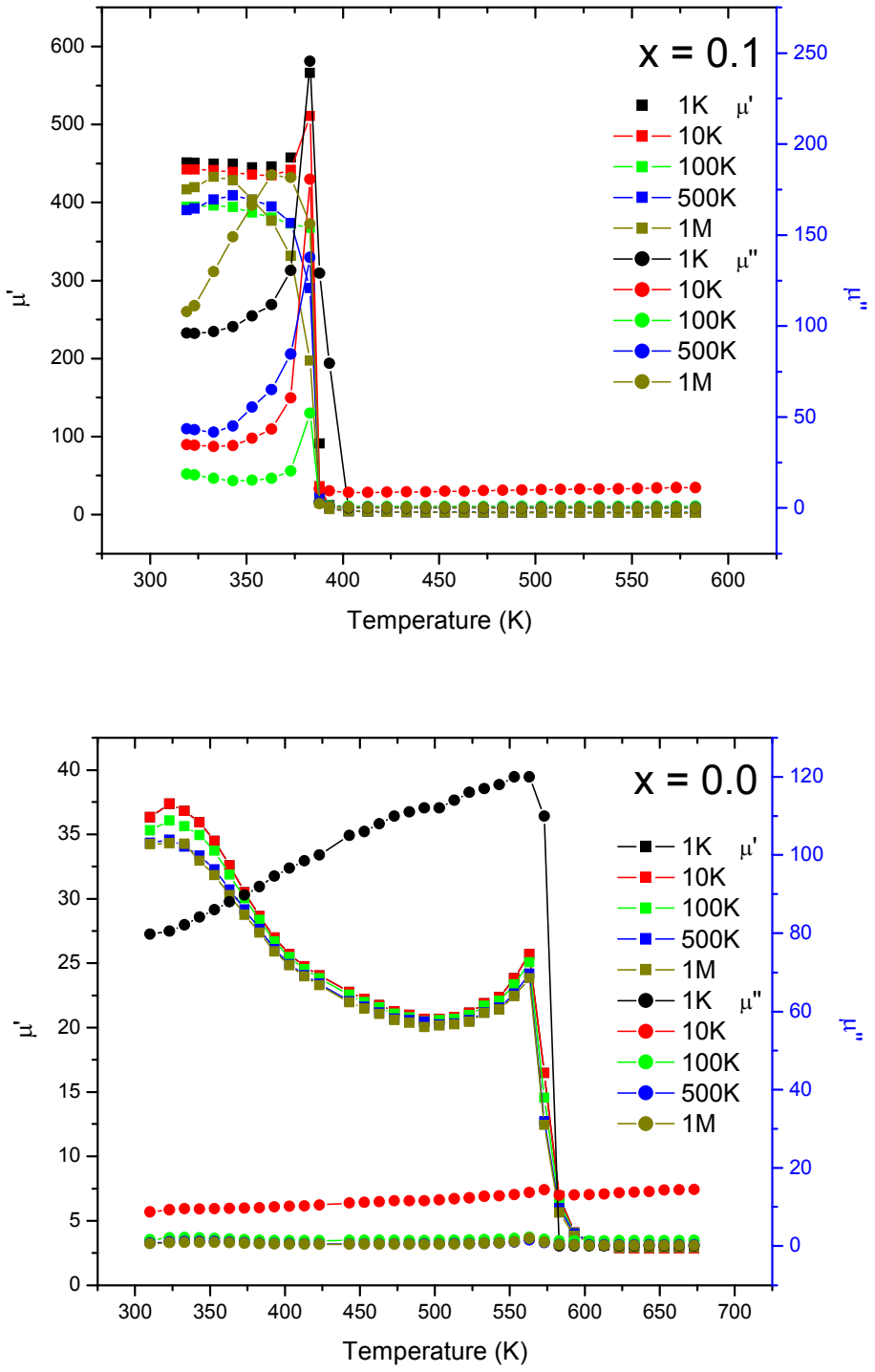

Figure 4.8.3 Thermal variation of real (μ') and imaginary (μ'') parts of permeability as a function of frequency for $Zn_{0.3}Mn_{0.7+x}Si_xFe_{2-2x}O_4$ system.

Temperature variation of initial permeability, μ', is shown in Figure 4.8.3. Increase in temperature of the samples with x = 0.1, 0.2 and 0.3, μ', initially increases gradually and then decreases rapidly. Near the transition temperature, T_p, μ' drops off sharply. The sharp drop in μ' during phase transition also suggests the single phase formation of all the substituted samples (x = 0.1,0.2 and 0.3). This fact is confirmed by X-ray diffraction pattern analysis. For the sample with x = 0.0, μ' increases slowly and drops off near T_p with tailing effect. Similar tailing effect due to paramagnetic contribution has been reported by Velenzulea et al [15]. In the present case these may be due to the presence of anti ferromagnetic α-Fe_2O_3 phase in $Zn_{0.3}Mn_{0.7}Fe_2O_4$ (x = 0.0) composition as evident from X-ray diffraction pattern analysis. The temperature at which μ' becomes zero is closed to Neel temperature (T_N) of that composition. The Neel temperatures determined from μ'(T) curves are in agreement with those determined form ac susceptibility measurements for substituted ferrites. Furthermore, the absence of an additional peak in μ' versus T curves suggest that there is no excess Fe^{2+} ion formation in the system [14].

In most of the magnetic materials, μ' increase with temperature upto the Neel temperature or Curie temperature, T_N. This is because the anisotropy field usually decreases faster with temperature than Ms [16] Both Enz [17] and Otha [18] have shown that the μ' is maximum at the temperature where the anisotropy constant K_1 changes sign. In our studies we have not observed any profound peaking in the μ'(T) variation for x = 0.3 composition. This may be because the rates of change of M_s and K_1 with temperature are nearly same. From the

thermal variation of μ'' it is seen that with the increase of temperature μ'' increases, reaches a maximum near T_N and then falls sharply near to T_N. The loss becomes large near to T_N, which may be due to the damping effect on the domain walls [19].

Illustrative calculations

Domain wall energy per unit area (σ_ω) is given by [10]: $\sigma_\omega = 2.36\frac{M_s^2.D}{\mu'-1}$

Here, for x = 0.1 composition, μ' = 444 at 300K (f = 10 kHz), grain diameters, D ~ 10μm saturation magnetization, Ms = $\rho_x.\sigma_s$ at 300K.

= 5.02 g.cm^3 * 66.7 emu/gm = 334.83 emu/cm^3

$$\sigma_\omega = \frac{2.36*(334.83)^2*10*10^{-4}}{444-1}$$

$$\sigma_\omega = 0.60\ \text{erg/cm}^2$$

Conclusions

The important findings are summarized as follows.

(i) The initial permeability decreases on Si^{4+} substituted for x = 0.1 – 0.3 compositions, mainly due to cumulative effect of reduction in saturation magnetization and grain size as well as segregation of SiO_2 at the grain boundaries.

(ii) The permeability dispersion curves for different compositions showing relaxed spectra due to presence of closure domains for large grains. It is

established that along with size of the grains, uniformity and homogeneity of the grains play an important role in deciding the nature of permeability spectrum.

(iii) Thermal variation of permeability study confirms single phase nature of substituted ferrites. The Neel temperature determined from $\mu'(T)$ curves are in agreement to those determined from ac susceptibilities measurements.

(iv) Highest value of permeability and saturation magnetization, reasonably high resistivity values and high Neel temperature for $Zn_{0.3}Mn_{0.8}Si_{0.1}Fe_{1.8}O_4$ (x= 0.1) composition suggest its suitability for high frequency applications.

References

1 Alex Goldman Alex 2006 “Modern ferrite technology”, 2nd edition, Springer, USA p.30-31.

2 G T. Rado, Rev. Mod. Phys. 25 (1953) 81.

3 J.P. Bouchaud and P.G. Zerah, 1990, J. Appl. Phys. 67 (1990) 5512.

4 T. Nakamura , J. Appl. Phys. 88(1) (2000) 348.

5 J.J. Went and H.P.J. Wijn, Phys. Rev. 82 (1951) 269.

6 H.G. Brion and Nemback, Phys. Stat. Sol. (a) 26 (1974) 559.

7 G.T. Rado and A. Terris, Phys. Rev. 83 (1951) 117.

8 A. Globus, Euro. Phys. Soc. Conf. on Soft Magnetic Mater. (Cardiff) (1995) 2.

9 A. Globus, Int. Conf. Ferrites 2, Bellevue, France, suppl. 70 J.Phys. (1976) c1-1.

10 Om Prakash, R. Aiyer and C.M. Srivastava, Mater. Sci. Bull. 1(1) (1979) 49.

11 J. Smit and H.P.J. Wijn 1959 Ferrites (NY: John Wiley) 27 (1959).

12 C.M. Srivastava , S.N.Shringi, R. Srivastava and G. Nanadikar 1976 Phys. Rev. B. 14 (1976) 2032.

13 M. Drofenik, S. Besenicar and M.Limpel, Advances in Ceramics 16 (1985) 229.

14 M. Drofenik, J. Am. Ceram. Soc. Bul. 65 (1986) 656.

15 R. Velenzulea, J.Mater. Sci. Lett. 15 (1980) 3173.

16 J. Smit “Magntic Properties of Materials” (McGraw Hill Book Company) (1971).

17 U. Enz, Proc. IEEE 109 (1962) 246.

18 K. Ohta, J.Phys. Soc. Jpn. 18 (1963) 685.

19 A.M. Sankpal, S.V. Kakatkar, N.D. Chaudari, R.S. Patil, S.R. Swant and S.S. Suryavanshi S S, J.Mat. Sci. 9 (1998) 173.

4.9 Compositional and thermal variation of two probe dc resistivity

It was observed from the Table 4.2.1 that the highest observed value of bulk density (ρ) remains lower than the corresponding x-ray density (ρ_x) of the material. This suggests that even highly pressed and sintered pellets contain pores. The presence of intragranular pores is not possible to avoid and they enter into the material through synthesis process. Therefore, a correction for pore fraction has to be applied to obtain the crystalline value of electrical resistivity. This has been done using the relation [1].

$$\rho_{dc} = \rho_p [1 + f(1+f^{2/3})^{-1}]^{-1}$$

where, ρ_{dc} is the zero porosity corrected value,ρ_p is the measured value of dc resistivity and $f = (1 - \rho/\rho_x)$ is the pore fraction. This equation seems to hold well for $f < 0.4$. In the system under investigation $Zn_{0.3}Mn_{0.7+x}Si_xFe_{2-2x}O_4$ (x = 0.0 – 0.3) 'f' is much less than 0.4 (Table 4.2.2).

The compositional dependence of dc resistivity (ρ_{dc}) values at 400K is shown in Table 4.9.1. It is found that the ρ_{dc} value shows random variation with Mn – Si content (x). In the present system magnetic Fe^{3+} ion is replaced by magnetic Mn^{2+} and non-magnetic Si^{4+} ions. The incorporation of Si^{4+} ions which do not participate in the conduction process limits the degree of Fe^{2+} - Fe^{3+} conduction that occurs. Thus, the resistivity is expected to increase with increase in Si^{4+} content (x) in the system, but this is not the case. The observed random

variation of ρ_{dc} with composition may be due to the random occupancy of Fe^{3+} ions and formation of Fe^{2+} ions at the octahedral (B-) sites of the spinel lattice.

According to the Maxwell-Wagner model and the Koop's theory [2,3] one character of ferrite microstructures is that the conduction grains are separated by the high resistive grain boundaries. To enhance the resistivity, the approach often adopted is doping of non magnetic impurities like CaO, SiO_2 and Nb_2O_3. Regarding SiO_2 , it is well studied and accepted fact that SiO_2 segregated at the grain boundaries and raise the resistance between the adjacent grains [4].

The electrical resistivity of Si^{4+} - substituted Mn – Zn ferrites is expected to increase by raising the electrical resistivity of the spinel matrix and grain boundary and also the reduction of grain size, which contributes to increasing the possibilities of intersection of the grain boundary with eddy current. Furthermore, it has been reported that when the sintering temperature is sufficiently high (> 1250^{o}C), some of the Si ions can diffuse into the grains. The concentration of Si ions at the grain boundary is about 5 – 10 times; as compared to that at inter grain [5]. On the other hand, Si concentration beyond a certain value not only enhances the sintering rate but also leading to intra grain pore filled microstructure [6] as observed in the present investigation (Figure 4.4.1).

Based on the above facts, now it is possible to explain compositional variation of dc resistivity (ρ_{ac}) for the substituted ferrites (x = 0.1, 0.2, 0.3) in the light of Si^{4+}- substitution in the system. Initially, for x = 0.1 and 0.2 compositions on Si^{4+}- substitution, majority of Si^{4+} ions reside at the grain boundaries and

hence increase the grain boundary resistivity. The segregations of Si^{4+} ions at the grain boundaries increases with increasing x for x = 0.1 to 0.2 and as a result dc resistivity increases with increase in Si^{4+} concentration (x). On the other hand, for x = 0.3 composition Si^{4+} concentration is beyond a particular limit as discussed earlier and hence enhances the sintering rate. Thus, large fraction of Si^{4+}- ions enters into the grain and thereby decreases the grain boundary resistivity. This in turn, result in low value of resistivity for x = 0.3 composition as compared to x = 0.1 and 0.2 compositions of $Zn_{0.3}Mn_{0.7+x}Si_xFe_{2-2x}O_4$ system.

The electrical resistivity as a function of temperature for the system $Zn_{0.3}Mn_{0.7+x}Si_xFe_{2-2x}O_4$ in the form of Arrhenius plots of $\log\rho$ versus $10^3/T$ are shown in Figure 4.9.1 for all the four compositions. It is observed that the resistivity values for a particular ferrite composition do not differ much from sample to sample as well as no significant difference in resistivity values during heating and cooling cycles occurs. All the samples show typical semiconducting behavior i.e. the resistivity decreases with increasing temperature. In general, the slope of $\log\rho$ versus $10^3/T$ curve changes at the Neel temperature. This anomaly strongly supports the influence of magnetic ordering upon the conduction process [7]. We have not observed such break or inflexion over the temperature range studied, indicating stable oxidation state of cations.

The temperature dependence of resistivity is given by the Arrhenius equation:

$$\rho = \rho_0 \exp(\Delta E/k_B T)$$

where, k_B is the Boltzmann constant (8.6 x 10^{-5} eV/K), ΔE is the activation energy and T is the absolute temperature. The activation energy for the different composition is calculated from the equation using the simplified relation:

$$\Delta E = 8.6 \times 10^{-5} * 2.303 \times 10^{3} * \text{slope}$$

$$\Delta E = 0.1981 * \text{slope}$$

The activation energy increases with increase in Mn-Si concentration (x) in the system (Table 4.9.1).

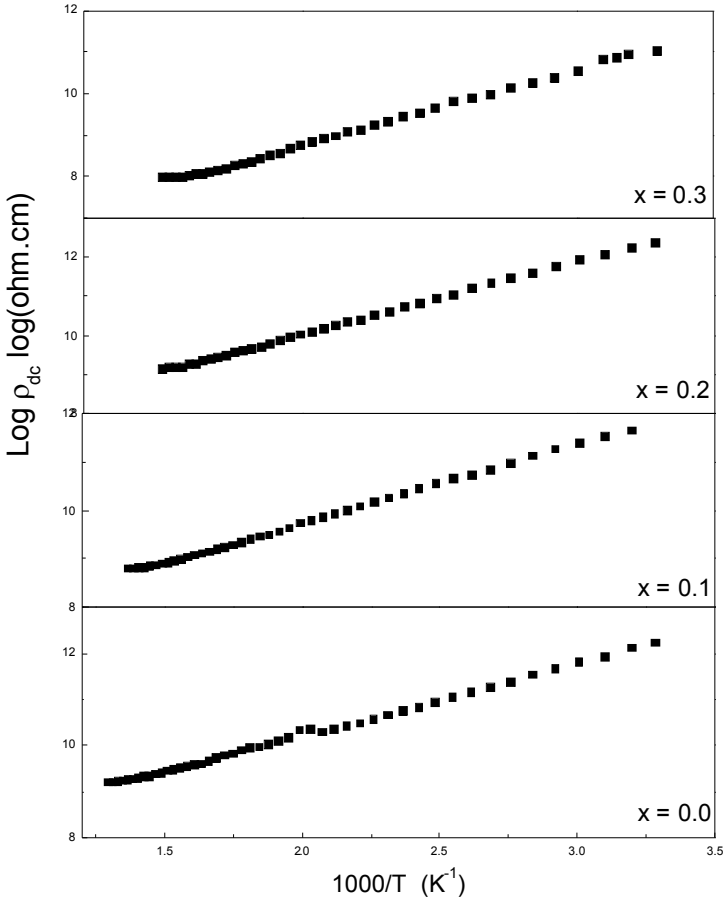

Figure 4.9.1 Electrical resistivity versus temperature for x = 0.0, 0.1, 0.2 and 0.3 compositions of $Zn_{0.3}Mn_{0.7+x}Si_xFe_{2-2x}O_4$ system.

The activation energy for all the four composition is much higher than the ionization energy of donors or accepters (i.e 0.1 eV) and thus one can rule out possibility of band type conduction. On the other hand, these values are smaller than the small polaron hopping energy (≥ 0.5 eV) but comparable with the electron transition energy (E_e = 0.2 eV). The energy needed for holes as the entity of charge carriers is of the order of ~ 1.5 eV. Thus, electron hopping between ferrous (Fe^{2+}) and ferric (Fe^{3+}) ions in the octahedral coordination of the spinel lattice is quite probable, given by: $Fe^{2+} \leftrightarrow Fe^{3+} + e^-$

The increase in the lattice constant value (Table 4.2.2) manifests itself as a increases in the inter-ionic distances and consequently a increase in barrier height encountered by the hopping charge carriers. Therefore, one can expect a increase in the activation energy with Mn – Si content (x).

The observed increase in the activation energy with Mn – Si substitution (x) in the system can be explained as follows. In the present case, the decrease in Fe^{3+} ion concentration from the system as well as from the octahedral (B – site) on Mn – Si substitution, results in an increase resistivity in general and activation energy values in particular. In other words, charge carrier jumps between differently charged ions of the same metal residing on equivalent crystallographic sites get restricted and as a result, activation energy increases with increasing (x).

Table 4.9.1 Resistivity (ρ) and activation energy (E_e) for $Zn_{0.3}Mn_{0.7+x}Si_xFe_{2-2x}O_4$ system.

Mn-Si content (x)	$\rho_{dc} * 10^5$ (Ohm.cm) (400K)	E_e (eV)
0.0	27.60	0.31
0.1	08.45	0.32
0.2	15.10	0.36
0.3	01.05	0.37

The activation energy is also influenced by the grain size. Bigger grain size implies increased grain to grain contact area for the charge carrier to flow and therefore, a lower barrier height. Since, in the present system grain size is found to decease with Mn – Si substitution (x), the activation energy is expected to increase. This explains the increase in the activation energy on Mn – Si substitution [8].

As already pointed out, the 'kink' as determined by the difference between the activation energies in the ferromagnetic and paramagnetic regions or change in slope of logρ versus reciprocal of temperature curve, will be large for cases in which there is a strong exchange interaction between the outer and inner electrons. The size of this kink can be smaller or larger in various ferrites, depending on their structural peculiarities and also on the value of electrical resistance. The earlier experiments have shown that the large kinks are characteristic of ferrites that have small specific resistance because in these materials the activation energy is comparable with the magnitude of the energy of the spontaneous magnetization that is 'released' as a result of magnetic transition [9].

In general, the high activation energy goes hand in hand with higher resistivity of the ferrite [10]. However, no such correlation has been observed, this may perhaps be attributed to the structural peculiarities of the ferrite specimens under investigation. The lower value of resistivity for x = 0.3 composition as compared to x = 0.1 and 0.2 compositions, may be due to oxygen vacancy conduction [11]. During high temperature sintering process, Zn^{2+} ions escape from the spinel structure due to its volatile nature, there by, creating anion vacancies.

Conclusions

In summary (i) all the ferrite compositions show normal semiconducting behavior as a function of temperature without any slope change in vicinity to the Neel temperature(ii) activation energy increases with increasing Mn – Si substitution and that is attributed to increase in lattice constant value, decrease in grain size and decrease in Fe^{3+} ion concentration from the B – site on increasing Mn – Si content in the system (iii) no correlation has been observed between the values of activation energy and electrical resistivity perhaps be attributed to the structural peculiarities of the ferrite materials under study. (iv) the compositional variation of dc resistivity value can be explain in the light of Si^{4+} substitution in the system.

References

1 H. W. Russel, J. Am. Ceram. Soc. 18 (1935) 1.

2 K. Wagner, Ann. phys. 40 (1913) 817.

3 C. Koops, Phys. Rev. 83 (1951) 121.

4 M. Han, D. Liang and L. Deng, Appl. Phys. lett. 90 (2007) 192507.

5 Y. Wu, Z.W. Li, L. Chen, S. J. Wang and C.K. Ong, J. Appl. Phys. 95(8) (2004) 4235.

6 G. S. N. Rao, O. F. Caltun, K. H. Rao, B. P. Rao,H. L. Wamocha and H H. Hamdeh, Hyper. Inter. 184 (2008) 179.

7 S. A. Mazen and B. A. Subrah, Thermochim Acta 105 (1986) 1.

8 V. K. Lakhani and K. B. Modi, J. Phys. D : Appl. Phys. 44 (2011) 245403.

9 D. Ravinder, J. Appl. Phys. 75(10) (1996) 6118.

10 J. Smit and H. P. J. Wijn, Ferrites, Philips Tech. Library Series (Cleaver Home, London) 1959) p. 234.

11 N. Sivakumar et al. J. Phys. D : Appl. Phys. 39 (2006) 4688.

4.10 Thermoelectric power study

(a) Temperature dependence of Seebeck coefficient

In order to understand the mechanisms responsible for electrical conduction, Seebeck coefficient measurements and Hall effect measurements are used. In the case of low mobility materials such as spinel ferrites, garnets and perovskites it may be difficult to measure the Hall effect. In such circumstances, the thermoelectric power measurement is the only alternative. The Seebeck coefficient measurement is straightforward and its sign gives vital information regarding the type of charge carriers (electrons or holes) responsible for the conduction process. It enables one to calculate the Fermi energy, charge carrier concentration, mobility of charge carrier etc. [1-4].

The values of Seebeck coefficient,α, ($=\Delta V/\Delta T$, ΔV = thermoelectric voltage, ΔT = temperature difference between hot and cold junctions) does not depend significantly upon heating and cooling cycles and we have obtained repeatable values within the accuracy of $\pm$10 % in successive observations. The variation of α with hot junction temperature (T) for the studied compositions is depicted in Figure 4.10.1.

The first observation suggests that for x = 0.0 0.1,0.2 and 0.3 compositions, α is negative . That means majority charge carriers are electrons or n-type conduction is dominant. According to Pankov et al [5], Mn-Zn ferrites prepared without special measures (synthesis in an oxygen atmosphere at an elevated pressure) contains oxygen vacancies, which lead to partial reduction of Fe^{3+} ion to Fe^{2+} ion in the system. The presence of Fe^{3+} in other oxidation state (

Fe^{2+} or Fe^{4+}) entails important modifications to the electrical properties of ferrties [5-7]. The hopping of electron between Fe^{2+} and Fe^{3+} at the octahedral sites of the spinel lattice takes place by the mechanism: $Fe^{2+} \leftrightarrow Fe^{3+} + e^{-}$.

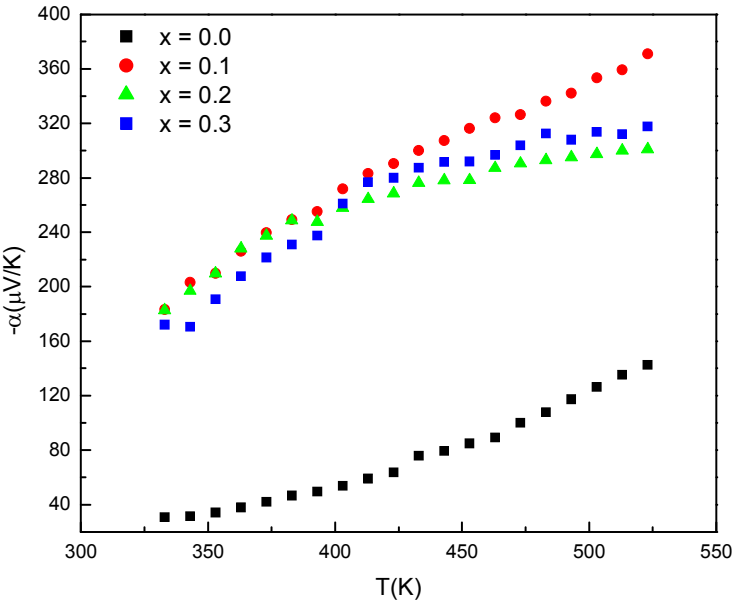

Figure 4.10.1 Thermoelectric power versus hot junction temperature for $Zn_{0.3}Mn_{0.7+x}Si_xFe_{2-2x}O_4$ system.

Based on the assumption that two hopping mechanisms are involved, the pre-dominance of one over the other depends upon the concentration of substituted cation (x) and temperature (T). If the electron exchange mechanism ($Fe^{2+} \leftrightarrow Fe^{3+} + e^{-}$) dominates to the hole exchange mechanism (Mn^{3+} -- $Mn^{2+} + e^{+}$) the spinel ferrite composition might conduct as a n-type semiconductor (or vice versa).

The second observation is that, Seebeck coefficient increases with increasing temperature for x = 0.0, 0.1, 0.2 and 0.3 compositions. Initially, Seebeck coefficient, α, increases rapidly within small range of temperature (300 - 425K) while for further increase in temperature α increases slowly. This

variation of α with temperature can be explained based on the fact that in the case of n-type semiconducting material the hot surface becomes positively charged, as it loses some of its electrons. The cold surface of the semiconductor becomes negatively charge due to the diffusion of free electrons from the hot portion. On increasing temperature, conduction mechanism $Fe^{2+} \leftrightarrow Fe^{3+} + e^{-}$ becomes more probable which generates electrons. These electrons are accumulating on the cold surface and as a result, potential difference (ΔV) developed increases α in the temperature range 300 - 424K. Further increases in temperature shows a small change in α conjuring (i) saturation in the electron generation, (ii) recombination of liberated electrons with holes, produced due to $Mn^{3+} \leftrightarrow Mn^{2+} + e^{+}$ transition in the system.

It is observe from Figure 4.10.1 that α in the temperature range studied is dependent upon temperature. On the basis of classifications suggested by Bashikiriv and Liberman [8], these ferrites are classified as non-degenerate semiconductor as Seebeck coefficient (α) is temperature dependent.

In the case of hopping conduction, the Seebeck coefficient (α) is given by the Heikes formula [9]:

$$\alpha = -\frac{k}{e}\left[\frac{S_T}{k} + \ln\frac{1-c}{c}\right]$$

where, S_T is the effective entropy transport by the charge carriers which is temperature independent. The S_T/k is generally very small in oxides / ferrites and it contributes less than 10 μV/K [10], thus neglected. Here, c is given by n/N,

where, N is the number of available states and n is the number of carriers in the states. Neglecting the term S_T/k from the above relation gives:

$$\alpha = -\frac{k}{e}\left[\ln\frac{1-c}{c}\right]$$

Doumerc et al [11] have derived a more general formula for systems containing mixed valency cations, M^{n+} / $M^{(n+1)+}$, accordingly:

$$\alpha = -\frac{k}{e}\ln\frac{1-c}{c} = \frac{k}{e}\ln\frac{1-c_h}{c_h}$$

where, c_h, the hole concentration (number of holes per active transport site) defined as $c_h = 1\text{-}c = p/N$ (p-number of holes).

Assuming that N is equal to the total number of Fe^{2+} and Fe^{3+} ions at the B-sites and n to the number of Fe^{3+} ions at this site , we obtain:

$$\alpha = -\frac{k}{e}\ln\left[\frac{Fe_B^{2+}}{Fe_B^{3+}}\right]$$

$$\left[\frac{Fe_B^{2+}}{Fe_B^{3+}}\right] = \exp\left(-\frac{\alpha\cdot e}{k}\right)$$

where, k is the Boltzmann constant and e is the electronic charge. Above equations contain no adjustable parameter and can be used to test various distribution models. This has been shown to be a suitable way for some spinels, such as ferrites [12, 13], magnetite [14], hausmannite [15] and manganite perovskites [4]. The subscripts A and B represent the tetrahedral sublattice and octahedral sublattice of the spinel structure respectively.

The ratio $(Fe_B^{2+})/Fe_B^{3+}$ can be obtained from the thermo electric power measurement, the estimation of ferrous ion (Fe^{2+}) concentration from the measurement is not straight forward and has not been attempted. The absolute concentration is typically obtained by wet-chemical analysis.

Illustrative calculations

x = 0.2, α = -257.95 μV/k at T = 403K.

$$\frac{(Fe_B^{2+})}{(Fe_B^{3+})} = \exp\left(-\frac{\alpha.e}{k}\right)$$

$$= \exp\left(-\frac{257.95*10^{-6}\,V/k*1.6*10^{-19}}{1.38*10^{23}}\right)$$

$$= \exp\left(-299.07*10^{-2}\right)$$

$$= \exp(-2.991)$$

$$\frac{(Fe_B^{2+})}{(Fe_B^{3+})} = 5.02*10^{-2}$$

$$\left[Fe_B^{2+}\right] = 2.033(wt\%)$$

$$= \frac{(Fe_B^{2+})}{(Fe_B^{3+})} * \frac{1}{2} \text{ concentration of } Fe^{3+} \text{ ion on the B-site}$$

$$* \text{atomic weight of Fe}(55.85\ amu)$$

Table 4.10.1 Seebeck coefficient (α) and cationic concentration for $Zn_{0.3}Mn_{0.7+x}Si_xFe_{2-2x}O_4$ system at 373K.

Mn-Si content (x)	α (μV/K) (373K)	$\frac{(Fe_B^{2+})}{(Fe_B^{3+})}10^{-2}$	$(Fe_B^{2+})(wt\%)$	$(Fe_B^{2+})(Fe_B^{3+})*10^{-1}$	$E_F(0)$ (0K) (eV)
0.0	-41.9	61.52	28.35	6.43	0.170
0.1	-239.6	6.22	2.74	1.34	0.174
0.2	-237.3	6.38	2.58	1.22	0.156
0.3	-221.3	7.68	2.88	1.24	0.168

The high temperature (373K) Seebeck coefficient values, have been used to determine the relative concentration of Fe^{2+}/Fe^{3+}, the absolute concentration of Fe^{2+} ion, and the product of (Fe^{2+}) (Fe^{3+}) ions residing at the B- sites of the spinel lattice (Table 4.10.1). This is further used to determine the actual cation distribution and oxygen deficiency (δ) for each composition and are summarized in Table 4.10.1. These are used to explain the variation and origin of dc resistivity with Mn-Si content (x).

Table 4.10.2 Cation distribution and oxygen deficiency (δ) for $Zn_{0.3}Mn_{0.7+x}Si_xFe_{2-2x}O_4$ system.

Mn-Si content (x)	Actual cation distribution	Oxygen deficiency (δ)
0.0	$(Zn^{+2}_{0.25}Mn^{+2}_{0.40}Fe^{+3}_{0.35})[Zn^{+2}_{0.05}Mn^{+2}_{0.30}Fe^{+3}_{1.02}Fe^{+2}_{0.63}]O_{3.68}$	0.32
0.1	$(Zn^{+2}_{0.25}Si^{+4}_{0.10}Mn^{+2}_{0.43}Fe^{+3}_{0.22})[Zn^{+2}_{0.05}Mn^{+2}_{0.37}\ Fe^{+3}_{1.49}Fe^{+2}_{0.09}]O_{3.95}$	0.05
0.2	$(Zn^{+2}_{0.25}Si^{+4}_{0.15}Mn^{+2}_{0.45}Fe^{+3}_{0.15})[Zn^{+2}_{0.05}Si^{+4}_{0.05}Mn^{+2}_{0.45}\ Fe^{+3}_{1.36}Fe^{+2}_{0.09}]\ O_{3.95}$	0.05
0.3	$(Zn^{+2}_{0.25}Si^{+4}_{0.21}Mn^{+2}_{0.48}Fe^{+3}_{0.06})[Zn^{+2}_{0.05}Si^{+4}_{0.09}Mn^{+2}_{0.52}\ Fe^{+3}_{1.24}Fe^{+2}_{0.10}]\ O_{3.95}$	0.05

The percentage variation of the Fe^{2+} - concentration and the product of $(Fe^{2+})(Fe^{3+})$ ions on the B-sites for the substituted compositions is ~ 10%. This means that, the variation of electrical resistivity cannot exceed by 10%, if the variation originates from the change in these two parameters.

(a) Fermi energy determination

The energy corresponding to the highest filled state in energy band structure of solids at 0K is called the Fermi energy, $E_F(0)$. An attempt has been made to determine $E_F(0)$ by extrapolating values of E_F (T) to 0K. According to Bosman

and Crevecoem et al [16], in the region where conduction is due to either holes or electrons (not both), the relation between α and E_F is given by:

$$E_F\,(T) = e\alpha T - AkT$$

where, e, k and T are charge of carrier, Boltzmann constant (1.38×10^{-23} J/K = 8.62×10^{-5} eV/K) and hot junction temperature in Kelvin, respectively. Here, A is a dimension-less constant connected with the kinetic energy of charge carrier. The plots of thermal variation of E_F for two values of A, (A = 0 and 2), for the compositions with x = 0.0, 0.1, 0.2 and 0.3 compositions are shown in Figure 4.10.2. The extrapolation of the two series of E_F for A = 0 and A=2 intercept at one point on y-axis at T = 0K. The values of E_F (T) extrapolated to 0K yield the value of $E_F(0)$ (Table 4.10.1). The interception point lies below zero (negative value), but we have to consider its magnitude only, as E_F (0) cannot be negative [17].

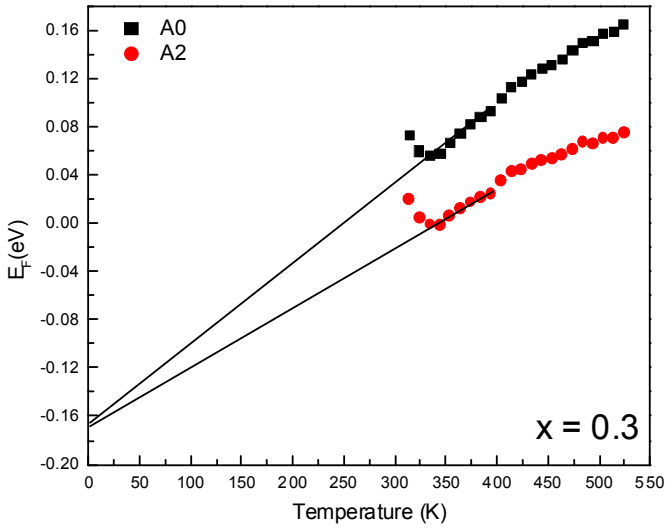

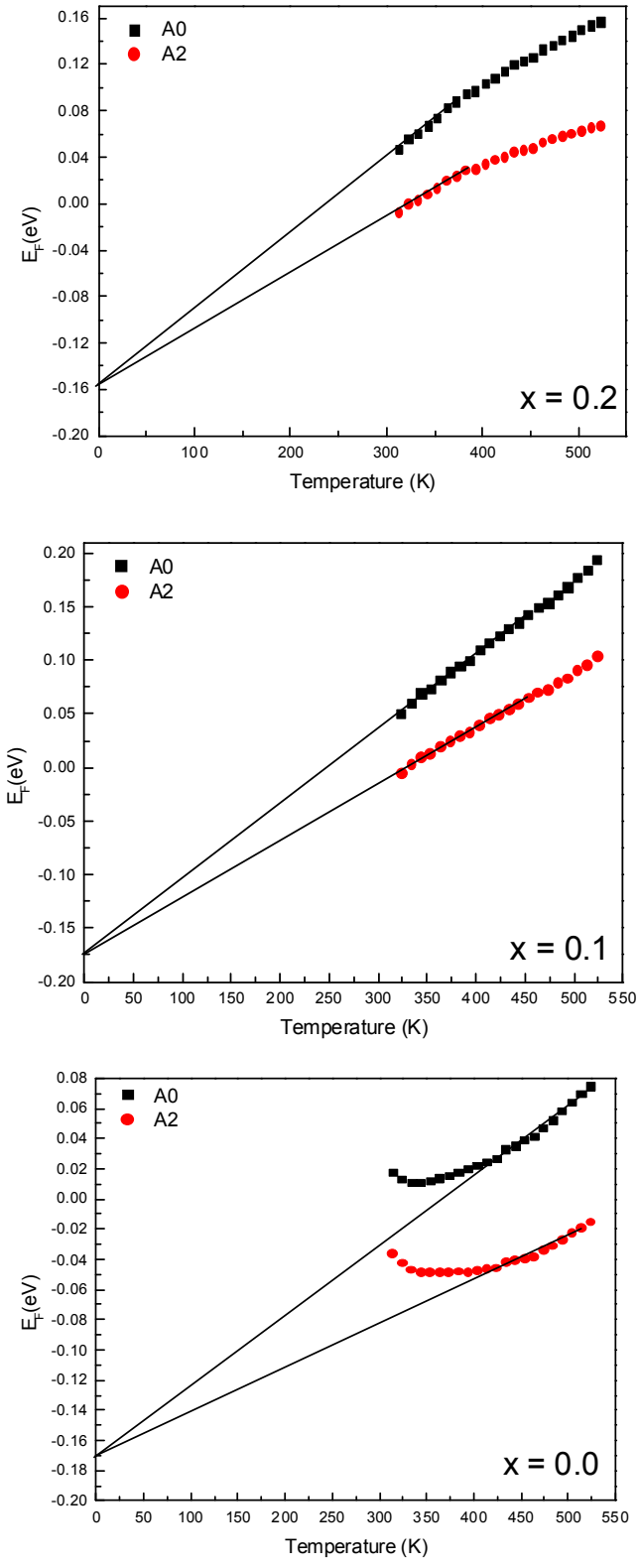

Figure 4.10.2. Variation of Fermi energy with temperature for $Zn_{0.3}Mn_{0.7+x}Si_xFe_{2-2x}O_4$ system.

Table 4.10.1 shows the values of $E_F(0)$ for the different compositions. It is seen that $E_F(0)$ remains constant for all the ferrite compositions. Such behavior of $E_F(0)$ can be attributed to the contribution of Fe^{2+} in the system.

Conclusions

(i) The compositions under investigation are non-degenerate semiconductors.

(ii) The dominant conduction mechanism is electron exchange between Fe^{2+} and Fe^{3+} ions at the octahedral; (B-) site of the spinel lattice.

(iii) The ratio Fe^{2+}/Fe^{3+}, absolute concentration of Fe^{2+} and Fe^{3+} as well as oxygen deficiency can be determined from Seebeck coefficient measurement.

(iv) Fermi energy remains constant for all the compositions, attributed to the contribution of Fe^{2+} ion in the system.

References

1 S. A. Mazen and H. M. Zaki, J. Magn. Magn. Mater. 248 (2002) 200 and references there in.

2 S. A. Mazen and A. Ifalaky, J. Magn. Magn. Mater. 195 (1999) 148.

3 V. K. Lakhani, P. U. Sharma, K. G. Saija, K. B. Zankat and K. B. Modi Ind. J. Phys. 80(8) (2006) 789.

4 J. J. U. Buch, T. K. Pathak, V. K. Lakhani, N. H. Vasoya and K. B. Modi, J. Phys. D: Appl. Phys. 40 (2007) 5306.

5 M. I. Ivanovskaya, A. I. Tolstik, D. A. Kotsikau and V. V. Pankov, Russ. J. Phys. Chem. A., 83(12) (2009) 2081.

6 A. A. Mazen, Mater. Chem. Phys. 62 (2) (2003) 131.

7 S. A. Mazen, A. Elfalaky and H. A. Hashem, Appl. Phys. A. 61 (5) (1995) 557.

8 S. A. Bashikirov, A. B. Liberman and V. V. Parfenov, Inorg. Mater. 15 (1979) 404.

9 R. R. Heikes, in Thermoelectricity eds., R. R. Heikes and R. W. Ure 45 (1961) (NY: Wiley Interscience)

10 J. B. Goodenough, Prog. Solid State Chem. 5 (1971) 145.

11 J. P. Doumerc, J. Solid State Chem. 109(2) (1994) 419.

12 J. Topfer, A. Feltz, P. Dordor and J. P. Doumerc, Mater. Res. Bull. 29 (1994) 225.

13 N. H. Vasoya, V. K. Lakhani, P. U. Sharma, K. B. Modi, Ravi Kumar and H. H. Joshi, J. Phys: Condens. Mater. 18 (2006) 8063.

14 C. C. Wu and T. O. Mason, J. Am. Ceram. Soc. 64 (1981) 520.

15 S. E. Dorris and T. O. Mason, J. Am. Ceram. Soc. 71 (1988) 379.

16 A. J. Bosman and C. Crevecoeur
Phys. Rev. 144 (1966) 763.

17 F. J. Morin, Phys. Rev., 93 (1954) 1199.

4.11(a) CCNR type high field instability study in Mn-Si substituted Mn-Zn ferrites.

Introduction

Current (I) versus voltage (V) characteristic of any materials in low applied electric field region is Ohmic (linear) due to the presence of thermally generated charge carriers. In most metallic materials, with increasing field I-V behavior becomes non linear (non-Ohmic). The current rises rapidly with voltage. Taking the form of a power relation or exponential dependence on voltage prior to electronic or thermal breakdown called electrical switching of the material. If the high resistivity material in the form of thin film sandwiched between suitable metal electrodes, than the I-V characteristic shows largely reproducible and reversible unstable conduction regions before the ultimate irreversible breakdown of the sandwich material occurs. In general, there are three unstable conduction regions, where conductivity switches from one state to another state via unstable regions. The switching phenomena are of three types (i) Voltage controlled negative resistance (VCNR) or N-type (ii) Current controlled negative resistance (CCNR) or S-type (iii) bi stable or memory switching.

Switching and memory properties exhibited by thin oxide films and other semi insulating materials in sandwich configuration are of considerable interest to the digital computers, data processing circuits, and microelectronic industries. The forming process, incubation time before switching, the dependence of voltage on geometry and temperature of CCNR devices, presence of regenerative negative resistance region are some of the limiting and undesirable

features in the switching devices. In spite of these limitations it is possible to produce long life, reproducible, radiation insensitive, slow switching device from thin oxide films.

A large number of oxides and semiconducting materials exhibit similar conduction phenomenon at high electric field. In all such cases, the space charge limited (SCL) flow trapping and recombination process play an important role. However, the high field transport properties are poorly understood. The detailed study must involve the structure changes, forming process, incubation period, field dependent conductivity, electron emission, photo response and electro luminance effects

Yamashiro [1] was the first to report the electrical switching phenomenon in polycrystalline, stoichiometric, bulk copper ferrite, $CuFe_2O_4$. Similar anomalous electrical transport and switching action in lithium ferrite, $Li_{0.5}Fe_{2.5}O_4$, is reported by Histake et al [2] and in Mg-Mn ferrites, single crystalline Si-doped yttrium iron garnet,$Y_3Fe_5O_{12}$ and Ti-doped yttrium ortho ferrite ($YFeO_3$) have been reported by Kaplan et al [3]. Later on, such electrical breakdown has been reported for the various spinel ferrite compositions and systems. Switching phenomenon in the case of non-stoichiometric $CuFe_2O_4$, and thermally treated $CuFe_2O_4$ has been reported by Patil et al [4] and Vainganker et al [5] respectively. This phenomenon in the $Cu_{1-x}Zn_xFe_2O_4$ (x = 0.0 – 1.0), $Cd_xCu_{1-x}Fe_2O_4$ (x = 0.0,0.2,0.40.6,0.8 and 1.0), $Cd_xCo_{1-x}Fe_{2-y}Cr_yO_4$ (x = 0.0, 0.25,0.50, 0.75 and 1.0; y = 0.0, 0.15,0.30) spinel ferrite systems has been investigated by different workers [6-8]. We have observed such high electric field induced resistance switching in multi catonic

bulk ferrite systems: $Zn_xCo_{1-x}FeAlO_4$ [9] and $Zn_{0.3}Mn_{0.7+x}$ $Ti_xFe_{1.9-2x}Al_{0.1}O_4$ [10]. Recently, CCNR type high field instability has been reported for nanocrystalline Al^{3+}- substituted $NiFe_2O_4$ and Cr^{3+}- substituted $NiFe_2O_4$ spinel ferrite systems prepared by the chemical co-precipitation route [11,12]. Very recently, we have reported resistive switching phenomenon in $Cd_{0.25}Co_{0.75}Fe_2O_4$ ferrite thin film [13]. On the other hand, electrode dependent resistive switching in Ca-doped ceramic bismuth ferrite, $Bi_{0.9}Ca_{0.1}Fe_2O_4$, has been reported by Levy et al [14,15]. They have found that the appearance of the effect is dependent on the fabrication procedure of the metallic electrode.

The reversible and non-volatile change of the materials resistance on the application of pulsed electrical stimulus i.e. voltage or current is known as restive switching (RS)[14,15].

Electric Pulse Induced Resistive (EPIR) switching phenomena observed in some oxide compounds has opened up new horizons for potentially most viable alternative to non-volatile memory devices [17]. The mono-stable threshold switching and the bi-stable memory switching of current-controlled negative resistance (CCNR) between high-resistance state (OFF state) and low resistance state (ON state) were originally reported and investigated in thin films of chalcogenide semiconductors, ZnSe–Ge heterostructures [18,19]. The memory behavior of oxides, based on current-induced bi stable resistance effects or voltage-controlled negative resistance phenomena, as observed in compounds such as Nb_2O_5, MnO_2, ZnO, ZrO_2, TiO_2, Ta_2O_5, NiO etc. has been studied in all oxide thin-film heterostructures involving ferroelectrics and simple metal–

insulator–metal (MIM) structures [20-23]. More recently, the observation of room-temperature resistive switching driven by electric fields in various perovskite oxides such as Cr doped $SrTiO_3$ [24] and manganite $Pr_{0.7}Ca_{0.3}MnO_3$ [25] has triggered a lot of interests due to the their potential use for nonvolatile resistance random access memory (RRAM) applications. The latter showed memory retention times exceeding 18 months. Several models based on either the bulk or the interfaces effect, such as the Schottky barrier model, the filamentary model, the space charge limited current model, and the model involving the dislocations from oxygen content, have been proposed, although these mechanisms cannot fully explain the universal resistance switching behaviors [26-30]. In addition, several obstacles, such as the compatibility to modern semiconductor processes, the uniformity of memory behavior, and the retention property of RRAM devices need to be overcome before potential device applications can be considered. There is therefore a growing need to explore new oxides for RRAM applications.

Keeping in mind the latest developments and growing interests in the resistance switching in mixed oxides, we have tried to revisit the classic ferrite system to understand the high field instability causing resistance switching in multi cationic spinel ferrite system: $Zn_{0.3}Mn_{0.7+x}Si_xFe_{2-2x}O_4$ (x = 0.0, 0.1, 0.2 and 0.3)

The plots of current (I) versus electric field (E), rather than current versus voltage, for these samples are presented in Figure 4.11(a).1, which makes it easy to compare the I-V characteristics of the samples of different thickness at a

glance. It is evident from the figure that for the compositions with x = 0.0 and 0.1 compositions switching was recorded at T $\geq$ 373K and T $\geq$ 323K respectively for x = 0.2 and 0.3 compositions, it was recorded at T $\geq$ 473K and T $\geq$ 523K, respectively. It is found that for the substituted ferrites (x = 0.1, 0.2 and 0.3), the electric field (E) required and temperature (T_s) at which switching action takes place increase with increasing Mn-Si concentration (x) in the system. According to Vaingankar et al [5], it has been suggested that switching is a structure sensitive phenomenon [5]. This is in accordance with the subsequent increase in the unit cell dimension (Table 4.2.2).

From the Figure 4.11(a).1 one can see the nature of the switching phenomenon in the ferrite compositions. The deviation from the Ohm's law becomes more prominent with increase of voltage across the sample when the electric field is just over the value indicated by 'A' in figure. For the first cycle, the breakdown suddenly occurs and field falls to the value indicated by B, denoted as the first breakdown field; after this, the current increases monotonically, from B to C. Average resistance switching ratio (R_{high}/R_{low}) estimated for different compositions is better than 200% (Figure 4.11(a).1) at the corresponding switching temperature (T_s).

The average ON state current is found to be ~ 179 mA for different compositions and different temperatures. Further, the switching properties of the samples were found to be unaltered even when the cycle was repeated after two weeks. Thus, indicating there is no 'ageing effect' in these ferrites. The ferrite

samples were subjected to a second cycle of switching, which was run immediately after the first cycle. For these samples, it was found that the smaller field was required for breakdown to occur, leading to Joule-self heating during electrical switching.

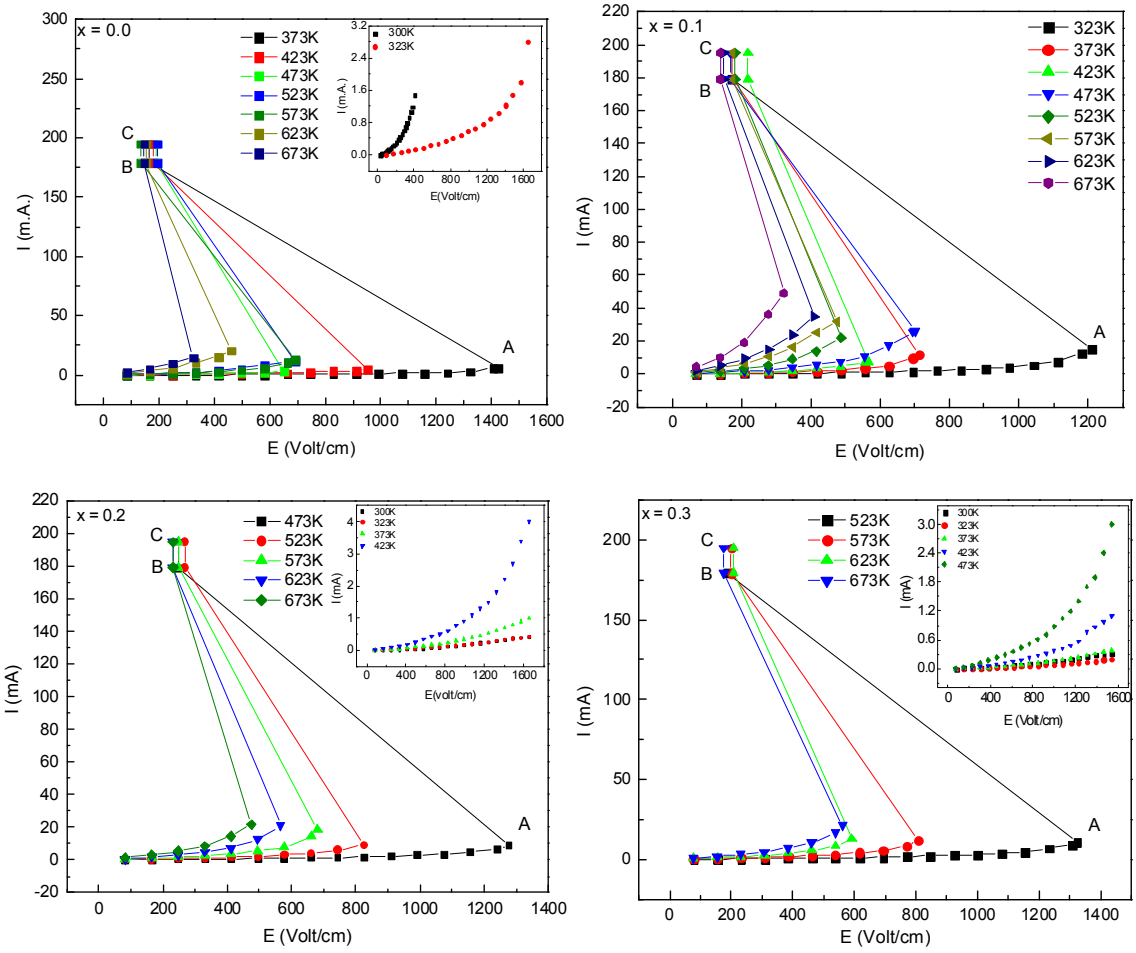

Figure 4.11(a).1. Temperature dependent I-E relationship for x = 0.0, 0.1, 0.2 and 0.3 compositions.

In the view of the fact that many different systems exhibit this phenomenon, it will be rather difficult to point out any particular property as being the cause of electrical switching and it may be different for different systems. In

general, systems with Jahn-Teller ions like Cu^{2+} and Mn^{3+} are probable candidates for switching action [15]. The system under investigation is a Jahn-Teller ion free system, thus this phenomenon cannot be attributed to Jahn-Teller ions as suggested by Yamashiro et al [1]. The structural transformation observed by Vaingankar et al [5] also cannot be accepted as the general cause of the phenomenon as neither of these compositions exhibited any structural transformation at any temperature, which otherwise, would have been reflected in temperature dependence dc resistivity measurements. The oxygen deficiency which is common to such ferrites, as also the inherent non-stoichiometry with respect to zinc, as it is volatile in nature, should also be taken in to consideration. This possibility is less probable as ratify by EDAX.

Table 4.11(a).1. Electric field strength (E) and temperature for switching (T_S) for x = 0.0 – 0.3 compositions.

Mn-Si content (x)	E (V/cm)	(T_s(K))
0.0	1416	373
0.1	1208	323
0.2	1276	473
0.3	1321	523

The formation of Jahn-Teller, Mn^{3+} ions, from Mn^{2+} is quite probable in such systems and at the same time formation of equivalent amount of Fe^{2+} ions is expected in order to maintain charge neutrality. If switching, in the present case is attributed to the existence of Jahn-Teller Mn^{3+} ion in the system, the required electric field and temperature should decrease with increase in Mn-Si

concentration (x), but this is not the case. Furthermore, our thermo electric power measurements have shown that the compositions under investigation are electronic conductors. Thus switching due to co-operative Jahn-Teller distortion transformation does not appear to be tenable. From the cation distribution formulae (Table 4.2.3), it is clear that increasing the Mn-Si content (x), reduced the Fe^{3+} ion concentrations from the B-site and the system itself; this limits the electron exchange between $Fe^{3+} \Leftrightarrow Fe^{2+}$ ions, and as a result, the required electric field and temperature increases. Further, the switching action may also be caused by space charge limiting current (SCLC) in the system. There is a possibility, according to band theory of insulators, that the additional carriers are injected by metal electrode, through the metal insulator contact. The log I versus log V plot of Figure 4.11(a).2 can be fitted well with lines that have a slope of 1.8 to 2.8, which indicates that the conduction mechanism in the high resistance state is static induction current (SIC) or the space charge limited current (SCLC) type. In SCLC through insulating layers, a large current increase occurs when trapping sites in the insulating bulk are fully occupied at a threshold voltage, V_T. Typically, V_T is beyond 200 V in the initial process of resistance switching in our system. Above the threshold voltage, current abruptly increases as can be seen in Figure 4.11(a).1. This drastic increase in current may be induced by trap-charge space charge limiting current (TC-SCLC). Thus, when the density of thermally generated free carriers inside the system is greater than that of the injected charge carriers, Ohmic (I α V) behavior is observed. Thus as can be inspected by graphs of log I versus log V (Figure 4.11(a).2) which show that at

low voltage current obeys Ohm's law and at breakdown voltage the slope of this curve increases, indicating existence of SCL currents which could be cited as the possible cause of electrical switching in the present system [31,32]. This is also an essential feature of CCNR –type of electrical switching.

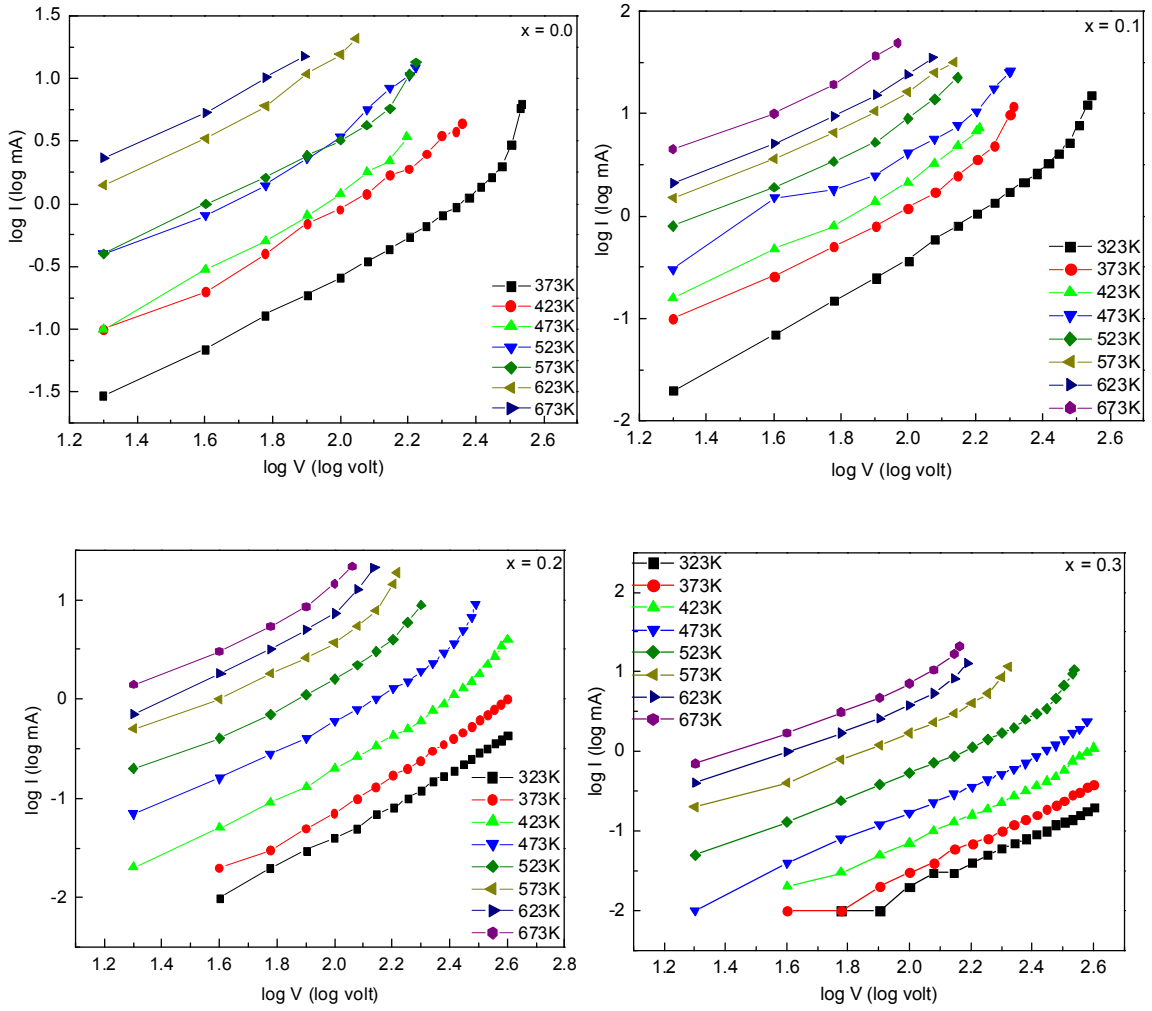

Figure 4.11(a).2 Temperature dependent Log I versus Log V characteristics of $Zn_{0.3}Mn_{0.7+x}Si_xFe_{2-2x}O_4$ ferrites.

Finally, the nature of the I-V characteristics exhibit slow switching which can be thought of due to current controlled negative resistance (CCNR) type,

while fast switching can only be expected with voltage controlled negative resistance (VCNR) type. The I-E characteristics which are exhibited by this ferrite system is very similar to the switching action of thyristor which is three junction, four layer diode. The phenomenon is observed in all the compositions of the series irrespective of ferrimagnetic or paramagnetic in nature. These experimental results are important as they will lead to development of electrical field induced resistance switching devices, viz. non-volatile memory.

Conclusions

Reproducible high electric field induced resistance switching in bulk spinel ferrite, $Zn_{0.3}Mn_{0.7+x}Si_xFe_{2-2x}O_4$ (x = 0.0 -0.3) system has been investigated. Both, temperature and composition dependence of electric field induced resistance instability showed as high as 200% resistance switching ratio at corresponding temperature of switching. The important findings are summarized as:

(i) Though none of the models can satisfactorily explain the electrical switching in the present system, the existence of SCL-current could be possible cause of switching phenomenon.

(ii) The increase in electric field and temperature required for switching is found to increase with increasing Mn-Si content (x) is due to the subsequent increase in the lattice dimension and reduction in Fe^{3+} ion concentrations from the octahedral (B-) site.

(iii) The switching phenomenon observed for all the compositions is CCNR- type.

References

1 T. Yamashiro, Jpn. J. Appl. Phys. 12 (1973) 148.

2 K. Histake, K. Nakayama and K. Ohta, Jpn. J. Appl. Phys. 12 (1973) 1116.

3 J. Kaplan, D. C. Bullock, D. Adler, and D. J. Epestein ,
Appl. Phys. Lett. 20 (1972) 439.

4 S. A. Patil, B. K. Chougule and R. N. Patil, Proceedings of Nuclear Physics & Solid State Phys. Symposium, Calcutta, Vol. 18C (1975) 134.

5 A. S. Vaingankar, S. A. Patil, M. M. Todkar, A. Y. Khot, and V. B. Devale, Proceedings of Symposium on Nuclear Physics and Solid State Physics, New Delhi, Vol. 23C (1980) p. 250, Department of Atomic Energy, India.

6 S. R. Sawant and R. N. Patil, Ind. J. Phys. 56A (1982) 233.

7 A. S. Vaingankar, P. N. Kamble and V. R. Kulkarni, Ind. J. Pure Appl. Phys. 28 91990) 508.

8 P. N. Vasambekar, C. B. Kolekar and A. S. Vaingankar, Mater. Res. Bull. 34 (2009) 165402.

9 N. H. Vasoya, V. K. Lakhani , P. U. Sharma , K. B. Modi, Ravi Kumar and H. H. Joshi, J. Phys. Cond. Matter. 18 (2006) 8063.

10 K. G. Saija, U. S. Joshi, V. K. Lakhani and K. B. Modi
J. Phys. D. : Appl. Phys., 42 (2009) 165402.

11 S. M. Patange, S. E. Shrsath, K. S. Lohar, S. S. Jadhav, N. Kulkarni and K. M. Jadhav, Physica B, 406 (2011) 663.

12 S.M. Patange, Sagar E. Shirsath, S.S. Jadhav, K.S. Lohar, D.R. Mane and K.M. Jadhav, Mater. Lett., 64 (2010) 722.

13 U. V. Chhaya, B. V. Mistry, K. H. Bhavsar, M. R. Gadhvi, V. K. Lakhani, K. B. Modi and U. S. Joshi., Ind. J. Pure Appl. Phys., 499 (2011) 833.

14 D. Rubi, F. G. Marlasca, M. Reinoso, P. Bonville and P. Levy, Mater. Sci. Engg. B. 177 (2012) 471 and references therein.

15 D. Rubi, F. G. Marlasca, P. Bonville, D. Colson and P. Levy, Physica B doi.:10.1016/physb.2011.12.048

16 L. M. Kukreja, A. K. Das and L. Mishra, Bull. Mater. Sci., 32 (2009) 247.

17 A. Sawa, Materials Today 11 (2008) 28.

18 S. R. Ovshinsky, Phys. Rev. Lett. 21 (1968) 1450.

19 H. J. Hovel and J. J. Urgell, J. Appl. Phys. 42 (1971) 5076.

20 W. R. Hiatt and T. W. Hickmott, Appl. Phys. Lett. 6 (1965) 106.

21 F. Argall Solid-State Electron. 11 (1968) 535.

22 S. Seo, M. J. Lee, D. H. Seo, E. J. Jeoung, D. S. Suh, Y. S. Joung, I. K. Yoo, I. S. Byun, I. R. Hwang, S. H. Kim, I. S. Byun, J. S. Kim, J. S. Choi and B. H. Park, Appl. Phys. Lett. 85 (2004) 5655.

23 J. Joshua, M. D. Pickett, X. Li, D. A. A. Ohlberg, D. R. Stewart and R. S. Williams, Nature Nanotechnology, 2 (2008) 1.

24 Y. Watanabe, J. G. Bedonorz, A. Bietsch, C. H. Gwrber , D. Widmer, A. Beck and S. J. Wind, Appl. Phys. Lett. 78 (2001) 3738.

25 S. Q. Liu, N. J. Wu, and A. Ignatiev, Appl. Phys. Lett. 76 (2000) 2749.

26 H. Inoue, S. Yasuda, H. Akinaga, and H. Takagi, Phys. Rev. B 77 (2008) 035105.

27 N. Das, S. Tsui, Y. Y. Xue, Y. Q. Wang, and C. W. Chu, Phys. Rev. B 78 (2008) 235418.

28 Y. R. Nian, J. Strozier, N. J. Wu, X. Chen and A. Ignatiev, Phys. Rev. Lett. 98 (2007) 146403.

29 U. S. Joshi, S. J. Trivedi, K. H. Bhavsar, U. N. Trivedi, S. A. Khan and D. K. Avasthi, J. Appl. Phys. 105 (2009) 073704.

30 A. Baikalov, Y. Q. Wang, B. Shen, B. Lorenz, S. Tsui, Y. Y. Sun, Y. Y. Xue, and C. W. Chu, Appl. Phys. Lett. 83 (2003) 957.

31 S. M. Sze and K. K. Ng, Physics of Semiconductors Devices 3rd Ed., Wiley (India) (2008) pp 586.

32 M. S. Sagare, A. S. Vaingankar and S. G. Kulkarni, (1997) J. Phys. IV France 7 C1-157 Colloque C1, Supplement au Journal de Physique III de mars .

4.11(b) Structural, micro structural and I-V characteristic study on $Zn_{0.3}Mn_{0.8}Si_{0.1}Fe_{1.8}O_4$ ferrite thin film grown by pulsed laser ablation.

High quality ceramic target of $Zn_{0.3}Mn_{0.8}Si_{0.1}Fe_{1.8}O_4$ (ZMSFO)(x = 0.1) with 18 mm diameter was used for pulsed laser deposition (PLD) using KrF excimer laser (λ = 248 nm). As received $Pt/SiO_2/Si$ substrates of area 15x15 mm^2 were used for the film growth. For the PLD experiments, the laser pulse repetition rates and laser powers were fixed at 10 Hz and 2.1 J, respectively. Substrate temperature of 700 ºC with 1 mTorr of oxygen partial pressure was controlled throughout the depositions. The ZMSFO was deposited on Pt/SiO2/Si by using a metal shadow mask on 10x15 mm^2 area. Typical film thickness was controlled to be ~260 nm. High purity Ag was thermally evaporated on ZMSFO active layer through a metal shadow mask to form the top electrode of area 400 x 300 μm^2. Schematic of cross section of $Ag/ZMSFO/Pt/SiO_2/Si$ sandwich geometry is shown as an inset in Figure 4.11(b).1. The $Ag/ZMSFO/Pt/SiO_2/Si$ heterostructure was characterized by grazing incidence X-ray diffraction (GIXRD, PANalytical), AFM (Nanosurf AG), cross sectional SEM (Raith GmbH), stylus surface profiler (DekTac. 3.2, Veeco), I-V (Keithley 4200 Semiconductor characterization system). All the measurements were performed at room temperature (300K).

Figure 4.11(b).1 shows the GIXRD and two dimensional AFM images of PLD grown ZMSFO film on Pt/SiO2/Si substrate. All the peaks corresponding to single fcc phase is evident. The unit cell parameter estimated from the GIXRD was 8.43 Å, which is lower than that of the reported bulk ferrite composition (a = 8.488 A) (Table 4.2.2). AFM images show uniform grain distribution and the

average particle size estimated form the AFM is in the range of 50-65 nm. The root means square (RMS) roughness estimated from the AFM image is ~ 6.8 nm, which is fairly small suggesting a smooth morphology.

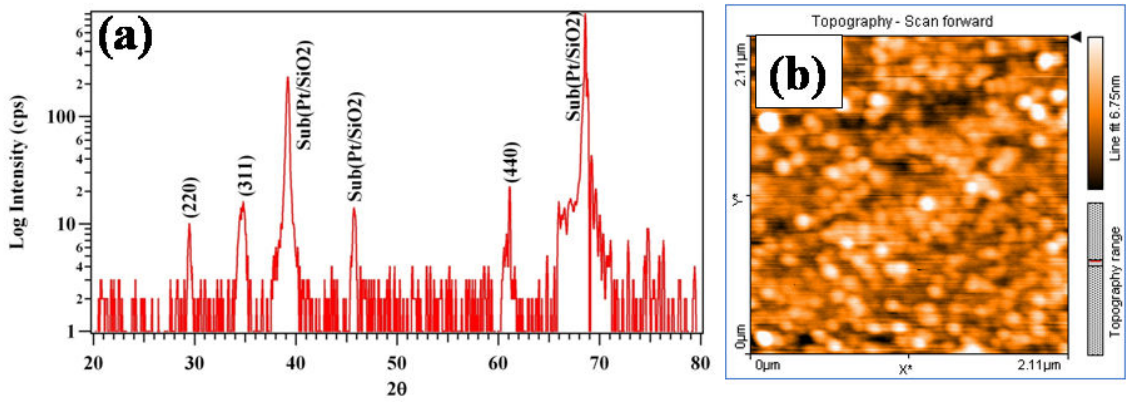

Figure 4.11(b).1. GIXRD pattern of ZMSFO film grown on Pt/SiO_2/Si substrate. Single cubic phase can be seen. (b) Bi-dimensional AFM surface topography of ZMSFO/Pt/SiO_2/Si heterostructure.

Electrical properties of Ag/ZMSFO/Pt/SiO_2/Si heterostructure were evaluated by using two probe technique and are displayed in Figure 4.11(b).2. Inset of Figure 4.11(b).2(a) shows typical sample geometry used for the I-V measurements.

As can be seen in Figure 4.11(b).2(a), only linear I-V curves were traced for all the voltage sweeping cycles for the Ag/ZMSFO/Pt/SiO_2/Si structures suggesting no resistance switching behavior. These results indicate that the interface related electrical transport seems less probable for the resistance switching phenomenon in the ferrite systems in thin film form.

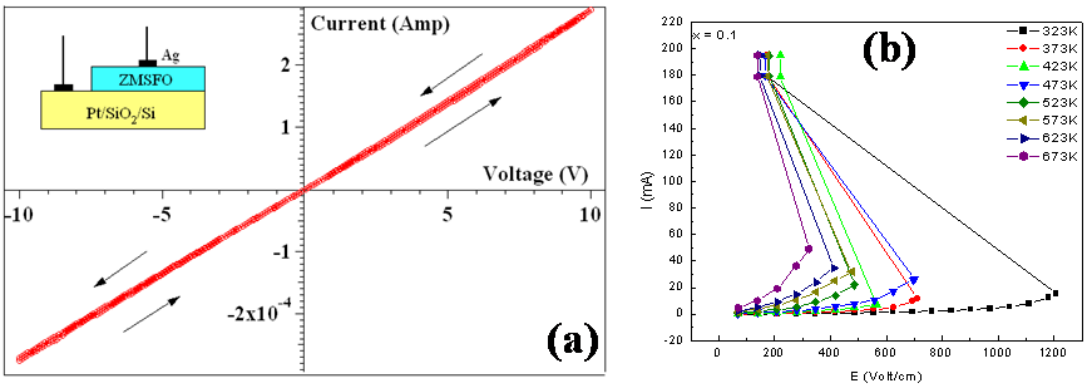

Figure 4.11(b).2. **(a) I-V characteristics of Ag/ZMSFO/Pt/SiO_2/Si heterostructure. Inset shows the schematic of measurement geometry and arrows indicate typical voltage sweeping cycles (b) I-E characteristics of bulk ZMSFO system showing a sharp resistance switching with temperature dependence.**

Conclusions

(i) We have investigated the microstrcutural and electrical properties of Ag/ZMSFO/Pt/SiO_2/Si heterostructure fabricated by PLD. Nanostructure growth with smooth surface was confirmed in the single phase ZMSFO film..

(ii) Current versus voltage characteristics show only a linear behavior without any resistance switching.

4.12 AC resistivity and Dielectric properties study

Figure 4.12.1 shows the variation of ac resistivity ($\log\rho_{ac}$) with frequency measured at different temperatures.

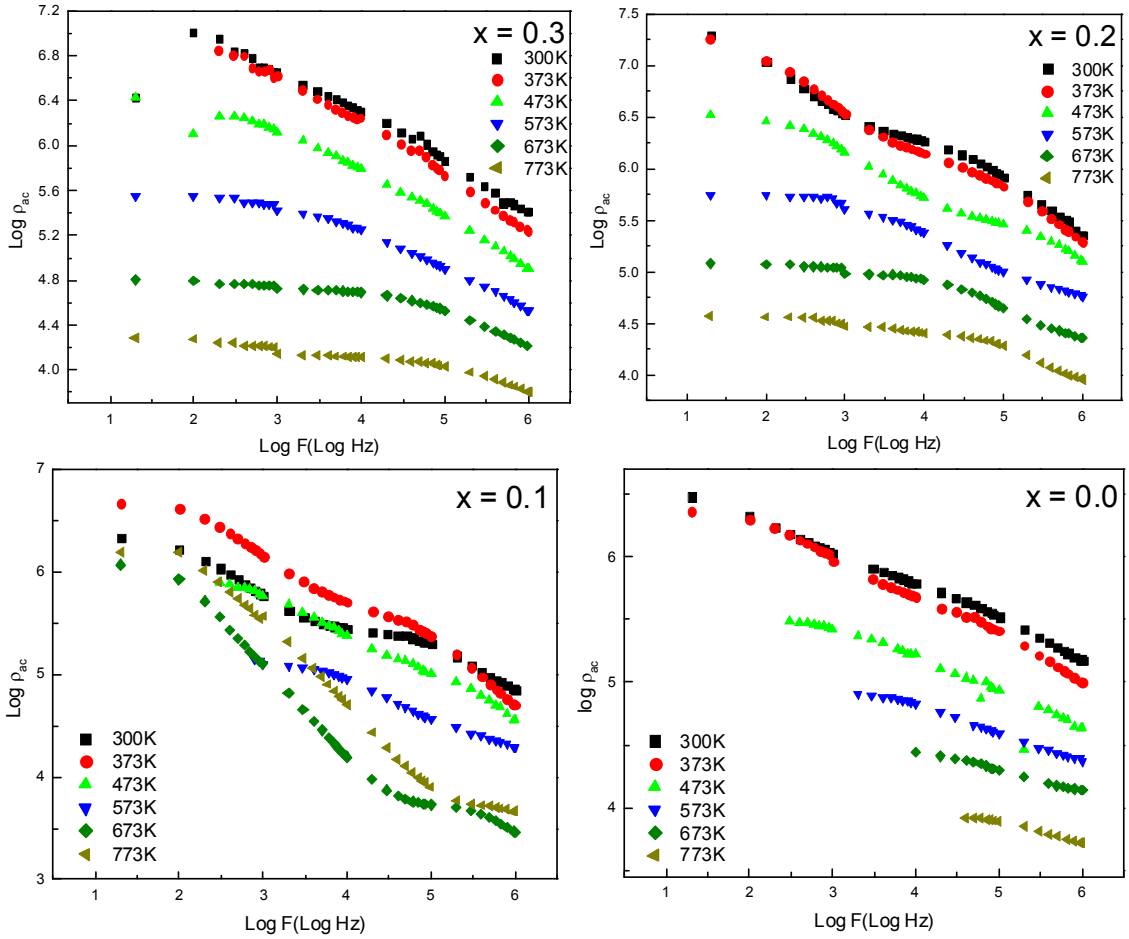

Figure 4.12.1. Frequency dependent ac resistivity behavior of x = 0.0 – 0.3 compositions at different temperatures.

All the samples show decrease in ρ_{ac} with increase in frequency from 100 H_z – 1MH_z which is the normal behavior of ferrites. The conduction mechanism in ferrites can be explained on the basis of hopping change carriers between Fe^{2+} and Fe^{3+} ions on the B-site. The increase in frequency of the

applied field enhances the hopping of charge carriers resulting in an increase in the conduction process thereby decreasing the resistivity. It has been observed that for x = 0.0 and 0.1 compositions the variation of ρ_{ac} is sensitively dependent on the frequency and temperature. This indicates that grain boundary effects are not sufficiently minimized for highly pressed pellets even at high temperatures. It is found for x = 0.2 and x = 0.3 compositions, the ρ_{ac} is temperature dependent but having less effect of frequency at high temperatures. This suggests that for these compositions grain boundary contributions are negligible at least at higher temperature.

The frequency (f) dependence plots of the real (ε') and imaginary (ε") parts of the complex dielectric permittivity (ε*) and the dielectric loss tangent (tanδ) for all the compositions of $Zn_{0.3}Mn_{0.7+x}Si_xFe_{2-2x}O_4$, x = 0.0, 0.1, 0.2 and 0.3 system at several temperatures are plotted in Figure 4.12.2 – 4.12.4.

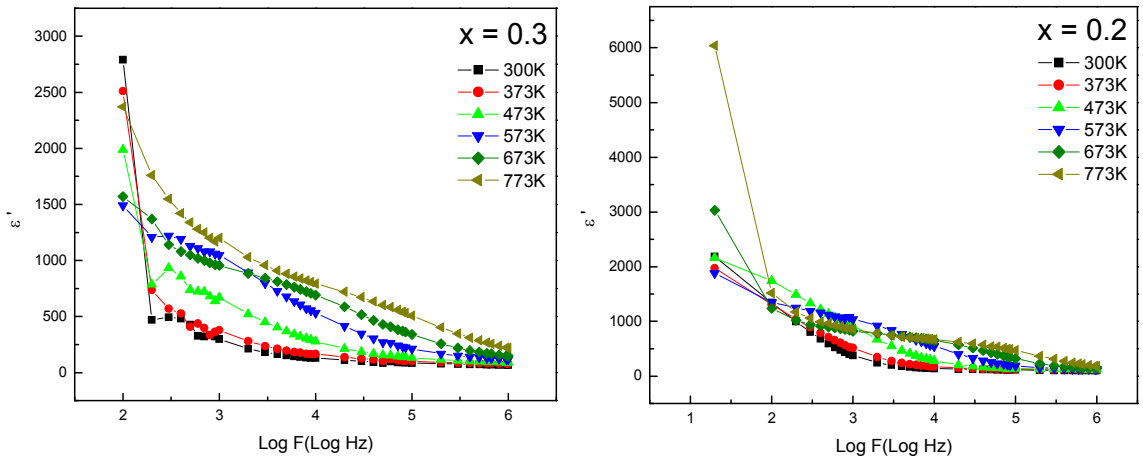

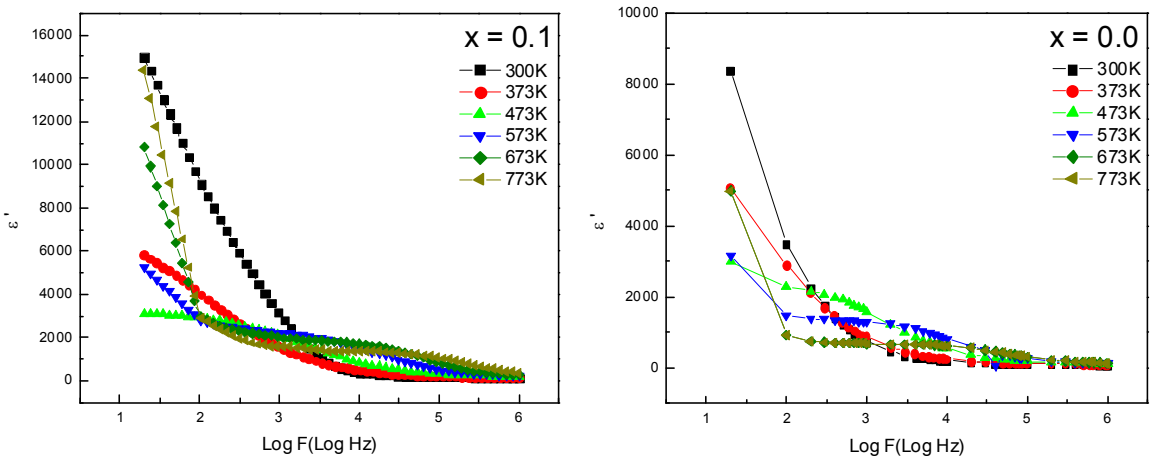

Figure 4.12.2. Frequency dependent behavior of real (ε') part of permittivity at different temperatures for x = 0.0 – 0.3 compositions.

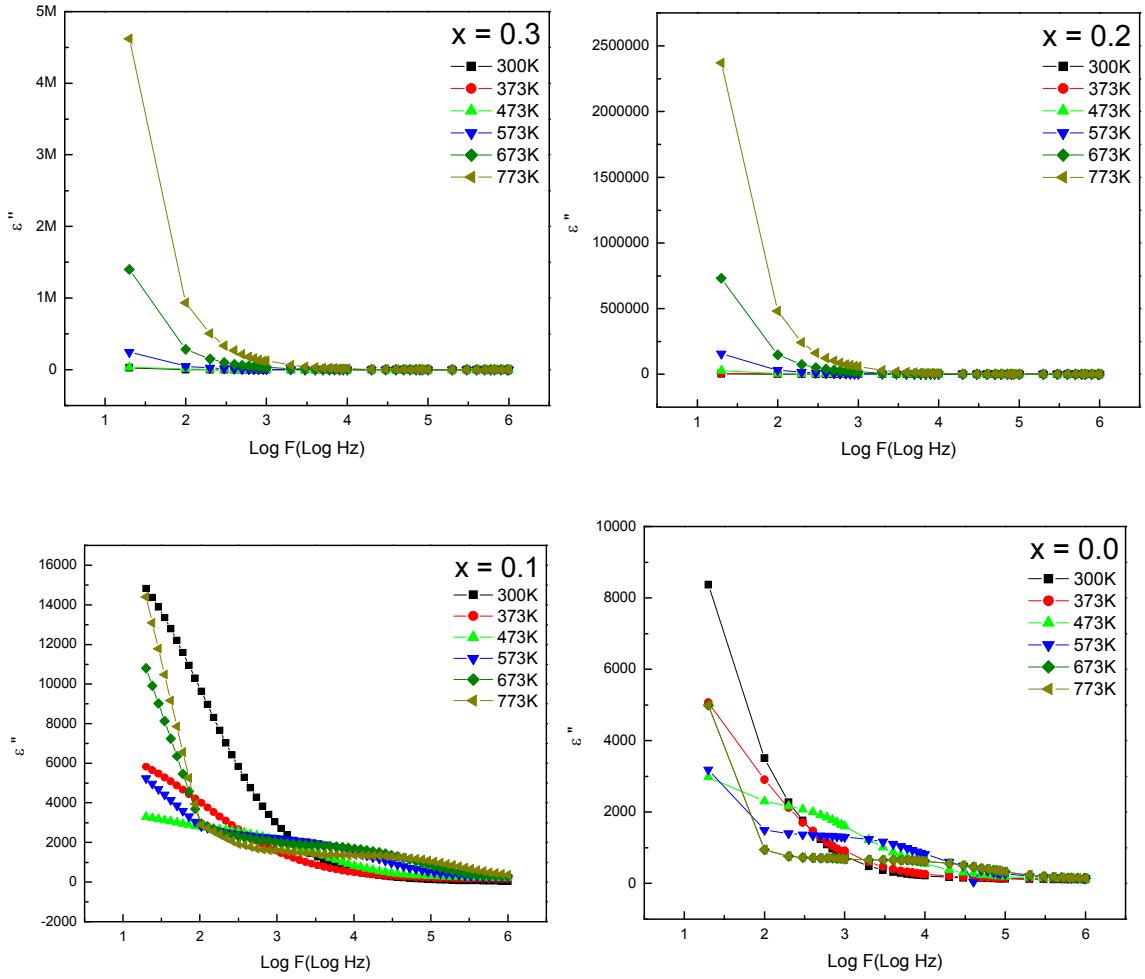

Figure 4.12.3. Frequency dependent behavior of imaginary (ε'') part of permittivity at different temperatures for x = 0.0 – 0.3 compositions.

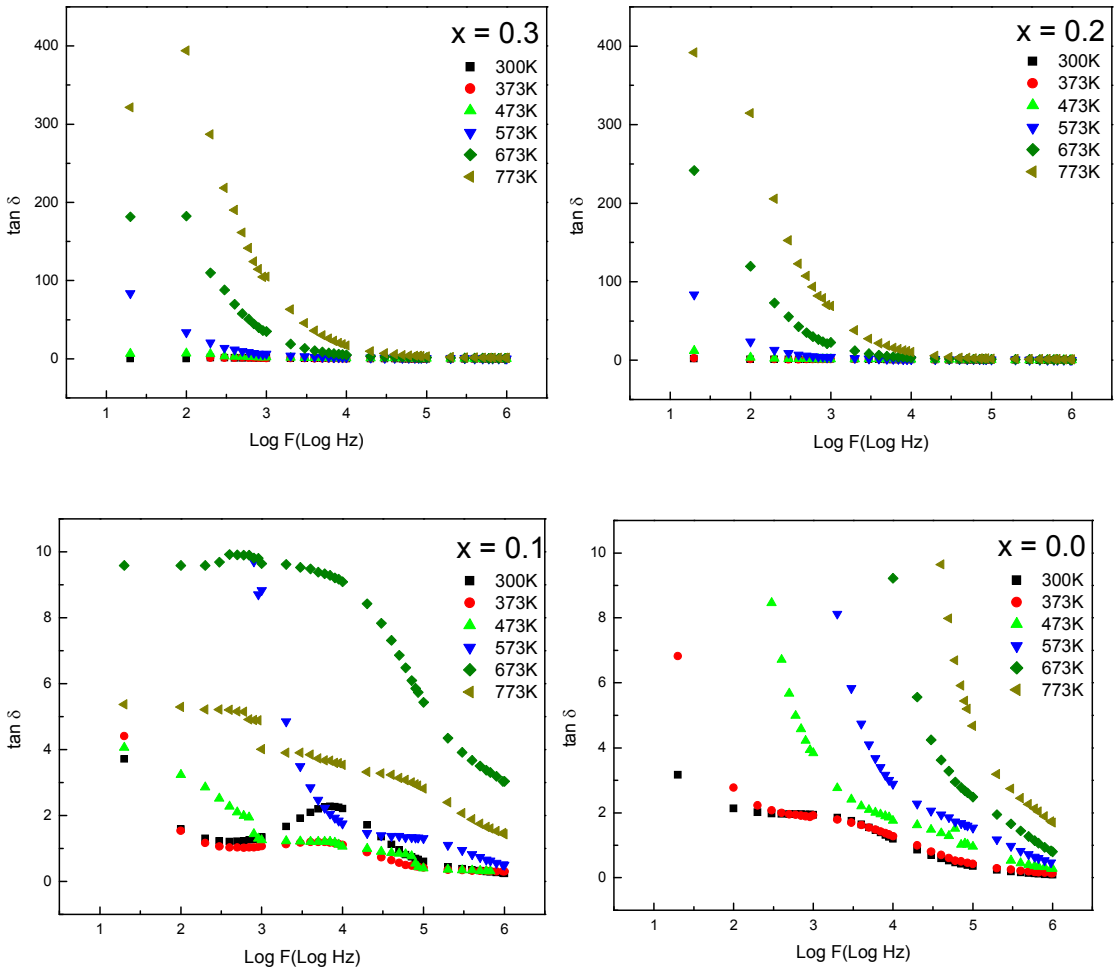

Figure 4.12.4. Frequency dependent behavior of loss tangent at different temperatures for x = 0.0 – 0.3 compositions.

The bird eye view of Figures 4.12.2- 4.12.4 show following main features.

(i) The ε' and ε" decrease as the frequency increases from 100 Hz and 1 MHz.

(ii) The dielectric constant decreases rapidly in low frequency region and the rate of decreases is slow in high frequency region, the behavior almost approaches to frequency independent behavior.

(iii) The ε" is found to decrease faster than ε' in the low frequency region and the variation is same as ε' in higher frequency region.

The phenomenon of dielectric dispersion in ferrites may be attributed to 'free' charge buildup at interfaces within the bulk of the samples, (interfacial Maxwell – Wagner – Sillars (MWS) polarization [1]) and the interface behavior the sample and the electrodes (space charge polarization [2]). The polarization in ferrites is through a mechanism similar to conduction process. In this model the exchange of electrons between Fe^{2+} and Fe^{3+} at the octahedral (B-) site of spinel lattice results in local displacement of charge carriers in the direction of applied field, which causes polarization. The polarization decreases with increase in frequency and then reaches a constant value due to the fact that beyond a certain frequency of external field the electron exchange cannot follow the alternating field.

The higher values of dielectric constant (ε') observed at lower frequencies are also explained on the basis of Maxwell –Wagner two layer model [3,4] and Koop's phenomenological theory of dielectric [5]. In ferrites, it is well known that the samples consist of well conducting grains separated by poorly conducting grain boundaries [5]. In ferrites the permittivity is directly proportional to the square root of conductivity [6], therefore, grains have high value of permittivity

and grain boundaries have smaller values of permittivity. At lower frequency the grain boundaries are more effective than grain in electrical conduction. Thinner the grain boundary higher is the value of dielectric constant.

The loss tangent or tanδ is defined as the ratio of the imaginary part of the dielectric constant (ε') to the real part of (ε'). The variation of tanδ with frequency at different temperature for x = 0.0 -0.3 composition is studied. The tanδ decreases with increasing frequency and can be explained on the basis of Koop's phenomenological model [5].

Conclusions

The frequency variation of dielectric parameters can be explained in the light of Maxwell-Wagner interfacial polarization and Koop's phonological theory of dielectrics.

References

1 P. Hedving, Dielectric Spectroscopy, edited by J. R. Macdonald, (Wiley, New York) (1987) Chap. 2.

2 A. Kyritsis, P. Pissis and J. Grammatikakis, J. Polym. Sci. Polym. Phys., 33 (1995) 1737.

3 J. C. Maxwell, Electricity and magnetism, Vol.1, Oxford University Press, (1977) p. 328.

4 K. Wagner, Ann. Phys., 40 (1993) 817.

5 C. G. Koop, Phys. Rev., 83 (1951) 121.

Chapter – 5

Results and discussion

5. Brief review on some physical properties of Ti^{4+} substituted Al^{3+} containing Mn-Zn ferrites, $Zn_{0.3}Mn_{0.7+x}Ti_xFe_{1.9-2x}Al_{0.1}O_4$ (x = 0.0, 0.1, 0.2, 0.3) (Mn-Ti system), and comparative study with $Zn_{0.3}Mn_{0.7+x}Si_xFe_{2-2x}O_4$ system (Mn-Si system).

With the aim to ratify the purity and surety of the chemical compositions EDAX characterization was carried out. The EDAX spectra for typical compositions, x = 0.0 and 0.2 of $Zn_{0.3}Mn_{0.7+x}Ti_xFe_{1.9-2x}Al_{0.1}O_4$ spinel ferrite system are shown in Figure 5.1.

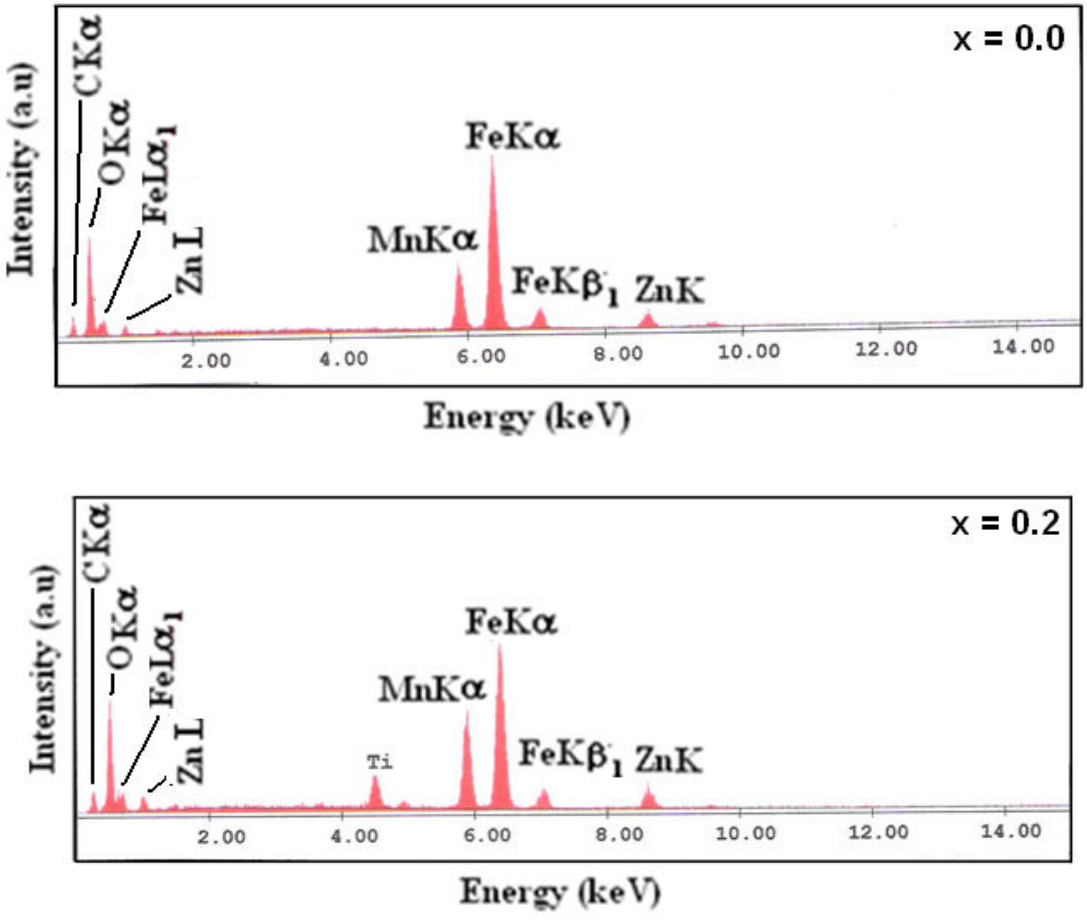

Figure 5.1. EDAX patterns for x = 0.0 and x = 0.2 compositions of Mn-Ti system.

On the basis of various bands assignment and weight percentage calculations for the different elements present in the system, it is confirm that the compositions are stoichiometric compositions.

Particle size distribution curve for x = 0.2 composition of Mn-Ti system is shown in Figure 5.2. The nature and the values of different parameters thus determined are consisting with Mn-Si system.

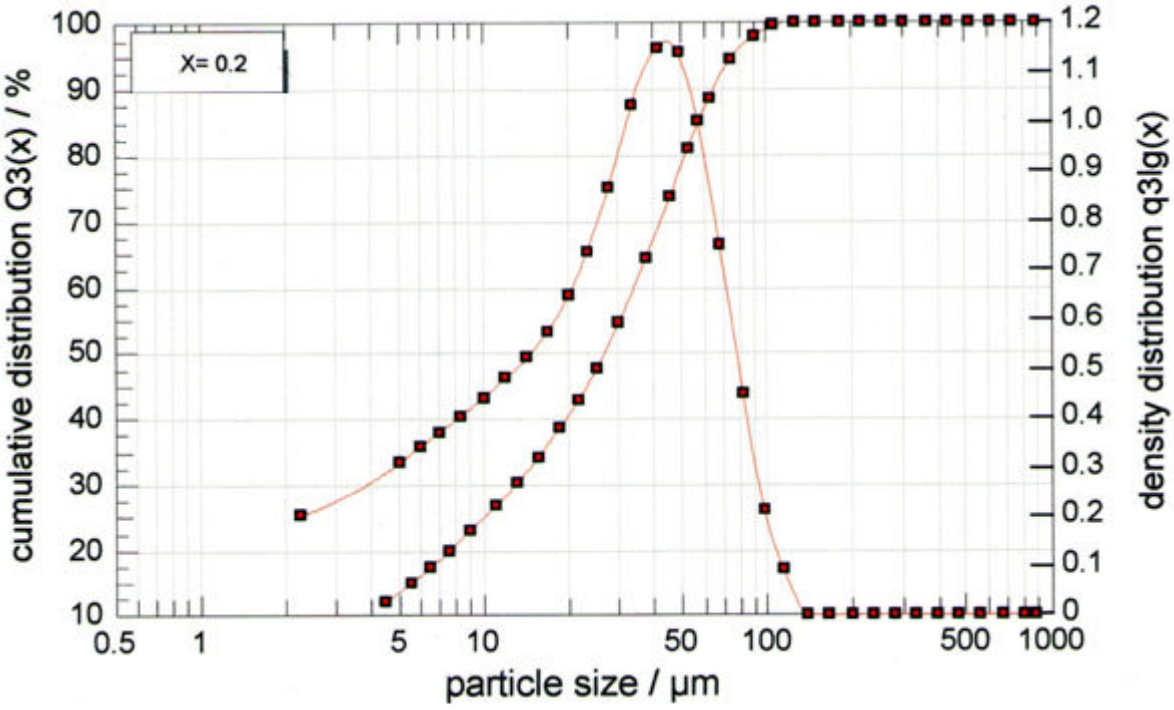

Figure 5.2. Particle size distribution curve for x = 0.2 composition of $Zn_{0.3}Mn_{0.7+x}Ti_xAl_{0.1}Fe_{1.9-2x}O_4$ system.

Figure 5.3 shows Rietveld fitted X-ray powder diffraction patterns for x = 0.0 and 0.3 compositions. The analysis leads to conclude that un-substituted composition, x = 0.0, possesses single phase spinel structure. On the other hand, un-substituted composition of Mn-Si system has shown minor hematite phase. This may be due to the presence of very small amount of Al^{+3} ion in the system, as other synthesis parameters are kept identical for both the systems. Furthermore, compositions with x > 0.1 of Mn-Ti system show formation of alpha Fe_2O_3 phase, that was absent in Mn-Si system.

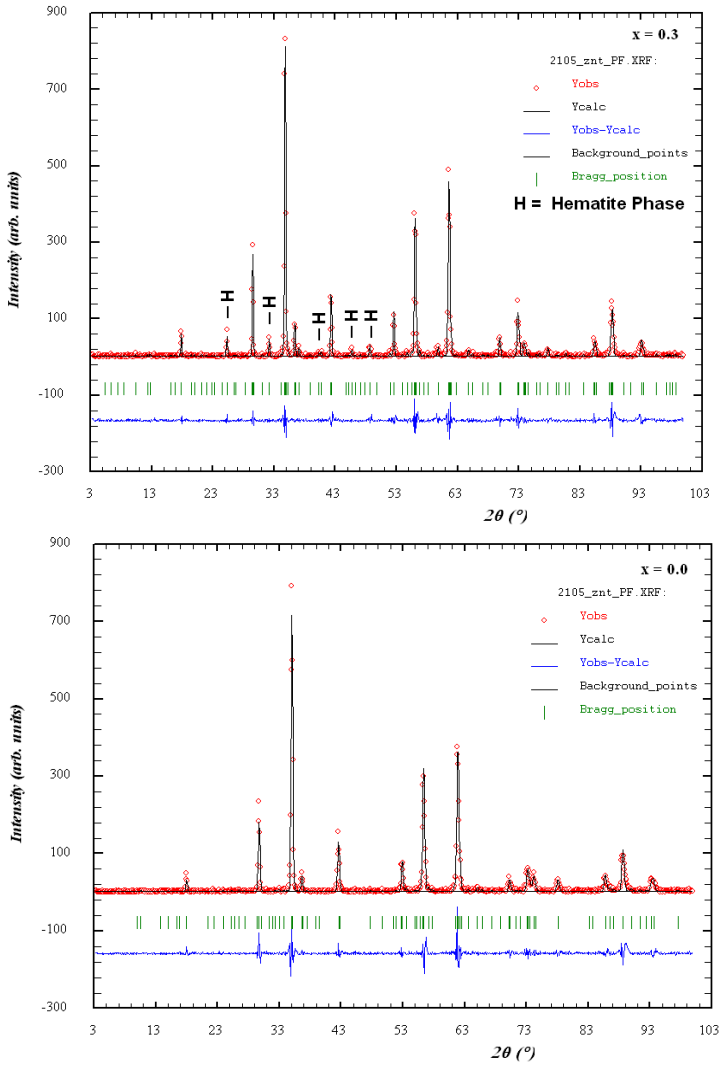

Figure 5.3.

Observed (Solid Circles) and calculated (Solid line) x-ray powder diffraction patterns for the $Zn_{0.3}Mn_{0.7+x}Ti_xAl_{0.1}Fe_{1.9-2x}O_4$ (x = 0.0 and 0.3) system at 300K. The difference between the observed and calculated spectra is plotted at the bottom. The ticks indicate allowed Bragg peaks positions.

Table 5.1 Cation distribution and lattice constant for Mn-Ti system.

Mn-Si content (x)	Cation distribution	a(Å) ±0.002Å
0.0	$(Zn_{0.25}Al_{0.05}Mn_{0.40}Fe_{0.30})[Zn_{0.05}Al_{0.05}Mn_{0.30}Fe_{1.6}]O_4$	8.478
0.1	$(Zn_{0.25}Al_{0.05}Ti_{0.05}Mn_{0.43}Fe_{0.22})[Zn_{0.05}Al_{0.05}Ti_{0.05}Mn_{0.37}Fe_{1.48}]\ O_4$	8.485
0.2	$(Zn_{0.25}Al_{0.05}Ti_{0.1}Mn_{0.45}Fe_{0.15})[Zn_{0.05}Al_{0.05}Ti_{0.1}Mn_{0.45}Fe_{1.35}]\ O_4$	8.491
0.3	$(Zn_{0.25}Al_{0.05}Ti_{0.15}Mn_{0.48}Fe_{0.06})[Zn_{0.05}Al_{0.05}Ti_{0.15}Mn_{0.52}Fe_{1.23}]\ O_4$	8.500

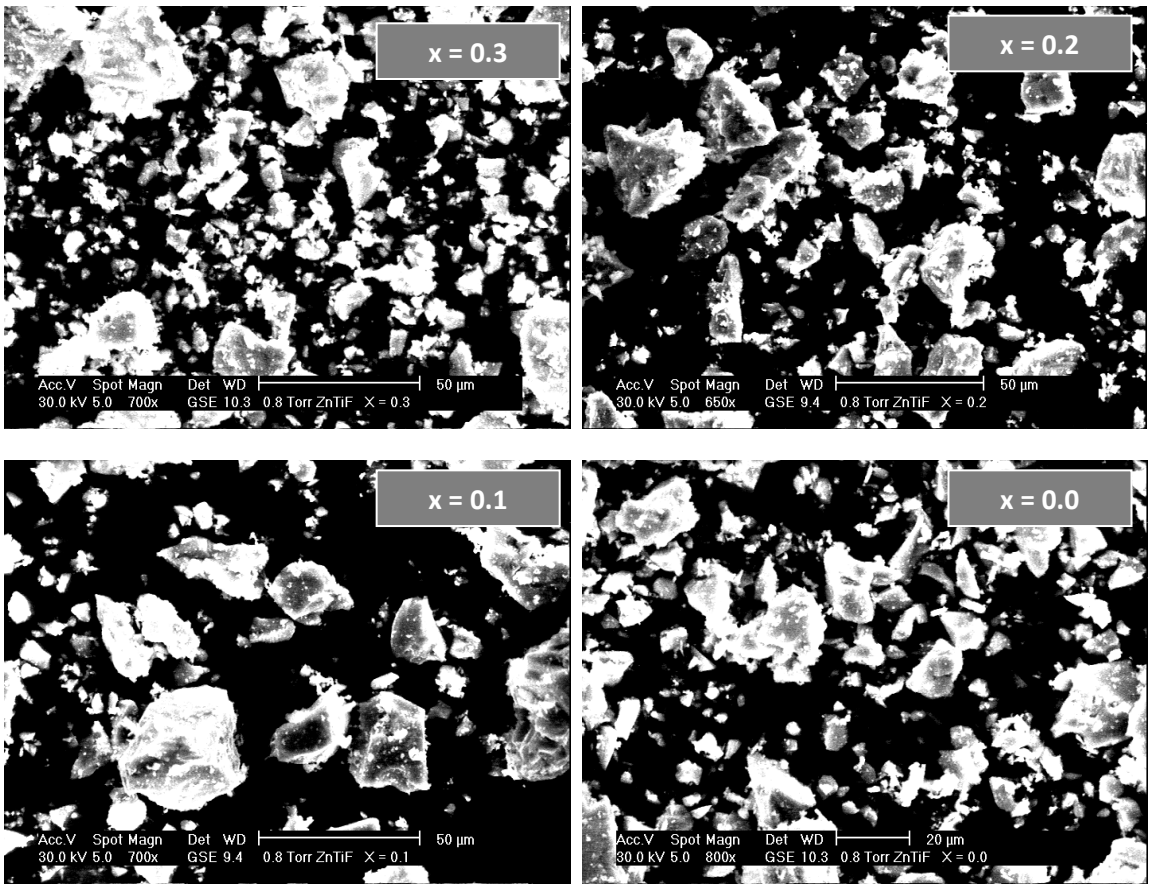

Figure 5.4. Scanning electron micrographs for $Zn_{0.3}Mn_{0.7+x}Ti_xAl_{0.1}Fe_{1.9-2x}O_4$ spinel ferrite system.

Scanning electron micrographs of Mn-Ti system are shown in Figure 5.4. The SEMs were taken on powdered samples instead of broken pellet as in the case of Mn-Si system, thus no conclusive observations can be made.

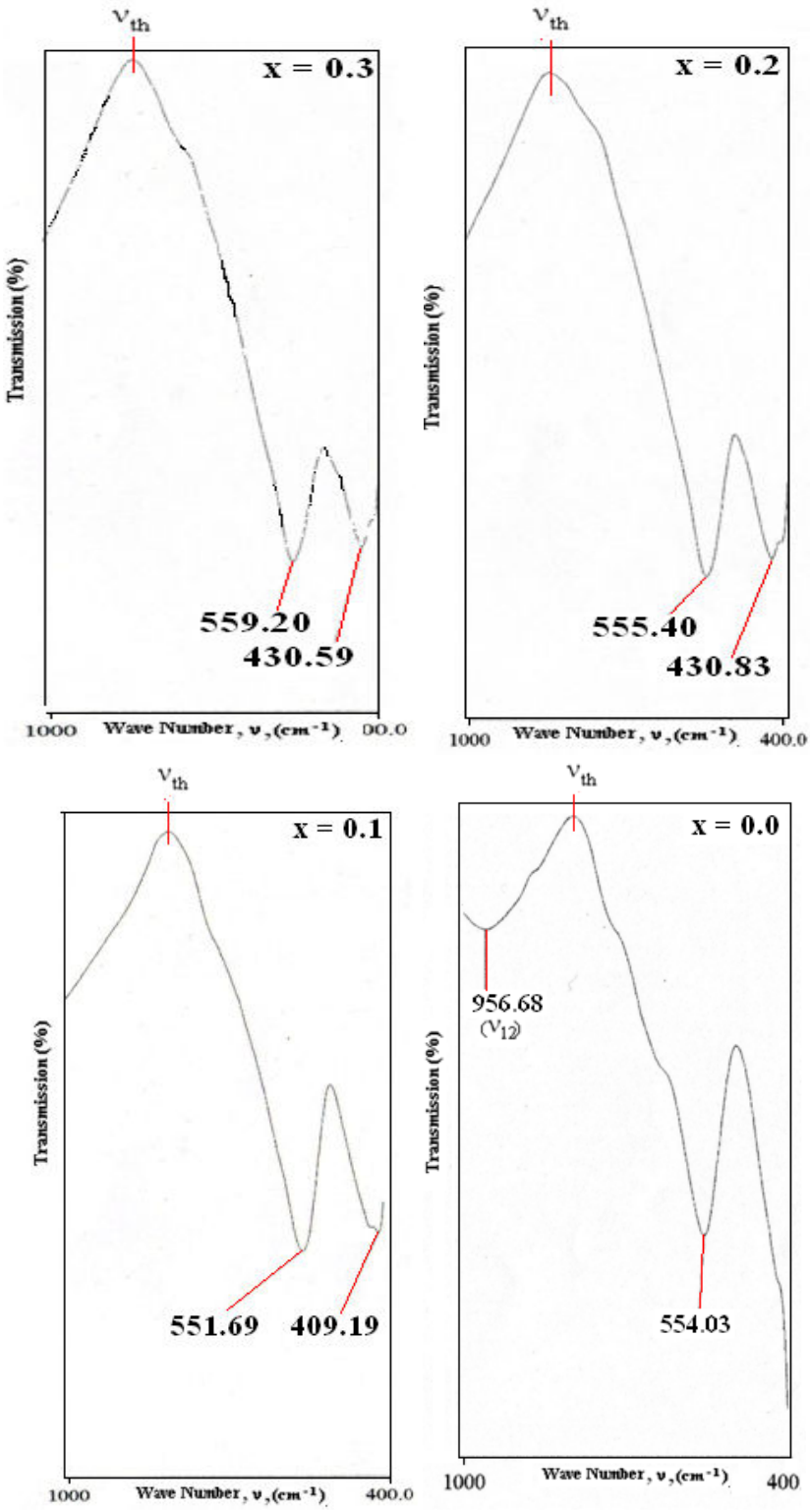

Figure 5.5. Infrared absorption spectra for $Zn_{0.3}Mn_{0.7+x}Ti_xAl_{0.1}Fe_{1.9-2x}O_4$ (x=0.0-0.3) system at 300K.

The room temperature infrared absorption spectra for all the ferrites studied are shown in Figure 5.5. The nature of spectra for Mn-Ti system is similar to that for Mn-Si system with minor differences in band positions, intensity and band width. Furthermore, for all the substituted compositions linear combitional bands just above to the Vth band are absent which were observed for all the compositions of Mn-Si system.

High field slope to magnetization curves (Figure 5.6), suggests canted spin structure for all the studied compositions. The saturation magnetization value for x = 0.0 composition of Mn-Ti system is much higher than the Mn-Si system while for x = 0.1,0.2 and 0.3, σ_s values are smaller than the corresponding compositions of Mn-Si system.

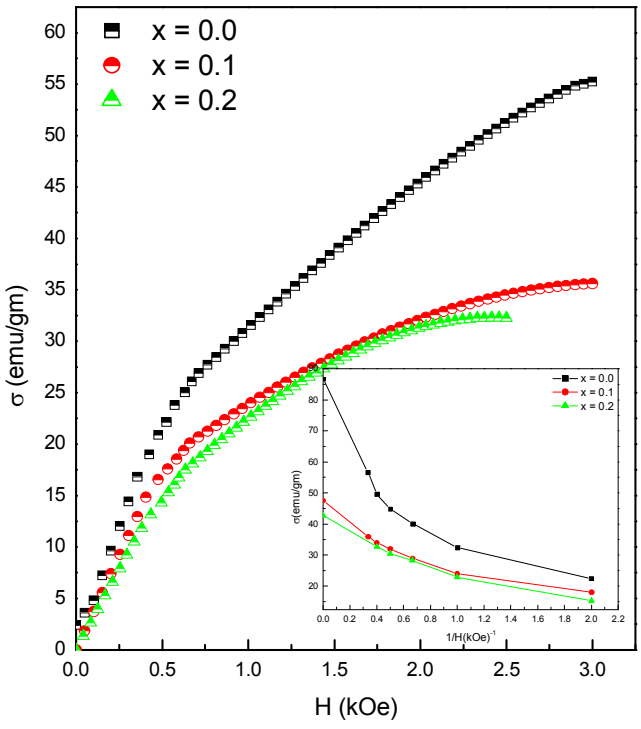

Figure 5.6.

Field dependence of magnetization at 300K.

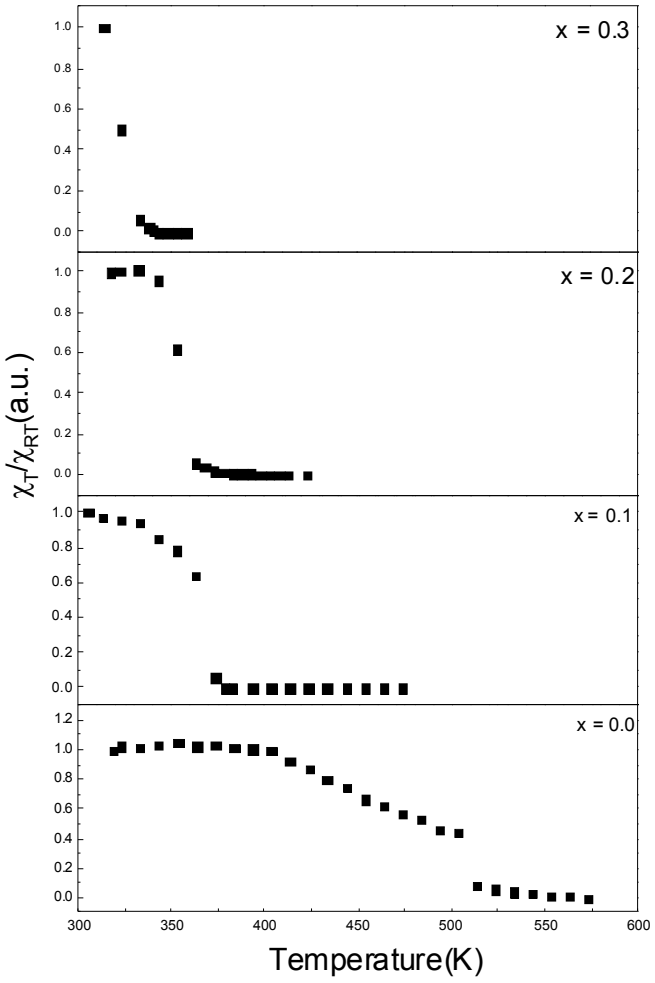

Figure 5.7. Temperature dependent ac susceptibility for $Zn_{0.3}Mn_{0.7+x}Ti_xAl_{0.1}Fe_{1.9-2x}O_4$ (x=0.0-0.3) system.

Variation of low field ac susceptibility with temperature for x = 0.0 – 0.3 compositions of Mn-Ti system is shown in Figure 5.7. The Neel temperatures determined for Mn-Ti system are found lower than the Mn-Si system, may be due to weakening in A-B interactions by the presence of non-magnetic Al^{+3} ion in the system or change in cation distribution.

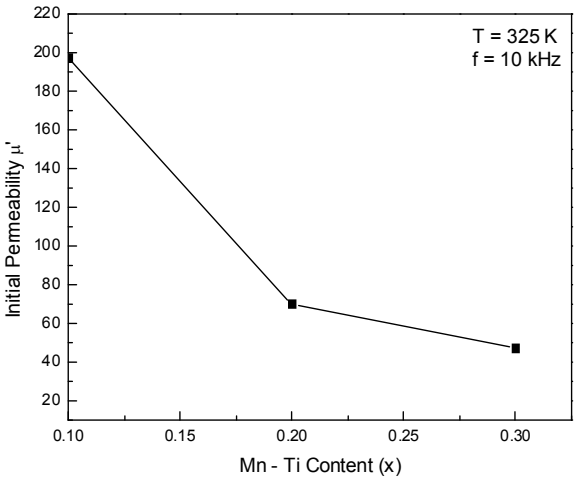

Figure 5.8(a). Variation of μ' with Mn-Ti concentration (x) at 325K at applied frequency of 10kHz.

The variation of initial permeability with composition, frequency and temperature for Mn-Ti system is similar to that of Mn-Si system with expected difference in magnitude of initial permeability and Neel temperatures values.

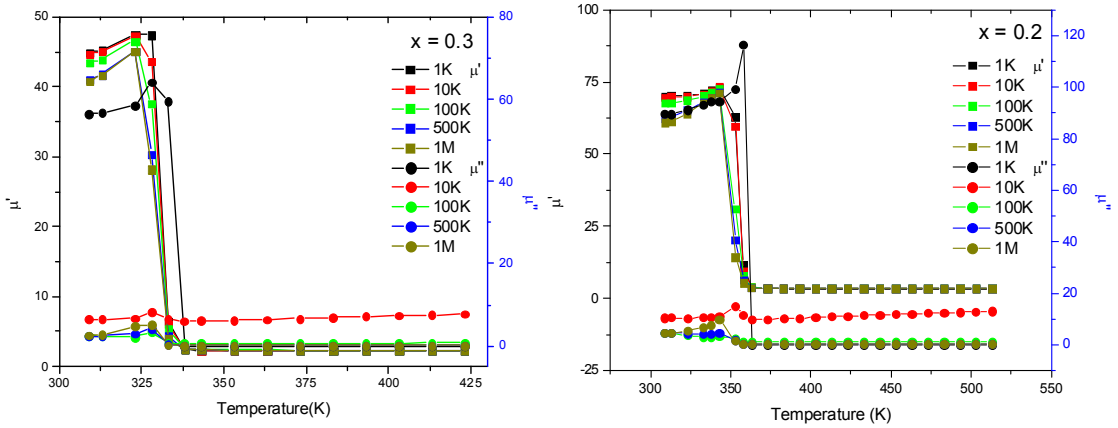

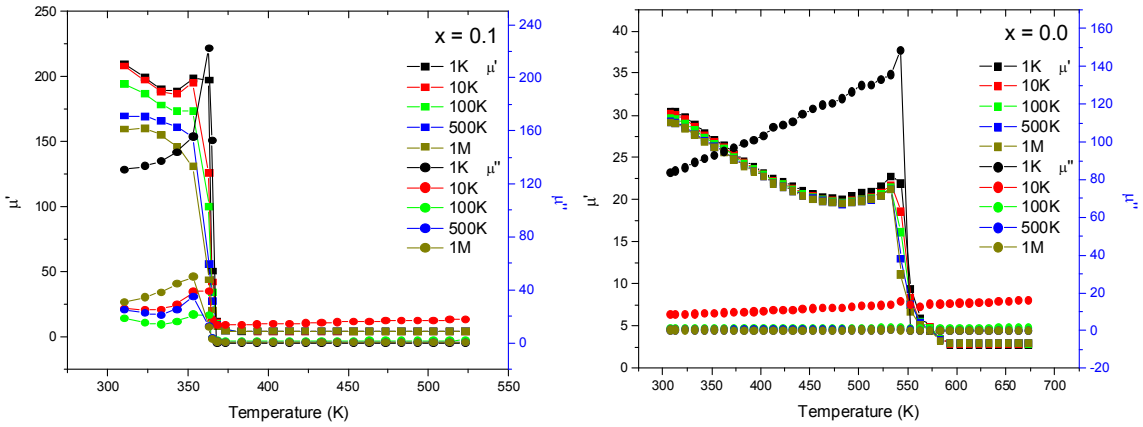

Figure 5.8(b) Thermal variation of real (μ') and imaginary (μ'') parts of permeability at differentas frequencies for Mn-Ti system.

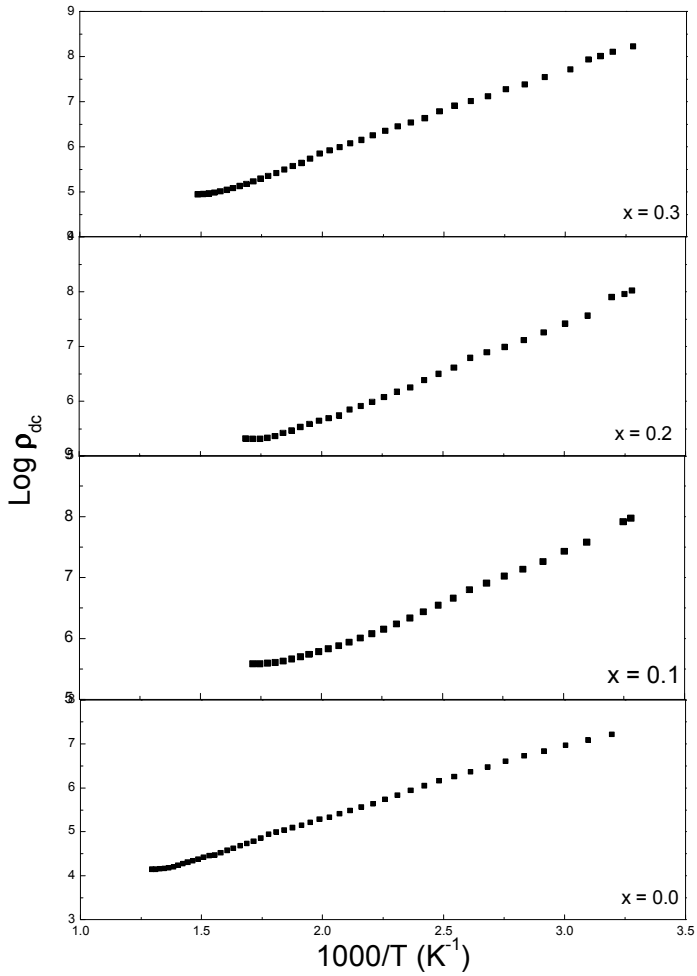

Figure 5.9 Electrical resistivity versus temperature for x = 0.0, 0.1, 0.2 and 0.3 compositions of $Zn_{0.3}Mn_{0.7+x}Ti_xAl_{0.1}Fe_{1.9-2x}O_4$ system.

Two probe DC resistivity as a function of reciprocal of temperature is depicted in Figure 5.9. All the compositions of Mn-Ti system show normal semiconducting behavior without any change of slope in vicinity to the corresponding Neel temperature, similar to that of Mn-Si system. The activation energies are slightly higher for Mn-Ti system.

Table 5.2 Activation energy (E_e) for Mn-Ti system

Mn-Ti content (x)	Ee (eV)
0.0	0.32
0.1	0.33
0.2	0.34
0.3	0.37

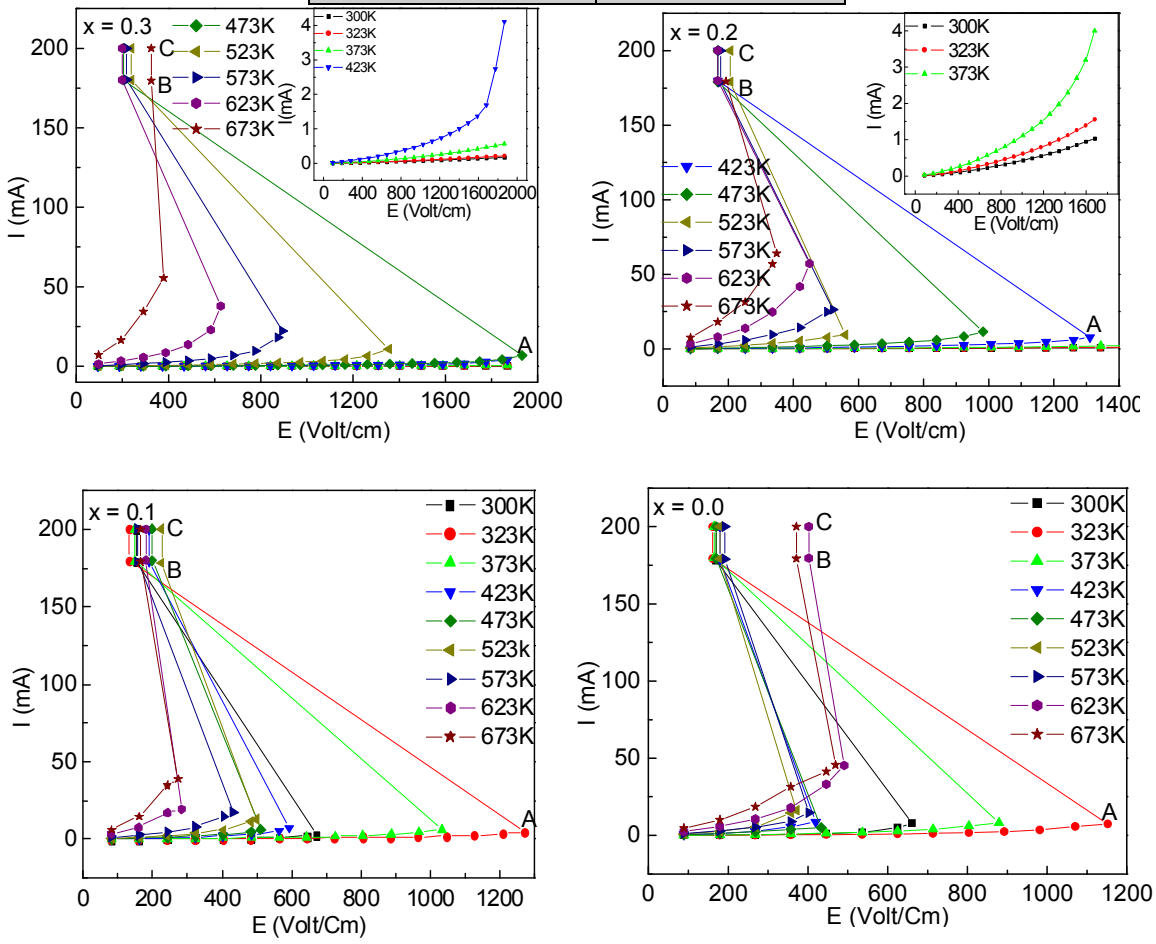

Figure 5.10(a). I-E relationship at different measuring temperatures for x = 0.0-0.3 compositions of Mn-Ti system.

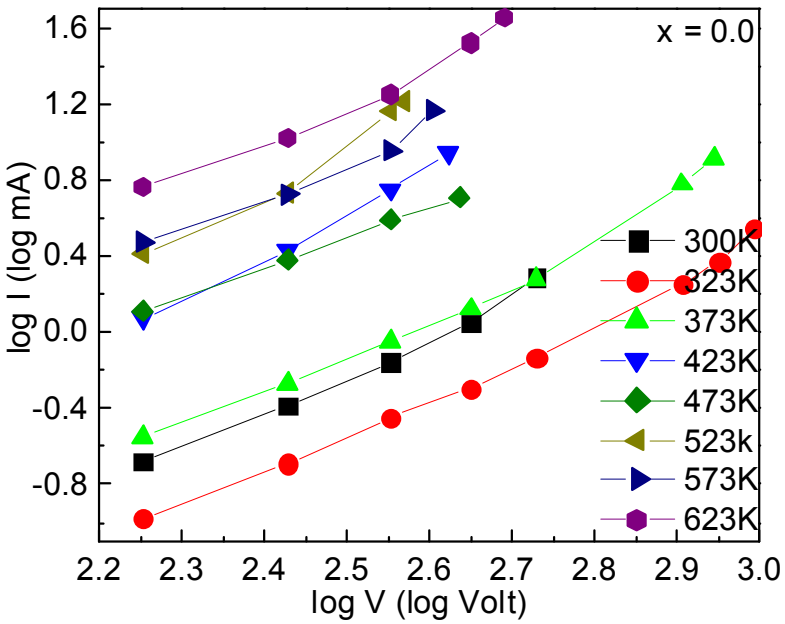

Figure 5.10(b). Log I versus Log V characteristics at different temperatures for x = 0.0 composition of Mn-Ti system.

The current controlled negative resistance (CCNR) type electrical switching or electrical break down has been observed for all the compositions of Mn-Ti system. The strength of electric field and temperature at which switching takes place for different compositions are shown in Table 5. It is found that for the compositions with x = 0.0, 0.1 and 0.2, electrical field strength and temperature of switching are lower for Mn-Ti system while they are higher for x = 0.3 composition as compared to Mn-Si system. The difference may be due to difference in the cation distribution for both the systems.

Table 5.3 Electric field strength (E) and switching temperature (T_s) for Mn-Ti system.

Mn – Ti content (x)	E (V/cm)	Ts(K)
0.0	661	300
0.1	673	300
0.2	1311	423
0.3	1932	473

List of publications

1. Study of electric and dielectric properties of Mn^{4+}- substituted cobalt ferrite
   V.K. Lakhani, P.U.Sharma, **K.G.Saija** K.B.Zankat and K.B.Modi
   Indian Journal of Physics 80 (8) (2006) 789-796
2. Structural properties of magnesium and aluminum co-substituted lithium ferrite.
   K.B.Modi, J.D.Gajera, M.C.Chhantbar, **K.G.Saija**, G.J.Baldha and H.H.Joshi
   Materials Latters 57(2003) 4049-4053
3. Study of cation distribution and macromagnetic properties of magnesium and aluminium co-substituted lithium ferrite
   G. J. Baldha, **K.G. Saija**, K.B. Modi, H.H. Joshi, and R.G. Kulkarni
   Materials Letters 53(2002) 233-237
4. Temperature Dependent Dielectric Behaviour of Mn^{4+} Substituted Cobalt Ferrite
   V.K.Lakhani, H.G.Vora, **K.G.Saija**, K.B.Modi and G.J.Baldha
   Solid State Physics (India) (2004) 74.
5. Unusual magnetic properties of nanocrystalline $Mg_xMn_{1-x}Fe_2O_4$ (x = 0.2, 0.4) synthesized by co-precipitation method
   T. K. Pathak, V. K. Lakhani, N. H. Vasoya, **K. G. Saija**, A. G. Makwana and K. B. Modi
   52nd DAE Solid State Physics Symposium (2007) University of Mysore, Mysore.
6. CCNR type high field instability in Ti4+-substituted Mn–Zn ferrites
   K G Saija, U S Joshi, V K Lakhani and K B Modi
   J. Phys. D: Appl. Phys. **42** (2009) 165402.
7. Magnetic properties of the mixed spinel $Li_{0.5x}Fe_{2.5x}Mg_{1-x}Al_{2-2x}O_4$
   K.G.Saija, K.P.Thummer and G.J.Baldha
   39th DAE Solid State Physics Symposium (1996) BARC, Mumbai.

8. Elastic constants determination for bulk metallic glasses and alloys –A simple theoretical approach
K.B.Zankat, V.K.Lakhani, N.H.Vasoya, V.R.Rathod and **K.G.Saija**
51st DAE Solid State Physics Symposium (2006) Barkatullah university, Bhopal

Conferences/Workshops/Seminar attended

1. DAE-BRNS Symposium on Electroceramics, March 13-15, 1996, Saurashtra University, Rajkot.
2. XVIII Gujarat Science Congress, March 13, 2004, Saurashtra University, Rajkot.
3. Current Trends in Materials Research, February 28, 2005, Saurashtra University, Rajkot.
4. Recent Advances in Condensed Matter and Space Physics, March 21, 2006, Saurashtra University, Rajkot
5. Seminar on Advanced in Material Research, February 15, 2008, Saurashtra University, Rajkot
6. Current Trends In Research In Physics & Industrial Applications
17 January, 2010, M. M. Science College, Rajkot
7. Nanoscience and Nanotechnology: A Curriculum Devlopment Approach, 21 February, 2010, Matushri Virbai Mahila Science and Home Science College, Rajkot